GEORG-AUGUST-UNIVERSITÄT
GÖTTINGEN

Diploma Thesis

Untersuchung turbulenter Strömungen auf der Umweltforschungsstation Schneefernerhaus (Zugspitze)

Investigation of turbulent flows at the Umweltforschungsstation Schneefernerhaus (Zugspitze)

prepared by

Steffen Risius

from Emden

at the Institute for Nonlinear Dynamics

Thesis period:	16th June 2011 until 16th March 2012
First referee:	Prof. Dr. E. Bodenschatz
Second referee:	Prof. Dr. A. Dillmann

Abstract

This thesis reports measurements of the large scale property and the tetrad-based velocity gradient tensor of the turbulent flow at the environmental research station Schneefernerhaus (UFS) at a height of 2700m near the top of Zugspitze, the highest mountain in Germany. The measurements were conducted with five 3-D ultrasonic anemometers sampling at 10 Hz and arranged in the configuration of two nearly isotropic tetrahedra.

The wind at UFS is dominantly in the east-west direction and nearly horizontal. These flow conditions and the high Reynolds number of up to $R_\lambda \approx 10^4$ make it a good site for the investigation of turbulence. The continuous recordings are used to determine velocity correlations, second and third order structure functions, Reynolds stresses and integral length scales. These results are used to study the normalized energy dissipation rate and the invariants of the anisotropic Reynolds stress tensor as a function of Reynolds number. The normalized energy dissipation rate is approximately $C_\epsilon \approx 0.5$, which is in agreement with earlier measurements. It was found that the normalized energy dissipation rate is slightly larger for wind from the east than for wind from the west, which is most likely related to the difference in topology.

In the case of east wind and Reynolds numbers up to $R_\lambda \approx 3000$ the isotropy of the flow is found to increase with Reynolds number, in agreement with the 'return to isotropy principle'. However, in the case of large Reynolds numbers ($3000 < R_\lambda < 6000$) a return to isotropy could not be observed, which suggests that a deeper investigation of anisotropic high Reynolds number flows is necessary.

The tetrad-based velocity gradient tensor, an extension of velocity gradients into large scales at which the velocity field is not differentiable, is used to study turbulence dynamics in the inertial range. The joint probability density function (PDF) of its invariants (R and Q) is found to be slightly increased along the so-called Vieillefosse tail, which corresponds to bi-axial stretching, in agreement with previous observations in laboratory flows and direct numerical simulations (DNS). The skewness of the joint PDF is larger for east wind, which may be explained by the more isotropic flow conditions.

As a measure of the sizes of coherent structures in the flow, the correlation lengths of R and Q are computed for strain- and vorticity-dominated regions. For small to moderate Reynolds numbers, the correlation lengths corresponding to regions with $Q < 0$ (strain-dominated) are larger than that for $Q > 0$ (vorticity-dominated). The differences, however, decrease with Reynolds number and at high Reynolds numbers ($R_\lambda \gtrsim 5000$), the two correlation lengths are almost the same, indicating that there is little or no structure difference between strain-dominated regions and vorticity-dominated regions. This observation is consistent with recent DNS results at high Reynolds numbers, which show that the complexity of eddy structure geometry increases rapidly with Reynolds number.

Contents

1 Introduction **1**

1.1 Fluid motion . . . 1

1.1.1 Laminar and turbulent flows . . . 1

1.1.2 Equations of fluid motion . . . 2

1.1.3 Reynolds number . . . 5

1.1.4 Strain and vorticity . . . 5

1.1.5 Difficulties of solving the Navier-Stokes equation . . . 6

1.2 Turbulent flows . . . 6

1.2.1 Characteristics of turbulence . . . 6

1.2.2 Statistical approach to turbulence . . . 7

1.2.3 Reynolds decomposition . . . 9

1.3 Kolmogorov's theory . . . 10

1.3.1 The Richardson cascade . . . 11

1.3.2 Kolmogorov's hypotheses . . . 12

1.3.3 Structure functions . . . 13

1.3.4 Correlations . . . 15

1.3.5 Taylor micro-scale . . . 16

1.3.6 Kármán-Howarth equation and the 4/5 law . . . 18

1.4 Motivation and outline of the study . . . 18

1.4.1 Anisotropic flow . . . 19

1.4.2 The velocity gradient tensor . . . 19

2 Measurement technique and experimental setup **23**

2.1 Location of the measurement site . . . 24

2.2 Experimental setup . . . 26

2.3 Ultrasonic anemometers . . . 26

2.3.1 Measurement principle . . . 26

2.3.2 Sensor specifications . . . 28

2.3.3 Measurement limitations 28
2.4 Data recording 33
2.4.1 Errors during data recording 33
2.5 Data processing 34
2.5.1 Pre-processing data 34
2.5.2 Main processing 36
2.5.3 Averaging and calculating the joint PDF 38
2.6 Taylor's frozen turbulence hypothesis 38

3 Large scale flow **41**
3.1 Overview over the general weather condition 41
3.1.1 Wind conditions 42
3.2 Turbulence parameters 45
3.2.1 Correlations and integral length scales 46
3.2.2 Distribution and mean of turbulence parameters 48
3.2.3 Anisotropy of the flow 51
3.3 Structure functions 52
3.3.1 Normalized energy dissipation rate 53
3.4 Large scale anisotropy and the return to isotropy principle 55
3.4.1 Theoretical background 55
3.4.2 Dependency on the wind direction 57
3.4.3 The return to isotropy 57
3.4.4 The influence of wind shear 59
3.4.5 Comparison to laboratory flows 64

4 The velocity gradient tensor **67**
4.1 Theoretical background 67
4.1.1 Definition of Invariants 67
4.1.2 Evolution equation of the velocity gradient tensor 68
4.1.3 Restricted Euler model 69
4.1.4 The tetrad model 70
4.1.5 The filtered velocity gradient tensor 72
4.1.6 Characteristic features of the 'true' velocity gradient tensor . . 73
4.2 Measurements and simultions 74
4.2.1 Measurement of the filtered velocity gradient tensor 74
4.2.2 Reproduction of characteristic features by the tetrad model . . 75

4.3 Description of the current study 76
4.4 Results 77
4.4.1 Joint PDFs of R and Q 77
4.4.2 Dependence on the wind direction 80
4.4.3 Correlation of strain- and vorticity-dominated regions 82

5 Conclusion and outlook **87**
5.1 Summary and Conclusion 87
5.2 Outlook 89

Appendices **91**

A Investigation of transducer shadowing effects **93**
A.1 Introduction 93
A.2 Summary of the Results 94
A.3 Number of evaluated measurements 94
A.4 Wind Speed 95
A.4.1 Dependence on different bin sizes (100, 101, 102, 103) 95
A.4.2 Dependence on evaluated time range (month) (104, 105, 105, 106) 95
A.4.3 Dependence on vertical angle θ (107, 108, 109, 110) 95
A.4.4 Dependence on horizontal angle ϕ (111, 112, 113, 114) 96
A.5 Horizontal Angle ϕ 97
A.5.1 Dependence on different bin sizes (115, 116) 97
A.5.2 Dependence on evaluated time range (month) (117) 98
A.5.3 Dependence on vertical angle θ (119) 98
A.5.4 Dependence on absolute wind speed (120) 98
A.6 Vertical Angle θ 99
A.6.1 Dependence on different bin sizes (121) 99
A.6.2 Dependence on evaluated time range (month) (122) 99
A.6.3 Dependence on absolute wind speed (123) 99
A.7 Histograms and probability density functions 99

B Large scale flow properties in 2011 **125**

C Distribution of turbulence parameters after averaging chunks of constant wind speed **133**

Nomenclature

Abbreviations

Abbreviation	Meaning
DNS	Direct Numerical Simulation
DWD	Deutscher Wetterdienst
LEM	Lagrangian Exploration Module
LIDAR	Light Detection And Ranging
ODE	ordinary differential equation
PDF	Probability Density Function
SAT	Sonic Anemometer and Thermometer
UFS	Umweltforschungsstation Schneefernerhaus
VKS	von Kármán swirling flow
r.m.s.	root-mean square
sgn	signum function

Latin Letters

Notation	Meaning
$\boldsymbol{A}$	velocity gradient tensor
$\tilde{\boldsymbol{A}}$	filtered velocity gradient tensor
a_{ij}	anisotropic part of the Reynolds stress tensor
a_{ij}	dimensionless velocity gradient tensor
b_{ij}	normalized anisotropy tensor
C_n	Kolmogorov's constant related to the n-th order structure function
D_{ij}	second order structure function
D_{NN}	transverse second order structure function

Notation	**Meaning**
D_{LL}	longitudinal second order structure function
$\hat{D}_{LL}$	dimensionless structure function
D_{LLL}	third order structure function
D_n	n-th order longitudinal structure function
d	acoustic path length
d_1	bin size used to generate histograms of wind speed
d_2	bin size used to generate histograms of angles Φ and θ
e	vapor pressure
$\boldsymbol{e}_i$	unit vector in the i-coordinate direction
$f(r,t)$	longitudinal velocity autocorrelation function
f_l	limiting frequency resolved by SAT
$g(r,t)$	transverse velocity autocorrelation function
$\boldsymbol{g}$	moment of inertia tensor
H^p_{ij}	trace-free part of the pressure Hessian
H^ν_{ij}	viscous part of the pressure Hessian
I, I_t	turbulence intensity (threshold)
Kn	Knudsen number
k	turbulent kinetic energy
$\tilde{L}$	characteristic length scale
$\mathcal{L}$	geometric length scale of the flow
l_0	characteristic length scale of the largest eddies
l	length scale
$\boldsymbol{M}$	tetrad-based velocity gradient tensor
$\boldsymbol{m}$	'true' velocity gradient tensor
m	marker, which marks recording errors
$\overline{P}$	mean pressure
p	(modified) pressure
$\bar{p}$	modified pressure
Q	invariant of the velocity gradient tensor
$Q_\star$, Q_r	normalized invariant of the VGT
Q_S	invariant of the velocity gradient tensor
q	dimensionless invariant of the VGT
R	third order invariant of the VGT
$R_\star$, R_r	normalized invariant of the VGT

Notation	**Meaning**
R_S	invariant of the VGT
R_{ij}	velocity correlation
Re	Reynolds number
R_L	turbulence (large scale) Reynolds number
R_c	critical Reynolds number
R_η	Kolmogorov scale Reynolds number
R_λ	Taylor scale Reynolds number
r	dimensionless invariant of the VGT
S	velocity derivative skewness
S	strain rate
$\boldsymbol{S}$	rate-of-strain tensor
$S^\star_{T_L}$, $S^\star_{\tau_\eta}$	normalized strain rates
T_v	virtual temperature
t	time
t_0	characteristic time of the VGT
t_{int}	internal time of the sensor clocks
U	velocity
$\boldsymbol{U}(\boldsymbol{x},t)$	Eulerian velocity
$\overline{U}$	mean velocity
$\tilde{U}$	characteristic velocity scale
$\langle U \rangle$	ensemble average of velocity
$\boldsymbol{u}(\boldsymbol{x},t)$	fluctuating velocity
u'	r.m.s. of velocity fluctuations
u_η	Kolmogorov velocity scale
u_0	characteristic velocity scale of the largest eddies
$\overline{u_i u_j}$	Reynolds stress tensor
V	volume
V	invariant of the VGT
V_d	velocity along acoustic path
v_{abs}	absolute wind speed
v_x,v_y,v_z	component of the wind velocity in x, y and z direction
$\boldsymbol{x}$	position
x,y,z	Cartesian coordinates
II_b,III_b	invariants of Reynolds-stress anisotropy tensor

Greek Letters

Notation	Meaning
α	parameter of the tetrad model
β	parameter of the tetrad model
Δ	discriminant of the VGT
δ_{ij}	Kronecker delta
ϵ	rate of dissipation of turbulent kinetic energy
ε_{ijk}	alternating symbol
η	Kolmogorov length scale
η	invariant of Reynolds-stress anisotropy tensor
$\boldsymbol{\eta}$	stochastic forcing
θ	vertical angle of wind direction
λ	mean free path of air molecules
λ_i	eigenvalue
λ_α	largest eigenvalue of the VGT
λ_β	intermediate eigenvalue of the VGT
λ_γ	smallest eigenvalue of the VGT
λ_f	longitudinal Taylor microscale
λ_g	transverse Taylor microscale
λ_l	limiting wavelength resolved by SAT
μ	dynamic viscosity
ν	kinematic viscosity
Π_{ij}	'projection operator' for the evolution equation of the tetrad-based VGT
ρ	density
$\boldsymbol{\rho}^a(t)$	position of particle a at time t
σ	standard deviation
τ_{ij}	shear stress
τ_0	characteristic time scale of the largest eddies
τ_η	Kolmogorov time scale
Φ	horizontal angle of wind direction
ξ	invariant of Reynolds-stress anisotropy tensor
Ω_{ij}	rate-of-rotation tensor
$\boldsymbol{\omega}$	vorticity

List of Figures

1.1 Rising smoke (Barstow, 2004) 2
1.2 Trace of the x-component of wind velocity measured by one sonic sensor at Zugspitze for 12 hours. Strong and random fluctuations of the wind speed can be found at all resolved time scales. The bottom graph shows a close up view of a one minute chunk. 8
1.3 Visualization of the energy cascade (from Frisch (1995)). 11
1.4 Visualization of the longitudinal velocity autocorrelation function and the Taylor micro-scale by Pope (2000). The Taylor scale, λ_f, corresponds to the zero-crossing of a parabola, $p(r)$, which osculates $f(r)$ at $r = 0$. 17

2.1 View from the south-east into the Schneeferner valley. (Picture taken by Xtream (2009).) 23
2.2 Experimental setup, consisting of five ultrasonic anemometers arranged as two nearly isotropic tetrahedra, located on top of UFS. . . 24
2.3 View of the measurement terrace from the west. Based on Wörmann (2009a). 25
2.4 View of the measurement terrace from the top. Based on Wörmann (2009b). 25
2.5 Dimensional drawings of the sonic anemometers with all length scales given in mm (Thies, 2009). 29
2.6 Misalignment of the lower sensors relative to the top sensor. Plotted is the deviation of the horizontal angle Φ (in degrees) for wind coming from the west, before correction. 32
2.7 Misalignment of the lower sensors relative to the top sensor. Plotted is the deviation of the horizontal angle Φ (in degrees) for wind coming from the east, before correction. The histograms for the vertical angle θ look similar. 32

2.8 Excerpt of a data file recorded by one sonic anemometer in one second. 34

2.9 Corrected excerpt of a new data file recorded in one second by one sonic anemometer, after pre-processing was applied. 35

3.1 Overview over average values of temperature, pressure, humidity and precipitation measured between 2000 and 2005 by Deutscher Wetterdienst (DWD) at UFS (UFS, 2011) 41

3.2 PDF of the wind direction as a function of the horizontal angle, Φ, exemplary for the months September, October, November and December 2010 from the top sensor. The dents in the PDF are due to transducer shadowing effects as described in section 2.3.3. 42

3.3 Definition of the horizontal angle, ϕ, and vertical angle, θ. Also shown are the axis of the sensor coordinate system and sensor position (used in table 2.1). 43

3.4 PDF of the vertical angle, θ, for the months September, October, November and December 2010 from the top sensor. 44

3.5 PDF of the absolute wind speed, v_{abs}, for September, October, November and December 2010, measured by the top sensor. The location of the mean wind speed is also shown for September: $v_{abs} = 3.9$ m/s, October: $v_{abs} = 4.2$ m/s, November: $v_{abs} = 4.7$ m/s and December: $v_{abs} = 5.3$ m/s. 45

3.6 Averaged normalized correlations, $f = \frac{R_{zz}}{\langle u_z(z)u_z \rangle}$ and $g_x = \frac{R_{xx}}{\langle u_x(z)u_x \rangle}$, $g_y = \frac{R_{yy}}{\langle u_y(z)u_y \rangle}$, plotted as a function of $\boldsymbol{r} = z$. The chunks have a mean wind speed between 3.5 and 4 m/s and come from the east. . . 46

3.7 Normalized correlations g and f, fitted with an exponential function $\frac{R_{ii}}{\langle u_i u_j \rangle} \sim e^{\gamma_i r}$. Only the fitted data range is shown. The plotted data is the same as in figure 3.6. 47

3.8 PDFs of the integral length scales of the x, y and z direction, where the z-axis of the coordinate system points into the mean wind direction. Also shown are the mean integral length scales, $\langle L_{xx} \rangle = 14.8$ m, $\langle L_{yy} \rangle = 20.8$ m and $\langle L_{zz} \rangle = 18.6$ m. The data was taken between the beginning of September and the end of December 2010. 49

3.9 PDFs of the integral length scales for wind coming from the west (left) and from the east (right). 49

3.10 PDFs of the isotropic components of the Reynolds stress tensor (left) and the square root of the components (right). The z-axis of the coordinate system points into the mean wind direction. Also shown are the averages. 50

3.11 PDFs of the large scale Reynolds number, R_L, (left) and the Taylor scale Reynolds number, R_λ, (right). The average Reynolds numbers are $\langle R_L \rangle = 2.6 \cdot 10^6$ and $\langle R_\lambda \rangle = 3700$. 51

3.12 Interpolated shear profile for wind from the west (left) and wind from the east (right). The measurement volume is projected into the y-z-plane and viewed from the west. The average deviation from the average wind speed is color coded and interpolated between the anemometers. 52

3.13 Second order structure function (left) and third order structure function (right) for a chunk with a constant mean wind speed of 4.9 m/s. A linear slope is fitted to the second order structure functions and also shown in the plot of the third order structure function, with the following parameters (as visualized by the dashed lines): $\epsilon_{D_{LL}} = 5.5 \cdot 10^{-3} \frac{\mathrm{m}^2}{\mathrm{s}^3}$, $\epsilon_{D_{NN}} = 5.8 \cdot 10^{-3} \frac{\mathrm{m}^2}{\mathrm{s}^3}$ and $C_2 = 2.11$. 53

3.14 Reduced plot of the second (left) and third (right) order structure functions for the same data as shown in figure 3.13. 54

3.15 Normalized energy dissipation rate, $C_\epsilon = \frac{\epsilon L}{u'^3}$, as a function of Reynolds number. C_ϵ was determined by fitting the second order structure functions. The value of C_ϵ is dependent on the wind direction, due to the topology. 54

3.16 Lumley triangle in the η and ξ plane. Figure taken from Choi and Lumley (2001). 56

3.17 Special states of the Reynolds stress tensor in terms of the invariants ξ and η and the eigenvalues λ_i of $\boldsymbol{b}$ (Pope, 2000). 56

3.18 The Lumley triangle plotted in the ξ-η-plane for wind coming from the west (left) and from the east (right) as a function of R_λ (color coded). For better visibility only 500 randomly chosen events have been plotted for each wind direction. 57

3.19 Linear interpolation of the invariants in the ξ-η-plane as a function of Reynolds number R_λ (color coded) for flows with $R_\lambda < 3000$ on top and for flows with $3000 < R_\lambda < 6000$ on the bottom. The left panels correspond to wind from the west, while the right panels correspond to wind from the east. Between 1500 and 2000 events have been averaged. 58

3.20 Normalized shear rate ($S^\star_{T_L} = \frac{Su'^2}{\epsilon}$) as a function of the Reynolds number R_λ for east wind (red) and west wind (blue). The crosses and circles represent single measurements, while the lines correspond to averages over bin sizes with $\Delta R_\lambda = 300$. 61

3.21 Reduced normalized shear rate $S^\star_{T_L}/R_\lambda \sim S\tau_\eta$ as a function of the Reynolds number for wind from the east (red) and west (blue). 62

3.22 Linear interpolation of the invariants in the ξ-η-plane as a function of the normalized shear parameter $S^\star_{T_L}$ (color coded), for a range of $0 < R_\lambda < 6000$. The left panels correspond to wind from the west, while the right panels correspond to wind from the east. The top graphs are for small shear parameters ($S^\star_{T_L} < 10$) and the bottom graphs are for large shear parameters ($S^\star_{T_L} > 10$). 63

3.23 Lumley triangle comparing the isotropy of the east wind to that of von Kármán swirling flow at $R_\lambda = 815$ and the flow generated by the Lagrangian exploration module at $R_\lambda = 195$. 64

4.1 Phase-space of the restricted Euler model in the R-Q plane: (a) trajectories of Q vs R, (b) dimensionless q vs r and the flow topology for each quadrant. Figures taken from Cantwell (1992). 71

4.2 Four points in space define the tetrad, as visualized by Chertkov et al. (1999). The velocities at the four points give the tetrad based velocity gradient. 72

4.3 The PDF of R and Q obtained in DNS at (a) $R_\lambda = 434$ (Luethi et al., 2009) and (b) $R_\lambda = 85$ (Chertkov et al., 1999). The probability is logarithmically spaced. In the left plot R and Q are normalized by the Kolmogorov time scale $Q_{\star\star} = Q\tau_\eta^2$ and $R_{\star\star} = R\tau_\eta^3$. In the right plot R and Q are normalized by the variance of strain $Q_\star = Q/\langle s^2\rangle$ and $R_\star = R/\langle s^2\rangle^{3/2}$ and determined by the tetrad model inside the dissipation range with $\rho/\eta = 2$. 74

4.4 Joint PDF of R and Q measured by the tetrad model in a DNS flow for several values of α: (a) $\alpha = 0.1$, (b) $\alpha = 0.5$, (c) $\alpha = 0.7$ and (c) $\alpha = 0.9$. Figures taken from (Pumir and Naso, 2010). 75

4.5 The tetrad-based velocity gradient tensor measured in VKS at Reynolds number $R_\lambda = 690$ for different sizes of the isotropic tetrads: (a) $\rho/L = 1/6$ and (b) $\rho/L = 1/3$ (Xu et al., 2011). 76

4.6 Joint PDF of R and Q measured at UFS for all chunks with a constant mean wind speed of at least 3 m/s. The PDF is slightly skewed along the Vieillefosse tail in the bottom right quadrant. The invariants are normalized as $Q_r = (r^2/\epsilon)^{2/3} Q$ and $R_r = (r^2/\epsilon) R$. 78

4.7 R-Q joint PDF for velocity chunks filtered with a five point Gaussian filter of $\sigma = 1$. 79

4.8 Trace of the fluctuating velocity measured (blue) and filtered (red) for the first 30 seconds of a chunk of constant wind speed. 79

4.9 R-Q joint PDF obtained by DNS for two different values of the noise amplitude: (a) small noise amplitude and (b) large noise amplitude at a scale of $\rho/L = 1/4$. The asymmetry decreases with increasing noise amplitudes. Results are taken from Pumir and Naso (2010). . . 80

4.10 Joint PDF of R_r and Q_r measured at UFS for wind from the east (red) and west (blue). The west wind is subject to a stronger shear and the overall size of velocity fluctuations is larger. The asymmetry of the PDF for east wind is slightly more pronounced. 81

4.11 Joint PDF of R and Q obtained by DNS in a homogeneous turbulent shear flow ($\boldsymbol{U} = (sy, 0, 0) + \boldsymbol{u}$) with the dimensionless shear parameter $S^\star = s(L^2/\epsilon)^{1/3}$ with $S = 0$ (red), $S = 1$ (green), $S = 6$ (blue) and for different sizes of the tetrad: (a) $r = L/8$ and (b) $r = L/16$. Results taken from Naso et al. (2006). 82

4.12 Correlation of the invariants R and Q conditioned on strain-dominated regions ($Q < 0$) and vorticity-dominated regions ($Q > 0$) for $R_\lambda \approx 3200$. 83

4.13 Correlation lengths of the invariants R and Q conditioned on strain-dominated regions ($Q < 0$) and vorticity-dominated regions ($Q > 0$) as a function of R_λ. The measured values are indicated by circles and crosses and the mean is shown by lines with corresponding colors. . . 84

4.14 Intense vorticity isosurfaces in direct numerical simulation by Ishihara et al. (2009) with $R_\lambda = 1131$. The black bars at the bottom indicate the integral length scale L, the Taylor micro-scale λ, and the Kolmogorov length scale η. The field consists of clouds of a large number of small eddies and void regions (Ishihara et al., 2009). 85

B.1 PDF of the wind direction as a function of the horizontal angle Φ from January to March 2011. 126
B.2 PDF of the wind direction as a function of the horizontal angle Φ from April to June. 126
B.3 PDF of the wind direction as a function of the horizontal angle Φ from July to September. 127
B.4 PDF of the wind direction as a function of the horizontal angle Φ from October to November. 127
B.5 PDF of the vertical angle θ from January to March. 128
B.6 PDF of the vertical angle θ from April to June. 128
B.7 PDF of the vertical angle θ from July to August. 129
B.8 PDF of the vertical angle θ from October to December. 129
B.9 PDF of the absolute wind speed v_{abs} from January to March. 130
B.10 PDF of the absolute wind speed v_{abs} from April to June. 130
B.11 PDF of the absolute wind speed v_{abs} from July to September. 131
B.12 PDF of the absolute wind speed v_{abs} from October to December. . . . 131

C.1 PDFs of the integral length scales. Averaging intervals are $\Delta\Phi, \Delta\theta = 20°$, $\Delta v = 0.2$ m/s (left) and $\Delta\Phi, \Delta\theta = 60°$, $\Delta v = 0.2$ m/s with at least five chunks averaged (right). 133
C.2 PDFs of the integral length scales for wind coming from the west (left) and from the east (right). The averaging intervals are $\Delta\Phi, \Delta\theta = 20°$, $\Delta v = 0.2$ m/s. 134
C.3 PDFs of the isotropic components of the Reynolds stress tensor. Averaging intervals are $\Delta\Phi, \Delta\theta = 20°$, $\Delta v = 0.2$ m/s (left) and $\Delta\Phi, \Delta\theta = 60°$, $\Delta v = 0.2$ m/s with at least five chunks averaged (right). 134
C.4 PDFs of the Taylor scale Reynolds number. Averaging intervals are $\Delta\Phi, \Delta\theta = 20°$, $\Delta v = 0.2$ m/s (left) and $\Delta\Phi, \Delta\theta = 60°$, $\Delta v = 0.2$ m/s with at least five chunks averaged (right). 135

List of Tables

2.1 Location of the sonic anemometers in a right handed coordinate system, with the x-axis pointing west, the y-axis pointing south and the z-axis pointing upwards. The origin of the coordinate system is at the top sensor and all coordinates are given in meters. 26
2.2 Technical data of the Thies Ultrasonic Anemometer 3D as specified in the user manual by Thies (2009). 28
2.3 Data format given by sonic anemometers. 33
2.4 Data format written into the new data file, after pre-analysis has been applied. 35

3.1 Relation between the horizontal angle, Φ, and the geographic direction where the wind comes from. 43
3.2 Relation between the vertical angle, θ, and direction where the wind comes from. 43
3.3 Comparison of integral length scales determined for averaged chunks, as presented in figures 3.6 and 3.7. All length scales are given in meters. 47

4.1 Comparison of the normalized moments of $Q_r = (r^2/\epsilon)^{2/3} Q$ and $R_r = (r^2/\epsilon) R$ for all chunks (fig. 4.6) and filtered chunks (fig. 4.7). The flatness in R and Q and the skewness in Q is slightly larger for filtered chunks, while the skewness in R is slightly larger for non-filtered chunks. 78
4.2 Comparison of the normalized moments of $Q_r = (r^2/\epsilon)^{2/3} Q$ and $R_r = (r^2/\epsilon) R$ for east and west wind. The skewness and flatness for the east wind is larger than for the west wind. 81

A.1 Comparison of the number of evaluated measurements. 94
A.2 Comparison of horizontal angles ϕ measured in the histogram with the sensor geometry. On the left side angles are given in multiples of π and on the right side corresponding angles are given in degrees. . . 97

1 Introduction

> Zen master Baoche of Mt. Mayu was fanning himself. A monk approached and said, "Master, the nature of wind is permanent and there is no place it does not reach. Why, then, do you fan yourself?"
> "Although you understand that the nature of the wind is permanent," Baoche replied, "you do not understand the meaning of its reaching everywhere."
> "What is the meaning of its reaching everywhere?" asked the monk again.
> The master just kept fanning himself. The monk bowed deeply.
> (Shobogenzo Genjokoan by Eihei Dogen Zenji in 1253)

1.1 Fluid motion

Fluid motion can be observed almost everywhere in our lives. Water and air are indispensable for us and we are surrounded by them almost all the time. Opening a window or drinking a glass of water are just two everyday examples where we get into contact with fluid motion. We move around in this world of fluids, just as naturally as a fish moves through the water or a bird moves through the air.

1.1.1 Laminar and turbulent flows

Motions of fluids are so familiar to us that most of the time we do not pay much attention to them. In case we do pay attention, however, we can easily recognize that fluids behave in two very different ways, both of which are shown in figure 1.1.1. At the bottom the flow has long streaks with parallel lines, which is referred to as a laminar flow, while the upper half shows mixed smoke lines and the ordered pattern is gone, which is known as a turbulent flow. Although it is the same fluid, air, which moves, the patterns formed are completely different from one another.

If we observe our environment and try to sort the observed fluid flows into laminar and turbulent flows, we will immediately see that most of them fall into the category of turbulent flows. Watching the smoke from a chimney, the swirling water in a river, the condensing breath at winter time or the milk we pour into our coffee, are examples of turbulent flows, which can frequently be observed. All of these flows are intrinsically turbulent, while laminar flows are a rare exception.

Figure 1.1: Rising smoke (Barstow, 2004)

1.1.2 Equations of fluid motion

Definition of Fluids

Matter can be classically divided into three states: solid, liquid and gas. While solids are usually resistant to changes in form and volume, liquids and gases are not. Thus liquids and gases are often combined into one category referred to as fluids. A more precise definition can be given by dividing forces which are acting on a material element into normal (F_n) and shear (F_s) forces.

A solid can then be characterized by the continuous resistance to shear stresses, while a fluid will undergo a continuous change in shape and readily will start to flow in case a shear force is applied (Britannica, 2003).

Newtonian fluids

A characteristic property of a fluid is its viscosity. Viscosity is caused by internal friction when a shear force is applied, i.e. the shape of a fluid is changed. In case the applied shear force is proportional to the strain-rate of the fluid, it is called a *Newtonian fluid*. For Newtonian fluids the proportionality between shear stresses, τ_{ij}, and strain-rates, $S_{ij} = \frac{1}{2}\left[\frac{\partial U_i}{\partial x_j} + \frac{\partial U_j}{\partial x_i}\right]$, is given by the *dynamic viscosity* μ:

$$\tau_{ij} = 2\mu S_{ij} \tag{1.1}$$

When the dynamic viscosity is divided by the density, ρ, one obtains the *kinematic viscosity*, $\nu = \mu/\rho$, which will be used more frequently.

Continuum hypothesis

In order to describe the motion of a fluid it is natural and helpful to assume a fluid to be a continuous medium, instead of looking at its molecular components. For that purpose it is assumed that 'infinitesimal material elements' or 'fluid particles' exist. These elements are small compared to the investigated volume, but large compared to molecular length scales.

This approach, referred to as *continuum hypothesis*, is justified by a comparison of typical length scales: The mean free path of air molecules (under atmospheric pressure) is 6×10^{-8} m, while the typical geometric length scales of flows are usually not less than $l = 10^{-4}$ m. The dimensionless Knudsen number $\mathrm{Kn} \equiv \lambda/l \approx 10^{-3}$ compares these two length scales and the continuum hypothesis proves to be valid for flows with $\mathrm{Kn} \ll 1$ (Pope, 2000).

Conservation of mass

Because mass can neither be created nor destroyed, the conservation of mass can be stated as

$$\frac{\partial \rho}{\partial t} = -\nabla \cdot (\rho \boldsymbol{U}) \,, \tag{1.2}$$

where ρ represents the density and $\boldsymbol{U}(\boldsymbol{x}, t)$ the velocity of the fluid. Equation (1.2) is known as the *continuity equation*. In case the density is constant, which usually can be assumed for homogeneous media with flow speeds much smaller than the speed of sound, the equation can be reduced to:

$$\nabla \cdot \boldsymbol{U} = 0 \tag{1.3}$$

Navier-Stokes equation

When applying Newton's second law to an incompressible Newtonian fluid, an equation of motion, known as the Navier-Stokes equation, can be derived[1] (Batchelor, 2000):

$$\rho \frac{D\boldsymbol{U}}{Dt} = -\nabla p + \mu \nabla^2 \boldsymbol{U} \tag{1.4}$$

[1] All external forces are neglected in this case.

Here $\frac{D(\ \cdot\ )}{Dt}$ denotes the *substantial* derivative[2] and gives the rate of change along a fluid element in the flow. The material derivative can be divided into a *local* and a *convective* part, which leads to the following terms in the Navier-Stokes equation:

$$\underbrace{\rho\frac{D\boldsymbol{U}}{Dt}}_{\substack{substantial\\derivative}} = \rho\left(\underbrace{\frac{\partial \boldsymbol{U}}{\partial t}}_{\substack{local\\derivative}} + \underbrace{(\boldsymbol{U}\cdot\nabla)\boldsymbol{U}}_{\substack{convective\\term}}\right) = -\underbrace{\nabla p}_{\substack{pressure\\gradient}} + \underbrace{\mu\nabla^2\boldsymbol{U}}_{\substack{viscous\\force}} \tag{1.5}$$

Simplifications For many flows constant density, $\rho = const$, is a good assumption and with $\bar{p} = \frac{p}{\rho}$ the Navier-Stokes equation (1.4) simplifies to:

$$\frac{D\boldsymbol{U}}{Dt} = -\nabla\bar{p} + \nu\nabla^2\boldsymbol{U} \tag{1.6}$$

For the rest of the text incompressibility is going to be assumed, so that equations of the form (1.3) and (1.6) will be used. With the further assumption of a non-viscous or 'dry' fluid (Feynman, 1970) with zero viscosity, one obtains the so-called *Euler equation*:

$$\frac{D\boldsymbol{U}}{Dt} = -\frac{1}{\rho}\nabla p \tag{1.7}$$

Dimensionless Navier-Stokes equation

It can be helpful to express the incompressible Navier-Stokes equation (1.6) in a dimensionless form. Considering a flow with a characteristic length scale, $\tilde{L}$, and a characteristic velocity scale, $\tilde{U}$, the Navier-Stokes equation can be made dimensionless by substituting $\boldsymbol{U} = \tilde{U}\boldsymbol{U}'$, $t = \frac{\tilde{L}}{\tilde{U}}t'$, $\frac{\partial}{\partial x} = \frac{1}{\tilde{L}}\frac{\partial}{\partial x'}$, $p = \rho\tilde{U}^2 p'$, where the primed variables are dimensionless. Thus one gets

$$\frac{D\boldsymbol{U}'}{Dt'} = -\nabla' p' + \frac{\nu}{\tilde{L}\tilde{U}}\nabla'^2\boldsymbol{U}' = -\nabla' p' + \frac{1}{Re}\nabla'^2\boldsymbol{U}'\ , \tag{1.8}$$

with the dimensionless Reynolds number, $Re = \dfrac{\tilde{L}\tilde{U}}{\nu}$.

[2] Also called *material* or *total* derivative.

1.1.3 Reynolds number

The Reynolds number plays a crucial role for the description of fluid motions and especially for turbulence theory. The question raised in chapter 1.1.1, whether a fluid motion is laminar or turbulent, can be answered by the magnitude of its Reynolds number.

For a physical interpretation, the Reynolds number can be seen as the ratio between inertial and viscous forces:

$$Re = \frac{\rho U^2 L^2}{\mu U L} = \frac{\text{inertial force}}{\text{viscous force}} \tag{1.9}$$

In case of $Re \ll 1$ the viscous force dominates over the inertial force, which leads to a laminar flow. In the other extreme of $Re \gg 1$ the inertial force dominates over the viscous force, which leads to a turbulent flow.[3]

For each type of flow a critical Reynolds number, R_c, can be defined beyond which a transition from laminar to turbulent flow occurs. Due to the low viscosity of most fluids the critical Reynolds number is usually exceeded and most of the observed flows are found to be turbulent, which is the explanation why turbulence appears to be the natural state of fluid motion while laminar flows are rather an exception (Davidson, 2004).

1.1.4 Strain and vorticity

The Navier-Stokes equation (1.6) can also be expressed in terms of vorticity, which is defined as $\boldsymbol{\omega} = \nabla \times \boldsymbol{U}$. By taking the curl of the Navier-Stokes equation (1.6) we get the *vorticity* or *Helmholtz* equation:

$$\underbrace{\frac{\partial \omega_i}{\partial t} + U_j \frac{\partial \omega_i}{\partial x_j}}_{\text{substantial derivative}} = \underbrace{\omega_j \frac{\partial U_i}{\partial x_j}}_{\text{stretching}} + \underbrace{\nu \frac{\partial \omega_i}{\partial x_j \partial x_j}}_{\text{viscous diffusion}} \tag{1.10}$$

The first term on the right refers to vortex stretching and the second is due to viscous diffusion. The velocity gradient tensor, $\dfrac{\partial U_i}{\partial x_j} = A_{ij}$, is a second-order tensor and can be decomposed into *isotropic*, *symmetric deviatoric* and *anti-symmetric deviatoric*

[3] Apart from the Reynolds number dependence, the question whether a flow is laminar or turbulent also depends on the initial conditions and boundary conditions.

parts:

$$A_{ij} = \frac{\partial U_i}{\partial x_j} = \underbrace{\frac{1}{3}\frac{\partial U_k}{\partial x_k}\delta_{ij}}_{isotropic} + \underbrace{\frac{1}{2}\left[\frac{\partial U_i}{\partial x_j} + \frac{\partial U_j}{\partial x_i}\right]}_{S_{ij}} + \underbrace{\frac{1}{2}\left[\frac{\partial U_i}{\partial x_j} - \frac{\partial U_j}{\partial x_i}\right]}_{\Omega_{ij}} \tag{1.11}$$

The isotropic part is zero for incompressible flows because of the continuity equation (1.3). The symmetric part, S_{ij}, is the rate-of-strain tensor, while the anti-symmetric part, Ω_{ij}, is the rate-of-rotation tensor. The rotation tensor, Ω_{ij}, and the vorticity, $\boldsymbol{\omega}$, are related via

$$\omega_i = -\varepsilon_{ijk}\Omega_{jk} = -\varepsilon_{ijk}\frac{1}{2}\left[\frac{\partial U_j}{\partial x_k} - \frac{\partial U_k}{\partial x_j}\right] \tag{1.12}$$

and

$$\Omega_{ij} = -\frac{1}{2}\varepsilon_{ijk}\omega_k \ , \tag{1.13}$$

where ε_{ijk} indicates the alternating symbol.

1.1.5 Difficulties of solving the Navier-Stokes equation

Except for some special cases solutions of the Navier-Stokes equation for fluid flow can usually not be found. The difficulty of solving the Navier-Stokes equation is caused by its nonlinearity and nonlocality. The nonlinearity is due to the convective term $(\boldsymbol{U} \cdot \nabla)\boldsymbol{U}$, which expresses the acceleration that a fluid element receives at different regions of the flow. An even more difficult problem may be seen in nonlocality, which can be viewed from two angles: 'dynamic' and 'kinematic' nonlocality. The dynamic nonlocality refers to the long range forces of the pressure, while kinematic nonlocality expresses the bidirectional coupling of small and large scales (Tsinober, 2009).

1.2 Turbulent flows

1.2.1 Characteristics of turbulence

Although a number of attempts have been made to define what turbulence actually is, so far no widely accepted definition exists. Instead, it is widely accepted that a good definition of turbulence does not exist at all. There are, however, some characteristics which turbulent flows have in common:

- The velocity field $\boldsymbol{U}(\boldsymbol{x}, t)$ shows strong and random fluctuation in space and

time. For visualization a velocity trace of a sonic anemometer measurement in the atmosphere is plotted in figure 1.2.

- Turbulence shows a wide range of fluctuating space and time scales. Large scales can be identified with the overall fluctuations of a graph seen in figure 1.2, while small scales correspond to the fine-scale 'fur'. At any scale in between the large and the small scale, the graph also appears to be fluctuating.

- The described fluctuations lead to strong energy dissipation at small scales and makes the constant supply of energy necessary, if turbulence is to be maintained.

- A difference in scales, at which energy is fed into the flow and at which it is dissipated, leads to the existence of an energy cascade. The cascade transfers energy from large to small scales in three dimensional turbulence.

- Turbulence shows a tendency to concentrate into individual 'bunches' which are surrounded by extensive flow regions with much smoother large-scale disturbances. This characteristic is known as *intermittency* and it increases with Reynolds number and/or as scale decreases (Monin and Yaglom, 2007).

- Enhanced transport of momentum, energy and passive objects. This property may be useful for example, in order to mix reactants in a combustion device. It may also be unwanted, when mixing of momentum increases the wall shear stress of an air plane wing.

- The flow field has a strong dependence on small disturbances. This extreme sensitivity to small changes in starting or boundary conditions, leads to the congestion that a statistical description of turbulence may be fruitful.

1.2.2 Statistical approach to turbulence

If the velocity at a single point in a turbulent flow is measured for a certain period and after a while the same measurement is repeated for the same length of time the two traces of the velocity will look very different. However, the probability density function (PDF) of the two velocity traces will look quite similar. This observation, of reproducible statistics, has lead to the idea to describe turbulence with the help of mean and fluctuating parts.

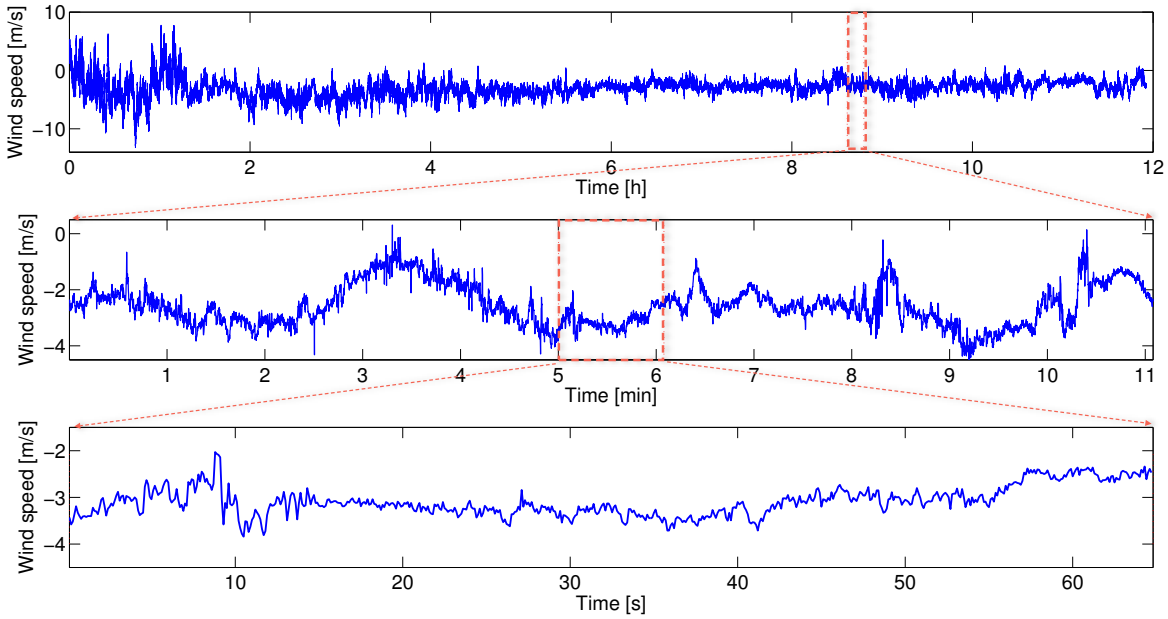

Figure 1.2: Trace of the x-component of wind velocity measured by one sonic sensor at Zugspitze for 12 hours. Strong and random fluctuations of the wind speed can be found at all resolved time scales. The bottom graph shows a close up view of a one minute chunk.

In principle three averaging methods are possible: time averages, $\overline{(\sim)}$, ensemble averages, $\langle(\sim)\rangle$, and spatial averages. For general turbulent flows the statistical description (e.g. Reynolds decomposition) is valid only in terms of ensemble averages, where the same experiment is reproduced many times. In the case of statistically steady flows time averages are assumed to be equal to ensemble averages, $\overline{(\sim)} = \langle(\sim)\rangle$, which is known as the *ergodicity* assumption.

If the statistical properties of the flow are independent of the position (homogeneous turbulence), ensemble averages are equal to volume averages. Because of the possible simplifications in statistically steady and homogeneous turbulence the three averages are the same. These conditions are often used in theories and numerical models and also attempted to achieve in experiments.

1.2.3 Reynolds decomposition

The velocity field, U_i, can be decomposed into a mean, $\langle U_i \rangle$, and a fluctuating part, $u_i = U_i - \langle U_i \rangle$. Substituting the decomposed velocity field into the continuity equation (1.3) and the Navier-Stokes equation (1.6) yields the following results:

$$\frac{\partial \langle U_i \rangle}{\partial x_i} = 0 \tag{1.14}$$

$$\frac{\partial u_i}{\partial x_i} = 0 \tag{1.15}$$

$$\begin{aligned} \frac{\partial \langle U_i \rangle}{\partial t} + \langle U_j \rangle \frac{\partial \langle U_i \rangle}{\partial x_j} &= -\frac{1}{\rho}\frac{\partial \langle P \rangle}{\partial x_i} + \nu \frac{\partial^2 \langle U_i \rangle}{\partial x_j \partial x_j} - \frac{\partial \langle u_i u_j \rangle}{\partial x_j} \\ &= \frac{1}{\rho}\frac{\partial}{\partial x_j} \left\{ \underbrace{-\langle P \rangle \delta_{ij}}_{\text{pressure term}} + \underbrace{\mu \frac{\partial \langle U_i \rangle}{\partial x_j}}_{\text{viscous stress}} - \underbrace{\rho \langle u_i u_j \rangle}_{\text{Reynolds stress}} \right\} \end{aligned} \tag{1.16}$$

The last equation (1.16) is referred to as the mean-momentum or the *Reynolds equation*. The viscous stress stems from molecular transport, while the Reynolds stress[4], $\langle u_i u_j \rangle$, origins in the fluctuating part of the velocity field. The Reynolds stress tensor is symmetric, $\langle u_i u_j \rangle = \langle u_j u_i \rangle$ and its diagonal components, $\langle u_i^2 \rangle$, are normal stresses, while the off-diagonal components, $\langle u_i u_j \rangle$, are shear stresses. The *turbulent kinetic energy* is half the trace of the Reynolds stress tensor,

$$k \equiv \frac{1}{2} \langle \boldsymbol{u} \cdot \boldsymbol{u} \rangle = \frac{1}{2} \langle u_i u_i \rangle \ , \tag{1.17}$$

which can be used to split the Reynolds stress tensor in an isotropic part, $\frac{2}{3}k\delta_{ij}$, and deviatoric part, $a_{ij} \equiv \langle u_i u_j \rangle - \frac{2}{3}k\delta_{ij}$. Furthermore a normalized anisotropy tensor can be defined

$$b_{ij} = \frac{a_{ij}}{2k} = \frac{\langle u_i u_j \rangle}{\langle u_l u_l \rangle} - \frac{1}{3}\delta_{ij} \ , \tag{1.18}$$

which makes it possible to restate the Reynolds stress tensor as

$$\langle u_i u_j \rangle = \frac{2}{3}k\delta_{ij} + a_{ij} = 2k\left(\frac{1}{3}\delta_{ij} + b_{ij}\right) \ . \tag{1.19}$$

[4] Also $\rho \langle u_i u_j \rangle$, with the density included, is often referred to as the Reynolds stress.

The Reynolds stress tensor can be transformed into a coordinate system, in which the eigenvalues correspond to the normal stresses, which are non-negative,

$$\lambda_{(i)} = \left\langle u_i^2 \right\rangle \geq 0 \ , \tag{1.20}$$

and shows that the Reynolds stress tensor is symmetric positive semi-definite.

The isotropic component, $\frac{2}{3}k$, can be combined with the pressure term of the Reynolds equation (1.16), showing that only the anisotropic component, a_{ij}, is transporting momentum. It should also be noted that the pressure term can also be expressed in the form of a Poisson equation, by taking the divergence of the Reynolds equation (1.16)

$$\frac{1}{\rho}\nabla^2 \langle P \rangle = \frac{\partial \langle U_i \rangle}{\partial x_j}\frac{\partial \langle U_j \rangle}{\partial x_i} + \frac{\partial^2 \langle u_i u_j \rangle}{\partial x_i \partial x_j} \ , \tag{1.21}$$

which shows the non-local nature of the pressure field.

The closure problem

The three Reynolds equations (1.16) together with the Poisson equation (1.21) or the mean continuity equation (1.14) describe a general three-dimensional flow. However, this set of equations cannot be solved, because the number of unknowns ($\langle U_i \rangle$, $\langle P \rangle$ and $\langle u_i u_j \rangle$) is bigger than the number of equations available. This problem is often referred to as the *closure problem* and can only be solved if additional assumptions are made.

1.3 Kolmogorov's theory

> One gets a similar impression when making a drawing of a rising cumulus from a fixed point; the details change before the sketch can be completed. We realise that big whirls have little whirs that feed on their velocity, and little whirls have lesser whirls and so on to viscosity.
> (Richardson, 1926)

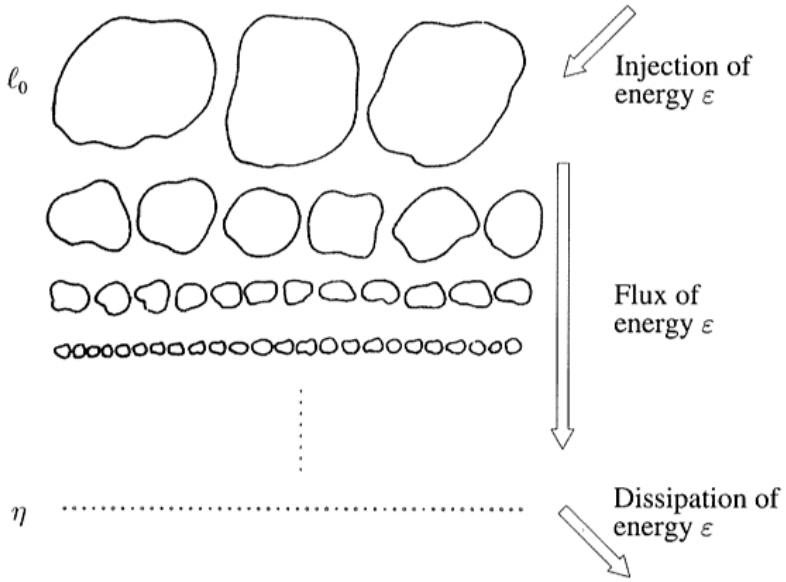

Figure 1.3: Visualization of the energy cascade (from Frisch (1995)).

1.3.1 The Richardson cascade

Richardson was the first to describe turbulence by the means of a cascade consisting of *eddies* with different sizes. The term 'eddy' refers to a coherent turbulent motion within a region of size l. For each eddy size a Reynolds number can be defined as $Re(l) = u(l)l/\nu$. The idea of the cascade assumes that large eddies, of size l_0, become unstable and break up into smaller ones. These smaller ones continue to break up into still smaller and smaller eddies until their Reynolds number, $Re(l)$, is sufficiently small for the motion to become stable.

The break-up process of eddies transfers energy from the large scales to the small scales as shown in figure 1.3. For large Reynolds numbers the viscous force is small and energy is transferred to smaller and smaller scales. As the size of scales decreases , so does the Reynolds number $Re(l)$. However, as long as $Re(l) \gg 1$, viscous effects can be neglected and the cascade is driven only by inertial forces. The break up process continues until the Reynolds number reaches order one and then energy is dissipated. Since energy is not dissipated along the cascade the rate at which energy is supplied into the cascade is the same as the rate of energy dissipation. It follows that the energy dissipation rate, ϵ, must then depend only on the rate of energy supply by the largest eddies, which have a characteristic velocity, u_0, and a characteristic time scale, $\tau_0 = l_0/u_0$. By dimensional analysis one gets the following

relationship:

$$\epsilon \sim \frac{u_0^2}{\tau_0} = \frac{u_0^3}{l_0} \tag{1.22}$$

The length scale of the largest eddies l_0 is about the same size as the geometric length scale of the flow $\mathcal{L}$. The characteristic velocity, u_0, is on the order of the r.m.s. of the velocity fluctuations u', which is defined as

$$u' \equiv \sqrt{\frac{2}{3}k} = \sqrt{\frac{1}{3}\langle u_i u_i \rangle} = \sqrt{\frac{1}{3}\left(\langle u_1^2 \rangle + \langle u_2^2 \rangle + \langle u_3^2 \rangle\right)} \, . \tag{1.23}$$

1.3.2 Kolmogorov's hypotheses

In 1941 Kolmogorov published two papers in which he set the idea of Richardson's cascade into a proper theoretical framework (Kolmogorov, 1941a,b). The theory is often referred to as K41 even though similar approaches were made independently by different scientists around the same time (Davidson et al., 2011). The rest of this chapter will follow in most parts chapter 6 of Pope (2000) but similar presentations can be found in Frisch (1995) or Monin and Yaglom (2007). As in all the works mentioned above, the K41 theory will be stated in the form of three hypotheses, assuming high Reynolds numbers and fully developed turbulence[5].

1. Hypothesis of local homogeneity and isotropy For high Reynolds numbers the smaller scales disregard the large scale geometry of the flow. The small scales are independent of the way energy is supplied to the system and the motion of scales l, with $l \ll l_0$, are statistically invariant under translation, rotation and reflection of the coordinate system. The invariance under translation is referred to as *homogeneity*, while the invariance under rotation and reflection is called *isotropy*.

2. Kolmogorov's first similarity hypothesis The small scale motions, with $l \ll l_0$, have a universal form and depend only on the energy dissipation rate ϵ and the viscosity ν. By using dimensional analysis the smallest scales of turbulence, known as *Kolmogorov scales*, can be obtained. Kolmogorov length, velocity and time scales

[5]Fully developed turbulence refers to the existence of a complete energy cascade (as described above), where all length and time scales are simultaneously present. Energy is continuously fed into the cascade at large scales and dissipated at small scales.

are defined as follows:

$$\eta \equiv \left(\frac{\nu^3}{\epsilon}\right)^{1/4} \tag{1.24}$$

$$u_\eta \equiv (\epsilon\nu)^{1/4} \tag{1.25}$$

$$\tau_\eta \equiv \left(\frac{\nu}{\epsilon}\right)^{1/2} \tag{1.26}$$

It should be noted that the definition of scales is consistent with the Kolmogorov scale Reynolds number, at which the dissipation of energy is taking place:

$$R_\eta \equiv \frac{u_\eta \eta}{\nu} = 1 \tag{1.27}$$

3. Kolmogorov's second similarity hypothesis There exists a range with $l_0 \gg l \gg \eta$ where the motions of scale l have a universal form, which is only dependent on ϵ. Because viscous effects are negligible and only inertial effects play a role, this range is referred to as the *inertial range*, or *inertial subrange*. For the inertial subrange characteristic velocity and time scales can also be formed by dimensional analysis:

$$u(l) = (\epsilon l)^{1/3} = u_\eta \left(\frac{l}{\eta}\right)^{1/3} \sim u_0 \left(\frac{l}{l_0}\right)^{1/3} \tag{1.28}$$

$$\tau(l) = \left(\frac{l^2}{\epsilon}\right)^{1/3} = \tau_\eta \left(\frac{l}{\eta}\right)^{2/3} \sim \tau_0 \left(\frac{l}{l_0}\right)^{2/3} \tag{1.29}$$

By comparison of large and small scales, it can be seen that the Reynolds number is bigger than unity inside the inertial range,

$$Re(l) \equiv \frac{u(l)l}{\nu} = \left(\frac{l}{\eta}\right)^{4/3} \gg 1 \ , \tag{1.30}$$

which is consistent with the assumption of an energy cascade without dissipation in the inertial range.

1.3.3 Structure functions

Kolmogorov's theory can also be expressed with the help of either velocity correlations or structure functions. This section is going to state Kolmogorov's theory again in terms of structure functions, while correlations are introduced in the next

section. The second order structure functions are defined as

$$D_{ij}(\boldsymbol{r}, \boldsymbol{x}, t) \equiv \langle [U_i(\boldsymbol{x}+\boldsymbol{r}, t) - U_i(\boldsymbol{x}, t)] \, [U_j(\boldsymbol{x}+\boldsymbol{r}, t) - U_j(\boldsymbol{x}, t)] \rangle \ , \tag{1.31}$$

which is the covariance of velocity differences between two points at $\boldsymbol{x}$ and $\boldsymbol{x}+\boldsymbol{r}$. Local homogeneity implies that D_{ij} is independent of the location $\boldsymbol{x}$. For isotropic turbulence the dependence of D_{ij} on the direction of $\boldsymbol{r}$ can be split up into a dependence on a longitudinal structure function, $D_{LL}(r)$, and a transverse structure function, $D_{NN}(r)$

$$D_{ij}(\boldsymbol{r}, t) = D_{NN}(r, t)\delta_{ij} + [D_{LL}(r, t) - D_{NN}(r, t)] \, \frac{r_i r_j}{r^2} \ , \tag{1.32}$$

where $r \equiv |\boldsymbol{r}|$. By differentiating (eq. 1.32) and using the continuity equation, one sees that D_{NN} and D_{LL} are related via

$$D_{NN}(r, t) = D_{LL}(r, t) + \frac{1}{2} r \frac{\partial}{\partial r} D_{LL}(r, t) \ . \tag{1.33}$$

In a coordinate system where $\boldsymbol{r}$ points into the x_1 direction, with $\boldsymbol{r} = \boldsymbol{e_1} r$, D_{LL} and D_{NN} are given by

$$D_{LL} = D_{11} \tag{1.34}$$

$$D_{NN} = D_{22} = D_{33} \tag{1.35}$$

$$D_{ij} = 0 \ , \text{ for } i \neq j \tag{1.36}$$

Kolmogorov's first similarity hypothesis can then be stated with help of a dimensionless structure function, $\hat{D}_{LL}(r/\eta)$, as:

$$D_{LL}(r, t) = (\epsilon r)^{2/3} \, \hat{D}_{LL}(r/\eta) \tag{1.37}$$

Inside the inertial range the second similarity hypothesis implies that D_{LL} is proportional to $(\epsilon r)^{2/3}$, which can be expressed with a universal constant, C_2, as

$$D_{LL}(r, t) = C_2 \, (\epsilon r)^{2/3} \ . \tag{1.38}$$

With this the relation between D_{LL} and D_{NN} (eq. 1.33) simplifies to

$$D_{NN}(r, t) = \frac{4}{3} D_{LL}(r, t) = \frac{4}{3} C_2 (\epsilon r)^{2/3} \ , \tag{1.39}$$

which completely specifies the second order structure functions in the inertial subrange, as a function of ϵ, r and C_2:

$$D_{ij}(\boldsymbol{r},t) = C_2(\epsilon r)^{2/3}\left(\frac{4}{3}\delta_{ij} - \frac{1}{3}\frac{r_i r_j}{r^2}\right) \tag{1.40}$$

Higher order structure functions

Apart from the second order structure function, higher order structure functions of order n can be defined as:

$$D_n(r) \equiv \langle[\Delta u(r)]^n\rangle = \langle[U_i(\boldsymbol{x}+\boldsymbol{r},t) - U_i(\boldsymbol{x},t)]^n\rangle \tag{1.41}$$

For these higher order structure functions dimensional analysis predicts a scaling of the form:

$$D_n(r) = C_n(\epsilon r)^{n/3} \tag{1.42}$$

1.3.4 Correlations

An equivalent description is possible with the help of correlation functions, introduced in this section. The two point velocity correlation is defined as

$$R_{ij}(r,t) \equiv \langle u_i(\boldsymbol{x}+\boldsymbol{r},t)u_j(\boldsymbol{x},t)\rangle \ , \tag{1.43}$$

which is independent of $\boldsymbol{x}$ for homogeneous and isotropic turbulence. Analog to equation (1.32) R_{ij} can be expressed in terms of the longitudinal autocorrelation, $f(r,t)$, and transverse autocorrelation, $g(r,t)$,

$$R_{ij}(\boldsymbol{r},t) = u'^2\left(g(r,t)\delta_{ij} + [f(r,t) - g(r,t)]\,\frac{r_i r_j}{r^2}\right) \ , \tag{1.44}$$

where u' indicates the r.m.s. of the velocity fluctuations and

$$f(r,t) = \frac{\langle u_1(\boldsymbol{x}+\boldsymbol{e_1}r,t)u_1(\boldsymbol{x},t)\rangle}{\langle u_1^2\rangle} \ , \tag{1.45}$$

$$g(r,t) = \frac{\langle u_2(\boldsymbol{x}+\boldsymbol{e_1}r,t)u_2(\boldsymbol{x},t)\rangle}{\langle u_2^2\rangle} \ . \tag{1.46}$$

The size of the largest eddies can be estimated by the longitudinal, L_{LL}, and

transverse, L_{NN}, integral length scales defined by

$$L_{LL}(t) \equiv \int_0^\infty f(r,t)dr \ , \tag{1.47}$$

$$L_{NN}(t) \equiv \int_0^\infty g(r,t)dr \ . \tag{1.48}$$

The continuity equation implies that $\frac{\partial R_{ij}}{\partial r_j} = 0$, which can be used to rewrite equation (1.44) as

$$g(r,t) = f(r,t) + \frac{1}{2} r \frac{\partial}{\partial r} f(r,t) \tag{1.49}$$

By use of the definitions (1.47) and (1.48) it follows that in isotropic turbulence the two length scales are related via

$$L_{NN} = \frac{1}{2} L_{LL} \ . \tag{1.50}$$

1.3.5 Taylor micro-scale

In between the large scales, measured by the integral length scales, and the small scales, defined by the Kolmogorov scale, it is often helpful to define intermediate scales, referred to as the *Taylor micro-scales*, λ_f and λ_g[6]:

$$\frac{1}{\lambda_f^2(t)} = -\frac{1}{2}\left[\frac{\partial^2 f}{\partial r^2}\right]_{r=0} = \frac{1}{2u'^2}\left\langle\left(\frac{\partial u_1}{\partial x_1}\right)^2\right\rangle \tag{1.51}$$

$$\frac{1}{\lambda_g^2(t)} = -\frac{1}{2}\left[\frac{\partial^2 g}{\partial r^2}\right]_{r=0} = \frac{1}{2u'^2}\left\langle\left(\frac{\partial u_1}{\partial x_2}\right)^2\right\rangle \tag{1.52}$$

In isotropic turbulence the Taylor micro-scales are also related by:

$$\lambda_g = \frac{\lambda_f}{\sqrt{2}} \tag{1.53}$$

Although the Taylor scale has no clear physical interpretation it is a well defined quantity and it is common to use the Taylor scale Reynolds number,

$$R_\lambda \equiv \frac{u'\lambda_g}{\nu} \sim \sqrt{R_L} \ , \tag{1.54}$$

where R_L indicates the turbulence Reynolds number based on the large flow scales.

[6]It is common that only λ_g is referred to as the *Taylor micro-scale* or *Taylor scale*.

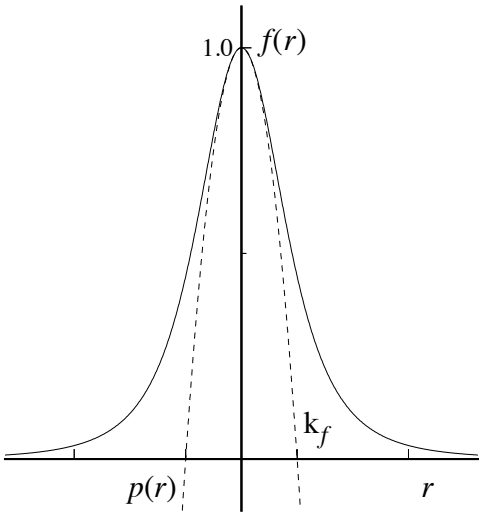

Figure 1.4: Visualization of the longitudinal velocity autocorrelation function and the Taylor micro-scale by Pope (2000). The Taylor scale, λ_f, corresponds to the zero-crossing of a parabola, $p(r)$, which osculates $f(r)$ at $r = 0$.

To obtain an exact relationship between the large flow scales and the Taylor micro-scale, note that the large eddies in the flow can also be characterized by

$$L \equiv \frac{k^{3/2}}{\epsilon} \tag{1.55}$$

with a turbulence Reynolds number defined as

$$R_L \equiv \frac{k^{1/2} L}{\nu} = \frac{k^2}{\epsilon \nu} \, , \tag{1.56}$$

which gives the same order of magnitude as the definition by integral length scales. The relation between the large scales, L, Kolmogorov scale, η, and Taylor micro-scale, λ_g, can then be summarized as follows:

$$\frac{\lambda_g}{L} = \sqrt{10} R_L^{-1/2} \tag{1.57}$$

$$\lambda_g = \sqrt{10} \eta^{2/3} L^{1/3} \tag{1.58}$$

$$\frac{\eta}{L} = R_L^{-3/4} \tag{1.59}$$

It can be seen from (eq. 1.59) that the separation between small and large scales grow, as the Reynolds number increases. An exact relation between the large scale

Reynolds number and the Taylor scale Reynolds number can then be given as

$$R_\lambda = \left(\frac{20}{3} R_L\right)^{1/2} = \left(15 \frac{u'^4}{\epsilon\nu}\right)^{1/2}. \tag{1.60}$$

1.3.6 Kármán-Howarth equation and the 4/5 law

From the Navier-Stokes equation an exact equation for $f(r,t)$ can be derived, which is known as the Kármán-Howarth equation (Kármán and Howarth, 1938). It can be expressed in terms of the longitudinal structure functions as (Monin and Yaglom, 2007):

$$\frac{3}{r^4}\int_0^r s^4 \frac{\partial}{\partial t} D_{LL}(s,t) ds = 6\nu \frac{\partial D_{LL}}{\partial r} - D_{LLL} - \frac{4}{5}\epsilon r \tag{1.61}$$

The Kármán-Howarth equation is stated above in terms of the second and third order structure functions, D_{LL} and D_{LLL}. For stationary turbulence the unsteady term on the left-hand side of the Kármán-Howarth equation vanishes. Inside the inertial subrange, the viscous term can be neglected. It follows one of the most important results in turbulence theory, which is known as Kolmogorov's 4/5 law:

$$D_{LLL}(r,t) = -\frac{4}{5}\epsilon r \tag{1.62}$$

1.4 Motivation and outline of the study

Kolmogorov's theory, based on the existence of an inertial range in which energy is transferred to smaller and smaller scales, has been verified in various experiments (e.g. Monin and Yaglom (2007)). However, it has also been found that Kolmogorov's theory is not sufficient for the description of many turbulent flows.

Special attention has been paid, for example, to the scaling of higher order structure functions, which deviates from the predictions made by Kolmogorov's theory (Frisch, 1995). The cause for the discrepancy is the intermittent character of turbulent flows, which refers to the observation that turbulence "displays activity during only a fraction of the time, which decreases with the scale under consideration" (Frisch, 1995). Various improved models have been proposed in order to account for the described discrepancy, which is also known as *anomalous scaling* of the structure functions (Frisch, 1995).

1.4.1 Anisotropic flow

One important question of turbulence theory is, whether and how far Kolmogorov's assumptions of local isotropy are applicable to turbulent flows found in the real world. Kolmogorov's assumption, that the large scale geometry of the flow can be neglected inside the inertial range, is essential for his theory. It has been extensively discussed up to which extent the assumption of local isotropy is justified and whether it is restored at increasing Reynolds numbers (Choi and Lumley, 2001). It was confirmed that at high Reynolds numbers ($R_\lambda \approx 10^3$) the assumption of local isotropy is well justified for second order quantities, such as variances and second-order structure functions, even for flows that are strongly anisotropic at large scales (Saddoughi and Veeravalli, 1994). However, the measurement of higher order mixed structure functions (composed of transverse and longitudinal velocity differences) showed that these are non-zero (Warhaft and Shen, 2002), as it would be expected in the case of local isotropy (Lumley, 1967). Until now it is not clear whether in the case of higher Reynolds numbers local isotropy will be found also for higher order structure functions, or if the assumption of local isotropy is not applicable to strongly anisotropic flows Warhaft (2009).

In the atmospheric boundary layer it is possible to reach Reynolds numbers of up to $R_\lambda \approx 10^4$. Thus it is possible to test Kolmogorov's hypotheses and investigate whether larger Reynolds numbers lead to an increase in local isotropy (Kurien and Sreenivasan, 2000; Warhaft and Shen, 2002). This thesis reports measurements of turbulent atmospheric flows with a Reynolds number up to $R_\lambda \approx 6000$, which leads to a well developed inertial range. The wide separation of scales inside the atmosphere, makes it a valuable testbed for the investigation of turbulence (Sreenivasan and Antonia, 1997). The measurement is conducted in the atmospheric boundary layer, which is typically subject to a strong shear in vertical direction. Furthermore the large scale geometry of the flow will be influenced by the surrounding landscape and buildings. The settings lead to strong anisotropy at the large scales. Chapter 3 describes the influence of the surroundings on the inertial range and also analyses whether local isotropy is restored as a function of Reynolds number.

1.4.2 The velocity gradient tensor

Since the beginning of turbulence research great interest has been directed towards the understanding of the velocity gradient tensor (VGT). As described in section

1.1.4 the VGT can be divided into symmetric and a anti-symmetric parts, which are referred to as vorticity and strain. The importance of vorticity in turbulence was first stressed by Taylor and Green (1937) and Taylor (1938), while Kolmogorov (1941a,b) focused on the dissipative nature of turbulence, which is dominated by straining regions. Fundamental properties of turbulence, such as the local dissipation rate, the rate of deformation and the shape of fluid material volumes are linked to the velocity gradient tensor (Meneveau, 2011). However, it took until 1987 before the first measurements of the VGT were reported, because of the great difficulties involved in its experimental investigation (Balint et al., 1987; Browne et al., 1987; Wallace, 2009). The VGT has been found to exhibit various characteristic features, which will be discussed in chapter 4.

One important observation for its investigation is that it can be characterized with the help of two invariants R and Q (Cantwell, 1992). The joint probability plot of R and Q has been found to exhibit a very particular shape, known as the *tear drop shape*. It is caused by a higher probability of $R > 0$ and $Q < 0$, which corresponds to the domination of two stretching directions and one compression direction in a turbulent flow (Chong et al., 1990).

Inside the inertial range, a related quantity can be defined, which is known as the *tetrad-based* velocity gradient tensor[7]. The tetrad-based VGT is determined by the measurement of velocity differences between four points in space, which make up the vertices of a tetrahedron. It can be viewed as an extension of the concept of the structure functions, which are defined by the measurement at two points, to a concept which considers velocity differences between four points. The velocity differences of all components of the three dimensional space are combined to give the tetrad-based velocity gradient tensor (Chertkov et al., 1999).

The tetrad-based VGT has been found to exhibit similar characteristics as the 'true' velocity gradient (Chertkov et al., 1999). The measurements reported here show the same tendency of the joint probability of R and Q to form a tear drop shape, which was found for the 'true' VGT. The results are also compared to earlier measurements in von Kármán swirling flow (Xu et al., 2011) and in direct numerical simulation (Naso et al., 2006; Pumir and Naso, 2010).

[7]The 'tetrad-based velocity gradient tensor' is sometimes called 'coarse grained velocity gradient tensor' in other publications. However, the term 'coarse grained velocity gradient tensor' ($\tilde{\boldsymbol{A}}$) has also been used to refer to the integral over the 'true' velocity gradient ($\boldsymbol{m}(\boldsymbol{x})$): $\tilde{\boldsymbol{A}} = \int_l \boldsymbol{m}(\boldsymbol{x}) d\boldsymbol{x}$. In order to prevent confusion the term 'coarse grained velocity gradient tensor' will be avoided in this thesis. A more detailed discussion of the definitions is included in chapter 4.

In the last section the correlation of the invariants R and Q are reported. They are used to find out more about strain- and vorticity- dominated regions, which may represent coherent structures that retain their identity for many eddy-turn-over times (Davidson, 2004). Long coherent structures of high vorticity ('vortex worms') have been observed before (e.g. Jiménez et al. (1993)). It has been found that the vorticity-dominated regions are well localized, while strain-dominated regions take up a wider domain (Nomura and Post, 1998). The correlation of strain- and vorticity-dominated regions are calculated with the aim to detect differences in their correlation lengths and as a measure of their spatial extension.

2 Measurement technique and experimental setup

Die Zugspitzbahn ist ein Triumph menschlichen Erfindergeistes, ein Wunder deutscher Technik, die Überwindung der Elementargewalten durch die Kraft der Beharrlichkeit und etwas völlig Blödsinniges. Wenn ich Zugspitze wäre: man müßte sich ja zu Tode schämen. Sieht man von den Ski-Leuten ab, die sich 'mit Brettln' im Winter da heraufziehen lassen können, um herrlich wieder herunter, zu Tal, zu fahren - der Berg ist gar kein Berg mehr. Entzaubert, von seinem Thron jäh heruntergeholt, eine Platitüde von dreitausend Metern. Oben stehen die Leute und wissen nicht genau, was sie da sollen.
(Vier Sommerplätze by Kurt Tucholsky in 1926)

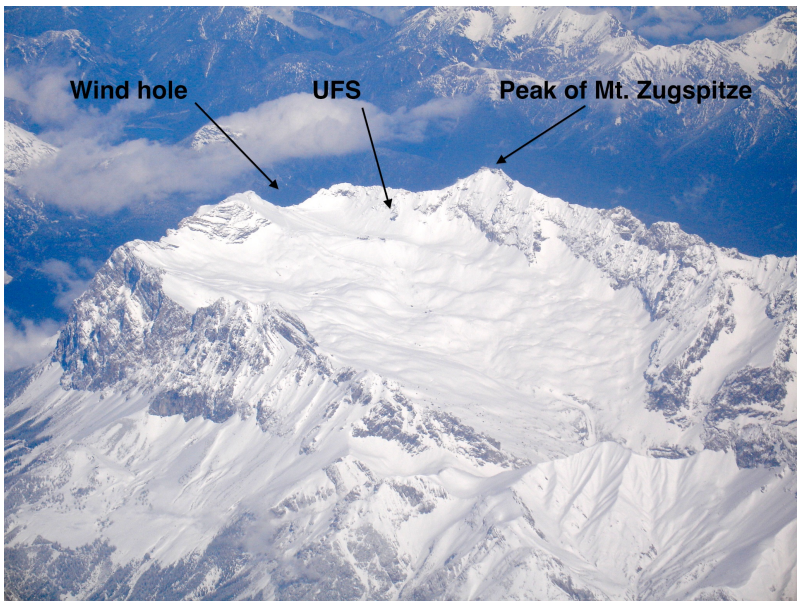

Figure 2.1: View from the south-east into the Schneeferner valley. (Picture taken by Xtream (2009).)

2.1 Location of the measurement site

Figure 2.2: Experimental setup, consisting of five ultrasonic anemometers arranged as two nearly isotropic tetrahedra, located on top of UFS.

The measurement site is located near the top of Zugspitze, the highest mountain of Germany. The mountain, 2962 meters above sea level (a.s.l.), is part of the Wettersteingebirge, which belongs to the Alps. The southern flank of the mountain is covered with Germany's largest glacier, the Schneeferner. It is surrounded by a mountain arc which shields the glacier from winds coming from north, west and south. The Schneeferner is unshielded towards the south-east where melt water streams run down the mountain. The mountain ridge on the west of the glacier is known as the Schneefernerkopf. Over a length of about 200 meters erosion has decreased its height significantly and the lowest point is about 175 meters lower than the Schneefernkopf summit. This part is known as the 'wind hole', because it directs the wind over the glacier like a funnel (Bayern, 2010; Engelbrecht, 2011).

North of the glacier and half way to the top of Zugspitz mountain, the Umweltforschungsstation Schneefernerhaus (UFS) is situated at a height of about 2650 meters a.s.l.. The UFS is a nine story building, constructed into the southern flank of the Zugspitze and on its top exists an old round cable car tower, which is about 6 meters higher

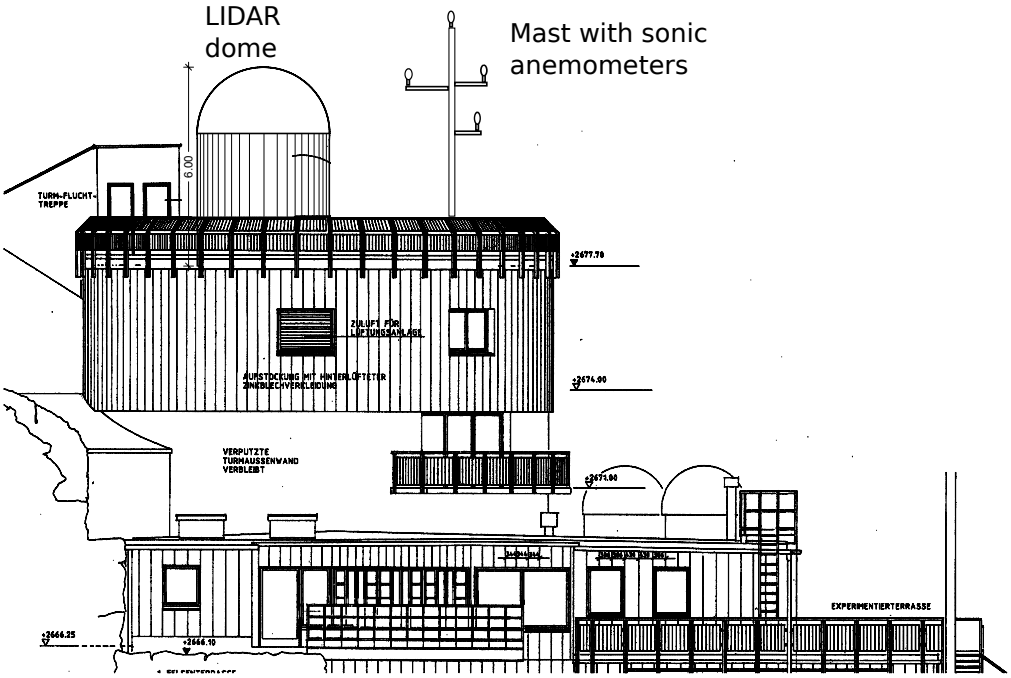

Figure 2.3: View of the measurement terrace from the west. Based on Wörmann (2009a).

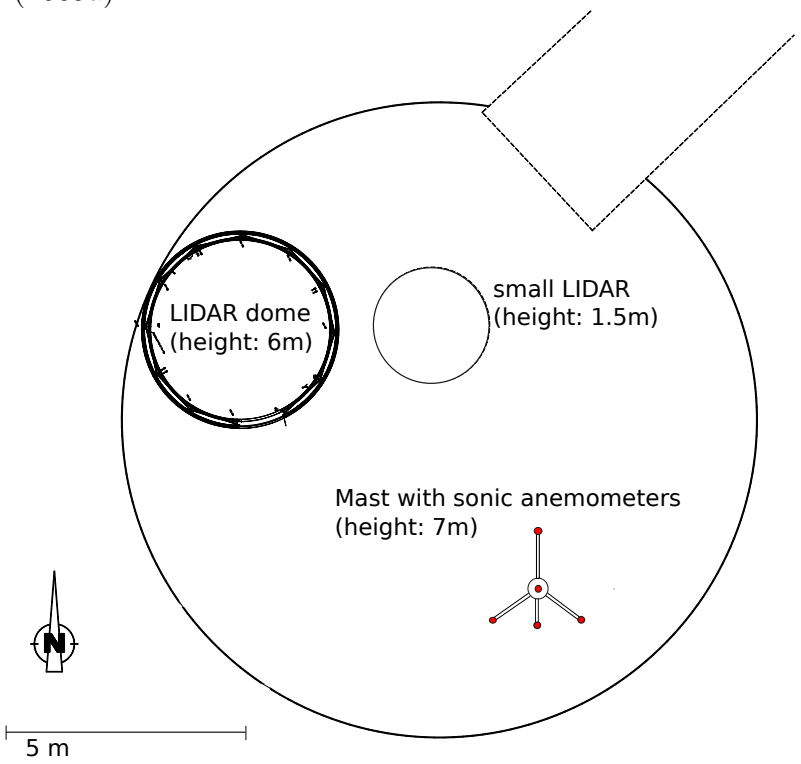

Figure 2.4: View of the measurement terrace from the top. Based on Wörmann (2009b).

than the rest of the building and has a diameter of about 13.5 m. The measurement setup is located on the roof of this old cable car tower, which now functions as a measurement terrace. Apart from the experimental setup, used for this study and described in the next section, there are two domes for Light Detection And Ranging (LIDAR) measurements located on the terrace which belong to other research groups. A schematic drawing of the terrace can be found in figures 2.3 and 2.4.

2.2 Experimental setup

The experimental setup consists of a mast, which has five ultrasonic anemometers mounted onto it. The anemometers are arranged in a configuration of two nearly isotropic tetrahedra. The top anemometer is located at a height of about 7 meters above the roof on the top of the mast. Three further anemometers are mounted on separate extension arms at a hight of about 5.5 meters. The arms are about 90 cm long and are about 120° apart from each other. The three sensors are facing towards the south-west, the south-east and north respectively. The last anemometer is located at a lower position, of 4 meters, and facing towards the south.

Sensor location	**Sensor number**	**x**	**y**	**z**
Center (top)	2001	0.0	0.0	0.0
South-West	2011	0.79	0.45	-1.30
South-East	2021	-0.84	0.49	-1.39
North	2031	0.0	-0.96	-1.55
South (bottom)	2041	-0.14	0.76	-3.01

Table 2.1: Location of the sonic anemometers in a right handed coordinate system, with the x-axis pointing west, the y-axis pointing south and the z-axis pointing upwards. The origin of the coordinate system is at the top sensor and all coordinates are given in meters.

2.3 Ultrasonic anemometers

2.3.1 Measurement principle

Sonic Anemometers and Thermometers (SAT) measure transmitting times of ultrasonic pulses between pairs of transducers. The acoustic pulses are generated by piezoelectric transducers, which act as receiver or emitter at alternating times. The

component of velocity, V_d, along the acoustic path, d, is given by

$$V_d = \frac{1}{2}\left([a+u]-[a-u]\right) = \frac{d}{2}\left(\frac{1}{t_{12}}-\frac{1}{t_{21}}\right), \tag{2.1}$$

where a is the speed of sound, u is the component of the wind velocity along the acoustic path and t_{12} and t_{21} define the time that a pulse needs to travel along the same path from both directions (McKeon et al., 2007). An advantage of the single path measurement is that, although the speed of sound depends weakly on pressure, gas composition and humidity, these factors do not influence the measurement of the wind velocity as they do not enter the equation (2.1).

Apart from the wind velocity, sonic anemometers can also be used to determine the virtual temperature. The virtual temperature is defined as the temperature at which dry air has the same density as moist air at the same pressure. The virtual temperature T_v can be approximated via

$$T_v = \frac{d^2}{1612}\left(\frac{1}{t_{12}}+\frac{1}{t_{21}}\right)^2 + \frac{1}{403}V_n^2 \tag{2.2}$$

where V_n indicates the velocity measured normal to V_d (Kaimal and Finnigan, 1994). The virtual temperature is related to the true temperature T_t via

$$T_t = T_v \frac{1}{1+0.32e/p}, \tag{2.3}$$

where e is the vapor pressure of water in air and p is the atmospheric pressure (McKeon et al., 2007). For low humidity levels, which are typical of the high altitude at Zugspitze, the dependence on humidity of the virtual temperature can be neglected.

In the experimental setup described here, the 'Ultrasonic Anemometer 3D', manufactured by the Thies Clima GmbH & Co. KG, is used. It has three individual paths to transit sound pulses back and forth, which makes it is possible to resolve the wind velocity in three orthogonal directions. In order to determine the complete wind vector it is necessary to send at least six ultrasonic pulses, two for each path. The time delay between single shots is about 1 millisecond plus a small additional time delay for data processing. In total, one cycle needs a little less than 10 ms, which leads to a theoretical maximum measurement frequency of about 100 Hz. However, since the wind velocity is averaged along the path length, the frequency response is limited by the attenuation in the spatial response (McKeon et al., 2007). A rule of thumb has

been introduced by Kaimal and Finnigan (1994) and was extended for unsteady and nonuniform velocity fields by Cuerva et al. (2003). The limiting wavelength can be estimated with the path length, $d = 0.2$ m, to be $\lambda_l = 2\pi d = 1.26$ m (Kaimal et al., 1968). Employing Taylor's frozen flow hypothesis (see chapter 2.6) and assuming a average wind speed of $V_d = 5$ m/s, the limiting frequency, after which low-pass filtering attenuation occurs, is found to be $f_l = u/\lambda_l \approx 4$ Hz. In the described experiment the sampling frequency is set to be 10 Hz, which is close to the maximum measurement frequency possible.

2.3.2 Sensor specifications

Wind velocity	Measuring range	$0.01 \ldots 65$ m/s
	Accuracy	$v_{rms} = \pm 0.2$ m/s for $v_{abs} \leq 5$ m/s $v_{rms} = \pm 2\%$ for $v_{abs} \geq 5$ m/s
	Resolution	0.01 m/s
Wind direction	Accuracy	$\pm 2°$ for 1 m/s $< v_{abs} <$ 50 m/s
Virtual temperature	Measuring range	-75 °C $\ldots +70$ °C
	Accuracy	± 0.5 K
	Resolution	0.01 K

Table 2.2: Technical data of the Thies Ultrasonic Anemometer 3D as specified in the user manual by Thies (2009).

2.3.3 Measurement limitations

There are three different limitations for measurements with sonic anemometers:

1. The main limitation of sonic anemometer measurements is due to in-line averaging as discussed above (Kaimal and Finnigan, 1994). In our case this error was accounted for by choosing the sampling frequency according to the limitations imposed by the acoustic path length.

2. The second kind of limitation is due to influences of the weather conditions, like rain, snow, ice and clouds.

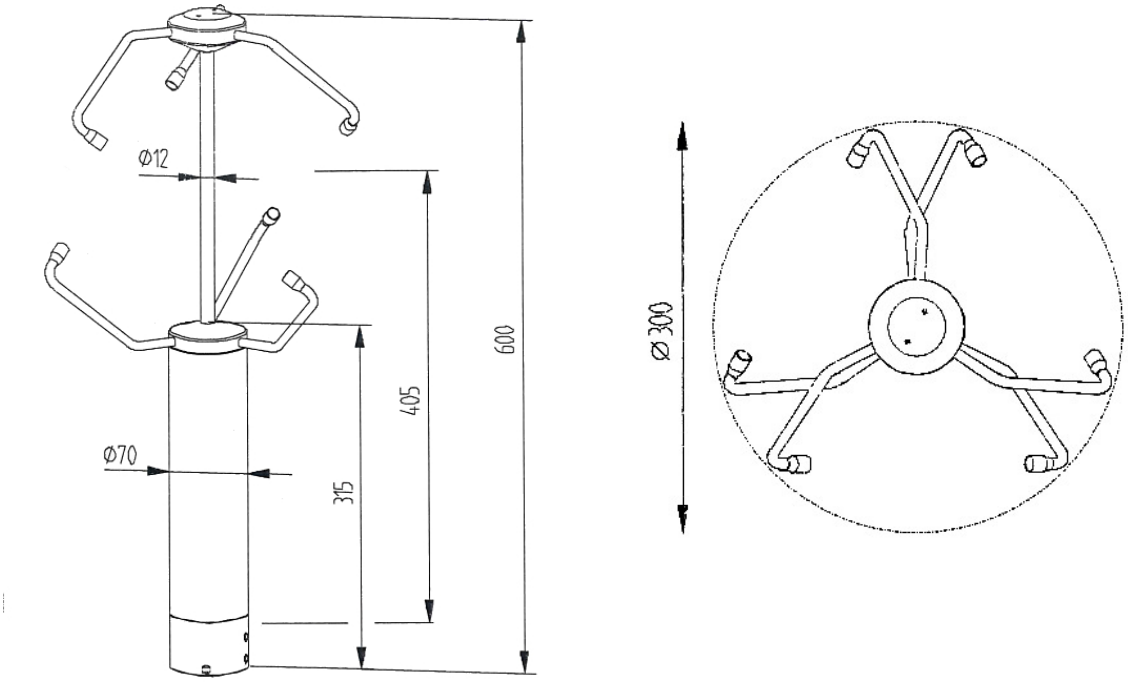

Figure 2.5: Dimensional drawings of the sonic anemometers with all length scales given in mm (Thies, 2009).

3. The third class is the limitation of the measurement accuracy caused by aerodynamic interferences, which are due to the anemometer's supporting structure and specific sensor geometry. The latter two will be discussed in more detail below.

Influence of weather conditions

Because sonic anemometers have no moving parts they are very robust to all weather conditions and widely used in atmospheric research (McKeon et al., 2007). When the ambient virtual temperatures drop below 2 °C the sensor arms and ultrasonic transducers are automatically heated, in order to prevent icing of the anemometer. The heating system guarantees that the sensor can be operated up to −75 °C (Thies, 2009). The influence of icing on the measurement accuracy has been investigated by Makkonen et al. (2001) which showed that the measurement accuracy is acceptable, if icing is not severe. For the heated anemometers installed at UFS an influence of icing on the measurements has not been observed.

A bigger problem for SATs is the direct impact of snow and rain droplets on the ultrasonic transducers. The receiving transducer cannot distinguish between a

phase change, caused by an sudden increase in wind velocity, or by the impact of a water particle. Raindrops or snow, which are hitting the transducer, cause the appearance of characteristic spikes in the measurement profile. In order to avoid wrong measurements the signal has to be de-spiked, which is done by defining a threshold for a maximum variation in wind velocity. Any variation that exceeds the threshold is detected by an internal algorithm, implemented into the anemometer and written out as an error (e.g. Hojstrup (1993); Lee et al. (2004); Vong and Kowalski (1995)).

The behavior of sonic anemometers under the influence of cloud droplets has been investigated by Siebert and Teichmann (2000). They show that cloud droplets have only small influence on the accuracy of wind speed measurements. However, if shallow water layers accumulate on the transducers it sometimes leads to a sudden change in wind velocity and also makes de-spiking necessary (Kowalski et al., 1997).

Influence of the sensors arm structure

Ultrasonic anemometers are always subject to systematic errors caused by the flow induced by the sensor's geometry. These effects are known as 'transducer shadowing' or 'angle of attack errors' and have been widely investigated for various types of anemometers (Gash and Dolman, 2003; Grelle and Lindroth, 1994; Heinemann et al., 1997; Kaimal and Finnigan, 1994; Kirtzel, 2002; Mortensen and Hojstrup, 1995; Nakai et al., 2006; van der Molen et al., 2004; Wieser et al., 2001; Wyngaard, 1981; Wyngaard and Zhang, 1985). The type of flow distortion varies significantly depending on the manufacturer and the specific geometry of the device. To compensate for transducer shadowing effects a calibration table is usually recorded in a wind tunnel, which is then implemented into the SAT's micro controller. However, it has been shown that the internal correction is not sufficient to correct for all errors induced by the sensor geometry (e.g. Wieser et al. (2001)). As the angle of attack errors of the Thies Ultrasonic Anemometer 3D have not been published before, an investigation of its transducer shadowing effect was performed as part of this study. A short summary of the results will be presented here, while a detailed analysis can be found in Appendix A.

The central rod falsifies the measurements of the wind velocity at low wind speeds, but the effect can be neglected at wind speeds higher than 4 m/s. The transducer arms of the anemometer mostly influence measurements of the horizontal angle, for which abnormalities are found in the histograms. These abnormalities also remain

at high wind speeds of up to 8 m/s. However, for wind directions close to the horizontal they can be neglected. The histograms for the vertical angle show similar abnormalities at specific wind directions. These can be related to the influence of the stand support and the central rod of the anemometer. However, at wind speeds above 5 m/s and horizontal wind directions these influences are also negligible.

As a conclusion from these measurements all further investigations were done separately for different ranges of directions and wind speeds.

Misalignment of sonic anemometers

In this study five sonic sensors were used simultaneously, which introduces misalignment between the sensors as a further source of possible error. Although great care was taken during the installation of the sensors, it was not possible to achieve perfect alignment. In order to correct for misalignment, sequences of high constant wind speed are analysed and the mean wind directions, measured by each sensor individually, are compared. The mean wind direction, measured by the top sensor is used as a reference and the deviations of the mean wind direction measured by the other sensors are computed. The histograms of the deviations are plotted separately for wind coming from the east (figure 2.6) and for wind coming from the west (figure 2.7). It can be seen that the width of the histograms differs for east and west winds. However, the most probable deviation is the same for all anemometers, except for the sensor 2011, which is pointing north and hence is prone to disturbances of the air flow due to the LIDAR dome located on the north-west of the measurement site. The histograms of deviations are in general narrower for east wind compared to the histograms for wind from the west (see also sections 3.2.3 and 3.4.2). Thus, the most likely deviation of the east wind is used to correct for the misalignment of the anemometers. The wind velocities measured by the other sensors are rotated accordingly into the coordinate system of the top sensor. After the rotation the r.m.s. deviation of the sonic anemometers is found to be less than two degrees.

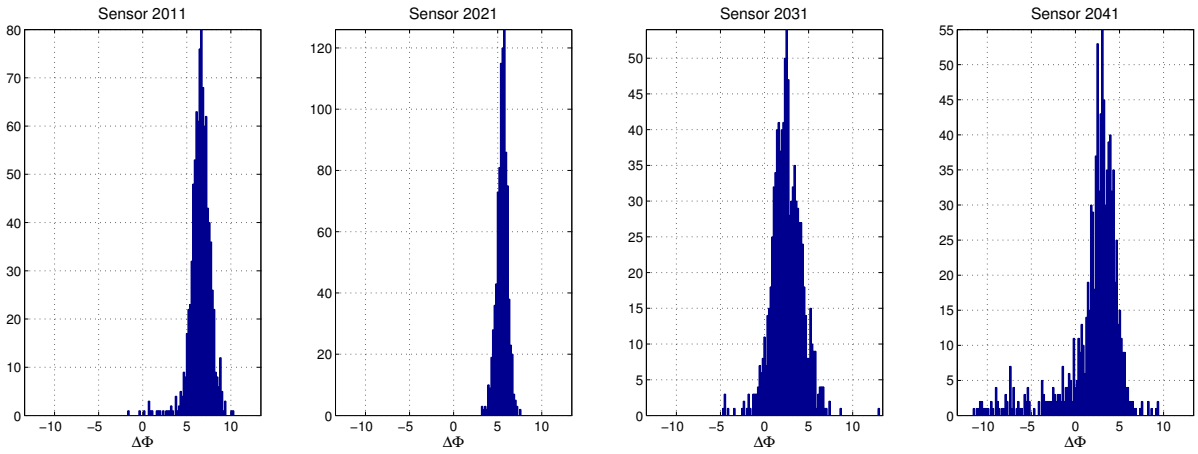

Figure 2.6: Misalignment of the lower sensors relative to the top sensor. Plotted is the deviation of the horizontal angle Φ (in degrees) for wind coming from the west, before correction.

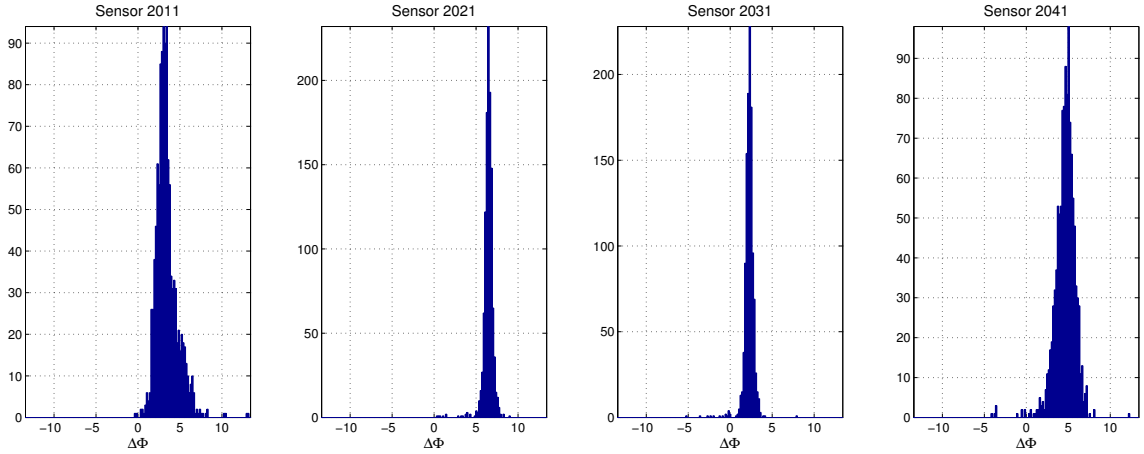

Figure 2.7: Misalignment of the lower sensors relative to the top sensor. Plotted is the deviation of the horizontal angle Φ (in degrees) for wind coming from the east, before correction. The histograms for the vertical angle θ look similar.

2.4 Data recording

In order to collect data from the sonic anemometers they are connected via their serial ports to a serial-to-ethernet converter, NetCom R813 RM Pro. The converter is connected on the ethernet side to a PC operated with a Linux system. On the PC a program is executed, which generates a 10 Hz trigger signal to synchronize the measurement of the five sensors and collects the data from all five sonic anemometers. For each sensor the data is written into an individual ASCII file, which is named after the sensor's number, date and starting time of the recording. The program records data and writes it into the same file until 864000 samples (corresponding to 24 hours) have been collected; afterwards a new file for the new day is generated.

Internal time	East wind	North wind	Wind from above	Virt. temp.
t_{int} [ms]	v_x [m/s]	v_y [m/s]	v_z [m/s]	T_v [°C]

Table 2.3: Data format given by sonic anemometers.

The sonic anemometers have been programed to write out data in the format given in table (2.3). An internal time is recorded, which refers to the time given by a clock inside the sonic anemometer. It has a resolution of 1 ms but is not synchronized to any external clock. The wind components v_x, v_y and v_z are positive for wind coming from the east, the north and above, and they are negative for winds coming from the west, the south and below respectively.

2.4.1 Errors during data recording

An excerpt of a recorded data file is shown in figure 2.8. Each line corresponds to one measurement, taken every 100 ms. It can be seen that one data point is given as "-1;0;0;0;0", which indicates that the sonic anemometer could not acquire a measurement at that time. These events may occur due to precipitation, as described in section (2.3.3), or may be caused by an occasional internal failure.

In rare cases (about once per day) it is also possible that data is not transfered completely. A possible cause may be a failure of the serial-to-ethernet converter. In that case a line is only written partially before the next sample is acquired and written into the next line.

Due to the exposed position of the measurement site, the mast is often struck by lightning, which trips the safety circuit breaker and makes a reboot of the sensors

```
056203159;-01.08;-00.21;+01.10;+01.87
056203259;-00.96;-00.23;+01.02;+01.81
056203359;-00.74;-00.07;+01.02;+01.47
056203459;-00.67;-01.01;+00.77;+01.58
056203559;-00.76;-00.80;+00.92;+01.87
056203659;-00.89;-00.15;+00.90;+01.74
056203759;-00.55;+00.56;+00.25;+01.38
-1;0;0;0;0
056203959;-01.06;-00.56;+01.42;+01.59
056204059;-00.70;-00.80;+01.04;+01.30
```

Figure 2.8: Excerpt of a data file recorded by one sonic anemometer in one second.

necessary.[1] For that purpose, functioning of the sensors is checked everyday via a VPN connection, which can be established over the internet.

2.5 Data processing

Because of the huge amount of data, each month about 10^8 data points are collected, most of the programs used for data processing are written in C++ and the code has a total of about 7300 lines. For plotting data and smaller parts of the processing *Matlab* is used, which is developed by MathWorks company.

The data processing is split into three parts: a pre-processing, in order to eliminate errors and align the recordings of the different sensors, a main processing, in which the analysis of the data is carried out, and a last part, in which sorting and averaging is done.

2.5.1 Pre-processing data

Synchronization and error elimination

In figure 2.9 the same data, which is shown in figure 2.8, is displayed after pre-processing was applied. Three additional columns are added to the file: an error indicator, m, a time difference, Δt, and a continuous time counter, t_{cont}. It can be seen that the erroneous line is replaced with the data of the line following it and the

[1] Often the circuit breaker is also hit accidentally when the snow is cleared from the terrace.

error indicator is set to "+1", as a label for further processing. For all other values, which are regarded as correct measurements, the indicator remains "0".

t_{int} [ms]	v_x [m/s]	v_y [m/s]	v_z [m/s]	T_v [°C]	m	Δt [ms]	t_{cont} [ms]

Table 2.4: Data format written into the new data file, after pre-analysis has been applied.

The time counter which was added in the last column, t_{cont}, gives the time from the beginning of the data file in milli-seconds by using the time of the internal sensor clock. The first line of each file starts with zero and grows for each step by about 100 ms. It usually happens that a small shift in timing occurs because the software generated trigger signal and the internal clock have only a limited accuracy. In case the time discrepancies grow too large, the drift is accounted for by inserting additional lines into the file. It should be stressed that the achieved accuracy of a few seconds per day is better than accuracy required for the conducted measurements.

```
+56203159; -1.08; -0.21; -1.10; +1.87; 0; -15; +57482085
+56203259; -0.96; -0.23; -1.02; +1.81; 0; -15; +57482185
+56203359; -0.74; -0.07; -1.02; +1.47; 0; -15; +57482285
+56203459; -0.67; -1.01; -0.77; +1.58; 0; -15; +57482385
+56203559; -0.76; -0.80; -0.92; +1.87; 0; -15; +57482485
+56203659; -0.89; -0.15; -0.90; +1.74; 0; -15; +57482585
+56203759; -0.55; +0.56; -0.25; +1.38; 0; -15; +57482685
+56203959; -1.06; -0.56; -1.42; +1.59; +1; +85; +57482885
+56203959; -1.06; -0.56; -1.42; +1.59; 0; -15; +57482885
+56204059; -0.70; -0.80; -1.04; +1.30; 0; -15; +57482985
```

Figure 2.9: Corrected excerpt of a new data file recorded in one second by one sonic anemometer, after pre-processing was applied.

The time difference, Δt, gives the time discrepancy compared to the time expected for the data point. The expected time is calculated using the first line of the data file as a reference and assuming a perfect 100 ms spacing between data points. These last two columns are added to the file in order to assure synchronous recording of all five sensors. For the same purpose an additional data file is written out, which contains the corrected measurements of all five sensors parallel to each other and allows to check for errors.

Another possible source of error is due to the limited amount of bytes available for the time format in the measurement protocol given out by the Ultrasonic Anemometer 3D. The internal clock of the sonic anemometer uses 7 bytes to represent its internal time, which causes no problem in case a hexadecimal encoding is used. However, by mistake the sensor protocol was set up to use a decimal representation of the internal time, which limits the highest possible number that can be resolved to be $8^7 = 268\,435\,456$. All higher numbers were displayed as "??????????" and could not be used for measurements which rely on synchronization of the sensors. After the error and its cause had been identified, the sensor protocols were switched to use a hexadecimal encoding of the internal time, which makes the resolution of all times possible. However, about a year of data was recorded with a decimal time setting before this error was corrected.

Histograms and error statistics

The pre-processing of the data contains a second part, which generates histograms of the wind velocities and wind directions. The components of the wind velocity (v_x, v_y, v_z) and the absolute wind speed (v_{abs}) were sorted with bin sizes of $d_1 = 0.01$, 0.02, 0.05, 0.1 m/s , while the vertical angle θ and horizontal angle ϕ were sorted with bin sizes of $d_2 = 0.01\pi$, 0.02π, 0.05π. As described in section 3.1.1 the histograms were used to get an overview over the wind conditions at the measurement site. Furthermore, these histograms were conditioned in various ways and used for the analysis of the transducer shadowing effect (Appendix A).

In order to check whether the error elimination works properly, some error statistics were calculated and written into a log file. Some of the checked parameters are the number of errors due to (a) failure of sensors, (b) transmission problems and (c) surpassing the maximum resolved time.

2.5.2 Main processing

Finding and aligning chunks of constant wind speed

For the main processing, the corrected data files of the top sensor are checked for chunks of one to two minutes length with a constant average wind speed. In order to find these chunks, the first step is to calculate the absolute wind speed for the first 600 measurement points (corresponding to one minute) of a data file. Then the mean wind speed is calculated and it is checked whether all points fulfil the condition

$u/\overline{U} < 0.25$ (see sections 2.6 and 3.2). In case they do not, the first measurement point is dropped and the next one is added, then the newly defined data chunk is checked again. In case a data chunk is found that fulfils the requirement, it is extended by another measurement point and checked again. The extension of the chunk continues until either the condition is not fulfilled, or the maximum of two minutes chunk length is reached. Then the process starts again with the next 600 measurement points.

In the second step, the corresponding data of the lower sensors is read into the program. All files are then checked whether the amount of erroneous lines is less than three percent. If that is the case, the chunks will be used for further processing, otherwise they are discarded.

In a third step the misalignment between the individual sensors is corrected. As described in section 2.3.3, the average discrepancies to the top anemometer are measured and used for correction. A rotation matrix is applied and the wind vectors of all sensors are turned into the coordinate system of the top sensor. Afterwards a five point Gaussian filter ($\sigma = 1$) was optionally used to reduce measurement noise of the velocity traces.

Turbulence parameters

For the determination of turbulence parameters the average wind direction of the top sensor is calculated for each chunk. Then a rotation is applied to the coordinate system such that the z-axis points into the mean wind direction. The new data is used to calculate u', Reynolds stresses, correlations, first and second order moments, energy dissipation and the integral length scales, according to the definitions given in chapter 1. The tetrad-based velocity gradient tensor is determined by a least square fit based on a singular value decomposition (Press et al., 2007). It is based on the theorem, which states that "any $m \times n$ Matrix $\boldsymbol{A}$ can be written as a product of an $m \times n$ column-orthogonal matrix $\boldsymbol{U}$, an $n \times n$ diagonal matrix $\boldsymbol{W}$ with positive or zero elements (the *singular values*), and the transpose of an $n \times n$ orthogonal matrix $\boldsymbol{V}$" (Press et al., 2007).

The relative position of the sensors is used to construct a matrix $\boldsymbol{A}$, while the measured velocity components are written accordingly into a vector $\boldsymbol{b}$. The VGT is then given by a vector $\boldsymbol{x}$ with $\boldsymbol{A} \cdot \boldsymbol{x} = \boldsymbol{b}$, which is determined by decomposing the

matrix $\boldsymbol{A}$ into $\boldsymbol{U}$, $\boldsymbol{W}$ and $\boldsymbol{V}$ and using the relation

$$\boldsymbol{x} = \boldsymbol{V} \cdot \boldsymbol{W}^{\star} \cdot \boldsymbol{U}^{T} \cdot \boldsymbol{b}, \tag{2.4}$$

with $\boldsymbol{W}^{\star} = \mathrm{diag}(1/w_j)$. Additionally, the incompressibility condition is used to construct the matrix $\boldsymbol{A}$ and forcing the VGT to have zero trace.

The definitions given in chapter 4 are used to calculate the invariants R and Q and the conditioned correlations for $Q \gtrless 0$. All parameters are written into separate files for further processing and a log file is generated which contains the location of the chunk, its wind speed and direction, and some of the turbulence parameters mentioned above.

2.5.3 Averaging and calculating the joint PDF

The last part of the program is used to sort the chunks by different parameters, such as wind speed, wind direction and turbulence intensity. Sorted chunks which have similar parameters can be averaged in order to reduce noise and improve statistics. The calculated values of R and Q are sorted with different bin sizes and used for the generation of the joint PDF, as shown in section 4.4. Afterwards all graphs are generated with Matlab.

2.6 Taylor's frozen turbulence hypothesis

Taylor's frozen turbulence hypothesis is widely used to investigate turbulence with a strong mean flow. It applies to the case that the fluctuating velocity is much smaller than the average velocity, $u' \ll \langle U \rangle$, which can also be expressed in terms of the turbulence intensity I as

$$I \equiv \frac{u'}{\langle U \rangle} \ll 1. \tag{2.5}$$

For eddies of size l two time scales can then be constructed. The time scale for the evolution of eddies is of the order of $\frac{l}{u'}$, which is much longer than the time needed to transport the eddies past a fixed point in the flow, approximately to $\frac{l}{\langle U \rangle}$. The turbulent velocity fluctuations are approximated to be frozen into the mean flow, such that temporal increments, δt, can be converted into spatial increments, δl, via

$$\delta l = \langle U \rangle \, \delta t. \tag{2.6}$$

That also implies that time correlations at fixed points are directly related to spatial correlations, which is found to be a good approximation for parallel or nearly parallel flows (e.g. Mathieu and Scott (2000)). (Possible corrections for Taylor's frozen flow hypothesis have been proposed for example by Lumley (1965), Pinton and Labbé (1994) and Hill (1996).)

Using Taylor's hypothesis in order to obtain spatial data from one point measurements limits the spatial resolution depending on the sampling frequency and the mean velocity of the flow. With a sampling frequency of 10 Hz and a typical mean wind speed of $\overline{U} = 5$ m/s, a spatial resolution of 0.5 m is reached, which is comparable to the sensor size of $d \approx 0.3$ m.

3 Large scale flow

Nature, with equal mind,
Sees all her sons at play;
Sees man control the wind,
The wind sweeps man away.
(Empeocles On Etna by Matthew Arnold in 1852)

3.1 Overview over the general weather condition

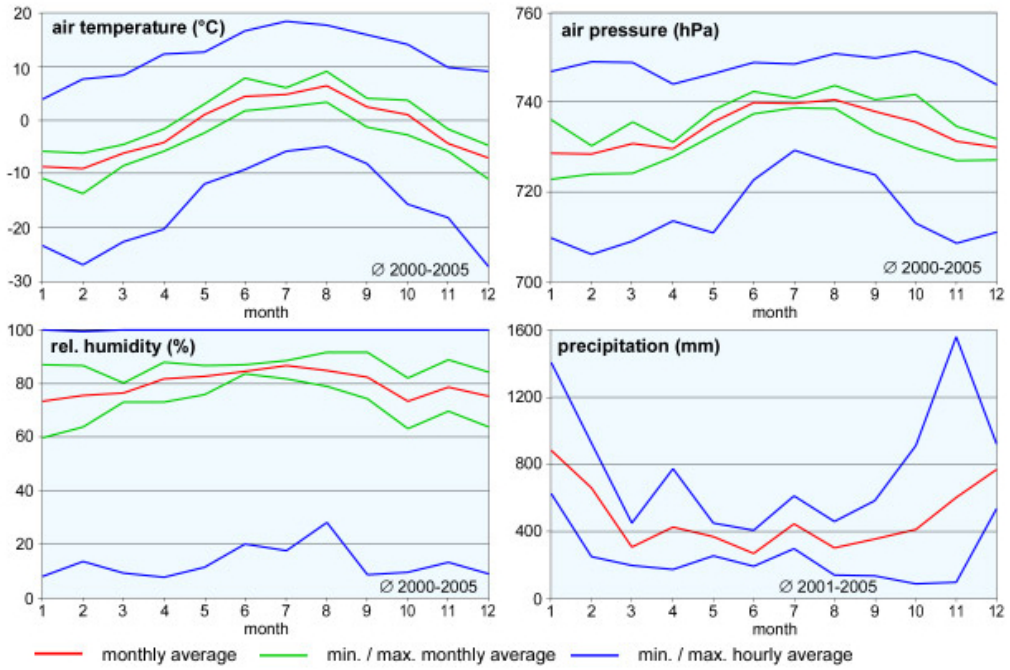

Figure 3.1: Overview over average values of temperature, pressure, humidity and precipitation measured between 2000 and 2005 by Deutscher Wetterdienst (DWD) at UFS (UFS, 2011)

The weather at Zugspitze is mainly influenced by the westerlies, which are strong prevailing winds in the middle latitudes. The winds often carry great masses of moist

air, leading to heavy precipitation on the north-west side of the Zugspitz massif. On the contrary to this, on about 60 days per year the weather is dominated by Foehn winds, which push against the massif from the south, resulting in relatively high temperatures during the winter time. The average temperature during the 'standard reference period' (1961 - 1990) was −4.8 °C and the average precipitation was 2003 mm per year (Siebler, 2010). The lowest temperature recorded at Zugspitze was −35.6 °C while the highest was 17.9 °C (DWD, 2000).

3.1.1 Wind conditions

The following description of wind conditions is based on data which was recorded between the 1st of September and end of December 2010. The graphs will show exemplary data for September, October, November and December. Data which was recorded between April 2010 and August 2010 is not presented here because the top anemometer was not aligned correctly during this period. When the mast was checked in August 2010 it was found that the top anemometer was not screwed tightly to the mast. The data collected in the year 2011 shows similar behaviour as the data in 2010 as presented here and is attached in Appendix B.

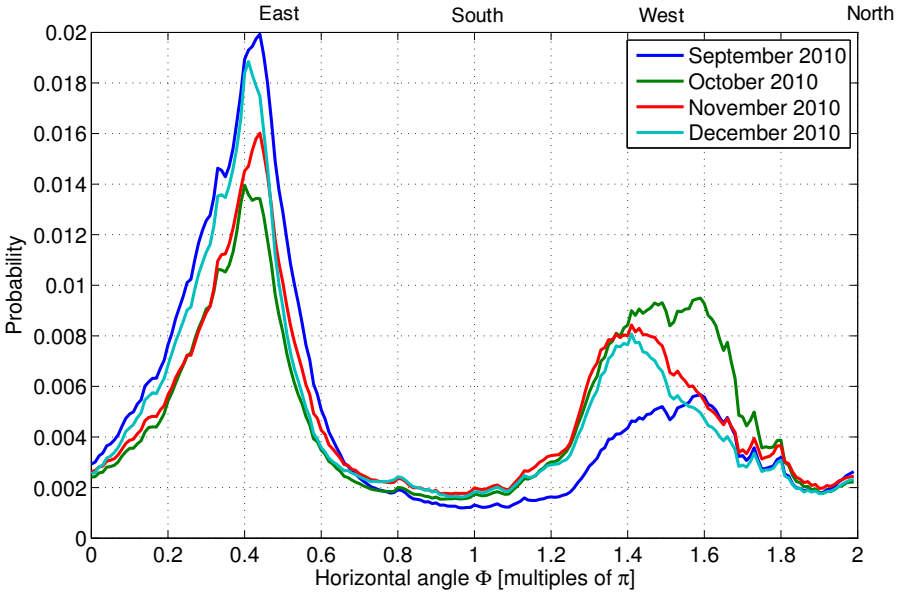

Figure 3.2: PDF of the wind direction as a function of the horizontal angle, Φ, exemplary for the months September, October, November and December 2010 from the top sensor. The dents in the PDF are due to transducer shadowing effects as described in section 2.3.3.

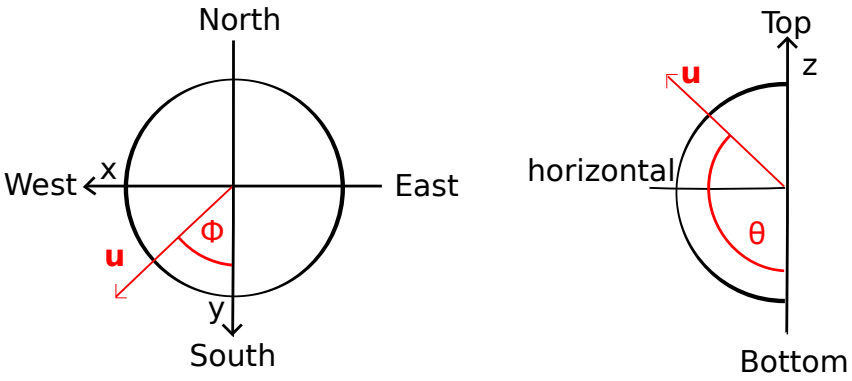

Figure 3.3: Definition of the horizontal angle, ϕ, and vertical angle, θ. Also shown are the axis of the sensor coordinate system and sensor position (used in table 2.1).

Horizontal angle, Φ, in multiples of π	Horizontal angle, Φ, in degrees	Geographic direction where the wind comes from
0/2	0°/360°	North
0.5	90°	East
1	180°	South
1.5	270°	West

Table 3.1: Relation between the horizontal angle, Φ, and the geographic direction where the wind comes from.

Vertical angle, θ, in multiples of π	Vertical angle, θ, in degrees	Direction where the wind comes from
0	0°	Wind from the above
0.5	90°	Wind horizontal
1	180°	Wind from below

Table 3.2: Relation between the vertical angle, θ, and direction where the wind comes from.

The probability density function (PDF) of the horizontal angle, Φ, has two peaks at $\Phi \approx 0.45\pi$ and at $\Phi \approx 1.5\pi$ (figure 3.2), which correspond to the wind from the west and from the east. (An overview over the measured angles and the corresponding geographic directions can be found in table 3.1 and figure 3.3.) The peaks in the PDF can be explained by the general weather situation and the surrounding geographic topology, as described in section 2.1. Mountains shield the measurement site towards the north and the south, which directs the wind into the dominating west-east and east-west directions. As the measurement site is open towards the south-east (see figure 2.1) the east wind is not perfectly aligned along the east-west direction but tends to come slightly more from the south-east.

The PDF of the vertical angle, θ, shows that the wind direction at the measurement site is mostly horizontal, corresponding to an angle of $\theta \approx 0.45$. Winds from the top are slightly more frequent than winds coming from below the measurement site.

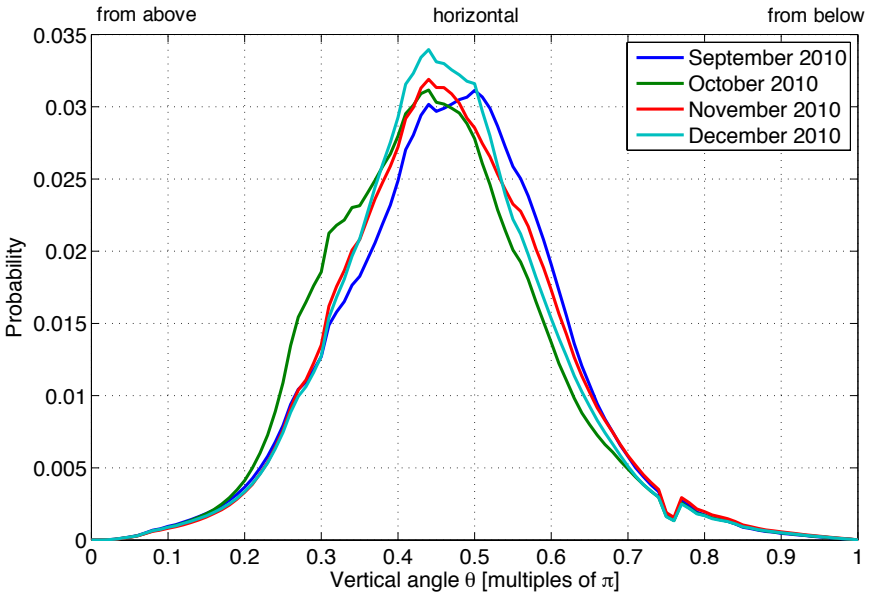

Figure 3.4: PDF of the vertical angle, θ, for the months September, October, November and December 2010 from the top sensor.

The mean wind speed at UFS is about 4 m/s and the PDF of the absolute wind speed, v_{abs}, is shown in figure 3.5. It can be seen that the average wind speed increases from September to December. The highest average wind speed recorded between September and December 2010 was 12.56 m/s on October 4th (with an averaging period of 1 minute length). The histograms are studied in more detail

in appendix A where the influences of wind speed, wind direction and bin sizes are compared.

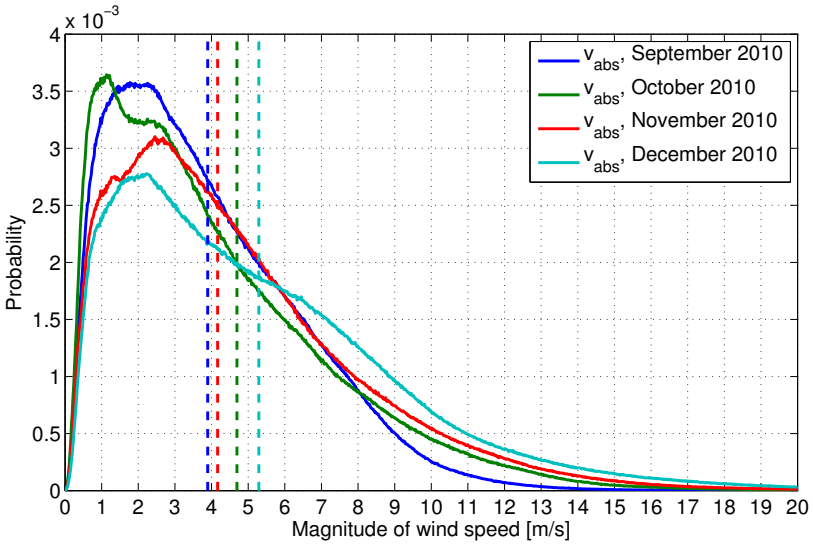

Figure 3.5: PDF of the absolute wind speed, v_{abs}, for September, October, November and December 2010, measured by the top sensor. The location of the mean wind speed is also shown for September: $v_{abs} = 3.9$ m/s, October: $v_{abs} = 4.2$ m/s, November: $v_{abs} = 4.7$ m/s and December: $v_{abs} = 5.3$ m/s.

3.2 Turbulence parameters

For the further analysis the measurements are separated into chunks of constant wind speed with a fluctuating wind speed of $u'/\overline{U} \leq I_t = 0.25$ and a duration between one and two minutes length. The threshold value for the turbulence intensity $I_t = 0.25$ was chosen in accordance with earlier measurements by Favre et al. (1958), Favre et al. (1957) and Fisher and Davies (1964) which showed that Taylor's frozen flow hypothesis is reliable up to this range.

For each chunk the coordinate system is turned, such that the z-axis of the new coordinate system points into the mean wind direction. Then Taylor's hypothesis is used to convert temporal information into spatial information. Afterwards the chunks are averaged over intervals with similar wind speeds, directions and turbulence intensities. The averaging is carried out for interval sizes of $\Delta\overline{U} = 0.1, 0.2, 0.5$ and 1 m/s, $\Delta\Phi, \Delta\theta = 20°$ and $60°$ and $\Delta I = 0.05$. The averaged chunks are used to determine the correlation functions, integral length scales, Reynolds stresses, energy dissipation rates, Reynolds numbers and structure functions.

3.2.1 Correlations and integral length scales

First, the two point velocity correlation tensor $R_{ij}(\boldsymbol{r}) = \langle u_i(\boldsymbol{r}) u_j \rangle$ is determined for each averaging interval as a function of distance $\boldsymbol{r} = z$ (mean flow direction), which is shown in the normalized form of f and g in figure 3.6. The integral length scales

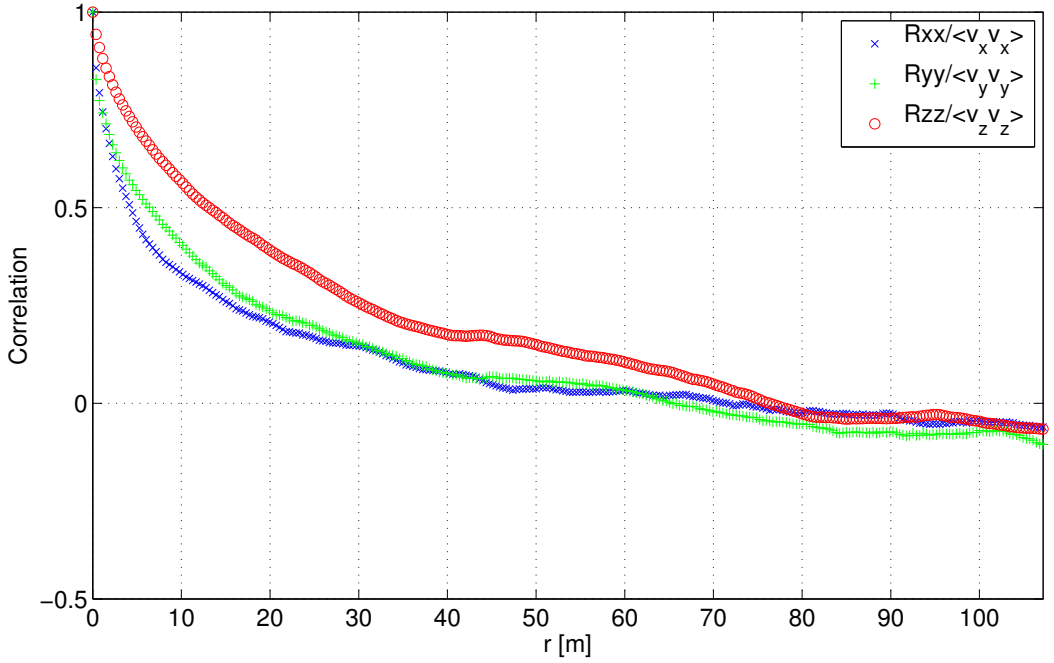

Figure 3.6: Averaged normalized correlations, $f = \frac{R_{zz}}{\langle u_z(z) u_z \rangle}$ and $g_x = \frac{R_{xx}}{\langle u_x(z) u_x \rangle}$, $g_y = \frac{R_{yy}}{\langle u_y(z) u_y \rangle}$, plotted as a function of $\boldsymbol{r} = z$. The chunks have a mean wind speed between 3.5 and 4 m/s and come from the east.

are defined in (eq. 1.47) and (eq. 1.48) as the integrals of the autocorrelation from zero to infinity. Since an integration to infinity is practically not possible different methods to estimate integral length scales have been proposed (e.g. Dias et al. (2004); O'Neill et al. (2004); Tritton (1988)). In the following two methods for the estimation of integral length scales are compared.

In the first method the integral length scales are determined by fitting an exponential function to the measured correlations with $\frac{R_{ii}}{\langle u_i u_j \rangle} \sim e^{\gamma_i r}$ and using $L_{ii} = \frac{1}{\gamma_i}$ to define the integral length scales. That corresponds to an integration up to the value where the autocorrelation function reaches $1/e$. A fit of the normalized autocorrelations is visualized in figure 3.7. As this method discounts a large portion of the autocorrelation functions it is expected to underestimate the integral lengths

(O'Neill et al., 2004).

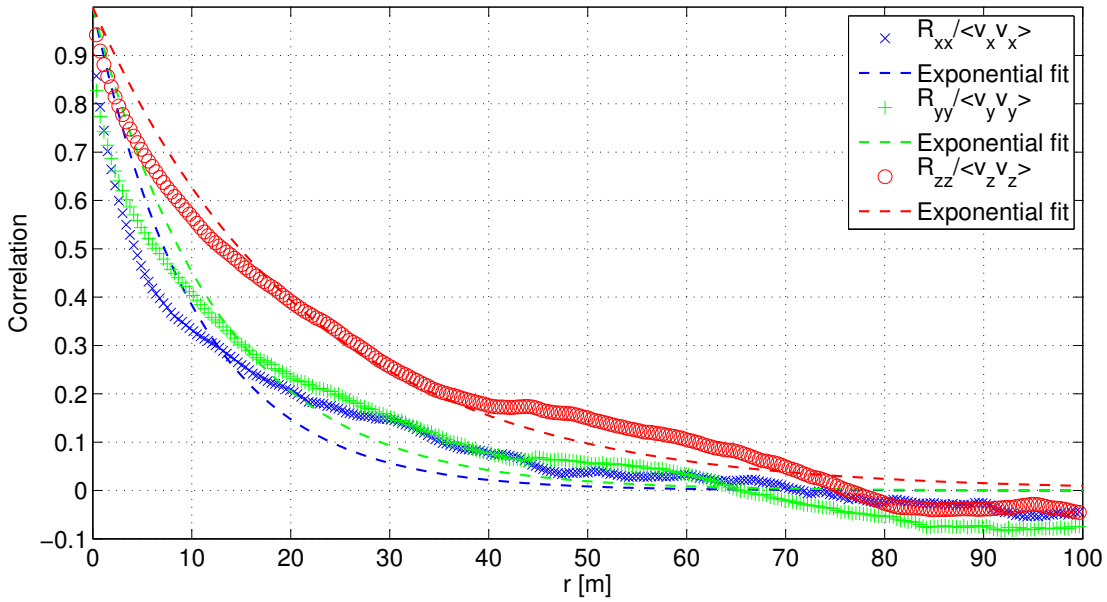

Figure 3.7: Normalized correlations g and f, fitted with an exponential function $\frac{R_{ii}}{\langle u_i u_j \rangle} \sim e^{\gamma_i r}$. Only the fitted data range is shown. The plotted data is the same as in figure 3.6.

An alternative method to determine the integral length scales is to integrate correlations up to the first zero crossing. The integral length scales of the chunk shown in figures 3.6 and 3.7 are compared in table 3.3. It can be seen that the scales are almost the same for both methods. A disadvantage of the exponential fit method is the uncertainty up to where the data should be fitted. Because of the expected underestimation of integral length scales and the difficulty involved in fitting the data, the second method, i.e. integration up to zero crossing, is used in order to define integral length scales for the rest of the analysis.

Method	R_{xx}	R_{yy}	R_{zz}
Exponential fit	10.4	16.6	21.5
Zero crossing	11.8	13.3	21.3

Table 3.3: Comparison of integral length scales determined for averaged chunks, as presented in figures 3.6 and 3.7. All length scales are given in meters.

3.2.2 Distribution and mean of turbulence parameters

The distribution and mean of integral length scales, Reynolds stresses and Reynolds numbers are plotted in the form of PDFs in the following subsections. The data presented here is computed with the individual chunks of constant wind speed without averaging. The same calculation was carried out for the averaged chunks and is presented in appendix C. However, it was found that the distribution and mean of these quantities are almost independent of the averaging intervals and the amount of averaged data chunks.

Average integral length scales

The PDFs of the integral length scales which were recorded between September and December 2010 are shown in figure 3.8. The average integral length scale is about $L \approx 19$ meters, which corresponds to the size of the biggest eddies in the flow (section 1.3.4). The measurement agrees well with the geometric flow scales of the surroundings, as the distance towards the mountains is about 20 m, at the height of the sonic anemometers (see figures 2.3 and 2.4).

The average integral length scales of wind coming from the east and from the west are compared in figure 3.9. It can be seen that the average longitudinal integral length scales are almost the same for both directions. The average transverse integral length scales are smaller for wind coming from the east, which may be caused by the more isotropic turbulence of east wind (see sections 3.2.3 and 3.4.2).

It can also be seen that the distributions of the integral length scales have long tails such that the mean of the distribution does not coincide with the highest probability. This observation can be accounted to the strong variations of the flow conditions as expected in an atmospheric flow.

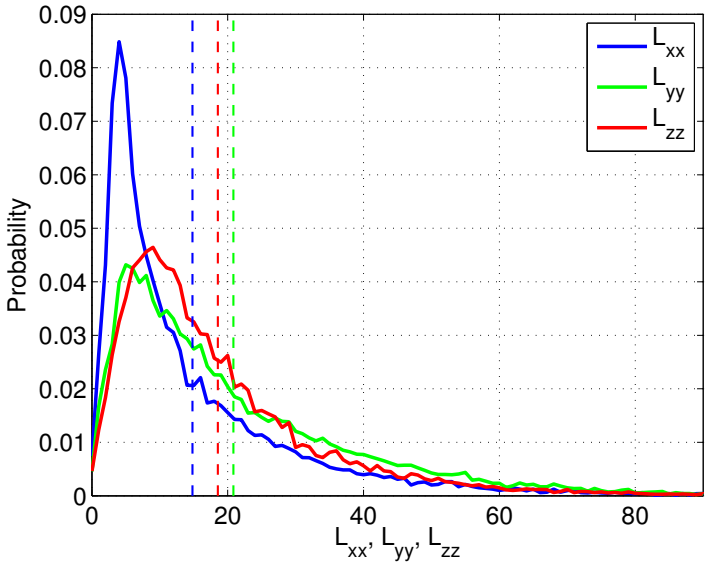

Figure 3.8: PDFs of the integral length scales of the x, y and z direction, where the z-axis of the coordinate system points into the mean wind direction. Also shown are the mean integral length scales, $\langle L_{xx} \rangle = 14.8$ m, $\langle L_{yy} \rangle = 20.8$ m and $\langle L_{zz} \rangle = 18.6$ m. The data was taken between the beginning of September and the end of December 2010.

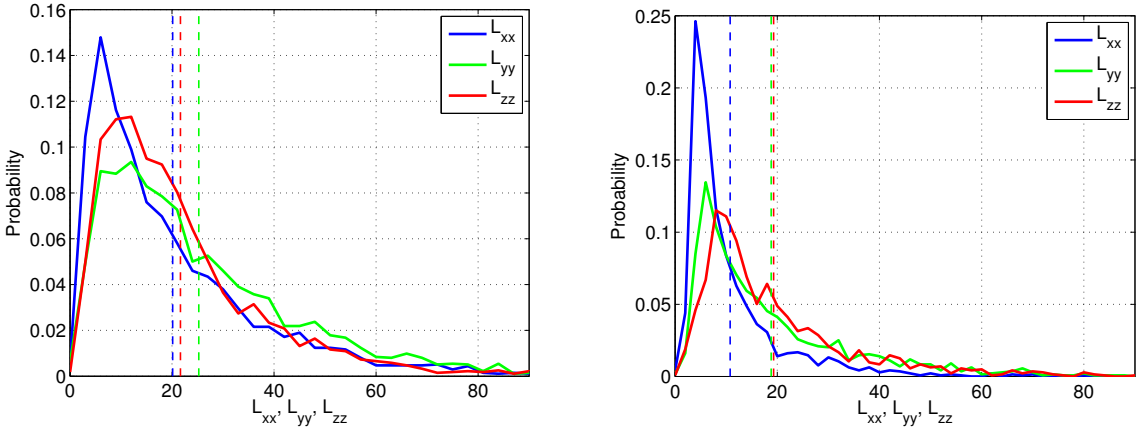

Figure 3.9: PDFs of the integral length scales for wind coming from the west (left) and from the east (right).

Reynolds stress tensor

The Reynolds stress tensor, $\langle u_i u_j \rangle$, was calculated for each chunk and its isotropic part was used to determine the r.m.s. of the fluctuating velocity

$$u' = \sqrt{\frac{1}{3}\langle u_i u_i \rangle} = \sqrt{\frac{1}{3}\left(\langle u_1^2 \rangle + \langle u_2^2 \rangle + \langle u_3^2 \rangle\right)} \,. \tag{3.1}$$

The PDFs of the isotropic part of the Reynolds stress tensor are shown in figure 3.10. The mean velocity fluctuation between September and December 2010 is found to be $\langle u' \rangle = 0.44$ m/s.

Reynolds number

The large scale Reynolds number is calculated as $R_L = \dfrac{k^2}{\epsilon\nu}$. The Taylor scale Reynolds number, based on the equation (1.60) is then used to determine the Taylor scale Reynolds number $R_\lambda = \sqrt{\frac{20}{3} R_L} = \sqrt{15 \frac{u'^4}{\epsilon\nu}}$. The maximum Reynolds number is about $R_L \approx 3.6 \cdot 10^7$ or respectively $R_\lambda \approx 1.5 \cdot 10^4$. About 200 events have a Taylor scale Reynolds number larger than 10^4 but only 35 events are larger than $1.25 \cdot 10^4$. The PDFs of the large scale and the Taylor scale Reynolds numbers can be found in figure 3.11.

It can be summarized that it is relatively easy to access large Reynolds number flows at the measurement site. However, it is not possible to influence the exact

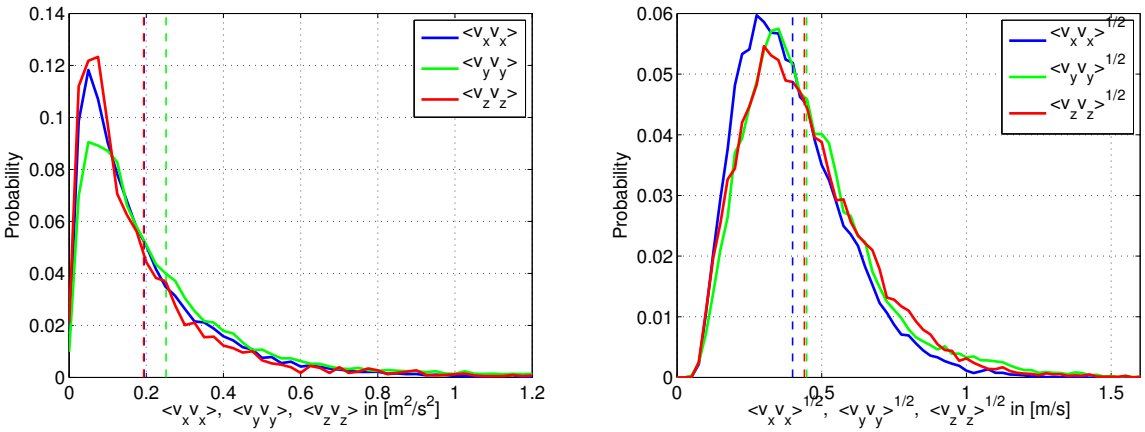

Figure 3.10: PDFs of the isotropic components of the Reynolds stress tensor (left) and the square root of the components (right). The z-axis of the coordinate system points into the mean wind direction. Also shown are the averages.

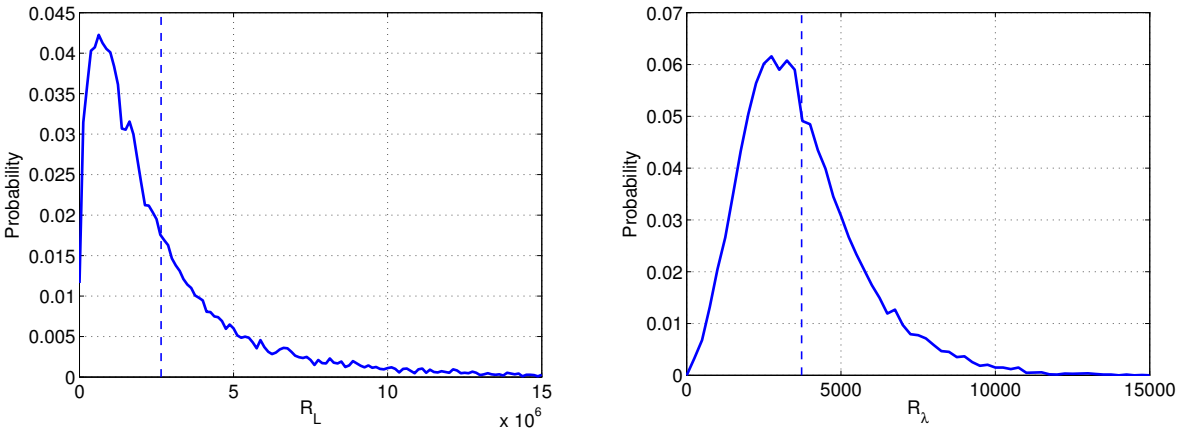

Figure 3.11: PDFs of the large scale Reynolds number, R_L, (left) and the Taylor scale Reynolds number, R_λ, (right). The average Reynolds numbers are $\langle R_L \rangle = 2.6 \cdot 10^6$ and $\langle R_\lambda \rangle = 3700$.

flow conditions, such as wind speed, wind direction and the level of isotropy. These parameters can only be chosen passively as one selects the events according to the conditions one is interested in.

3.2.3 Anisotropy of the flow

As stated in equation (1.50), the integral length scales in isotropic turbulence are related via $2L_{NN} = L_{LL}$. As the z-axis of each chunk is pointing into the mean wind direction the ratio

$$\frac{L_{LL}}{L_{NN}} = \frac{L_{zz}}{\left(L_{xx} + L_{yy}\right)/2} \tag{3.2}$$

should be equal to 2 in isotropic turbulence. The average value measured is $\left\langle \frac{L_{LL}}{L_{NN}} \right\rangle = 1.51$, which indicates that the large scale wind conditions at the measurement site are anisotropic. The large scale anisotropy can be explained by wind shear induced by surrounding buildings. The large LIDAR tower located in the north-west of the measurement site blocks the flow to the north of the mast. In figure 3.12 the average deviation from the mean wind speed is plotted separately for east and west winds. Because of the presence of the LIDAR tower a strong wind shear occurs at the measurement site for wind coming from the west. Wind coming from the east is less influenced because no constructions are located on the east of the measurement site. A weak shear of the average wind speed is probably due to the southern flank of the Zugspitz mountain.

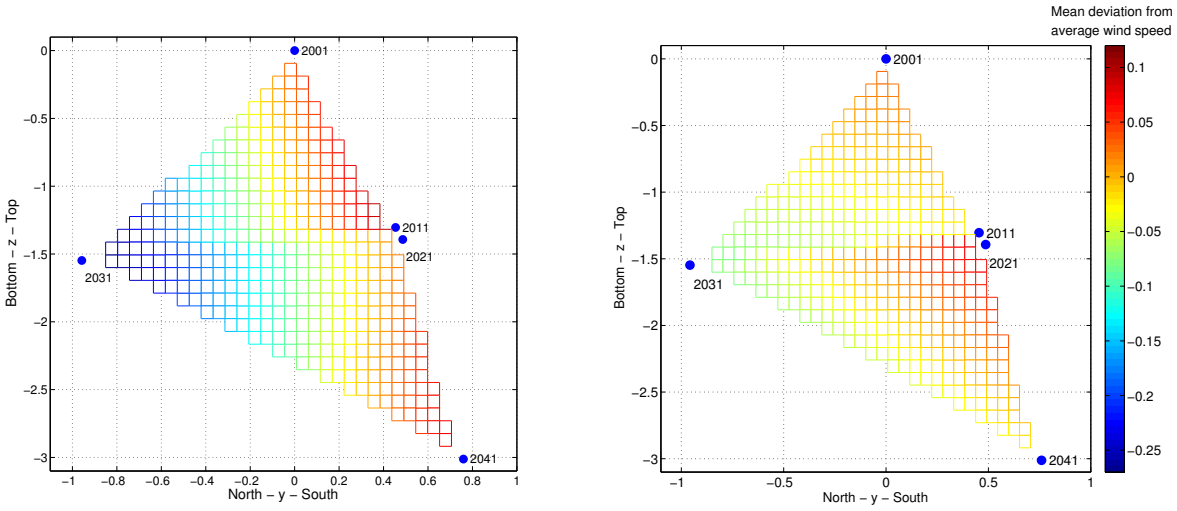

Figure 3.12: Interpolated shear profile for wind from the west (left) and wind from the east (right). The measurement volume is projected into the y-z-plane and viewed from the west. The average deviation from the average wind speed is color coded and interpolated between the anemometers.

A comparison of the integral length scales confirms that the east wind is generally more isotropic. The average ratio between the integral length scales (eq. 3.2) is closer to the value of 2 for wind coming from the east:

$$\text{West: } \frac{L_{LL}}{L_{NN}} = 1.26 \qquad \text{East: } \frac{L_{LL}}{L_{NN}} = 1.79$$

3.3 Structure functions

For the chunks with constant wind speed, i.e. $I \leq 0.25$, Taylor's hypothesis (see sections 2.6 and 3.2) is used in order to determine the second and third order structure functions, as defined by equation (1.41). Examples of the second and third order structure functions are plotted in figure 3.13. By dimensional analysis a scaling of $D_2(r) = C_2(\epsilon r)^{2/3}$ is expected for the second order structure function, which is used to fit C_2 and ϵ. The fitted ϵ is compared to the third order structure function with the help of the 4/5-law, $D_{LLL}(r) = \frac{4}{5}\epsilon r$ (eq. 1.62), as shown in figure 3.13.

For a better comparison of the estimated ϵ the structure functions are plotted in the reduced form, $\epsilon = \frac{D_n}{C_n r^{n/3}}$ and shown in figure 3.14. It can be seen that the smallest scales that can be resolved are on the order of $\Delta t \cdot \overline{U} \approx 0.5$ m, while the

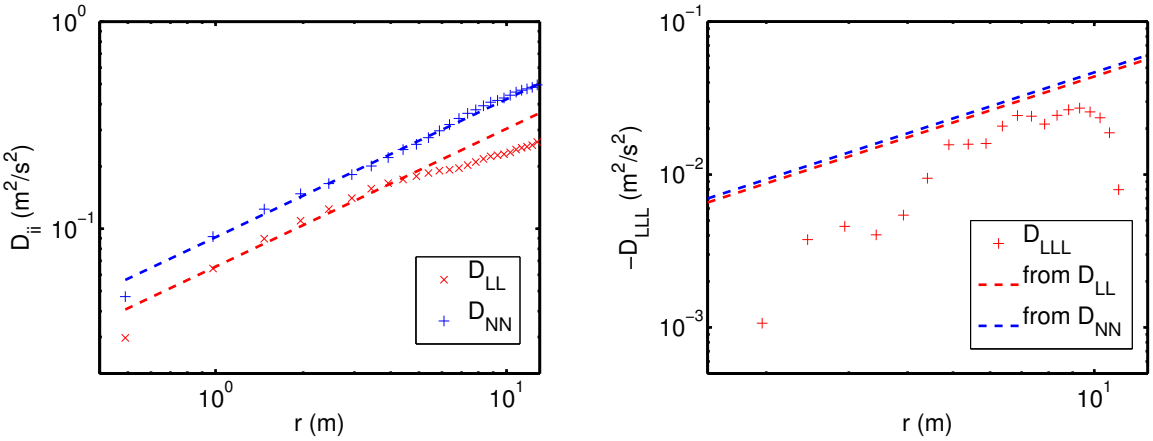

Figure 3.13: Second order structure function (left) and third order structure function (right) for a chunk with a constant mean wind speed of 4.9 m/s. A linear slope is fitted to the second order structure functions and also shown in the plot of the third order structure function, with the following parameters (as visualized by the dashed lines): $\epsilon_{D_{LL}} = 5.5 \cdot 10^{-3} \frac{\mathrm{m}^2}{\mathrm{s}^3}$, $\epsilon_{D_{NN}} = 5.8 \cdot 10^{-3} \frac{\mathrm{m}^2}{\mathrm{s}^3}$ and $C_2 = 2.11$.

largest scale for which the predicted scaling can be observed, is of the order of the integral scales $L_{LL} \approx 10$ m (from D_{LL}) and $L_{NN} \approx 40$ m (from D_{NN}). A comparison of the second and third order structure functions shows that the inertial range of D_{LLL} is shorter than then inertial range observed from D_{LL} and D_{NN}.

3.3.1 Normalized energy dissipation rate

It has been found that the normalized energy dissipation rate, $C_\epsilon \equiv \frac{\epsilon L}{u'^3}$, is a constant for a wide range of Reynolds numbers (Burattini et al., 2005; Pearson et al., 2002; Sreenivasan, 1998). This observation has also been called the "zeroth law of turbulence", as Kolmogorov's hypotheses assume that the mean energy dissipation rate is independent of the viscosity at high Reynolds numbers (Eyink et al., 2000; Pearson et al., 2004).

For the current measurement C_ϵ was estimated and plotted as a function of Reynolds number (figure 3.15). In agreement with earlier measurements C_ϵ has a value of about $C_\epsilon \approx 0.5$ (e.g. Pearson et al. (2002)). Furthermore it can be seen that the value of C_ϵ depends weakly on the wind direction, which can be attributed to the different flow conditions of east and west wind. As described in section 3.2.3 wind from the west is subject to a stronger shear than wind from the east. The weak

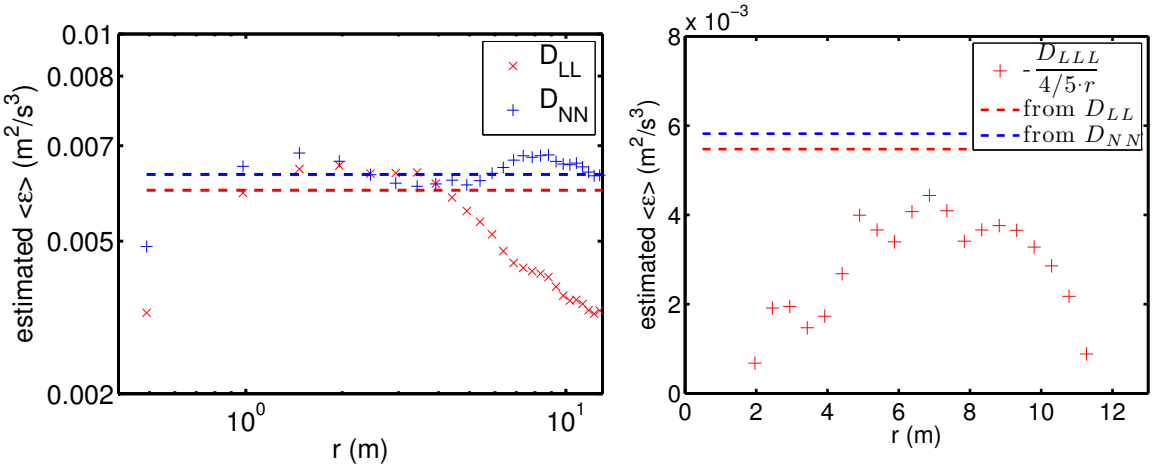

Figure 3.14: Reduced plot of the second (left) and third (right) order structure functions for the same data as shown in figure 3.13.

dependence on shear is in agreement with earlier measurements which show that an increase in shear leads to a smaller value of the energy dissipation rate (Sreenivasan et al., 1995).

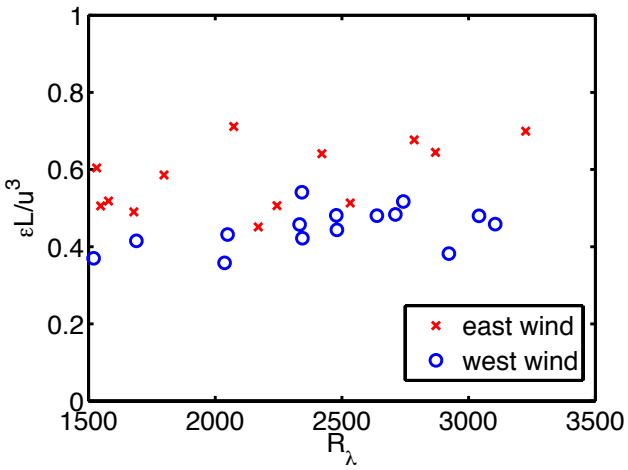

Figure 3.15: Normalized energy dissipation rate, $C_\epsilon = \frac{\epsilon L}{u'^3}$, as a function of Reynolds number. C_ϵ was determined by fitting the second order structure functions. The value of C_ϵ is dependent on the wind direction, due to the topology.

3.4 Large scale anisotropy and the return to isotropy principle

3.4.1 Theoretical background

The return to isotropy of anisotropic turbulent flows is a basic assumption of Kolmogorov's theory and has long been under investigation. A first model was introduced by Rotta (1951), which assumes a linear return to isotropy. A systematic investigation of the 'return to isotropy principle' was carried out by Schumann (1977) and Lumley and Newman (1977). In the latter the so-called Lumley triangle was introduced, which characterizes the Reynolds-stress anisotropy by a simple graphical representation (Pope, 2000)[1].

In principle the anisotropy of the flow is captured by the six components b_{ij} of the anisotropy tensor $\boldsymbol{b}$ (eq. 1.18). As the anisotropy tensor has zero trace ($b_{ii} = 0$), the tensor can be represented by two independent invariants. One possible choice to define the invariants can be made by transforming the matrix $\boldsymbol{b}$ into its principal axes. It can then be written in diagonal form with the eigenvalues λ_1 and λ_2 as

$$\tilde{b}_{ij} = \begin{bmatrix} \lambda_1 & 0 & 0 \\ 0 & \lambda_2 & 0 \\ 0 & 0 & -\lambda_1 - \lambda_2 \end{bmatrix} . \tag{3.3}$$

Two further choices of invariants are common and can be stated either in form of the pair η and ξ or in the form of II_b and III_b. These invariants are defined as follows:

$$6\eta^2 = -2\mathrm{II}_b = b_{ii}^2 = b_{ij}b_{ji} = 2\left(\lambda_1^2 + \lambda_1\lambda_2 + \lambda_2^2\right) \tag{3.4}$$

$$6\xi^3 = 3\mathrm{III}_b = b_{ii}^3 = b_{ij}b_{jk}b_{ki} = -3\lambda_1\lambda_2\left(\lambda_1 + \lambda_2\right) \tag{3.5}$$

Every Reynolds stress tensor is then represented by a point on a plane, which is spanned by a pair of invariants. As the eigenvalues of $\boldsymbol{b}$ have to be non-negative and real (eq. 1.20), the invariants lay within a certain range on the plane. This range is confined by three lines and referred to as the *Lumley triangle*. In the original paper by Lumley and Newman (1977) the definition of II_b and III_b was used, while the use of η and ξ can be found for example in Pope (2000). In the following the definition

[1] The further presentation of the theoretical background will be based mostly on chapter 11 of Pope (2000).

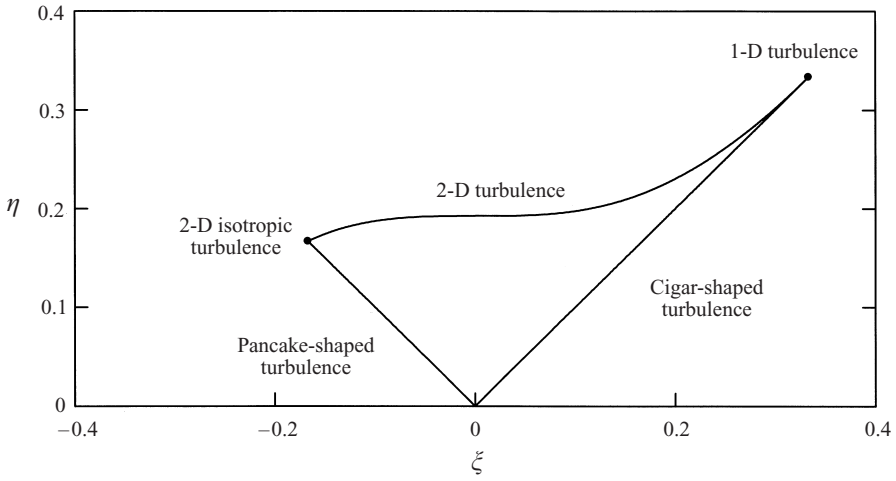

Figure 3.16: Lumley triangle in the η and ξ plane. Figure taken from Choi and Lumley (2001).

State of turbulence	**Invariants**	**Eigenvalues of $\boldsymbol{b}$**
Isotropic	$\xi = \eta = 0$	$\lambda_1 = \lambda_2 = \lambda_3 = 0$
Axisymmetric (one large eigenvalue) "cigar-shaped"	$\eta = \xi$	$-\frac{1}{3} \leq \lambda_1 = \lambda_2 \leq 0$
Axisymmetric (one small eigenvalue) "pancake-shaped"	$\eta = -\xi$	$0 \leq \lambda_1 = \lambda_2 \leq \frac{1}{6}$
Two-dimensional	$\eta = \left(\frac{1}{27} + 2\xi^3\right)^{1/2}$	$\lambda_1 + \lambda_2 = \frac{1}{3}$
One-dimensional	$\xi = \frac{1}{3}$, $\eta = \frac{1}{3}$	$\lambda_1 = \frac{2}{3}$, $\lambda_2 = \lambda_3 = -\frac{1}{3}$

Figure 3.17: Special states of the Reynolds stress tensor in terms of the invariants ξ and η and the eigenvalues λ_i of $\boldsymbol{b}$ (Pope, 2000).

of η and ξ will be used to investigate the anisotropy of the flow. It should be noted that the top side of the 'triangle' is not straight (figure 3.16).

The edges of the Lumley triangle correspond to certain states of turbulence with special symmetries. For the case of perfectly isotropic turbulence the eigenvalues and invariants of the anisotropy tensor are zero. Axisymmetric turbulence corresponds to the right and left boundaries of the triangle. In case the axial component is large ξ is bigger than zero, corresponding to the right side, while if $\xi < 0$ the axial component is small, which corresponds to the left side of the triangle. These states of turbulence are sometimes also referred to as cigar-shaped turbulence or pancake-shaped turbulence respectively. Two-dimensional turbulence is represented by the

line on top and one-dimensional turbulence corresponds to the top right corner of the triangle. The invariants and eigenvalues of $\boldsymbol{b}$ for these special states are again summarized in table 3.17.

3.4.2 Dependency on the wind direction

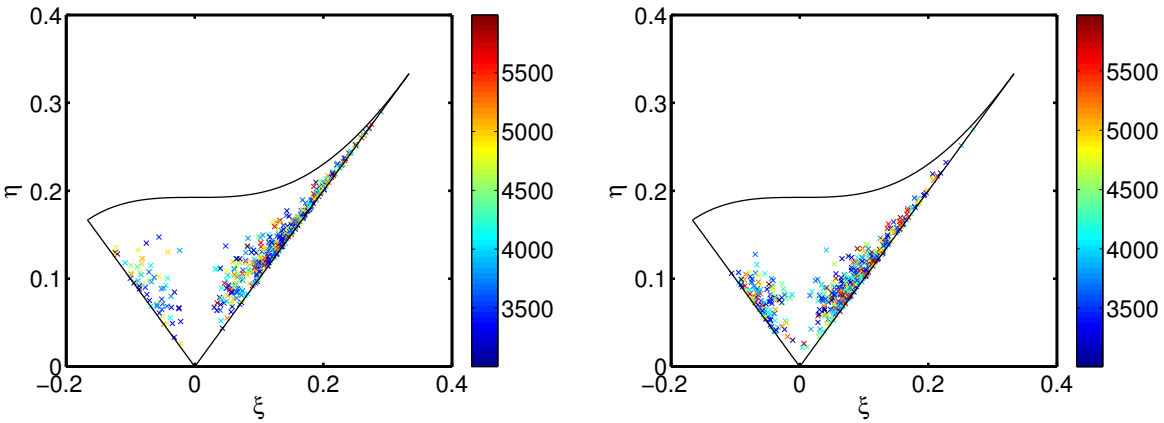

Figure 3.18: The Lumley triangle plotted in the ξ-η-plane for wind coming from the west (left) and from the east (right) as a function of R_λ (color coded). For better visibility only 500 randomly chosen events have been plotted for each wind direction.

The invariants ξ and η are plotted on the Lumley triangle for winds coming from the west and from the east separately (figure 3.18). The invariants for wind originating in the east show the tendency to be closer to the origin than wind from the west, which indicates that wind coming from the east is more isotropic than wind coming from the west. This result is in agreement with the findings of sections 3.2.3 and 3.3.1, which show a stronger shear of west winds caused by the surrounding buildings.

3.4.3 The return to isotropy

Reynolds number dependency

A basic assumption of Kolmogorov's theory is that high Reynolds number turbulence 'forgets' about the large-scale flow geometry and the anisotropy at large scales will not influence smaller scales (section 1.3.2). By dimensional analysis Lumley (1967) predicted the decay of anisotropy, caused by a constant mean shear, to be proportional to R_λ^{-1}.

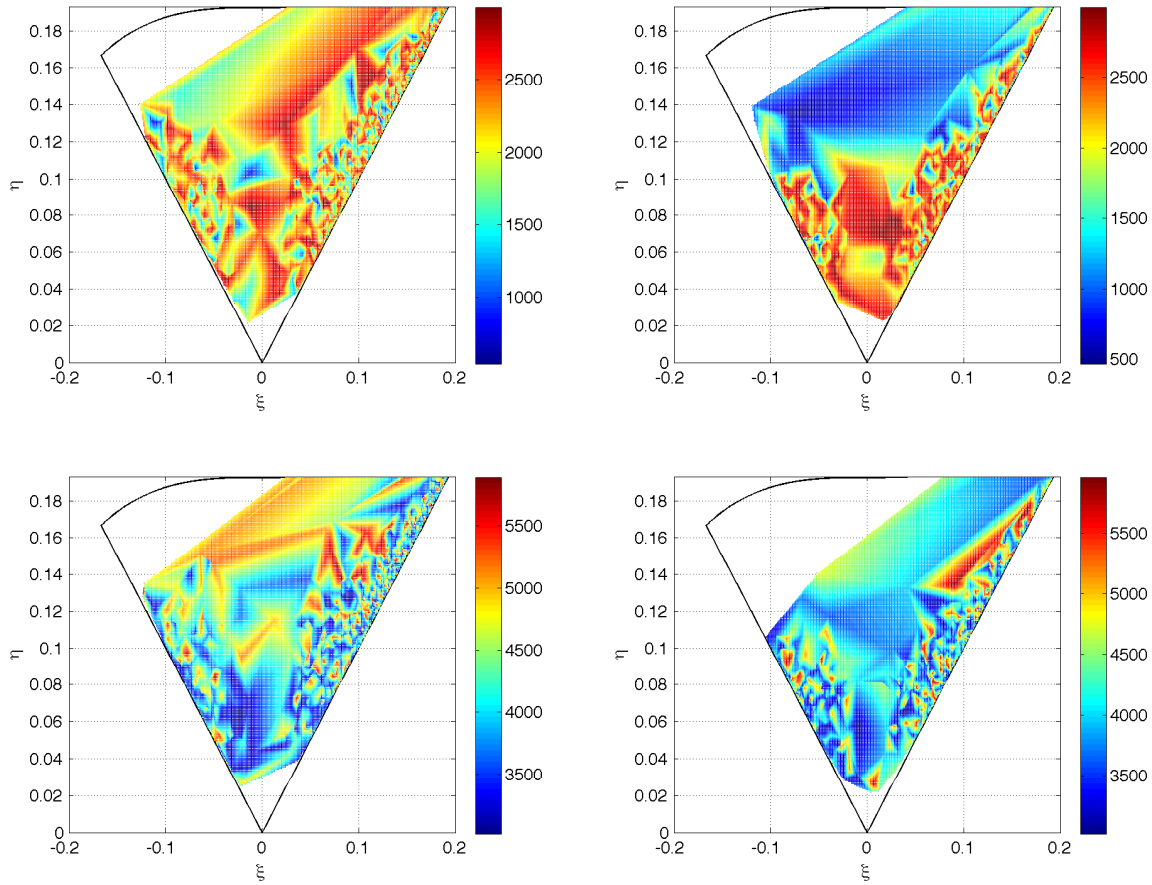

Figure 3.19: Linear interpolation of the invariants in the ξ-η-plane as a function of Reynolds number R_λ (color coded) for flows with $R_\lambda < 3000$ on top and for flows with $3000 < R_\lambda < 6000$ on the bottom. The left panels correspond to wind from the west, while the right panels correspond to wind from the east. Between 1500 and 2000 events have been averaged.

For the investigation of the influence of the Reynolds number on the isotropy of the flow the Lumley triangle is used. A linear interpolation of the invariants of figure 3.18 is plotted for two different ranges of R_λ. First we discuss Reynolds numbers with a range of $0 < R_\lambda < 3000$, shown in figure 3.19 on the top: For wind from the east more values with large R_λ are found close to the origin and it can be concluded that an increase in Reynolds number indeed leads to an increase in isotropy. The result is in agreement with the findings of a study by Shen and Warhaft (2000), which was carried out in a wind tunnel with an active grid and R_λ up to 1100. They observed that the anisotropic Reynolds stress is confined to the low wave numbers and decreases with wave number in consistency with the prediction

by Lumley (1967). For wind coming from the west such a clear dependence cannot be found, which is most likely due to flow interferences caused by constructions close to the measurement site, as described in section 2.1. These constructions lead to a strong shear of the flow that may prohibit the return to isotropy at high Reynolds numbers, as proposed by Schumacher et al. (2003).

In figure 3.19 at the bottom the Lumley triangle is plotted again for large Reynolds numbers, with $3000 < R_\lambda < 6000$. For these large Reynolds numbers it can be seen that isotropy does not increase with R_λ, neither for east nor for west winds. It may be conjectured that the shear rates increase along with the Reynolds number, which prohibits the return to isotropy even at high Reynolds numbers.[2]

3.4.4 The influence of wind shear

Systematic deviations from the return to isotropy principle were found in numerous investigations (Ferchichi and Tavoularis, 2000; Garg and Warhaft, 1998; Kurien and Sreenivasan, 2000; Pumir, 1996; Shen and Warhaft, 2000; Staicu and van de Water, 2003). A refined analysis, as presented in the following, suggests that also the strength of the shear has to be taken into account in order to make a prediction on the return to isotropy (Schumacher, 2004; Schumacher et al., 2003).

The large shear case Schumacher et al. (2003) analysed a homogeneous shear flow with a constant shear rate $S = \frac{dU}{dy}$, where $U(y)$ is the mean velocity in the streamwise direction x, and y is the direction of the shear. For the analysis they assumed that: (1) the term representing the coupling of the turbulent velocity component and the mean shear is large compared to the nonlinear advective transport term,

$$\left| u_i \frac{\partial U_j}{\partial x_i} \right| \gg \left| u_i \frac{\partial u_j}{\partial x_i} \right| , \tag{3.6}$$

and (2) the root-mean-square velocity in the streamwise direction is larger than that in the shear direction:

$$\left\langle u_x^2 \right\rangle^{1/2} \geq \left\langle u_y^2 \right\rangle^{1/2} \tag{3.7}$$

[2]The value of $R_\lambda = 3000$, which was used to divide 'small' and 'large' Reynolds numbers, was varied within a range of ± 1000. However, the results obtained for different limiting values were similar.

The right hand side of (eq. 3.6) is approximated with the Taylor micro-scale λ as $\frac{\langle u_x^2 \rangle}{\lambda}$, which leads to

$$\left\langle u_x^2 \right\rangle^{1/2} S \gg \frac{\langle u_x^2 \rangle}{\lambda} \ . \tag{3.8}$$

The shear rate can be normalized with the integral time scale $T_L = \frac{u'^2}{\epsilon}$ to give the normalized shear rate $S^\star_{T_L} = S \cdot T_L = \frac{Su'^2}{\epsilon}$. Together with $\epsilon = C_\epsilon \frac{u'^3}{L}$, $\frac{L}{\lambda} = \sqrt{\frac{R_L}{10}}$ and $C_\epsilon \sim \mathcal{O}(1)$ one finds for the normalized shear rate:

$$\frac{S^\star_{T_L}}{R_\lambda} = \frac{Su'^2}{\epsilon R_\lambda} \gg \sqrt{\frac{3}{200}} \approx \frac{1}{8} \tag{3.9}$$

Schumacher et al. (2003) conjecture that for the large shear case, "the effect of shear will always be felt no matter how high the Reynolds number."

The limit of local isotropy As the other extreme case, when local isotropy dominates the flow, a large separation between the shear time scale S^{-1} and the Kolmogorov time scale τ_η should exist (Corrsin, 1958). Thus, in the case of local isotropy one would expect to find $S^\star_{\tau_\eta} = S \cdot \tau_\eta \ll 1$ (Schumacher et al., 2003). The normalizations with the two different time scales are related by

$$S^\star_{\tau_\eta} = S^\star_{T_L} \sqrt{C_\epsilon} \left(\frac{3}{2}\right)^{1/4} R_L^{-1/2} \ , \tag{3.10}$$

which can be simplified with $C_\epsilon \sim \mathcal{O}(1)$ and $R_\lambda = \sqrt{\frac{20}{3} R_L}$ to give

$$S^\star_{\tau_\eta} = \frac{S^\star_{T_L}}{R_\lambda} \left(\frac{200}{3}\right)^{1/4} \ . \tag{3.11}$$

It follows that one expects local isotropy to prevail for the case of

$$\frac{S^\star_{T_L}}{R_\lambda} \ll \left(\frac{3}{200}\right)^{1/4} \approx 0.35 \ . \tag{3.12}$$

Results The normalized shear rate is plotted as a function of Reynolds number in figure 3.20. The plot was obtained by averaging the shear rates over Reynolds number ranges of $\Delta R_\lambda = 300$. It can be seen that the west wind is sheared more strongly than the east wind and that the normalized shear rate of west wind increases more rapidly. The data points from the west wind are also scattered over a much

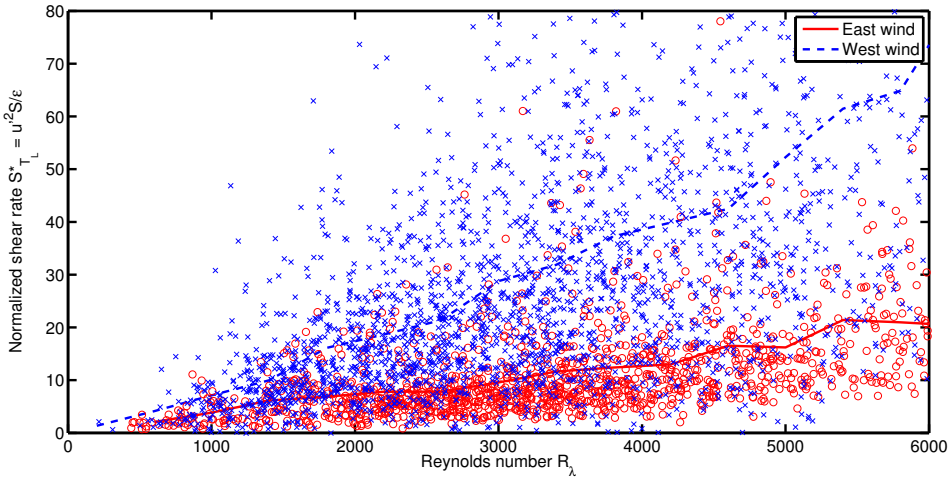

Figure 3.20: Normalized shear rate ($S^{\star}_{T_L} = \frac{Su'^2}{\epsilon}$) as a function of the Reynolds number R_λ for east wind (red) and west wind (blue). The crosses and circles represent single measurements, while the lines correspond to averages over bin sizes with $\Delta R_\lambda = 300$.

wider range, which may be accounted to the varying flow conditions induced by the LIDAR tower located on the west of the measurement site.

In order to investigate whether the wind shear at the measurement site prohibits a return to isotropy (eq. (3.9) and (3.12)), the reduced normalized shear rate $S^{\star}_{T_L}/R_\lambda$ is plotted as a function of R_λ in figure 3.21. It can be seen that $S^{\star}_{T_L}/R_\lambda \ll 0.35$, which congests that local isotropy should prevail for both wind directions. Thus, the conjecture by Schumacher et al. (2003) is not able to explain why the isotropy of the flow does not increase with Reynolds number for wind coming from the west. It must be assumed that the flow from the west is much more complicated than a homogeneous shear flow, so that the approximations used may not be appropriate.

In contrast, the flow from the east is almost undisturbed and the approximation of a homogeneous shear flow may be regarded as applicable. The plausibility of this approximation receives further support as the return to isotropy principle is fulfilled for Reynolds numbers up to $R_\lambda \approx 3000$. However, for wind from the east $S^{\star}_{T_L}/R_\lambda$ is almost constant and much smaller than 0.35 over the whole Reynolds number range. Thus, the missing return to isotropy at large Reynolds numbers ($3000 < R_\lambda < 6000$) still cannot be explained by the pure existence of a strong shear.

To further quantify the effect of shear rate on the Reynolds stress, the invariants of the anisotropy tensor are mapped onto the Lumley triangle as a function of the

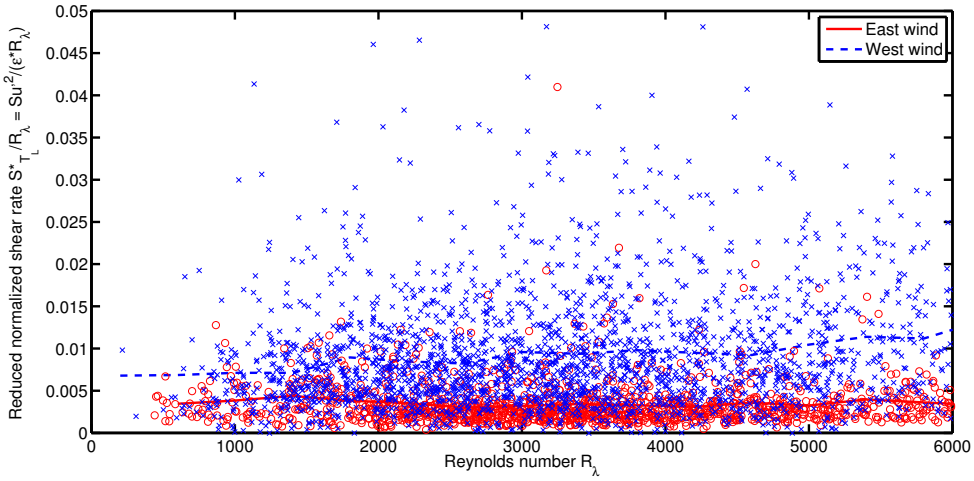

Figure 3.21: Reduced normalized shear rate $S^{\star}_{T_L}/R_\lambda \sim S\tau_\eta$ as a function of the Reynolds number for wind from the east (red) and west (blue).

normalized shear parameter $S^{\star}_{T_L}$. The analysis was carried out for small shear rates ($S^{\star}_{T_L} < 10$) and large shear rates ($S^{\star}_{T_L} > 10$) and is shown in figure 3.22. However, it was not possible to find a clear correlation between the shear parameter and the isotropy of the flow. Instead, the results suggest that a further investigation of anisotropic high Reynolds number flows is necessary.

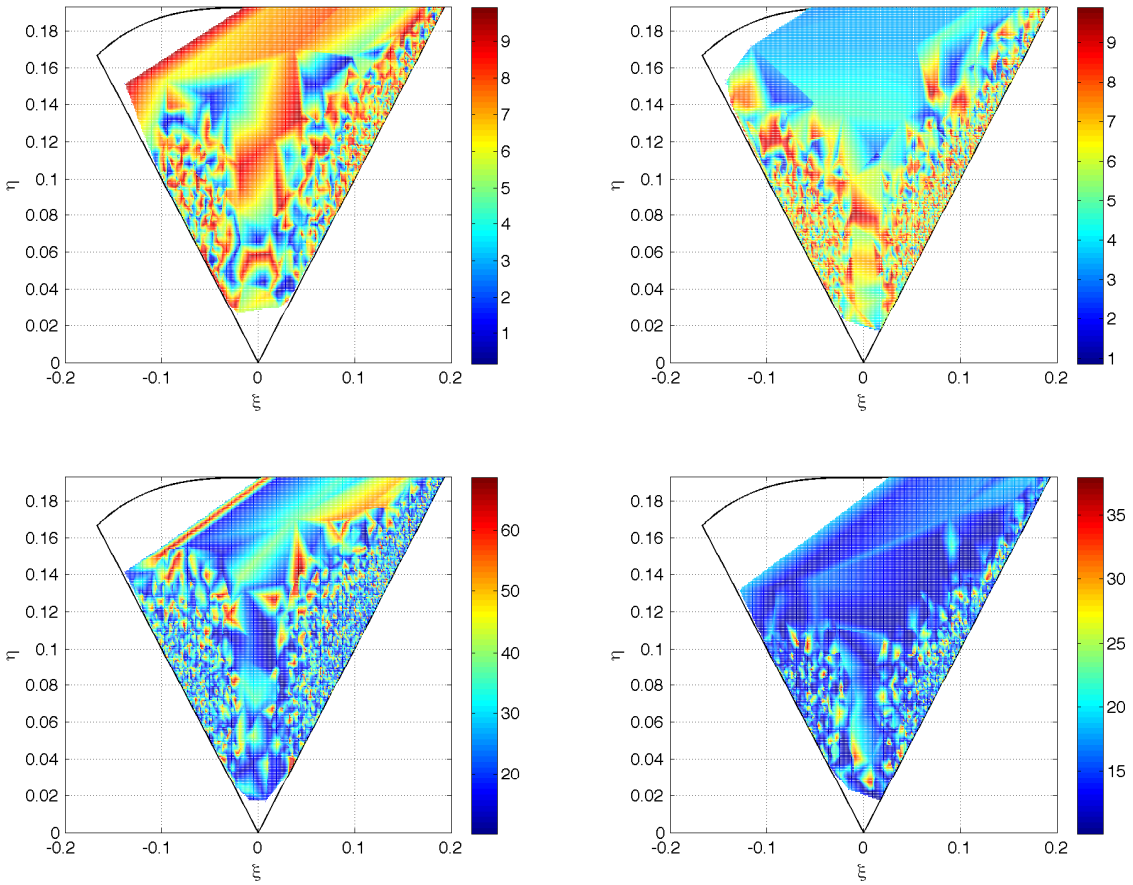

Figure 3.22: Linear interpolation of the invariants in the ξ-η-plane as a function of the normalized shear parameter $S^{\star}_{T_L}$ (color coded), for a range of $0 < R_\lambda < 6000$. The left panels correspond to wind from the west, while the right panels correspond to wind from the east. The top graphs are for small shear parameters ($S^{\star}_{T_L} < 10$) and the bottom graphs are for large shear parameters ($S^{\star}_{T_L} > 10$).

3.4.5 Comparison to laboratory flows

In laboratory study of turbulence a setup with two counter rotating discs is frequently used, which is known as the von Kármán swirling flow (VKS) or 'French washing machine'. The flow was first employed to investigate turbulent friction by von Kármán (Kármán, 1921) and has been used widely to investigate turbulence thereafter, because it is relatively easy to reach high Reynolds numbers of the order of 10^3 (e.g. Voth et al. (2002)).

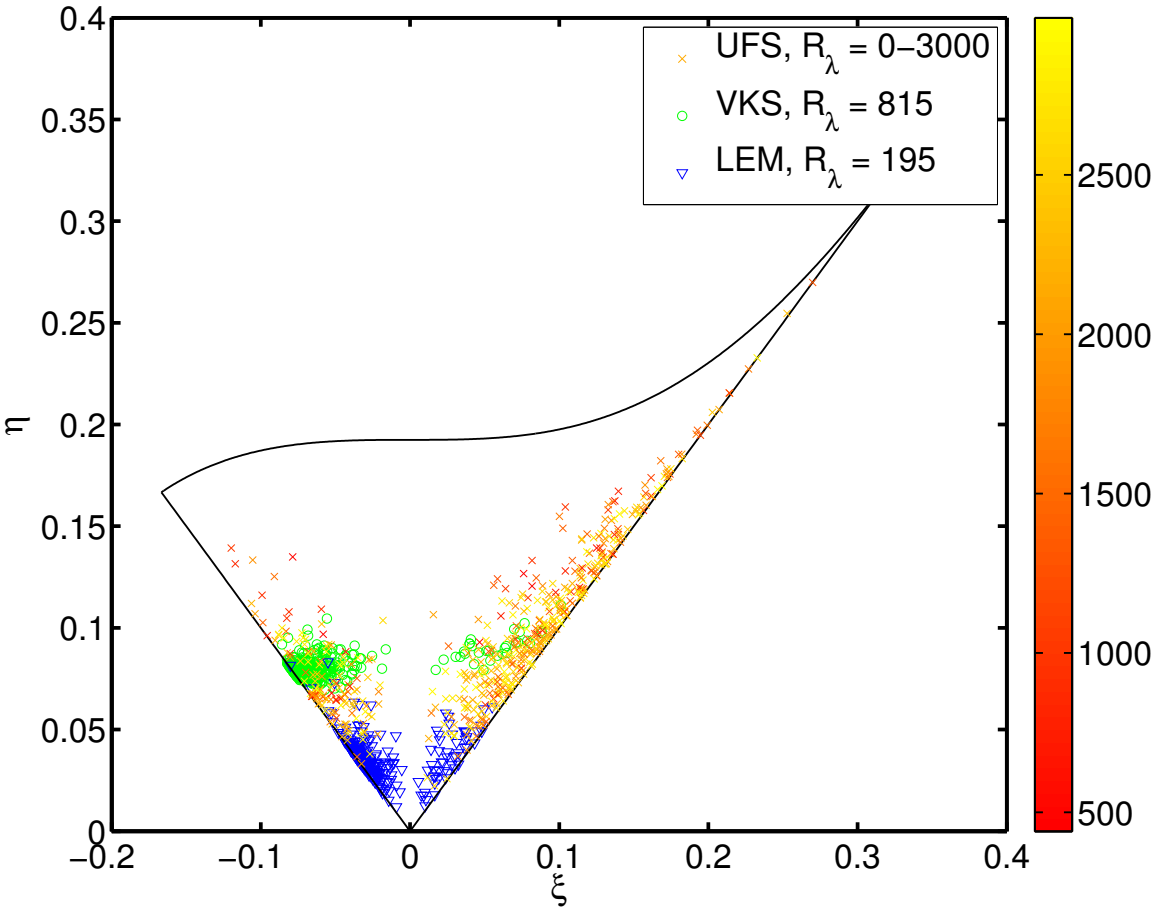

Figure 3.23: Lumley triangle comparing the isotropy of the east wind to that of von Kármán swirling flow at $R_\lambda = 815$ and the flow generated by the Lagrangian exploration module at $R_\lambda = 195$.

Recently a novel apparatus has been designed in order to study isotropic turbulence in the laboratory at comparably high Reynolds numbers. Because the apparatus has been built to conduct Lagrangian turbulence measurements (i.e. following

fluid particles) it is called the Lagrangian Exploration Module (LEM) (Zimmermann et al., 2010). The LEM is shaped as a regular icosahedron with a propeller in each of the 12 vertices, which are rotating in water at a constant frequency. The apparatus is described in detail in Zimmermann (2008).

In figure 3.23 the flow of the east wind at UFS is plotted on the Lumley triangle and compared to the turbulence generated by von Kármán swirling flow and the Lagrangian exploration module. It can be seen that the level of isotropy of the flow at UFS is often comparable or even better than the isotropy reached by VKS. The turbulence generated by the LEM is generally more isotropic than the flow at UFS but a few measurement points lay in the same range. It should be noted that the turbulence at UFS has typically much higher Reynolds numbers than the ones generated in the laboratory. Because the flow conditions at UFS are uncontrollable the data points are scattered over a wide range.

4 The velocity gradient tensor

> Jetzt weht der Wind von Norden, dann dreht er und weht von Süden, er dreht weiter und immer weiter, bis er wieder aus der alten Richtung kommt. (...) Ich beobachtete, was auf der Welt geschieht, und erkannte: Alles ist vergebliche Mühe - gerade so, als wollte man den Wind einfangen. (Ecclesiastes 1, 6&14; Bibelgesellschaft (2001))

4.1 Theoretical background

4.1.1 Definition of Invariants

For a neighbourhood in which the local velocity field is sufficiently smooth, the velocity field, $\boldsymbol{U}(\boldsymbol{x}, t)$, at an arbitrary point, $\boldsymbol{x_0}$, can be approximated via a linear expansion:

$$U_i(\boldsymbol{x}, t) = U_i(\boldsymbol{x_0}, t) + A_{ij}(\boldsymbol{x_0}, t)(x_j - x_{0j}) + \dots \tag{4.1}$$

In turbulent flows a smooth velocity field was found at length scales up to the order of the Kolmogorov scale η. If one is using a Lagrangian frame of reference, i.e. following the trajectory of a fluid particle, the velocity gradient tensor A_{ij} gives the velocity field surrounding the particle.

The velocity gradient tensor (VGT) was already introduced in chapter 1.1.4, as $A_{ij} = \dfrac{\partial U_i}{\partial x_j}$, and split into rate-of-strain S_{ij}, and rate-of-rotation Ω_{ij} tensors[1]:

$$A_{ij} = S_{ij} + \Omega_{ij} \tag{4.2}$$

$$S_{ij} = \frac{1}{2}\left(A_{ij} + A_{ji}\right) \tag{4.3}$$

$$\Omega_{ij} = \frac{1}{2}\left(A_{ij} - A_{ji}\right) \tag{4.4}$$

$\boldsymbol{S}$ can be expressed in a coordinate system of orthogonal eigenvectors with the

[1]The theoretical background, as it is presented here, is based mostly on Meneveau (2011).

three real eigenvalues λ_α, λ_β and λ_γ. For incompressible flows the velocity field is divergence free and the trace of $\boldsymbol{A}$ is zero, $A_{kk} = S_{kk} = \lambda_\alpha + \lambda_\beta + \lambda_\gamma = 0$. In case the eigenvalues are unequal, they can be sorted by magnitude to give the maximum rate of fluid extension ($\lambda_\alpha > 0$), the maximum rate of fluid contraction ($\lambda_\gamma < 0$) and an intermediate value (λ_β) that can be either positive or negative.

Because three scalars are required to specify the orientation of $\boldsymbol{A}$ in space, the eight independent components of $\boldsymbol{A}$ can be reduced to five intrinsic, orientation-invariant scalars, and it has been found useful to define the five invariants in the following way (Cantwell, 1992; Martín et al., 1998b):

$$Q = -\frac{1}{2} A_{im} A_{mi} \tag{4.5}$$

$$R = -\frac{1}{3} A_{im} A_{mn} A_{ni} \tag{4.6}$$

$$Q_S = -\frac{1}{2} S_{im} S_{mi} \tag{4.7}$$

$$R_S = -\frac{1}{3} S_{im} S_{mn} S_{ni} \tag{4.8}$$

$$V^2 = S_{in} S_{im} \omega_m \omega_n \tag{4.9}$$

Here the vorticity vector, $\omega_k = \varepsilon_{kij}\Omega_{ji}$ (chapter 1.1.4), was used to express the last invariant. (It is interesting to note that Q_S is related to the kinetic energy dissipation rate via $\epsilon = -4\nu Q_S$, which shows that Q_S has to be negative.)

4.1.2 Evolution equation of the velocity gradient tensor

By taking the gradient of the incompressible Navier-Stokes equation (eq. 1.6) one finds the time evolution of the velocity gradient tensor $\boldsymbol{A}$ along the trajectory of a fluid element, as

$$\frac{DA_{ij}}{Dt} = -A_{ik}A_{kj} - \frac{\partial^2 p}{\partial x_i \partial x_j} + \nu \frac{\partial^2 A_{ij}}{\partial x_k \partial x_k} \ , \tag{4.10}$$

where the substantial derivative ($\frac{D}{Dt} = \frac{\partial}{\partial t} + U_k \frac{\partial}{\partial x_k}$) was used. Employing the incompressibility condition, $A_{ii} = 0$, equation (4.10) can be re-expressed as a function of an anisotropic, trace-free part, H^p_{ij}, of the pressure Hessian and a viscous part, H^ν_{ij}, as

$$\frac{DA_{ij}}{Dt} = -\left(A_{ik}A_{kj} - \frac{1}{3}A_{mk}A_{km}\delta_{ij}\right) + H^p_{ij} + H^\nu_{ij} \ , \tag{4.11}$$

with

$$H_{ij}^{p} = \left(\frac{\partial^2 p}{\partial x_i \partial x_j} - \frac{1}{3} \nabla^2 p \delta_{ij} \right) \text{ and} \tag{4.12}$$

$$H_{ij}^{\nu} = \nu \frac{\partial^2 A_{ij}}{\partial x_k \partial x_k} \ . \tag{4.13}$$

Equation (4.11) is a set of nine coupled, non-linear ODEs, where the local and non-local parts of the pressure field have been separated. In order to solve the complete set of equations the terms H_{ij}^{p} and H_{ij}^{ν} have to be closed.

4.1.3 Restricted Euler model

A first instructive approach to solve the equations (4.11) was made by Vieillefosse (1982, 1984). He used the Euler equations (1.7), where $\nu = 0$ (and thus $H_{ij}^{\nu} = 0$) and neglected the anisotropic part of the pressure Hessian $H_{ij}^{p} = 0$:

$$\frac{DA_{ij}}{Dt} + \left(A_{ik}A_{kj} + \frac{1}{3} A_{mk}A_{km}\delta_{ij} \right) = 0 \tag{4.14}$$

The equations (4.14), known as restricted Euler system, are now closed and can be solved. By multiplying equation (4.14) with A_{ji} and $A_{jk}A_{ki}$ and using the Cayley-Hamilton theorem ($A_{im}A_{mn}A_{nj} + QA_{ij} + R\delta_{ij} = 0$ for $A_{ii} = 0$) one obtains a set of evolution equations for the invariants R and Q:

$$\frac{DQ}{Dt} = -3R \tag{4.15}$$

$$\frac{DR}{Dt} = \frac{2}{3} Q^2 \tag{4.16}$$

Using (eq. 4.15) to eliminate Dt in (eq. 4.16) one finds that the discriminant Δ is constant along the path of a fluid element:

$$\frac{D\Delta}{Dt} = \frac{D}{Dt} \left(\frac{27}{4} R(t)^2 + Q(t)^3 \right) = 0 \tag{4.17}$$

Hence Δ can be taken as the value of $Q_{R=0}^3 = Q_0^3$ when $R = 0$. The boundary at which the eigenvalues of the velocity gradient tensor change from real to complex

values is defined by $Q_0 = 0$, which corresponds to:

$$R = \pm \left(-\frac{4}{27} Q^3 \right)^{1/2} \text{ , or} \tag{4.18}$$

$$Q = -\left(\frac{27}{4} R^2 \right)^{1/3} \tag{4.19}$$

By introducing dimensionless variables $t_0 = |Q_0|^{-1/2}$, $r = Rt_0^3$, $q = Qt_0^2$, $a_{ij} = t_0 A_{ij}$ and $\tau = \frac{t}{t_0}$, equation 4.17 can be expressed as

$$\frac{27}{4} r^2 + q^3 = \text{sgn}(\Delta) \text{ ,} \tag{4.20}$$

where

$$\text{sgn}(\Delta) = \left\{ \begin{array}{ll} +1; & \Delta > 0 \\ -1; & \Delta < 0 \\ 0; & \Delta = 0 \end{array} \right\} \text{ .} \tag{4.21}$$

The R, Q phase-space flow of the restricted Euler system (eq. (4.15) and (4.16)) is shown in figure 4.1a (Cantwell, 1992). With increasing time the system evolves from left to right and approaches the so-called *Vieillefosse tail* $Q = -\frac{3}{2^{2/3}} R^{2/3}$. The upper half of the phase-space corresponds to rotation dominated flows with two complex eigenvalues of A_{ij} and $\Delta > 0$. Strain-dominated flows have three real eigenvalues and are found at $\Delta < 0$ (Chong et al., 1990). Figure 4.1b shows the three branches of the dimensionless system (eq. (4.20) and (4.21)). Also shown are the dominating streamline patterns as they would be seen by a co-moving observer (Cantwell, 1992).

4.1.4 The tetrad model

An unphysical result of the restricted Euler model is the 'finite-time singularity' in the evolution of the velocity gradient tensor (Vieillefosse, 1982). A couple of advanced models have been proposed in order to counteract the finite-time singularity by modeling the terms H_{ij}^p and H_{ij}^ν (Chevillard and Meneveau, 2006; Jeong and Girimaji, 2003; Martín et al., 1998a; Pope and Chen, 1990). This thesis focuses on a phenomenological model which was proposed by Chertkov et al. (1999) and is based on the Lagrangian dynamics of four fluid particles that form a tetrahedron. The relative particle position is defined by three vectors, $\boldsymbol{\rho}_i(t)$ $(i = 1, 2, 3)$, which can be written as a 3×3 matrix. The model splits the velocity field into a tetrad-based

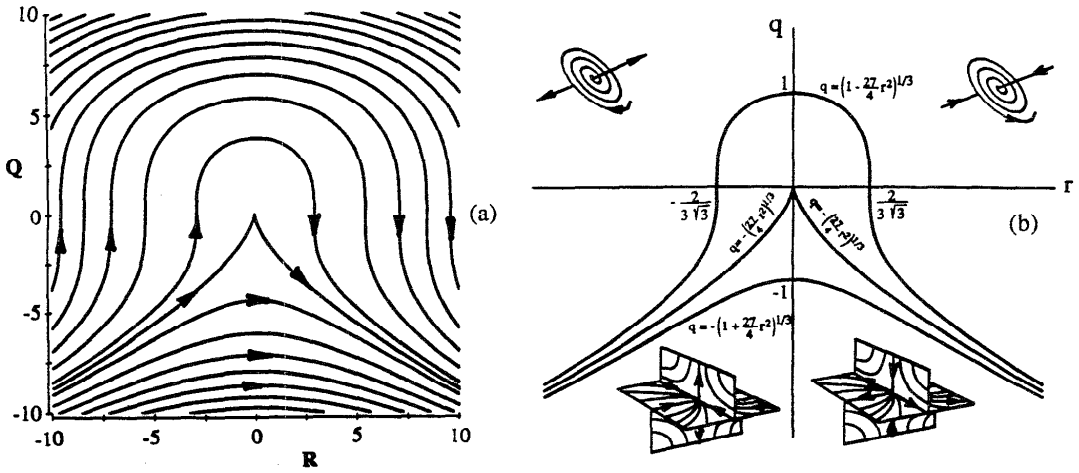

Figure 4.1: Phase-space of the restricted Euler model in the R-Q plane: (a) trajectories of Q vs R, (b) dimensionless q vs r and the flow topology for each quadrant. Figures taken from Cantwell (1992).

part and a stochastic part. The stochastic part corresponds to the incoherent small scale fluctuations. The dynamics of the tetrad-based velocity gradient $\boldsymbol{M}$ are governed only by the slow components of v_i^a, while the fluctuating part u_i^a is treated as Gaussian white noise. The decomposition may be written as

$$v_i^a = \rho_i^b M_{ab} + u_i^a \ . \tag{4.22}$$

By using the moment of inertia tensor $\boldsymbol{g} = \boldsymbol{\rho}^T \boldsymbol{\rho}$ and the stochastic forcing $\boldsymbol{\eta}$, a dynamic evolution equation is proposed for the tetrad model as (Chertkov et al., 1999)

$$\frac{DM_{ij}}{Dt} + (1-\alpha)\left(M_{ik}M_{kj} - \Pi_{ij}M_{mn}M_{nm}\right) = \eta_{ij} \tag{4.23}$$

$$\frac{dg_{ij}}{dt} = g_{ik}M_{kj} + g_{jk}M_{ki} + \beta\sqrt{M_{mn}M_{mn}}\left(g_{ij} - \frac{1}{3}g_{kk}\delta_{ij}\right) = 0 \ , \tag{4.24}$$

where the 'projection operator' $\Pi_{ij} = \dfrac{(\boldsymbol{g}^{-1})_{ij}}{(\boldsymbol{g}^{-1})_{kk}}$ imposes incompressibility. The parameter α reduces the non-linearity and completely cancels the self-stretching of the restricted Euler solution if $\alpha = 1$, as observed in numerical simulations (Borue and Orszag, 1998; Chertkov et al., 1999). The β-term tends to restore the isotropic shape of the tetrahedron, as it would be the case for a fluctuating white noise term (Naso and Pumir, 2005).

Physically the tetrad model may be pictured as tetrahedra which move along

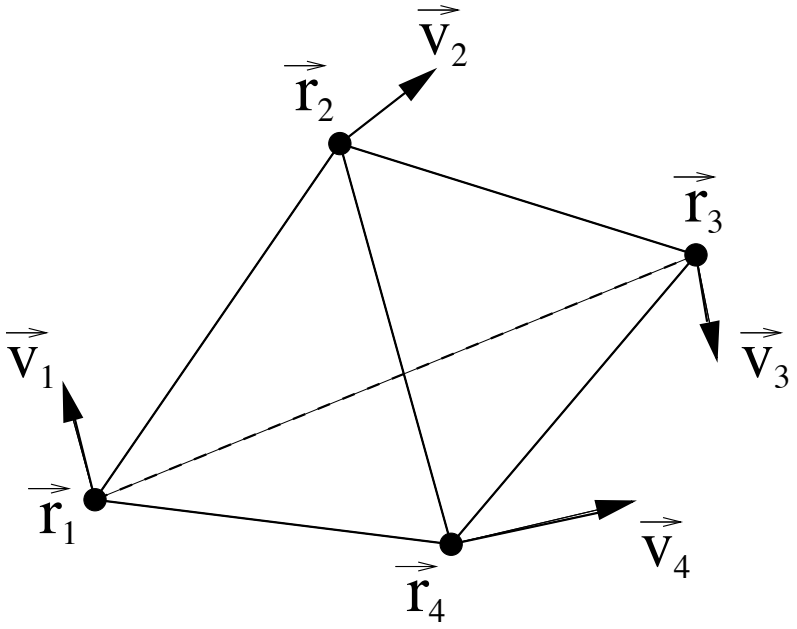

Figure 4.2: Four points in space define the tetrad, as visualized by Chertkov et al. (1999). The velocities at the four points give the tetrad based velocity gradient.

with the flow and are deformed by reduced restricted Euler dynamics and stochastic forcing. Its concept is similar to the study of the velocity structure functions as presented in chapters 1.3.3 and 3.13. Following the Lagrangian evolution of the tetrads may reveal important information about the turbulence cascade (Meneveau, 2011; Xu et al., 2011).

The definition of the tetrad-based velocity gradient tensor above is based on four points. When the size of the tetrahedron is smaller than the Kolmogorov length scale η, the true velocity gradient $\boldsymbol{m}$ is recovered (Pumir et al., 2012).

4.1.5 The filtered velocity gradient tensor

Furthermore a different quantity exists, that is known as the *filtered* or *coarse-grained* velocity gradient tensor $\tilde{\boldsymbol{A}}$ and used more frequently in the literature.[2] This

[2]In other publications the term 'coarse-grained velocity gradient tensor' is also used to refer to the quantity $\boldsymbol{M}$, which is avoided here in order to prevent confusion. In the following the term 'filtered velocity gradient tensor' will be used for $\tilde{\boldsymbol{A}}$, while 'tetrad-based velocity gradient tensor' will be used for $\boldsymbol{M}$.

quantity is defined as the average of the 'true' velocity gradient, $\boldsymbol{m}$, over the size l:

$$\tilde{\boldsymbol{A}} = \int_l \boldsymbol{m}(\boldsymbol{x}) d\boldsymbol{x} \tag{4.25}$$

The quantity $\tilde{\boldsymbol{A}}$ is studied for example by Luethi et al. (2007) and can be obtained experimentally by averaging over many points. Although the concepts of the 'true', filtered and tetrad-based velocity gradient are different from one another they have been found to exhibit many similarities (Luethi et al., 2007; Meneveau, 2011; Pumir and Naso, 2010; Xu et al., 2011).

It should be noted, that the measurement of the tetrad-based velocity gradient tensor is significantly easier than the measurement of the filtered velocity gradient tensor, since it requires 'only' the measurement of velocity differences between four discrete points. Furthermore the tetrad-based approach makes it easier to measure the Lagrangian properties of the flow, as four discrete tracer particles can be followed more easily than 'blob' of fluid.

4.1.6 Characteristic features of the 'true' velocity gradient tensor

Various characteristic features of turbulent flows have been found by studies of direct numerical simulation (DNS) and experimental investigations of the 'true' velocity gradient tensor:

1. The vorticity vector $\boldsymbol{\omega}$ is preferably aligned with the intermediate eigenvector (corresponding to the intermediate eigenvalue λ_β) of the strain-rate tensor $\boldsymbol{S}$ (Ashurst et al., 1987; Tsinober et al., 1992).

2. The turbulent straining has the highest probability to exhibit two directions of stretching and one direction of compression.(Ashurst et al., 1987; Kerr, 1987; Tsinober et al., 1992).

3. The joint probability density function of the R-Q invariants has a very particular shape. The PDF shows an increased probability of points along the Vieillefosse tail $Q = -\frac{3}{2^{2/3}} R^{2/3}$ inside the bottom right quadrant with $R > 0$ and $Q < 0$. The shape of the PDF, known as *tear drop shape*, is visualized in figure 4.3 and has been found in a variety of flows (Chong et al., 1998; Elsinga

and Marusic, 2010; Gulitski et al., 2007; Luethi et al., 2009; Nomura and Post, 1998; Ooi et al., 1999; Soria et al., 1994).

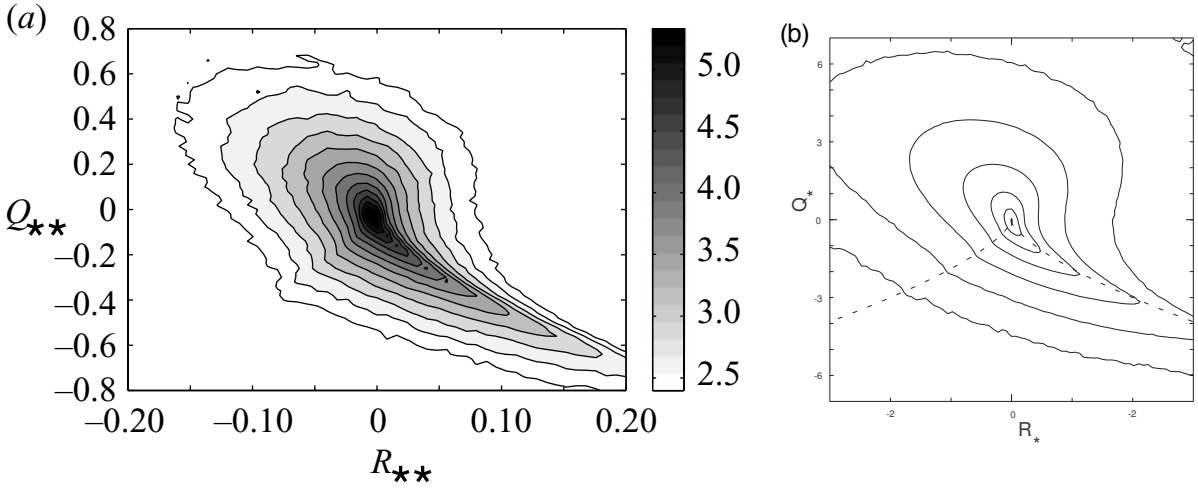

Figure 4.3: The PDF of R and Q obtained in DNS at (a) $R_\lambda = 434$ (Luethi et al., 2009) and (b) $R_\lambda = 85$ (Chertkov et al., 1999). The probability is logarithmically spaced. In the left plot R and Q are normalized by the Kolmogorov time scale $Q_{\star\star} = Q\tau_\eta^2$ and $R_{\star\star} = R\tau_\eta^3$. In the right plot R and Q are normalized by the variance of strain $Q_\star = Q/\langle s^2 \rangle$ and $R_\star = R/\langle s^2 \rangle^{3/2}$ and determined by the tetrad model inside the dissipation range with $\rho/\eta = 2$.

4.2 Measurements and simultions

4.2.1 Measurement of the filtered velocity gradient tensor

It is interesting to note that the filtered VGT was also found to exhibit the three features described above, "although the quantitative details depend weakly on scale" (Meneveau, 2011). The vorticity alignment and the preferential structure of the strain-rate eigenvalues were observed in atmospheric turbulence by Higgins et al. (2003) with an array of sonic anemometers. The characteristic shape of the R-Q joint PDF was found in DNS results at various scales (Borue and Orszag, 1998; Chertkov et al., 1999) and it was also observed by holographic optical measurements in pipe flow at scales of 30η (van der Bos et al., 2002).

4.2.2 Reproduction of characteristic features by the tetrad model

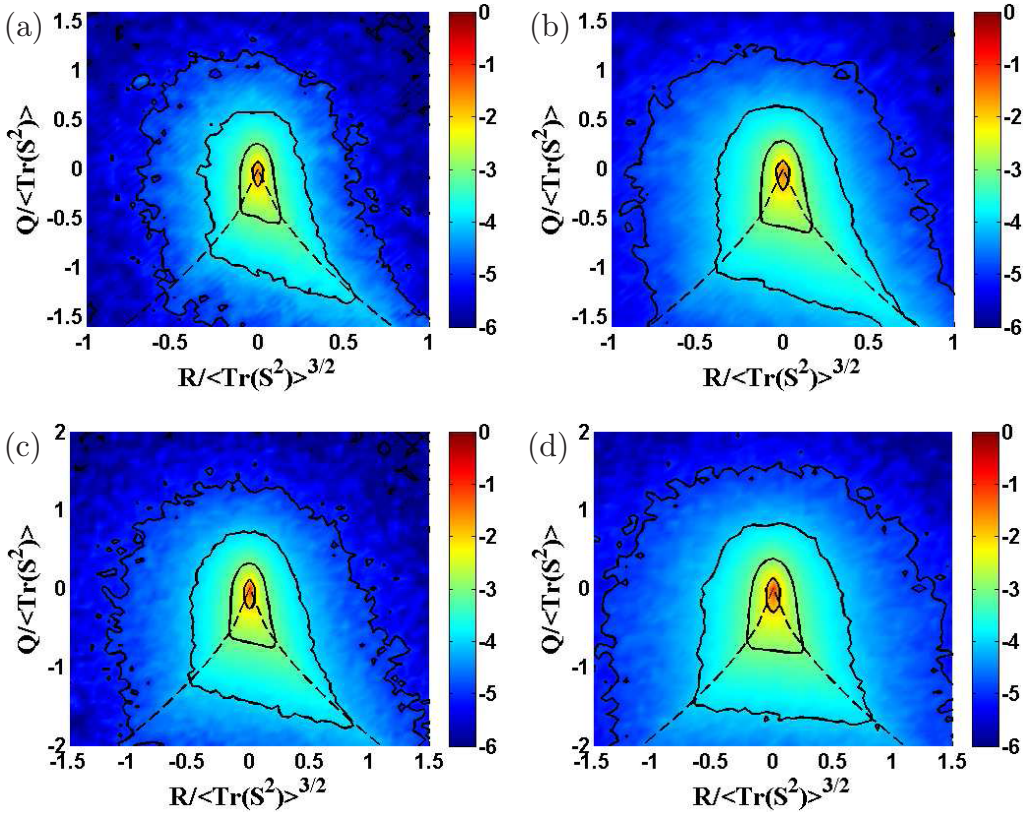

Figure 4.4: Joint PDF of R and Q measured by the tetrad model in a DNS flow for several values of α: (a) $\alpha = 0.1$, (b) $\alpha = 0.5$, (c) $\alpha = 0.7$ and (c) $\alpha = 0.9$. Figures taken from (Pumir and Naso, 2010).

The tetrad model (section 4.1.4) has been tested with DNS data (Chertkov et al., 1999; Naso and Pumir, 2005; Naso et al., 2006, 2007; Pumir and Naso, 2010) and is able to reproduce the three features presented above. Furthermore the joint PDF of R and Q (fig. 4.4) is found to be stretched along the Vieillefosse tail also inside the inertial range (Chertkov et al., 1999). As explained earlier, the Vieillefosse tail in the bottom right quadrant corresponds to the higher probability of two stretching and one compressive directions, which causes isotropic tetrahedrons to be deformed into sheet-like objects.

The model parameters have been tuned in order to achieve the best agreement with DNS results. As the value of α increases the non-linearity decreases, which is visible through a decreasing asymmetry in R (Pumir and Naso, 2010). Although α

is generally not a constant, the best agreement with DNS calculations of the 'true' VGT has been found for $\alpha \approx 0.45$, while other parameters are only of small influence (Naso and Pumir, 2005).

The tetrad-based VGT and its invariants R and Q have also been measured in von Kármán swirling flow at a Reynolds number of $R_\lambda = 690$ and the shape of the joint PDF agrees with the results obtained by VKS (Xu et al., 2011). As the scale of the tetrahedron is enlarged towards the integral length scale, the PDFs show increasingly Gaussian statistics (Xu et al., 2009, 2011), which is consistent with the general picture of turbulence (Batchelor, 2000; Christie and Domaradzki, 1994; Townsend, 1951) and agrees with observations in DNS (Chertkov et al., 1999).

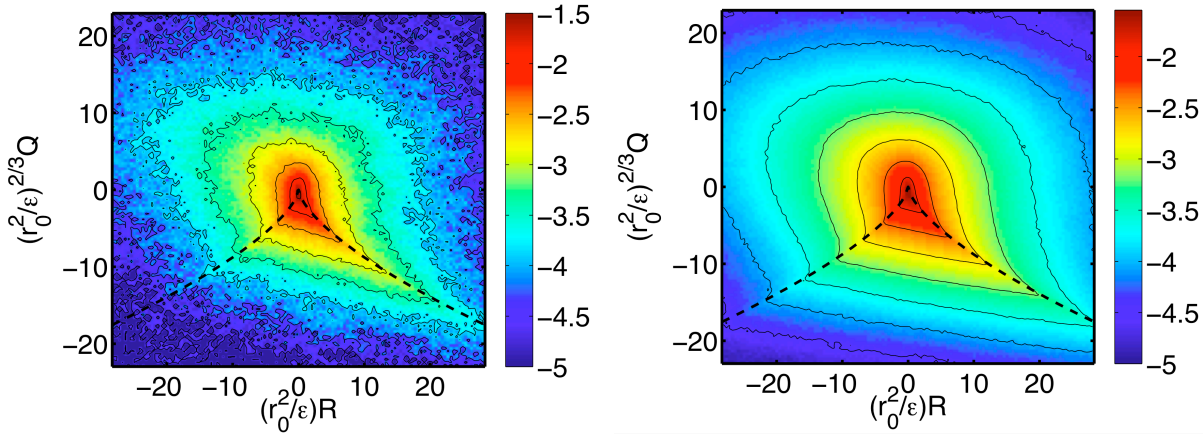

Figure 4.5: The tetrad-based velocity gradient tensor measured in VKS at Reynolds number $R_\lambda = 690$ for different sizes of the isotropic tetrads: (a) $\rho/L = 1/6$ and (b) $\rho/L = 1/3$ (Xu et al., 2011).

4.3 Description of the current study

For the study presented here the tetrad-based velocity gradient was measured in the turbulent atmospheric flow at UFS, where the average Kolmogorov scale is on the order of $\eta = (\nu^3/\epsilon)^{1/4} \approx 1$mm and the average integral scale is about $L \approx 19$m (section 3.2.1). The average distance between the sensors of about 1.7 m is inside the inertial range. The five sonic anemometers were arranged like two nearly isotropic tetrahedra in order to permit the study of the tetrad-based velocity gradient tensor. The relative position of the sensors is determined by measuring the distances between all sensors and calculating their location with respect to the top sensor, as given in table 2.1. The simultaneous measurement of all five anemometers plus

the incompressibility condition (eq. 1.3) over-determine the tetrad-based velocity gradient tensor. Thus, the tetrad-based velocity gradient tensor is calculated by a least square fit using the singular value decomposition algorithm (see Appendix 2.5 and Press et al. (2007)).

4.4 Results

4.4.1 Joint PDFs of R and Q

The R and Q invariants were calculated for chunks with a constant average wind speed. The wind speed was conditioned to be at least 3 m/s in order to reduce influences of the anemometer geometry and guarantee the development of a turbulent flow (see Appendix A). The obtained joint PDF of all measurements is plotted in figure 4.6. It can be seen that the PDF is close to a Gaussian distribution, which may be due to measurement errors. However, the probability is slightly increased in the bottom right quadrant along the Vieillefosse tail. This observation is quantified by the normalized moments (table 4.1), which shows a smaller skewness in R and a larger skewness in Q. It should be noted that the integral length scales of the different chunks vary, which also causes a variation in the relative sizes ρ/L of the tetrahedra. The superposition of measurements with different ρ/L is justified by the findings of Pumir et al. (2012), and Xu et al. (2009) and Xu et al. (2011).

The fact that the PDF is almost symmetric may be accounted to the inaccuracy of the sonic anemometers and the flow distortion caused by the sensors and the mast. The inaccuracy of the sonic anemometers is mostly caused by in-line averaging (section 2.3.1), which means that the obtained wind velocities are not measured at a single point, but averaged over a distance of $r \approx 20$ cm. Furthermore the velocity components are measured separately at three individual paths, which increases the averaging volume.The flow distortions caused by the anemometers are discussed in detail in Appendix A. It must be expected that the mast causes similar flow distortions, which are more difficult to quantify as the flow field around the mast is mostly unknown.

Apart from the two systematic errors discussed above, the measurement is also subject to a random error (i.e. measurement noise). In order to reduce measurement noise the velocity traces of the chunks were filtered with a five point Gaussian filter with a standard deviation of $\sigma = 1$. The noise in the velocity traces was effectively

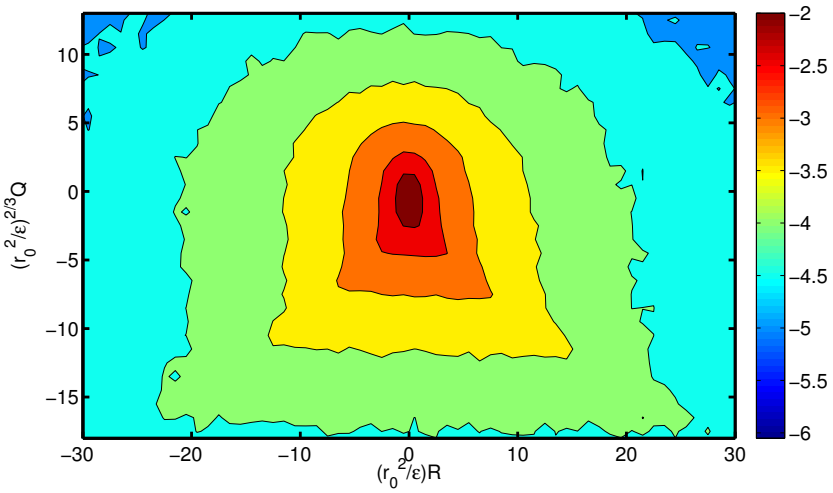

Figure 4.6: Joint PDF of R and Q measured at UFS for all chunks with a constant mean wind speed of at least 3 m/s. The PDF is slightly skewed along the Vieillefosse tail in the bottom right quadrant. The invariants are normalized as $Q_r = (r^2/\epsilon)^{2/3} Q$ and $R_r = (r^2/\epsilon) R$.

reduced (fig. 4.8). In contrast, the longer averaging range led to an increase in the Gaussian statistics of the R-Q joint PDF (fig. 4.7 and table 4.1), due to further averaging of velocity fluctuations. That congests that the measurement noise of the separate velocity traces is not the major cause for the Gaussian profile of the joint PDF. Instead, it must be assumed that the velocity differences between the sonic anemometers are subject to strong random fluctuations. As discussed above, these may be caused by the flow disturbances and the in-line averaging. Further support to this explanation is given by DNS results from Pumir and Naso (2010). The evolution equation of the VGT based on the tetrad-model (eq. 4.23) also contains

	$\langle R_r \rangle$	$\langle R_r^2 \rangle$	$\langle R_r^3 \rangle / \langle R_r^2 \rangle^{3/2}$	$\langle R_r^4 \rangle / \langle R_r^2 \rangle^2$
All chunks (fig. 4.6)	0.0006	2.72	0.33	1504
Filtered chunks (fig. 4.7)	0.0004	2.06	-0.096	1884
	$\langle Q_r \rangle$	$\langle Q_r^2 \rangle$	$\langle Q_r^3 \rangle / \langle Q_r^2 \rangle^{3/2}$	$\langle Q_r^4 \rangle / \langle Q_r^2 \rangle^2$
All chunks (fig. 4.6)	-0.0229	0.96	-23.98	1908
Filtered chunks (fig. 4.7)	-0.0181	0.70	-24.58	2289

Table 4.1: Comparison of the normalized moments of $Q_r = (r^2/\epsilon)^{2/3} Q$ and $R_r = (r^2/\epsilon) R$ for all chunks (fig. 4.6) and filtered chunks (fig. 4.7). The flatness in R and Q and the skewness in Q is slightly larger for filtered chunks, while the skewness in R is slightly larger for non-filtered chunks.

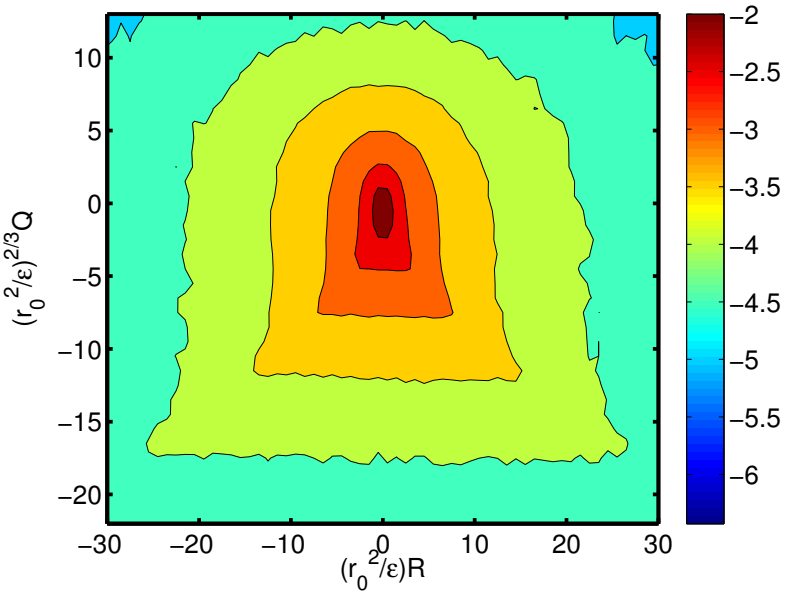

Figure 4.7: *R-Q* joint PDF for velocity chunks filtered with a five point Gaussian filter of $\sigma = 1$.

the noise term η_{ij}. The influence of the noise amplitude was investigated and it was found that an increase in noise "results in a strong reduction of the lack of symmetry $R \to -R$." (Pumir and Naso, 2010) The DNS results for two different values of the noise amplitude (C_η) are shown in figure 4.9, and it can be concluded that the systematic errors of the measurement device manifests itself as Gaussian noise in the measurement of the tetrad-based VGT.

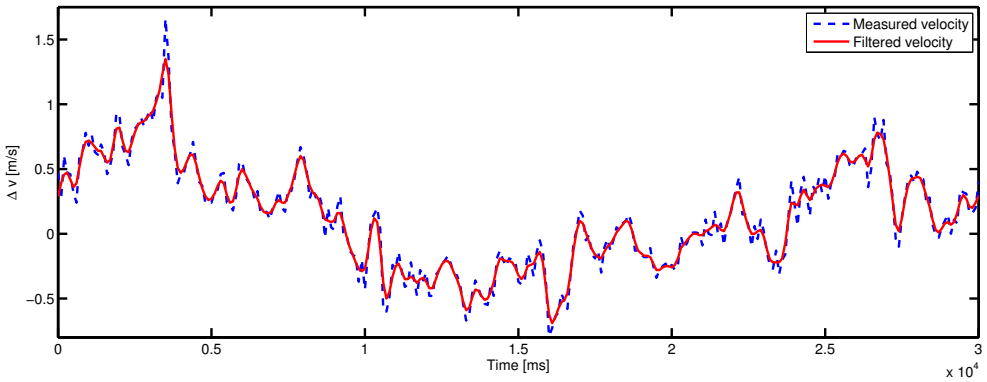

Figure 4.8: Trace of the fluctuating velocity measured (blue) and filtered (red) for the first 30 seconds of a chunk of constant wind speed.

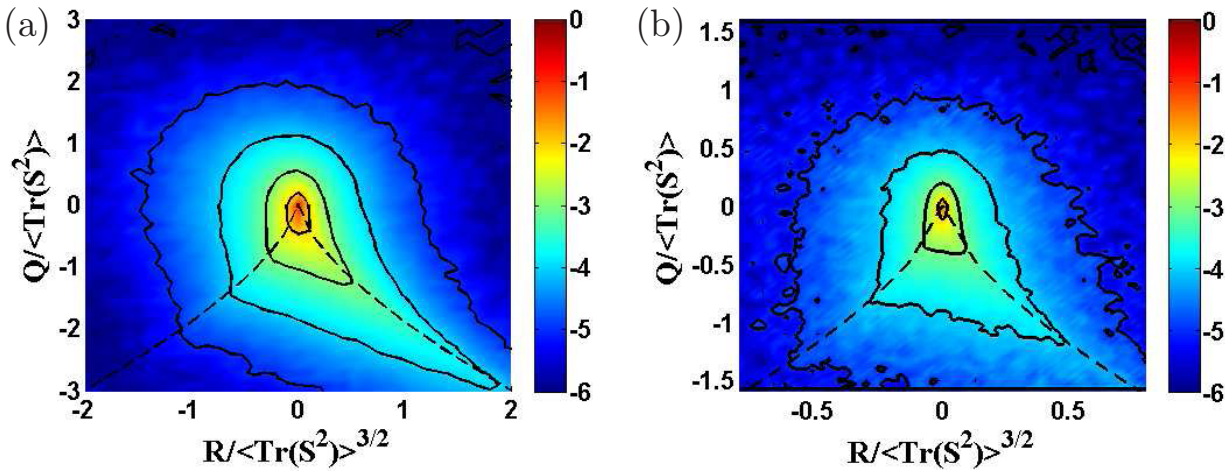

Figure 4.9: R-Q joint PDF obtained by DNS for two different values of the noise amplitude: (a) small noise amplitude and (b) large noise amplitude at a scale of $\rho/L = 1/4$. The asymmetry decreases with increasing noise amplitudes. Results are taken from Pumir and Naso (2010).

4.4.2 Dependence on the wind direction

Figure 4.10 compares the PDF for wind from the east (red) and wind from the west (blue). It can be seen that in general the overall size of the velocity fluctuations is increased for west wind, which is due to the stronger shear of west wind at the measurement site (sections 3.2.3 and 3.4.2). The finding of an increase in the size of velocity fluctuations is in agreement with the results obtained by Naso et al. (2006) who tested the influence of a large scale homogeneous shear flow in DNS (figure 4.11). It can also be seen that the asymmetry of the R-Q plot is more pronounced for wind from the east than for wind from the west. The skewness and flatness of the normalized values of R and Q are also compared in table 4.2 and support this observation.

It has been observed in DNS and VKS that the skewness of the joint PDF depends on the relative size of the tetrahedron compared to the integral scale ρ/L (Naso and Pumir, 2005; Xu et al., 2011). However, because the integral length scales of east and west winds are comparable (section 3.2.2) this observation cannot explain the larger skewness of the joint PDF of the east wind. It is more likely that the complexity and non-stationarity of the wake caused by the LIDAR dome causes the shape of the joint PDF to be closer to a Gaussian for west wind.

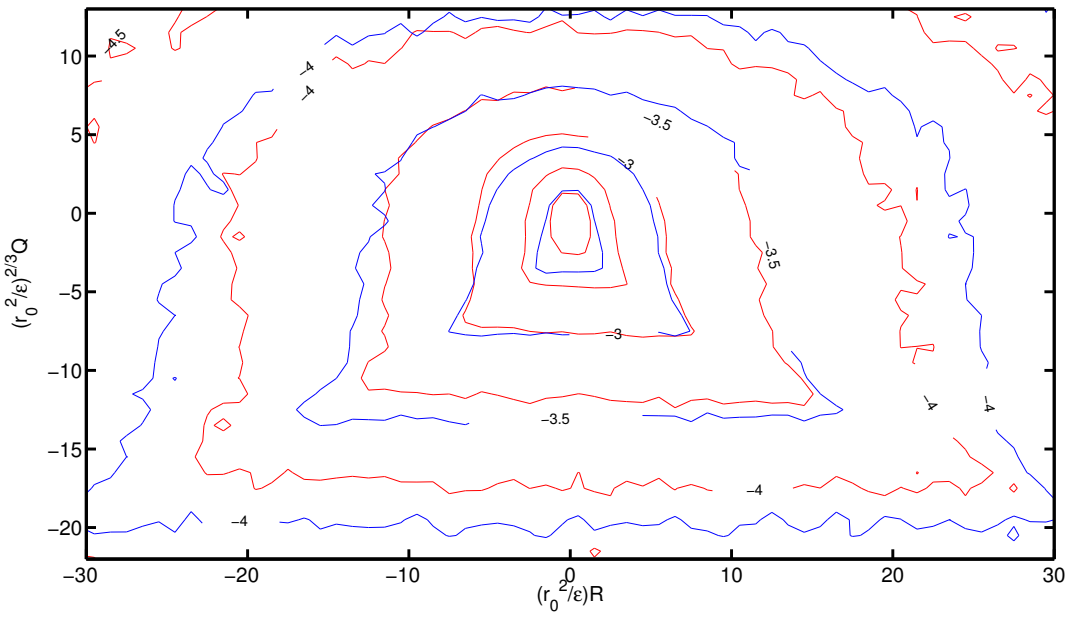

Figure 4.10: Joint PDF of R_r and Q_r measured at UFS for wind from the east (red) and west (blue). The west wind is subject to a stronger shear and the overall size of velocity fluctuations is larger. The asymmetry of the PDF for east wind is slightly more pronounced.

	$\langle R_r \rangle$	$\langle R_r^2 \rangle$	$\langle R_r^3 \rangle / \langle R_r^2 \rangle^{3/2}$	$\langle R_r^4 \rangle / \langle R_r^2 \rangle^2$
Wind from East	0.0015	1.89	1.55	2066
Wind from West	0.0001	3.32	-0.06	1254
	$\langle Q_r \rangle$	$\langle Q_r^2 \rangle$	$\langle Q_r^3 \rangle / \langle Q_r^2 \rangle^{3/2}$	$\langle Q_r^4 \rangle / \langle Q_r^2 \rangle^2$
Wind from East	-0.0182	0.68	-28.4	2556
Wind from West	-0.0264	1.16	-21.8	1610

Table 4.2: Comparison of the normalized moments of $Q_r = (r^2/\epsilon)^{2/3} Q$ and $R_r = (r^2/\epsilon)\, R$ for east and west wind. The skewness and flatness for the east wind is larger than for the west wind.

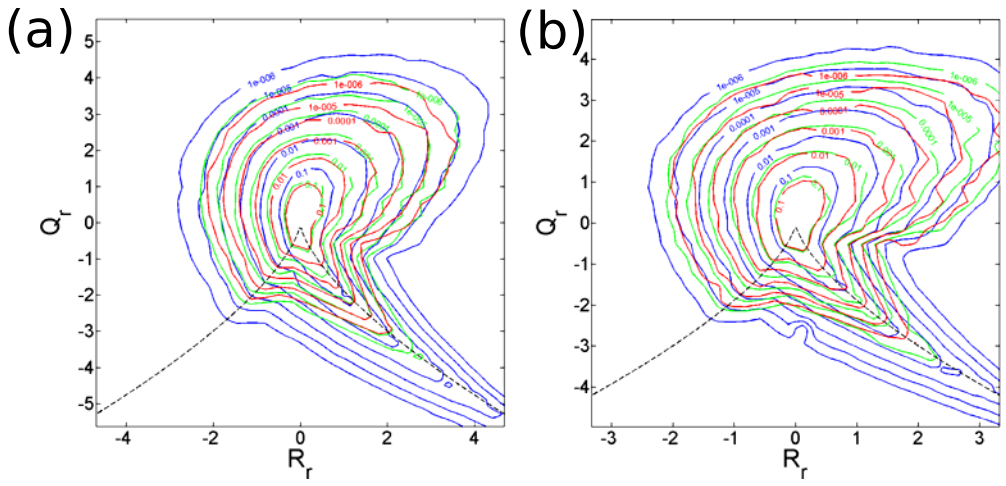

Figure 4.11: Joint PDF of R and Q obtained by DNS in a homogeneous turbulent shear flow ($\boldsymbol{U} = (sy, 0, 0) + \boldsymbol{u}$) with the dimensionless shear parameter $S^\star = s(L^2/\epsilon)^{1/3}$ with $S = 0$ (red), $S = 1$ (green), $S = 6$ (blue) and for different sizes of the tetrad: (a) $r = L/8$ and (b) $r = L/16$. Results taken from Naso et al. (2006).

4.4.3 Correlation of strain- and vorticity-dominated regions

Batchelor and Townsend (1949) were the first to show that Kolmogorov's theory is not sufficient for the description of the statistics of velocity gradients in turbulence. Especially higher order moments are effected by the intermittent behaviour of turbulence, which manifests itself in rare, intense small-scale events (e.g. Frisch (1995)). It has been observed that strong coherent, elongated vortices, which are also known as 'worms', exist in many turbulent flows (e.g. Douady et al. (1991); Hosokawa and Yamamoto (1990); Jiménez et al. (1993); Kaneda and Ishihara (2006); Kerr (1985); Siggia (1981); Vincent and Meneguzzi (1991)). These events are strongly localized and make up only a small fraction of the flow (e.g. Nomura and Post (1998)). Because the events are strongly dominated by vorticity, it follows that $Q > 0$ in these regions. Furthermore, because of their strong localization it may be assumed that the correlation of these vorticity-dominated regions is shorter than the correlation of the strain-dominated regions.

In order to test the flow for vortex filaments the correlation of R and Q was computed for vorticity-dominated ($Q > 0$) regions and strain-dominated regions ($Q < 0$) separately for different Reynolds numbers (figure 4.12). The correlation lengths of R and Q are determined by integrating the correlations up to the crossing

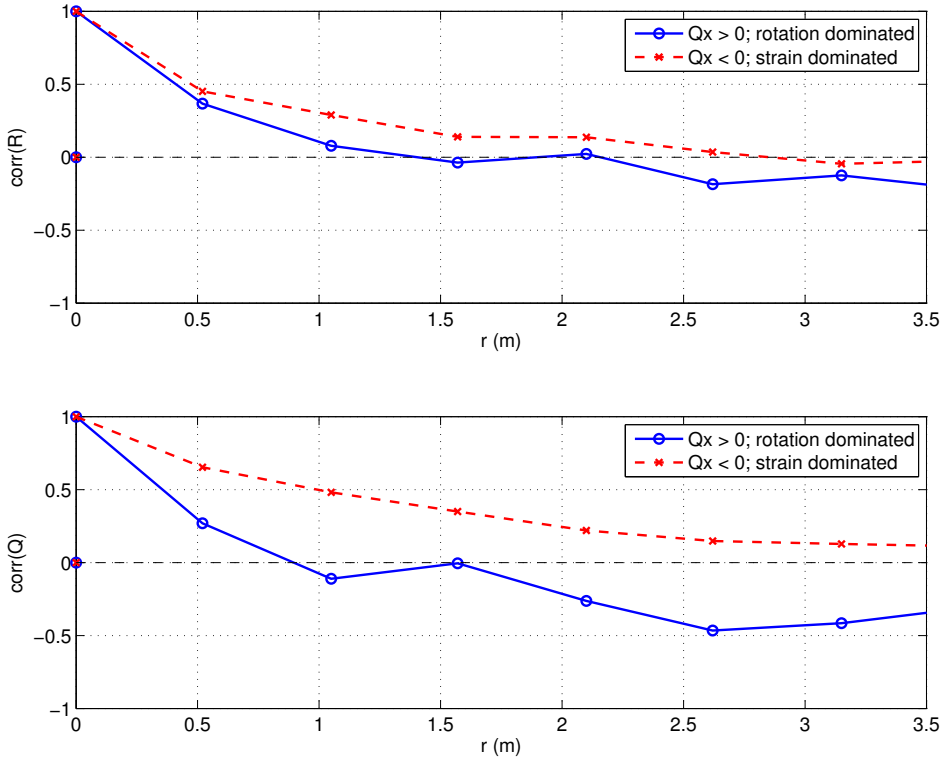

Figure 4.12: Correlation of the invariants R and Q conditioned on strain-dominated regions ($Q < 0$) and vorticity-dominated regions ($Q > 0$) for $R_\lambda \approx 3200$.

of $1 - 1/e \approx 0.63$. In figure 4.13 the correlation lengths are plotted as a function of Reynolds number. It can be seen that the correlation lengths of R are constant and independent of flow topology and of Reynolds number. The correlation lengths of Q for strain-dominated regions decreases slightly with Reynolds number, while the correlation lengths of Q for rotation dominated regions increases slightly with Reynolds number. Thus, the difference in correlation length between strain- and vorticity-dominated regions decreases as the Reynolds number increases and, at high Reynolds numbers ($R_\lambda \gtrsim 5000$), the two correlation lengths are almost the same. This observation agrees with the conjecture, that at high Reynolds numbers the vortex filaments themselves become turbulent, which causes them to become unstable and break down (Jiménez et al., 1993). Based on the assumption of vortex break down the existence of a phase transition of turbulence has been proposed to take place at a Reynolds number of $R_\lambda \approx 700$ (Tabeling and Willaime, 2002).

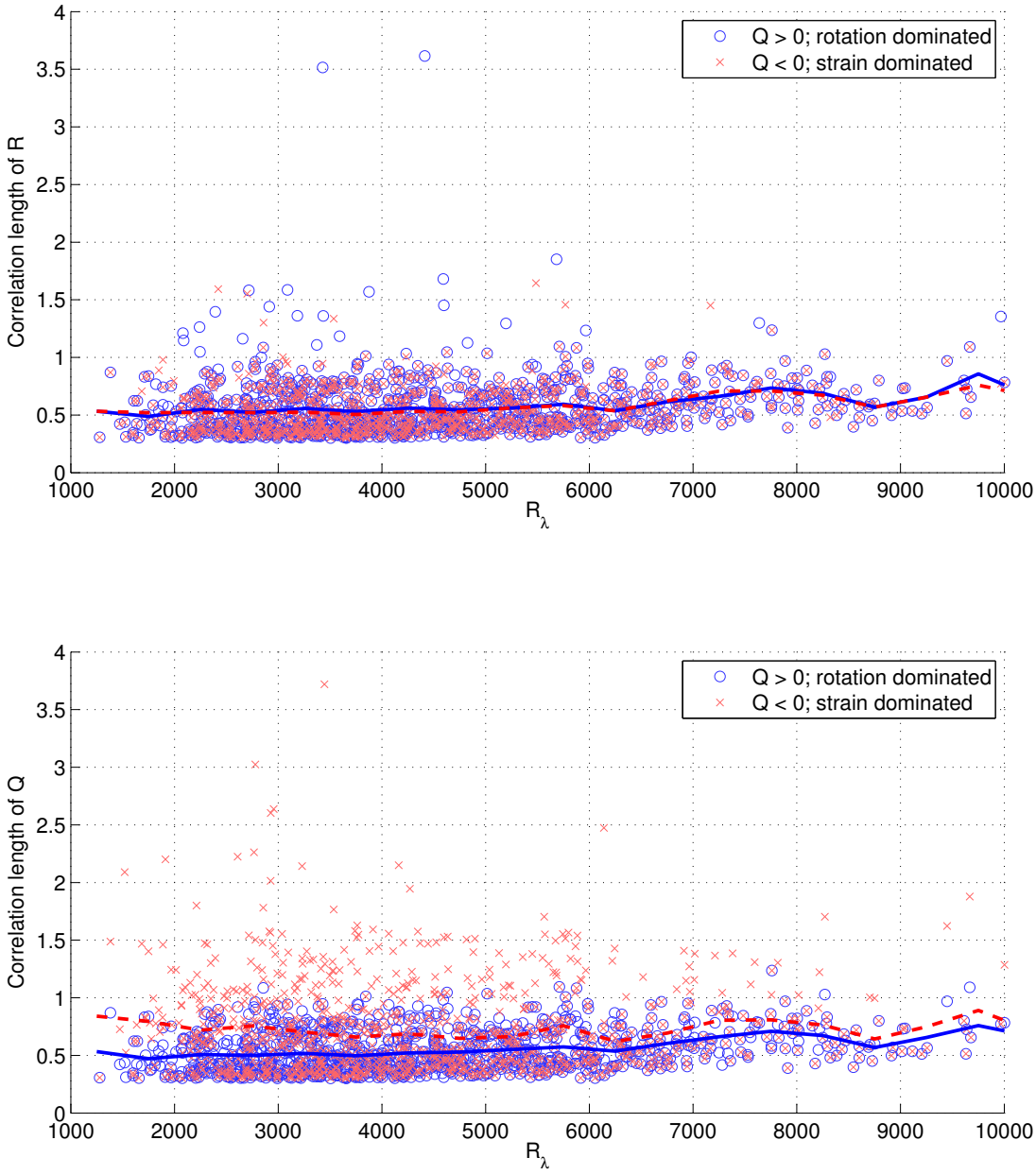

Figure 4.13: Correlation lengths of the invariants R and Q conditioned on strain-dominated regions ($Q < 0$) and vorticity-dominated regions ($Q > 0$) as a function of R_λ. The measured values are indicated by circles and crosses and the mean is shown by lines with corresponding colors.

DNS results at $R_\lambda \approx 1200$ by Ishihara et al. (2009) show that in high Reynolds number turbulent flows a large number of small eddies exist, which are clustered into clouds of small eddies and void regions (fig. 4.14). The observation "suggests [that] it is difficult in practice to trace the motions of all the small eddies in turbulence in the more complex geometries encountered in nature and technology" (Ishihara et al., 2009).

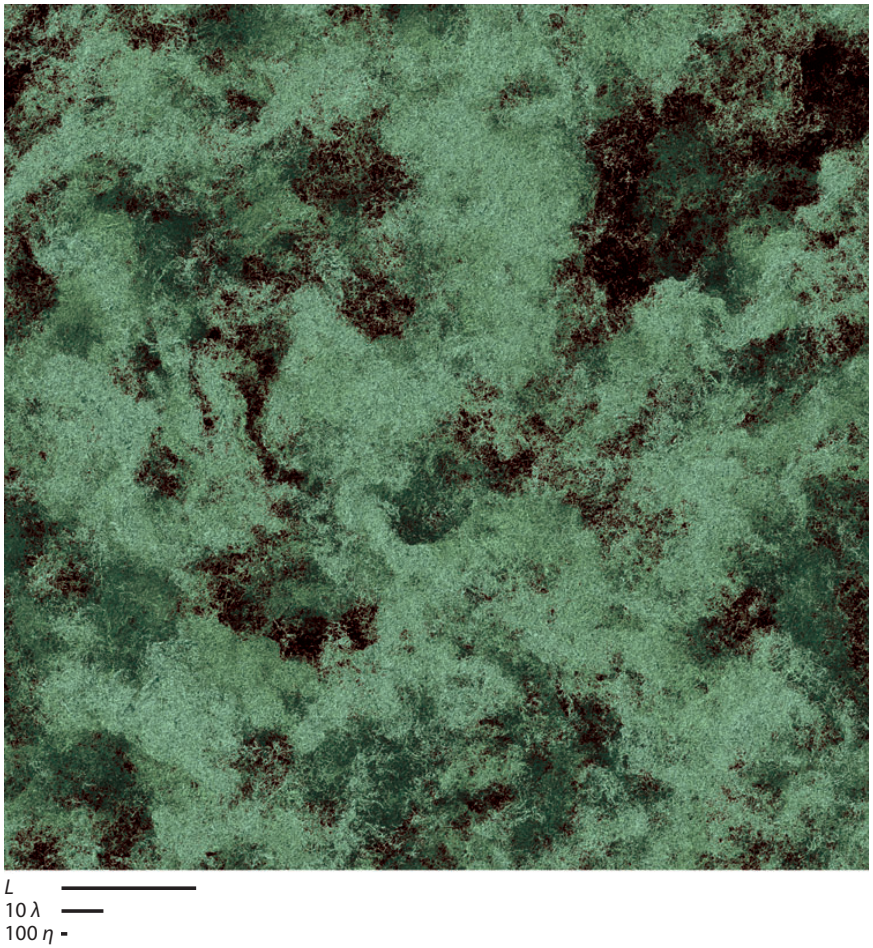

Figure 4.14: Intense vorticity isosurfaces in direct numerical simulation by Ishihara et al. (2009) with $R_\lambda = 1131$. The black bars at the bottom indicate the integral length scale L, the Taylor micro-scale λ, and the Kolmogorov length scale η. The field consists of clouds of a large number of small eddies and void regions (Ishihara et al., 2009).

5 Conclusion and outlook

O glücklich, wer noch hoffen kann,
Aus diesem Meer des Irrtums aufzutauchen!
Was man nicht weiß, das eben brauchte man,
Und was man weiß, kann man nicht brauchen.
(Faust I by Johann Wolfgang von Goethe in 1808)

5.1 Summary and Conclusion

This thesis reports measurements of the flow at the UFS close to the top of Mt. Zugspitze with five sonic anemometers. The large scale flow conditions, such as wind direction and wind speed at the measurement site are analysed. The average wind speed is about 4 m/s and it comes preferably from east or west, due to the topology of the surrounding mountains.

In order to determine turbulence parameters the recordings were split in chunks of one to two minutes length with nearly constant wind speed. The chunks were used to calculate the Reynolds stress tensor, two point velocity correlations and the second and third order structure functions. Integral length scales were determined by integration up to the first zero crossing of the velocity correlation, which gives more consistent results compared to the measurement of integral length scales via an exponential fit method. The average integral length scale of about 19 m was found to agree well with the geometric length scale of the flow. The ratio of the integral length scales in longitudinal and transverse direction were compared to the ratio of integral length scales of an isotropic flow. It was found that the wind from the east is more isotropic than the wind from the west. The finding was explained by a stronger shear of west winds which is caused by constructions at the measurement site. The maximum Reynolds number recorded was of the order of $R_\lambda \approx 10^4$ while the average Reynolds number was found to be $R_\lambda = 3700$. The normalized energy dissipation rate was computed by fitting second and third order structure functions,

and its value $C_\epsilon \approx 0.5$ agrees well with values reported in the literature for other turbulent flows, including wind tunnel and atmospheric measurements, as well as DNS results.

For a further investigation of the isotropy of the flow, the invariants of the Reynolds stress tensor are mapped on the Lumley triangle. It was confirmed that the wind from the east is more isotropic than the wind from west. For wind from the east the level of isotropy is often comparable to or even better than turbulence generated by von Kármán swirling flows achievable in a laboratory. In the case of Reynolds numbers up to $R_\lambda \approx 3000$ and wind from the east it could be observed that the level of isotropy increases with Reynolds number. For large Reynolds numbers ($3000 < R_\lambda < 6000$) a return to isotropy could not be observed. It was also not possible to find a simple correlation between shear parameter and the return to isotropy. These results indicate that a further analysis of anisotropic high Reynolds number flows is required.

It can be concluded that the roof of the UFS is a suitable place for the measurement of turbulent flows. Since the level of isotropy and wind shear depends on the wind direction, the measurement site offers the possibility to investigate turbulent flows under various conditions.

As a new approach for the investigation of atmospheric turbulence the tetrad-based velocity gradient tensor was measured. The invariants of the velocity gradient tensor, R and Q, and their joint PDF were computed. The joint PDF is slightly skewed into the direction of the Vieillefoss tail, that corresponds to bi-axial stretching, and is in agreement with measurements in a von Kármán swirling flow and direct numerical simulations.

The characterization of the flow field with R and Q invariants was used for the investigation of strain- and vorticity-dominated regions as a function of Reynolds number. The correlation lengths corresponding to regions with $Q < 0$ (strain-dominated) decrease with Reynolds number, while those for $Q > 0$ (vorticity-dominated) increase with Reynolds number. Thus, the difference between the correlation lengths decreases and, at high Reynolds numbers ($R_\lambda \gtrsim 5000$), the two correlation lengths are almost the same. This finding is in agreement with observations in DNS that show an increasing complexity of eddy structure geometry with increasing Reynolds numbers.

The tetrad model is a promising new approach for the description of turbulence. The increased probability of $R > 0$ and $Q < 0$, which corresponds to the higher

probability of isotropic tetrads to be deformed into disk like objects, appears to be a common feature of turbulent flows. The further investigation of the properties of the tetrad-based velocity gradient tensor and its invariants may lead to a better understanding and description of characteristic features of turbulence.

5.2 Outlook

In order to get a better picture of the flow conditions at UFS, it would be interesting to extend the statistics to longer time ranges and to condition the measurement not only on the wind direction but also on other weather parameters. That would be achievable by synchronizing the data with the measurements taken by the German whether service (DWD) at a location nearby. In that context it would be of special interest to investigate whether and how turbulence parameters change when the measurement site is surrounded by clouds compared to cloud free conditions. Furthermore the influence of the measurement time and of the yearly seasons could be investigated.

For the joint PDF of R and Q experimental and DNS results indicate that its exact shape depends on the ratio of the size of the tetrahedron to the integral length scale (ρ/L) (Naso and Pumir, 2005; Pumir et al., 2012; Xu et al., 2009, 2011). Although it is difficult to vary the size of the tetrahedron in the current measurement setup it might be possible to condition the data on the integral length scale L. For that purpose it would be good to use more data in order to generate representable statistics. A way to 'generate' more data for the velocity gradient tensor could be to use Taylor's frozen turbulence hypothesis for the calculation of velocity differences.

In order to investigate the influence of wind shear on the VGT it would also be interesting to condition the measurements of the velocity gradient tensor on the shear rate ($S^{\star}_{T_L}$) and the Reynolds number. Furthermore the odd moments of the velocity gradient, $\left\langle \left(\frac{\partial U}{\partial y}\right)^{2n+1} \right\rangle$, could be computed in order to study the influence of the large scale shear on the inertial range.

Another interesting experiment would be to conduct the measurements of a tetrad-based velocity gradient tensor under the well controlled conditions of a wind tunnel with a large scale anisotropy (e.g. shear), in order to see whether the results presented here can be reproduced.

Because the correlation of vorticity- and strain-dominated regions showed only

a week trend as a function of Reynolds number, one might look instead at the correlation of the rate-of-strain tensor and the rate-of-rotation tensor directly.

Another topic, which was not treated here, is the behaviour of passive scalars (for example temperature) in turbulent flows. The sonic anemometers are also measuring the virtual temperature as described in section 2.3.1. The temperature might be used to investigate scaling laws of passive scalars. It has been shown before that the anisotropy of passive scalars at large scales continues into the inertial range, which is in contrast to Kolmogorov's return-to-isotropy hypothesis (Mydlarski and Warhaft, 1998a,b; Mydlarski et al., 1998; Warhaft, 2000). These results could be checked with the current setup at UFS.

The measurement of the temperature can also be used to investigate temperature fluxes at the measurement site, inside and outside of clouds. For that purpose the setup was synchronized with a high speed thermometer (Haman and Malinowski, 1996; Malinowski and Leclerc, 1994) and measurements of several hours length were recorded. Further processing of the data is currently carried out and may be presented elsewhere.

A dream for the future would be to build a setup that has a better spatial and temporal resolution and of which the size of the tetrahedra can be varied over a wide range. The whole setup should be built in such a way that it will not interfere with the flow field. The resolution of the current setup can be increased by the use of faster sonic anemometers, which, however, are much more costly than the current ones used. Avoiding flow interferences is a bigger problem, which can hardly be achieved with a setup consisting of sonic anemometers but are acceptable for high wind speeds.

Appendices

A Investigation of transducer shadowing effects

A.1 Introduction

This appendix summarizes the results and interpretations from various histograms of the wind speed, horizontal angle and vertical angle measured by Thies 3D sonic anemometers at Schneefernerhaus (Zugspitze). The presented measurements were performed between September and November 2010.

The appendix consists of three parts:

1. Wind speed of the three orthogonal axes x, y, z and absolute wind speed. The axes are oriented into x (west), y (north) and z (vertically upwards) direction. The absolute wind speed is calculated as $v_{abs} = \sqrt{v_x^2 + v_y^2 + v_z^2}$.

2. Horizontal angle ϕ measures the angle between the north and the direction where the wind comes from. The angle is measured from the north ($y, \phi = 0°$) moving clock wise to the east ($x, \phi = 90° = \frac{\pi}{2}$), then south ($-y, \phi = 180° = \pi$) and then west ($-x, \phi = 270° = \frac{3\pi}{2}$).

3. Vertical angle θ measures the angle from the upwards pointing z-axis and the direction where the wind comes from. The angle starts from the upwards pointing z-axis ($\theta = 0°$), going to the horizontal x-y-plane ($\theta = 90° = \frac{\pi}{2}$) and then downwards to $-z$ ($\theta = 180° = \pi$).

Each chapter summarizes interesting findings and suggested explanations. Important findings are printed in **bold letters**. Suggested explanations by the author are printed in *italic letters*. All histograms and probability distribution functions (PDFs) are attached at the end of the appendix. They are referred to by use of their page number written in round brackets. Histograms are usually located on the top of the pages, while the corresponding PDFs can be found at the bottom.

A.2 Summary of the Results

All three parts of this investigation reveal abnormalities of the histograms at specific wind speeds and angles. The wind speed shows low measurement accuracy at less than 1 m/s and an abnormality when switching from positive to negative wind speeds (i.e. at 0 m/s). Since the abnormalities get stronger when the wind comes closer to the horizontal direction, *it leads to the assumption that the central rod of the anemometer causes flow distortions, generating the dent at 0 m/s.* The conclusion that the central rod is the main cause for the poor measurement accuracy of low wind speeds is in agreement with the finding that the histograms of v_x and v_y become smoother and more symmetric when only wind with a larger component perpendicular to the analysed wind component is taken into account.

The histograms of the horizontal angle ϕ show abnormalities at specific angles. Some of these can be explained with the geometric location of the measurement arms, but not all. The abnormalities of the horizontal angle ϕ decrease as the wind comes closer to the horizontal direction. This suggests that, in contrast to the wind speed, *the measurement of the horizontal angle is mainly influenced by the arms of the anemometer and not by the central rod.*

The histograms of the vertical angle θ show abnormalities at two specific angles. Again the distortion of the flow field seems to be a reasonable explanation. *The cause may be the central rod and the stand support of the anemometer.*

A.3 Number of evaluated measurements

Table 2 shows a comparison of the number of evaluated measurements. The sensors sample at $10Hz$ continuously. The number of measurements varies because of blackouts and measurement errors.

Sensor Number	Month	Number of Evaluated Measurements
0 (top)	September	$24752036 \approx 24.7 \cdot 10^6$
0 (top)	October	$20140208 \approx 20.1 \cdot 10^6$
0 (top)	November	$19620787 \approx 19.6 \cdot 10^6$
1 (south-west)	October	$19837852 \approx 19.8 \cdot 10^6$

Table A.1: Comparison of the number of evaluated measurements.

A.4 Wind Speed

A.4.1 Dependence on different bin sizes (100, 101, 102, 103)

The term 'bin size' refers to the size of the intervals which were used to calculate the histogram. The influence of bin sizes ranging from $d_1 = 0.01m/s$ - $0.10m/s$ are compared in this subsection. As it can be seen from the histograms (100, 101, 102, 103) that the characteristics of the histogram are the same for different bin sizes.

From the histograms of v_x, v_y it can be seen that there is an abnormality at $v_x, v_y = 0m/s$. Apart from the abnormality at 0 m/s the slopes of the histograms for positive and negative wind speeds are different (101, 102).

One possible explanation is the low measurement accuracy of the anemometer at low wind speeds (less than 1 m/s). The low accuracy may be caused by the geometry of the anemometer and its disturbance of the flow. Especially the central rod in the middle of the anemometer and the anemometer arms are likely to disturb the flow.

A.4.2 Dependence on evaluated time range (month) (104, 105, 105, 106)

The wind speed (absolute and component wise v_x, v_y, v_z) for September, October and November 2010 are compared. The absolute wind speed has a maximum probability between 1 and 3 m/s varying depending on the month (104). v_x, v_y, v_z show fluctuations at wind speeds less than 1 m/s (105, 105, 106) caused by the low measurement accuracy, as described above in subsection A.4.1.

A.4.3 Dependence on vertical angle θ (107, 108, 109, 110)

The influence of a restriction of the maximum vertical angle θ on the absolute wind speed as well as on v_x, v_y, v_z is investigated. Wind speeds with a varying maximum deviation from the horizontal direction are compared. In this case 0° corresponds to a horizontal wind direction and ±90° corresponds to wind in the vertical direction. In the histograms, deviations from the horizontal direction of up to a maximum of $\pm 10°, \pm 20°, \pm 30°, \pm 40°, \pm 45°$ and ±90° are compared (±90° corresponds to all wind directions being considered).

The histogram of v_z is skewed to positive wind speeds, which corresponds to more wind coming from below the measurement site (110). This is understood as

Schneefernerhaus is located at the side of the Zugspitze mountain. The more the deviation from the vertical direction is restricted, the more the skewness of v_z has to decrease, i.e. $\pm 10°$ is symmetric.

As the histograms of v_x and v_y are limited to be closer to the horizontal wind direction, the abnormalities of the histograms (especially around 0 m/s) become stronger (108, 109).

One possible explanation might be that the central rod is the main cause for the disturbance of the flow field. A more horizontal wind would then cause stronger disturbances as the flow has a larger component perpendicular to the rod. That might also explain why the histogram of v_z does not show similar abnormalities (110).

A.4.4 Dependence on horizontal angle ϕ (111, 112, 113, 114)

The dependence of the wind speed on the horizontal angle ϕ is analysed along the x-axis (west-east) and y-axis (north-south). First, the considered wind speed component is limited to a maximum deviation from the respective perpendicular axis of $\pm 0.1\pi$, $\pm 0.2\pi$, $\pm 0.3\pi$, $\pm 0.4\pi$ and $\pm 0.5\pi$ ($\pm 0.5\pi$ corresponds to all wind directions being considered).

The histograms become smoother and more symmetric the more the considered wind speeds are limited to the perpendicular direction. In other words, the histograms appear smoother when those wind directions which have a larger component parallel to the investigated direction are neglected (111, 112).

Wind with a large component parallel to the analysed wind direction is influenced stronger by the central rod, than wind which has a large component perpendicular to the direction of the analysed wind speed.

In a second step the considered wind speed components are limited to a maximum deviation from their own axis (113, 114). **It can be seen that lower wind speeds are affected stronger by the anemometer. Larger wind speeds (i.e. $v_x, v_y > 4m/s$) are almost not affected.**

A.5 Horizontal Angle ϕ

A.5.1 Dependence on different bin sizes (115, 116)

The histogram of the horizontal angle ϕ is evaluated with different bin sizes $d_2 = 0.01\pi, 0.02\pi$ and 0.05π (115). It can be seen that the main wind directions are west and east according to the two peaks at 0.4π and 1.5π.

At bin sizes of $d_2 = 0.01\pi$ and 0.02π the histograms show abnormalities at an angular distance of $\frac{2}{3}\pi = 120°$ and $\frac{1}{15}\pi = 12°$ (116). *The location of the abnormalities correspond to the geometric location of the six measurement arms (table A.2). The arms are arranged in paired arrays, where a top and a bottom arm are opposing each other. The green lines in the histograms correspond to the position of the arms, while the red lines mark the center of two arms which are located on top of each other (116).*

Histogram	Sensor Geometry	Histogram [deg]	Sensor Geometry [deg]
0.26	0.27	47	48
0.34	0.33	59	60
0.40	0.40	72	72
0.93	0.93	168	168
1.00	1.00	180	180
1.06	1.07	191	192
1.59	1.60	286	288
1.66	1.67	299	300
1.73	1.73	311	312

Table A.2: Comparison of horizontal angles ϕ measured in the histogram with the sensor geometry. On the left side angles are given in multiples of π and on the right side corresponding angles are given in degrees.

It can also be seen that there are further abnormalities at other locations which cannot be explained by the direct influence of the measurement arms.

As an attempt for an explanation the anemometer arms might be hit from the reverse side at an angle of $\phi_0 + \pi = \phi_0 + 180°$. That would lead to further flow distortions and to a regular pattern of abnormalities located at an angular distance of $\frac{1}{3}\pi = 60°$ (blue and black lines in (118)). **That could explain some but not all abnormalities found in the histograms, especially not the ones at**

$0.8\pi = 144°$ **and** $1.8\pi = 324°$**. For these abnormalities no good explanation has been found, so far.**

A.5.2 Dependence on evaluated time range (month) (117)

The histograms of September, October and November 2010 are compared and show abnormalities at the same angles (117).

A.5.3 Dependence on vertical angle θ (119)

The evaluated wind speeds are restricted to a maximum deviation from the horizontal direction of $\pm 10°, \pm 20°, \pm 30°, \pm 40°, \pm 45°$ and $\pm 90°$. **The abnormalities decrease as the wind is limited to more horizontal directions (119).** *In case the anemometer arms are the main cause for the flow distortion, their distortion of the flow becomes smaller, as the flow is closer to the horizontal.*

A.5.4 Dependence on absolute wind speed (120)

The histogram of ϕ is conditioned on a minimum absolute wind speed. The abnormalities, discussed earlier, start to disappear at a minimum wind speed of 8 m/s and show only small dependence when conditioned on lower minimum wind speeds (120).

A.6 Vertical Angle θ

A.6.1 Dependence on different bin sizes (121)

Histograms of θ with bin sizes of $d_2 = 0.01\pi, 0.02\pi, 0.05\pi$ and 0.10π are compared and show the same characteristics. At bin sizes larger then $d_2 = 0.02\pi$ the histograms are not smooth any more and their small scale characteristics disappear (121).

A.6.2 Dependence on evaluated time range (month) (122)

The histograms for September, October, November 2010 are compared and all show abnormalities at $0.44\pi = \frac{4}{9}\pi = 80°$ **and** $0.75\pi = \frac{3}{4}\pi = 135°$ **(122).** *An explanation may again be given through the distortion of the flow field by the anemometer's geometry. The abnormality at* $80°$ *corresponds to an almost horizontal wind direction, which is the direction most influenced by the central rod. Wind coming from* $135°$ *might be influenced by the anemometer base (Standfuß), which would cause an even stronger distortion in accordance with the histograms.*

A.6.3 Dependence on absolute wind speed (123)

As in subsection A.5.4 the histogram becomes smoother as the minimum absolute wind speed is increased. However the abnormalities are visible up to a minimum wind speed of 8 m/s (123).

A.7 Histograms and probability density functions

The histograms used for the analysis of the transducer shadowing effects and the corresponding normalized probability distribution functions (PDFs) are shown on the next pages.

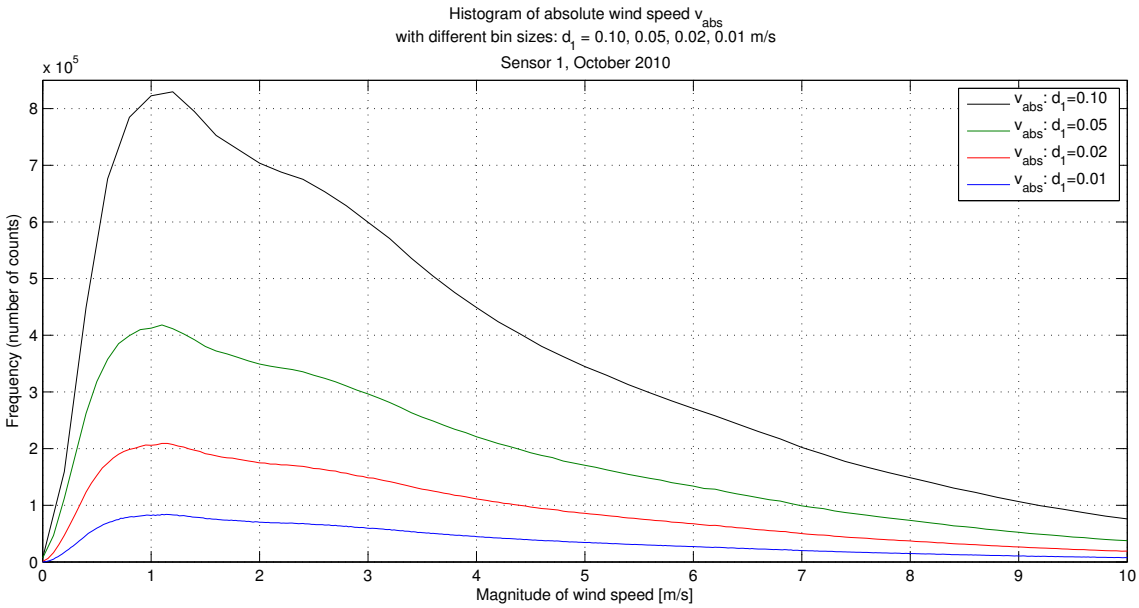
Histogram of absolute wind speed v_abs
with different bin sizes: d_1 = 0.10, 0.05, 0.02, 0.01 m/s
Sensor 1, October 2010
x 10^5
Frequency (number of counts)
Magnitude of wind speed [m/s]
v_abs: d_1=0.10
v_abs: d_1=0.05
v_abs: d_1=0.02
v_abs: d_1=0.01

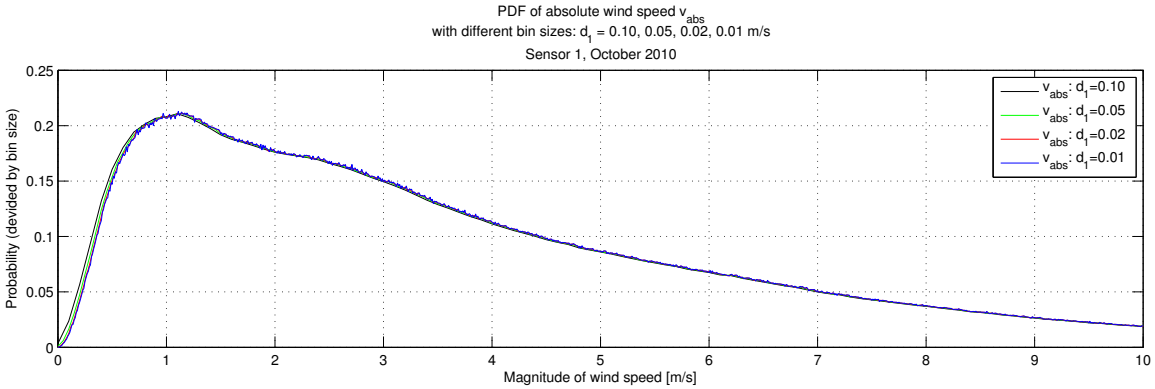
PDF of absolute wind speed v_abs
with different bin sizes: d_1 = 0.10, 0.05, 0.02, 0.01 m/s
Sensor 1, October 2010
Probability (devided by bin size)
Magnitude of wind speed [m/s]
v_abs: d_1=0.10
v_abs: d_1=0.05
v_abs: d_1=0.02
v_abs: d_1=0.01

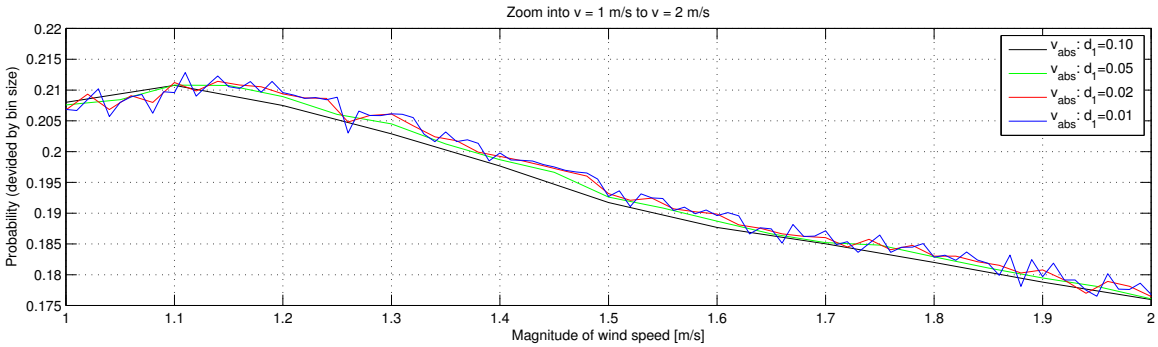
Zoom into v = 1 m/s to v = 2 m/s
Probability (devided by bin size)
Magnitude of wind speed [m/s]
v_abs: d_1=0.10
v_abs: d_1=0.05
v_abs: d_1=0.02
v_abs: d_1=0.01

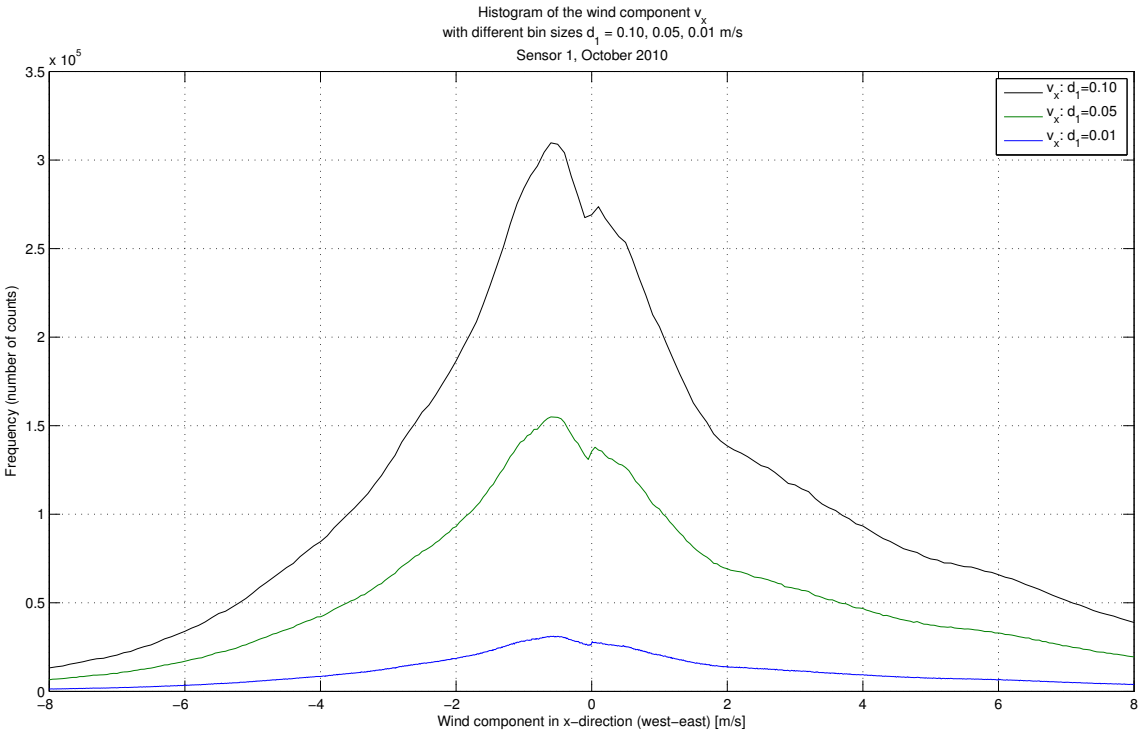
Histogram of the wind component v_x
with different bin sizes d_1 = 0.10, 0.05, 0.01 m/s
Sensor 1, October 2010
x 10^5
Frequency (number of counts)
Wind component in x−direction (west−east) [m/s]
v_x: d_1=0.10
v_x: d_1=0.05
v_x: d_1=0.01

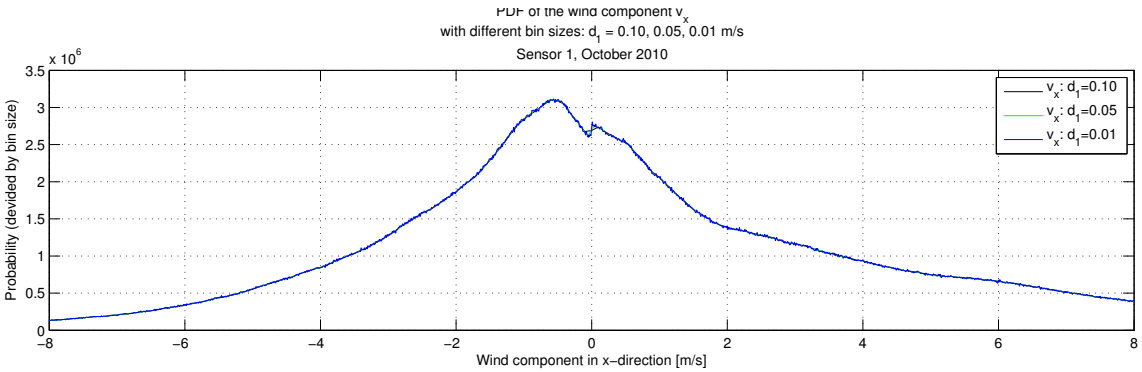
PDF of the wind component v_x
with different bin sizes: d_1 = 0.10, 0.05, 0.01 m/s
Sensor 1, October 2010
x 10^6
Probability (devided by bin size)
Wind component in x−direction [m/s]
v_x: d_1=0.10
v_x: d_1=0.05
v_x: d_1=0.01

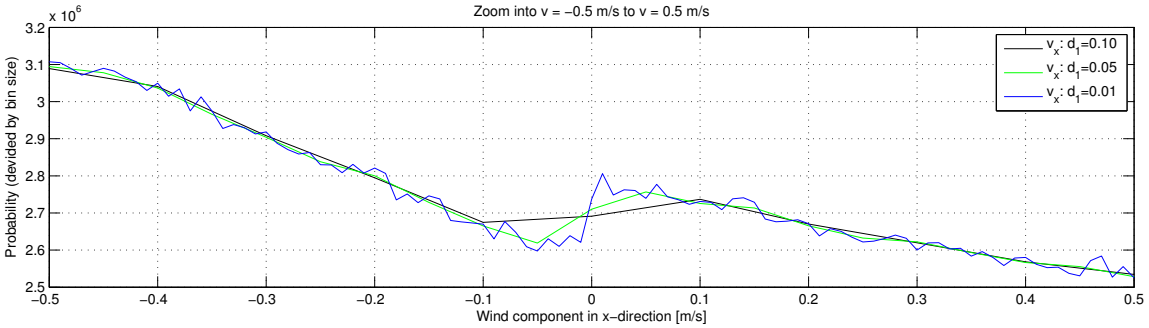
Zoom into v = −0.5 m/s to v = 0.5 m/s
x 10^6
Probability (devided by bin size)
Wind component in x−direction [m/s]
v_x: d_1=0.10
v_x: d_1=0.05
v_x: d_1=0.01

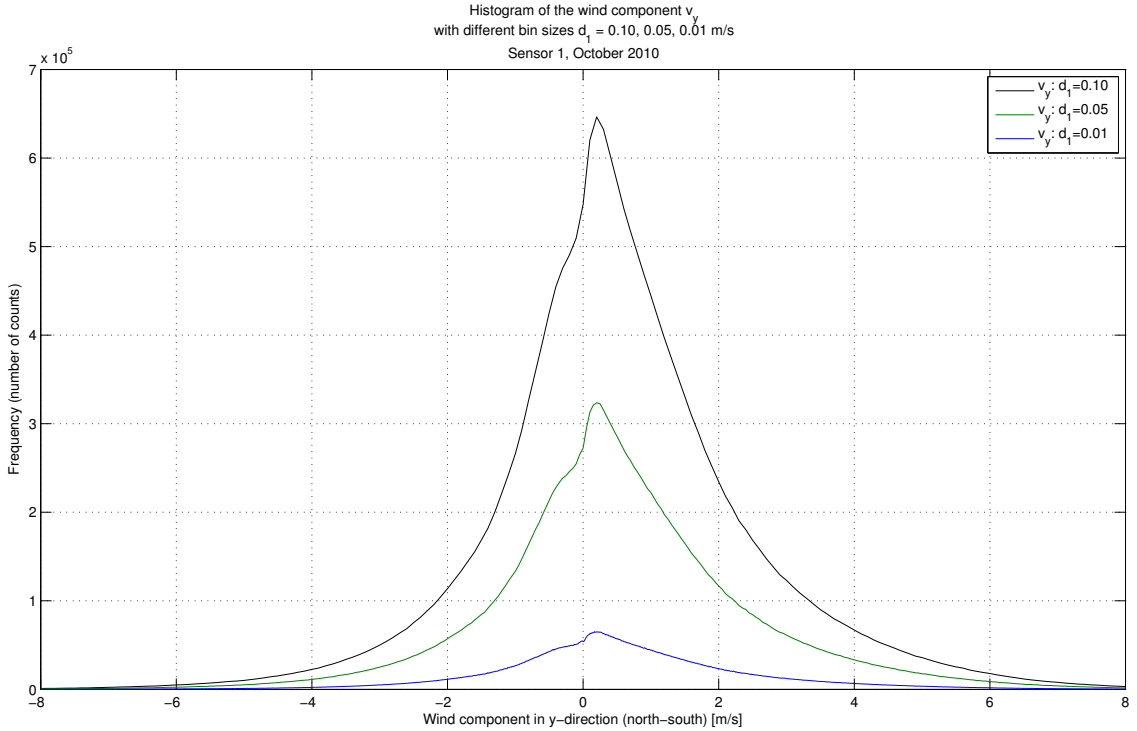
Histogram of the wind component v_y
with different bin sizes d_1 = 0.10, 0.05, 0.01 m/s
Sensor 1, October 2010
x 10^5
Frequency (number of counts)
Wind component in y−direction (north−south) [m/s]
v_y: d_1=0.10
v_y: d_1=0.05
v_y: d_1=0.01

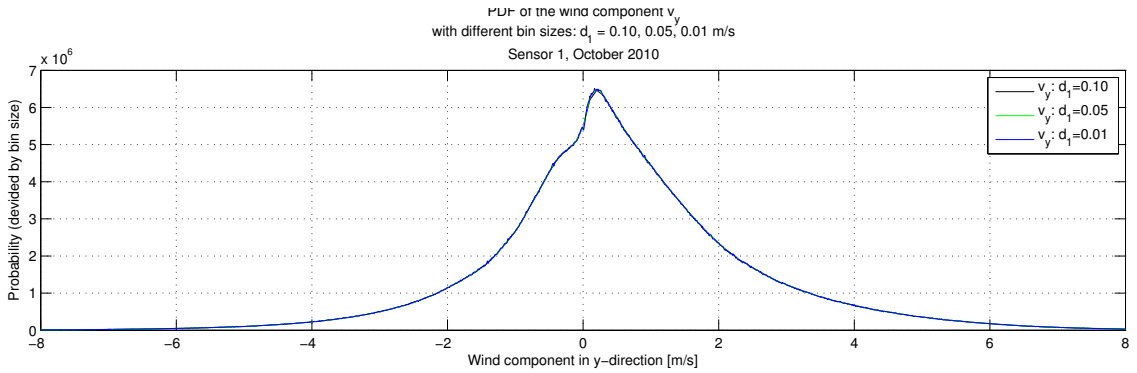
PDF of the wind component v_y
with different bin sizes: d_1 = 0.10, 0.05, 0.01 m/s
Sensor 1, October 2010
x 10^6
Probability (devided by bin size)
Wind component in y−direction [m/s]
v_y: d_1=0.10
v_y: d_1=0.05
v_y: d_1=0.01

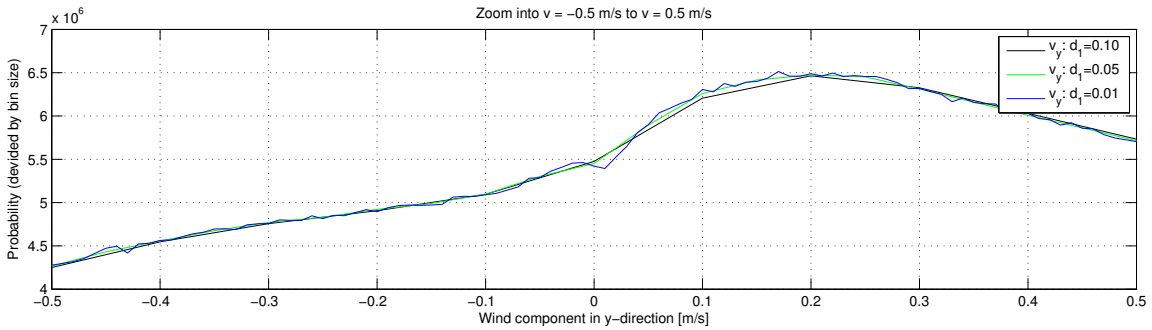
Zoom into v = −0.5 m/s to v = 0.5 m/s
x 10^6
Probability (devided by bin size)
Wind component in y−direction [m/s]
v_y: d_1=0.10
v_y: d_1=0.05
v_y: d_1=0.01

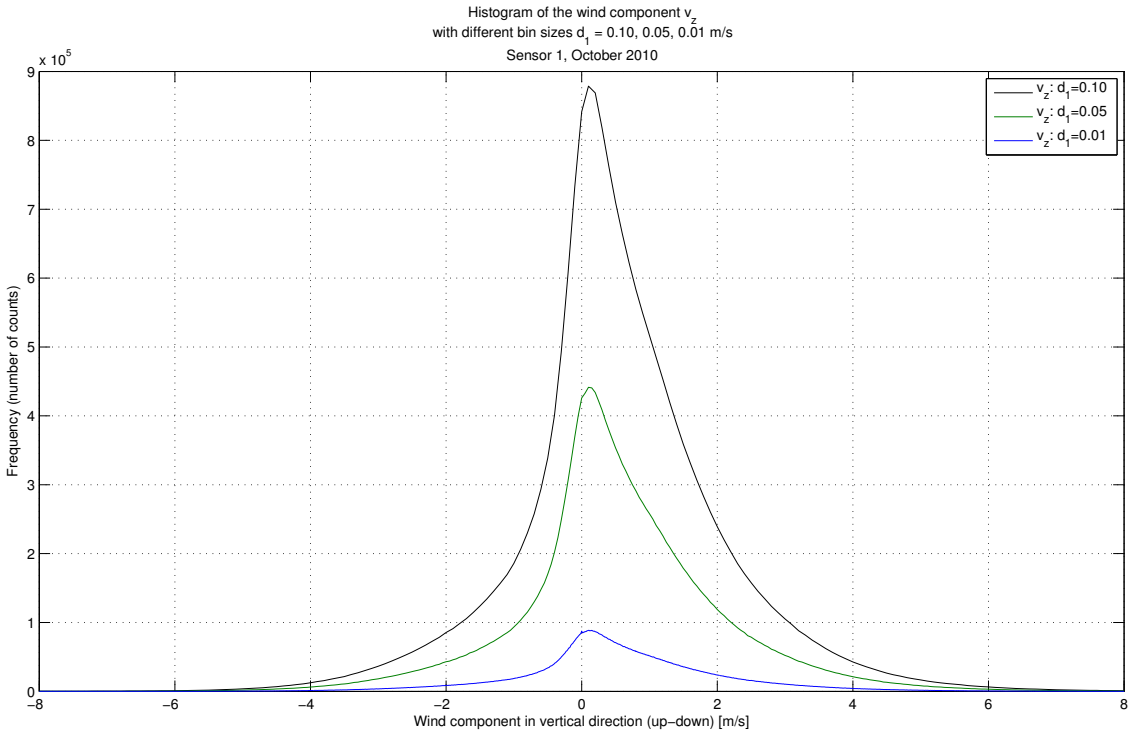
Histogram of the wind component v_z
with different bin sizes d_l = 0.10, 0.05, 0.01 m/s
Sensor 1, October 2010
x 10^5
Frequency (number of counts)
Wind component in vertical direction (up−down) [m/s]
v_z: d_l=0.10
v_z: d_l=0.05
v_z: d_l=0.01

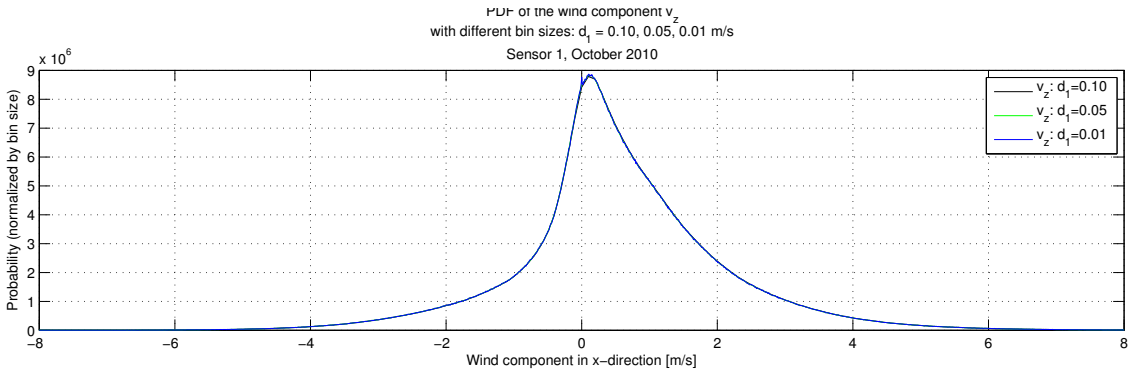
PDF of the wind component v_z
with different bin sizes: d_l = 0.10, 0.05, 0.01 m/s
Sensor 1, October 2010
x 10^6
Probability (normalized by bin size)
Wind component in x−direction [m/s]
v_z: d_l=0.10
v_z: d_l=0.05
v_z: d_l=0.01

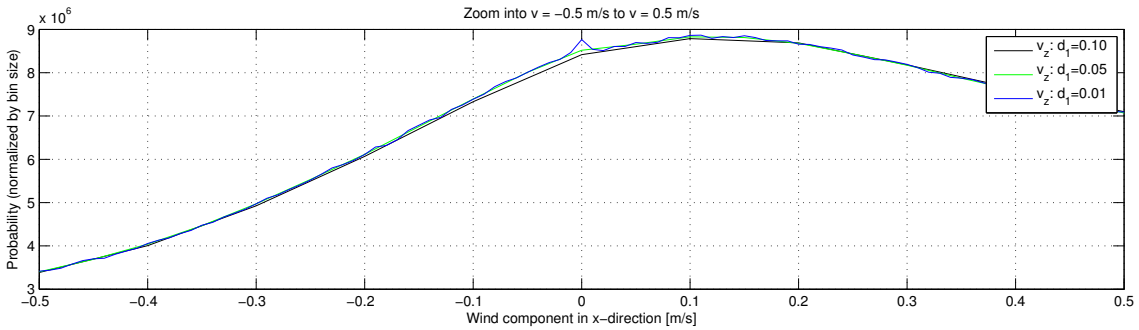
Zoom into v = −0.5 m/s to v = 0.5 m/s
x 10^6
Probability (normalized by bin size)
Wind component in x−direction [m/s]
v_z: d_l=0.10
v_z: d_l=0.05
v_z: d_l=0.01

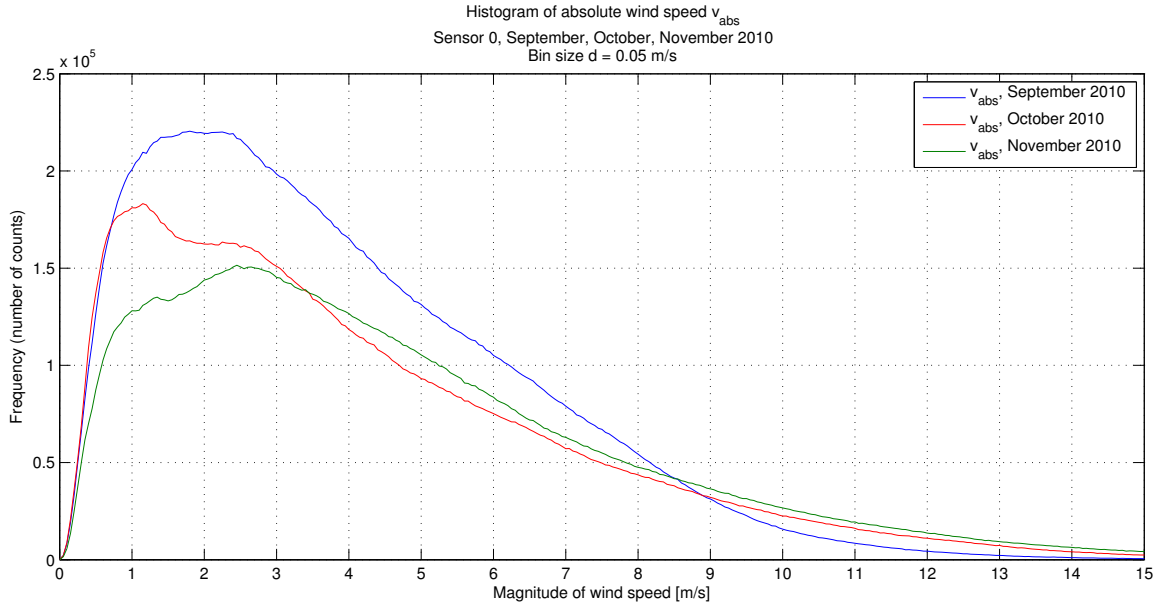
Histogram of absolute wind speed v_abs
Sensor 0, September, October, November 2010
Bin size d = 0.05 m/s
x 10^5
Frequency (number of counts)
Magnitude of wind speed [m/s]
v_abs, September 2010
v_abs, October 2010
v_abs, November 2010

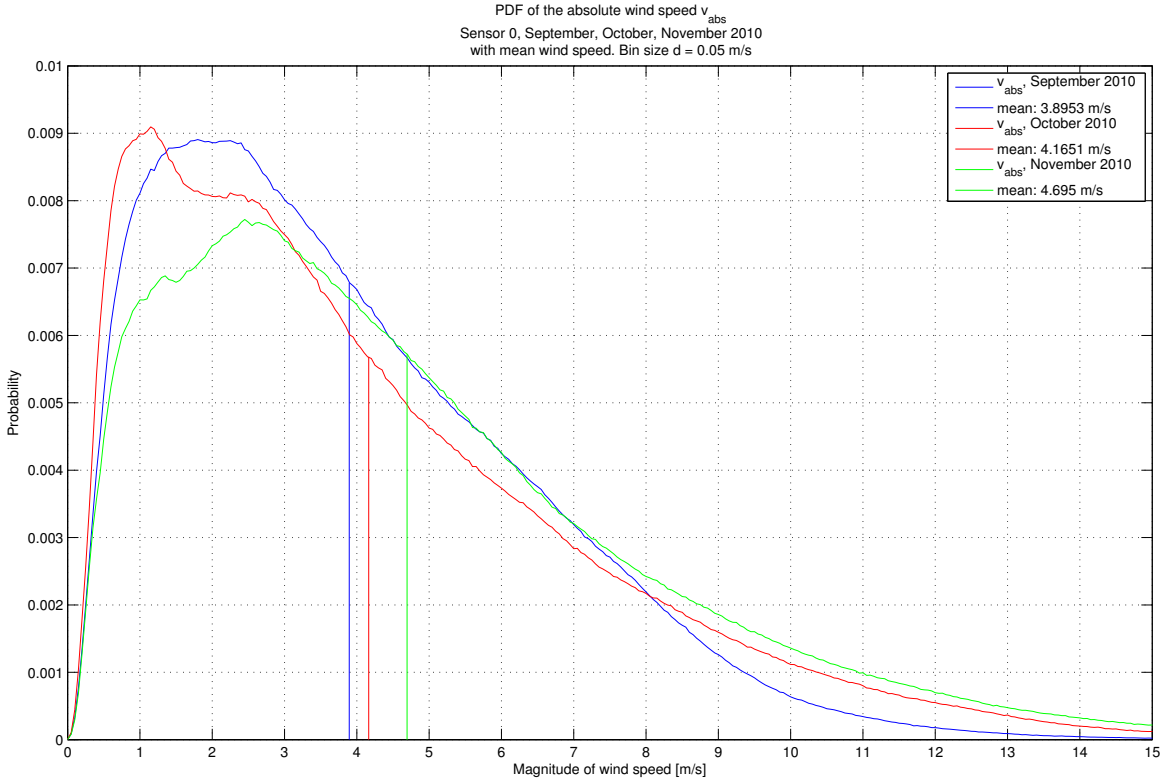
PDF of the absolute wind speed v_abs
Sensor 0, September, October, November 2010
with mean wind speed. Bin size d = 0.05 m/s
Probability
Magnitude of wind speed [m/s]
v_abs, September 2010
mean: 3.8953 m/s
v_abs, October 2010
mean: 4.1651 m/s
v_abs, November 2010
mean: 4.695 m/s

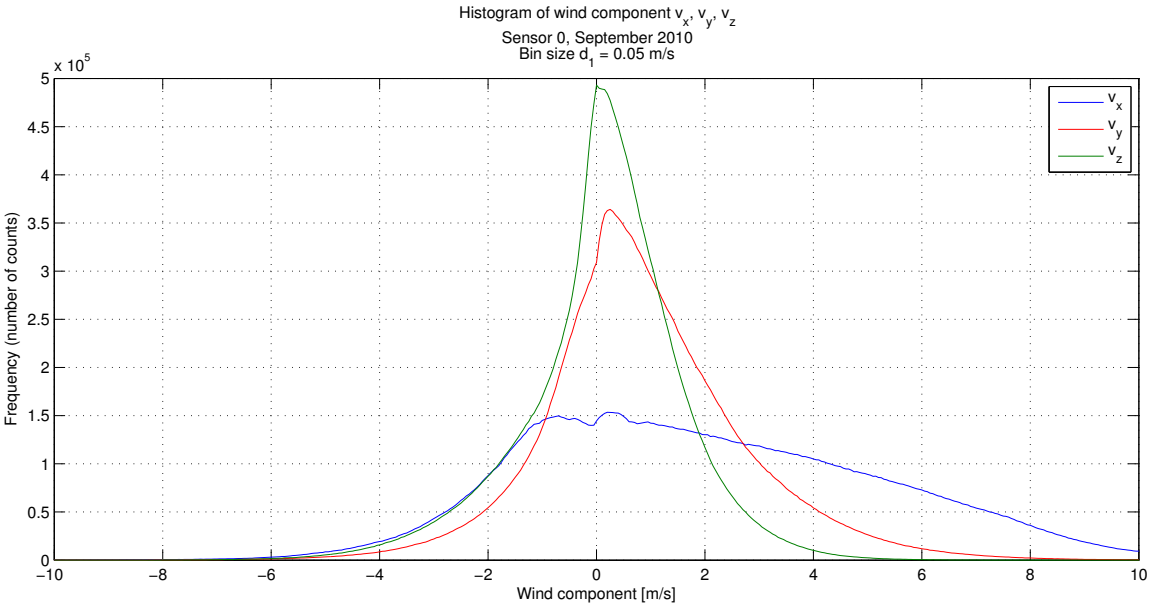
Histogram of wind component v_x, v_y, v_z
Sensor 0, September 2010
Bin size d_1 = 0.05 m/s
x 10^5
Frequency (number of counts)
Wind component [m/s]
v_x
v_y
v_z

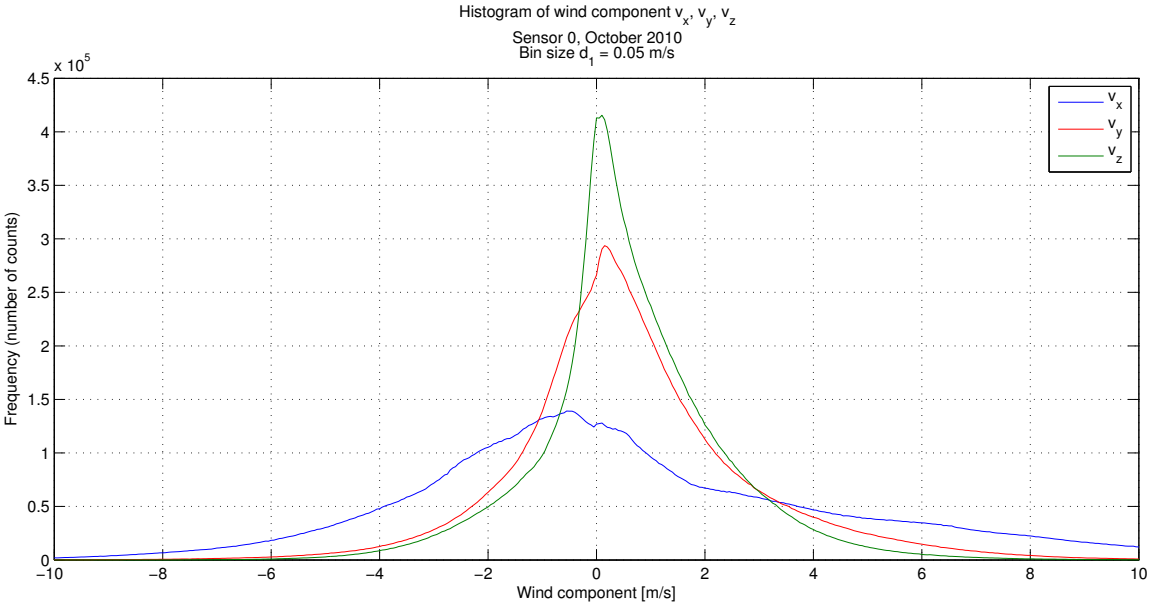
Histogram of wind component v_x, v_y, v_z
Sensor 0, October 2010
Bin size d_1 = 0.05 m/s
x 10^5
Frequency (number of counts)
Wind component [m/s]
v_x
v_y
v_z

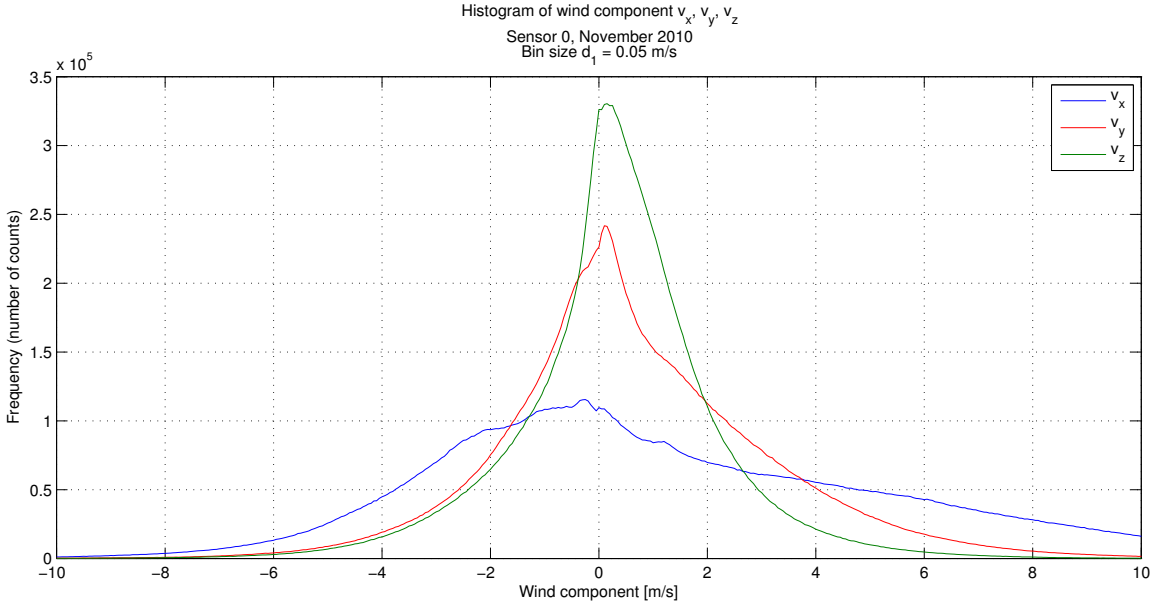
Histogram of wind component v_x, v_y, v_z
Sensor 0, November 2010
Bin size d_1 = 0.05 m/s
x 10^5
Frequency (number of counts)
Wind component [m/s]
v_x
v_y
v_z

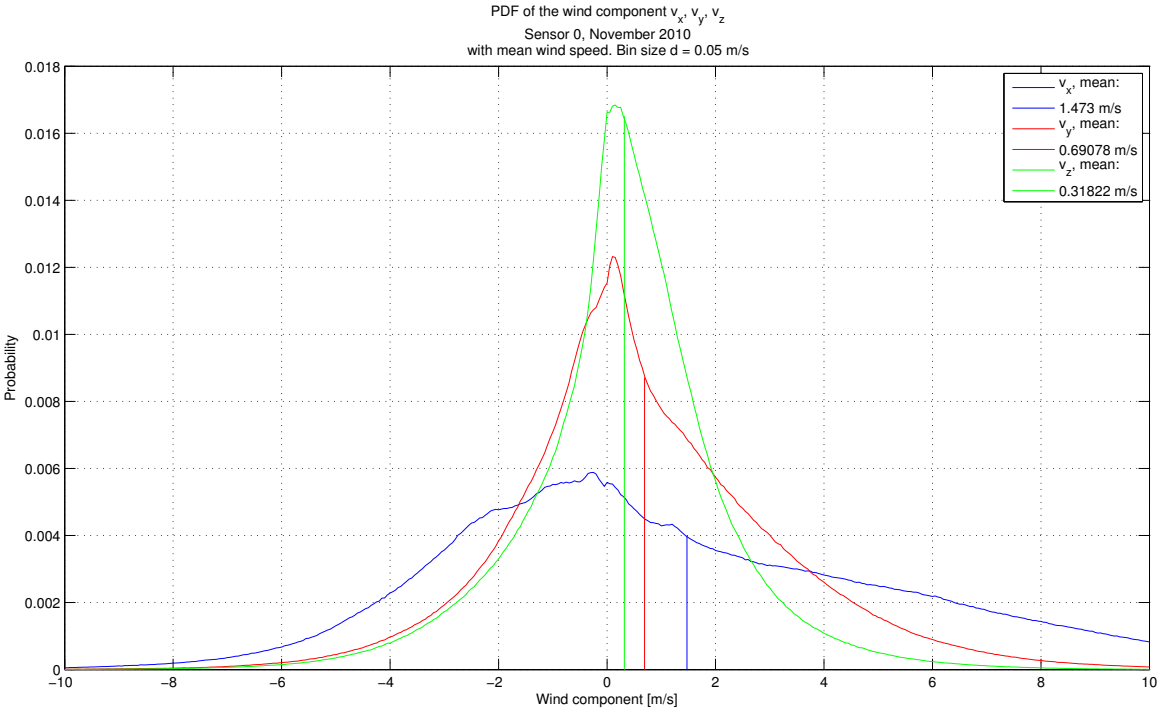
PDF of the wind component v_x, v_y, v_z
Sensor 0, November 2010
with mean wind speed. Bin size d = 0.05 m/s
Probability
Wind component [m/s]
v_x, mean:
1.473 m/s
v_y, mean:
0.69078 m/s
v_z, mean:
0.31822 m/s

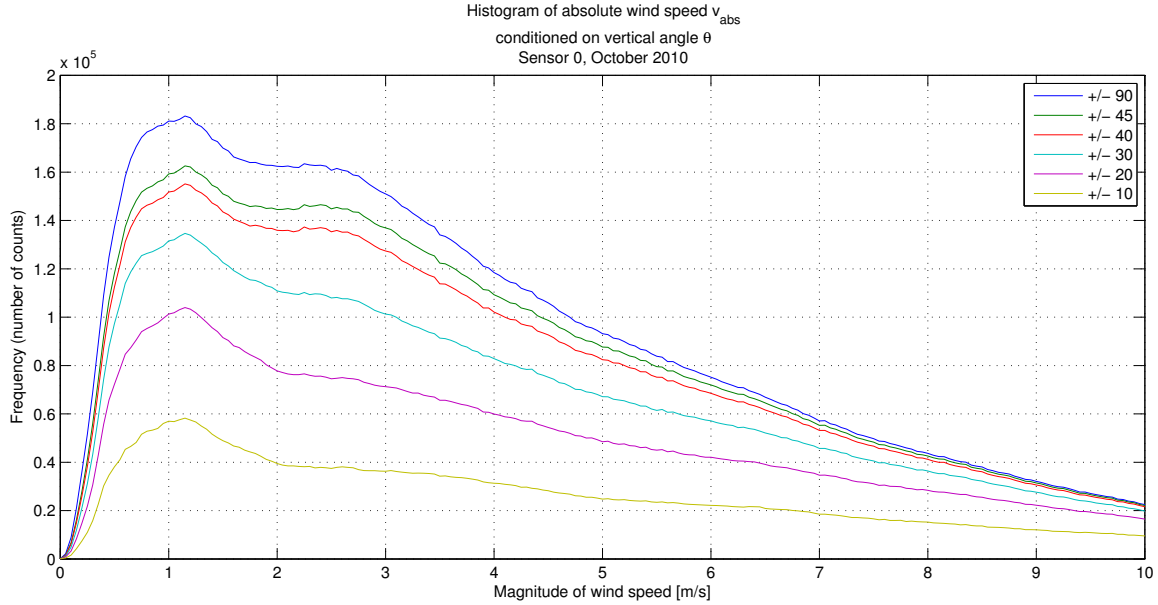
Histogram of absolute wind speed v abs
conditioned on vertical angle θ
Sensor 0, October 2010
x 10^5
Frequency (number of counts)
Magnitude of wind speed [m/s]
+/– 90
+/– 45
+/– 40
+/– 30
+/– 20
+/– 10

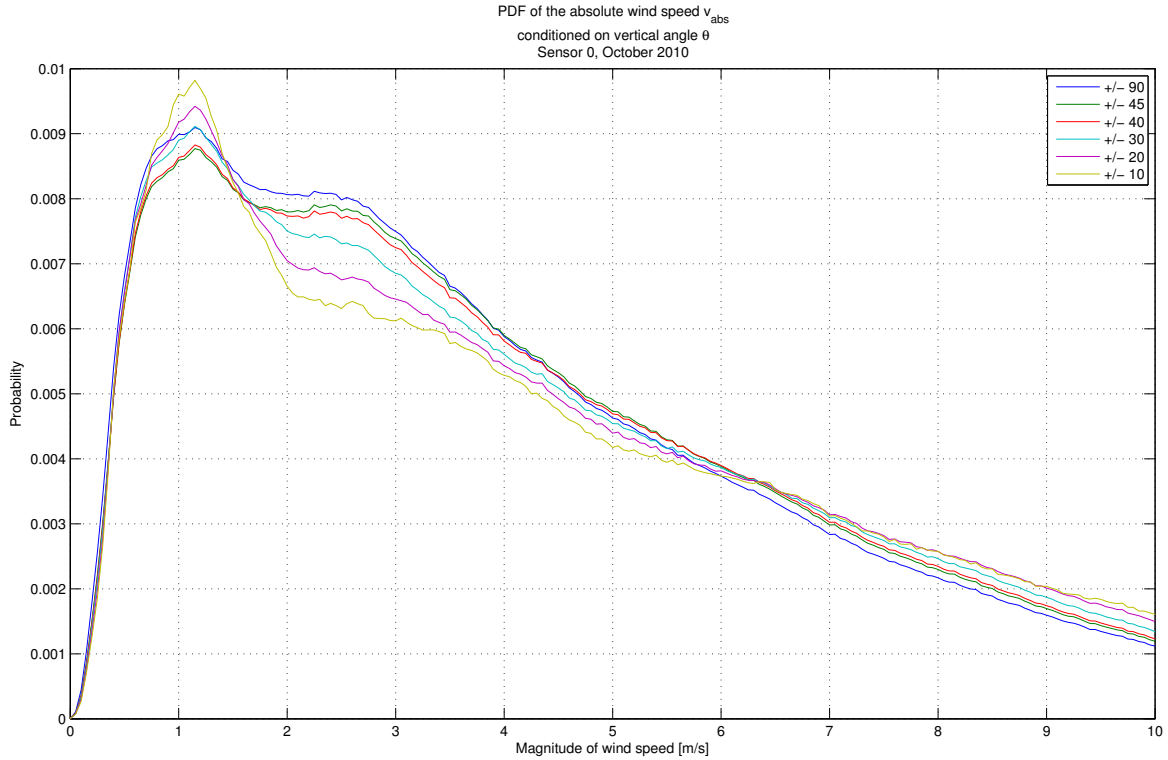
PDF of the absolute wind speed v abs
conditioned on vertical angle θ
Sensor 0, October 2010
Probability
Magnitude of wind speed [m/s]
+/– 90
+/– 45
+/– 40
+/– 30
+/– 20
+/– 10

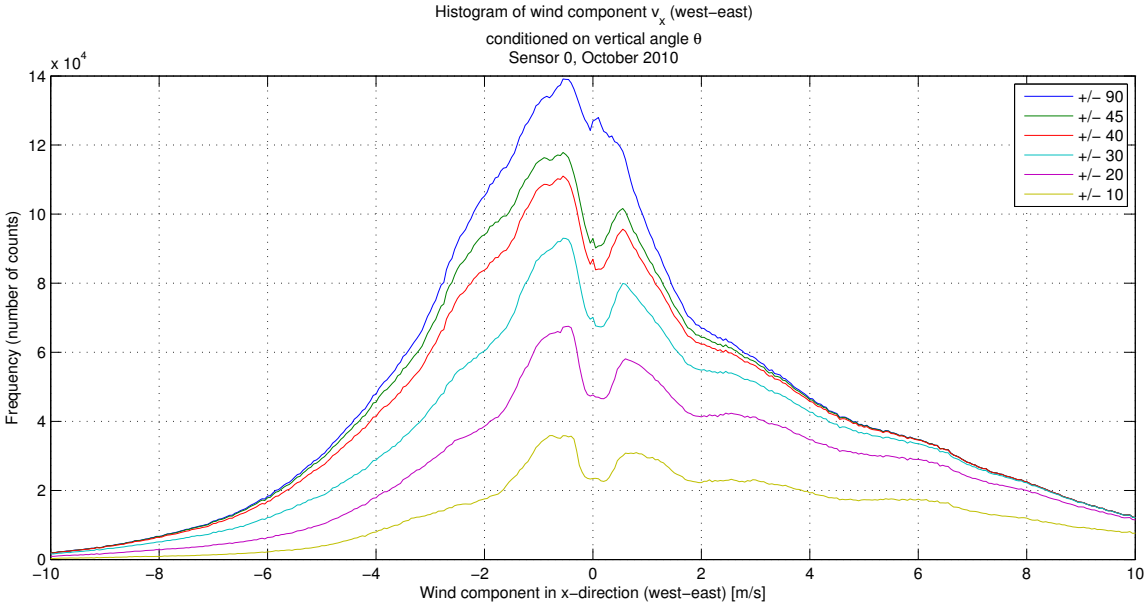
Histogram of wind component v_x (west−east)
conditioned on vertical angle θ
Sensor 0, October 2010
x 10^4
Frequency (number of counts)
Wind component in x−direction (west−east) [m/s]
+/− 90
+/− 45
+/− 40
+/− 30
+/− 20
+/− 10

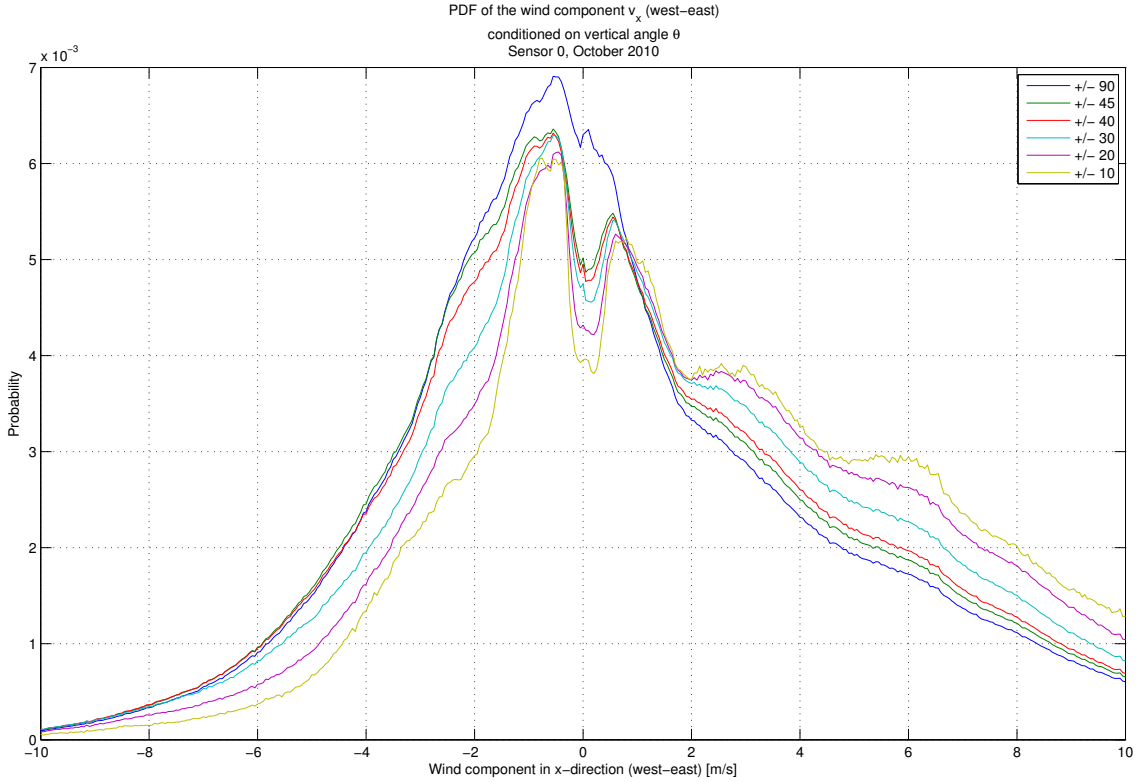
PDF of the wind component v_x (west−east)
conditioned on vertical angle θ
Sensor 0, October 2010
x 10^−3
Probability
Wind component in x−direction (west−east) [m/s]
+/− 90
+/− 45
+/− 40
+/− 30
+/− 20
+/− 10

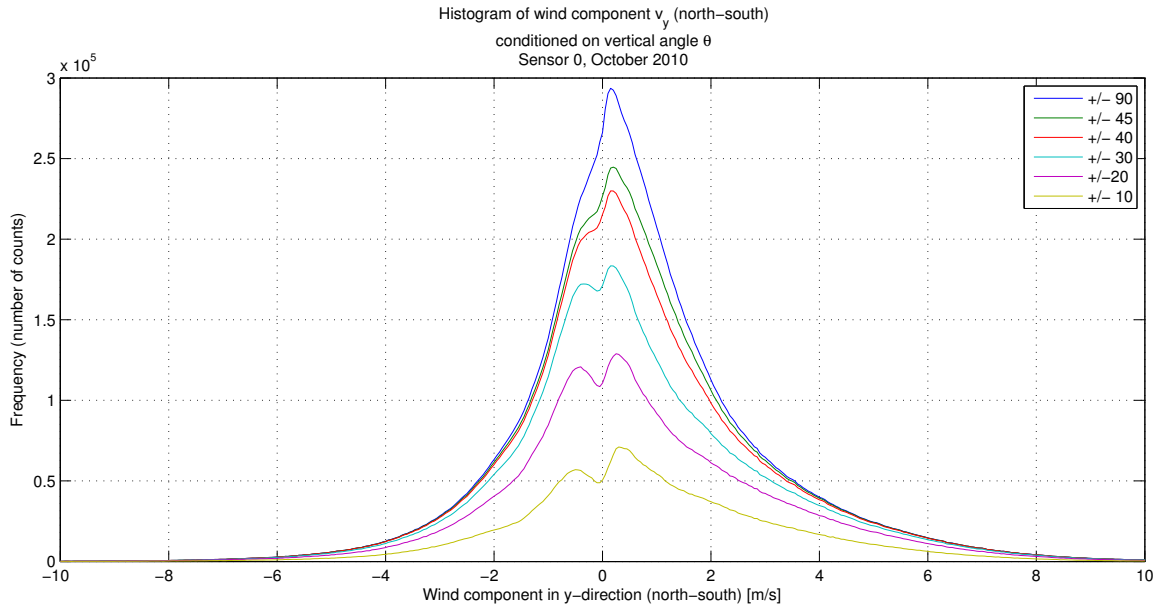
Histogram of wind component v_y (north−south)
conditioned on vertical angle θ
Sensor 0, October 2010
x 10^5
Frequency (number of counts)
Wind component in y−direction (north−south) [m/s]
+/− 90
+/− 45
+/− 40
+/− 30
+/−20
+/− 10

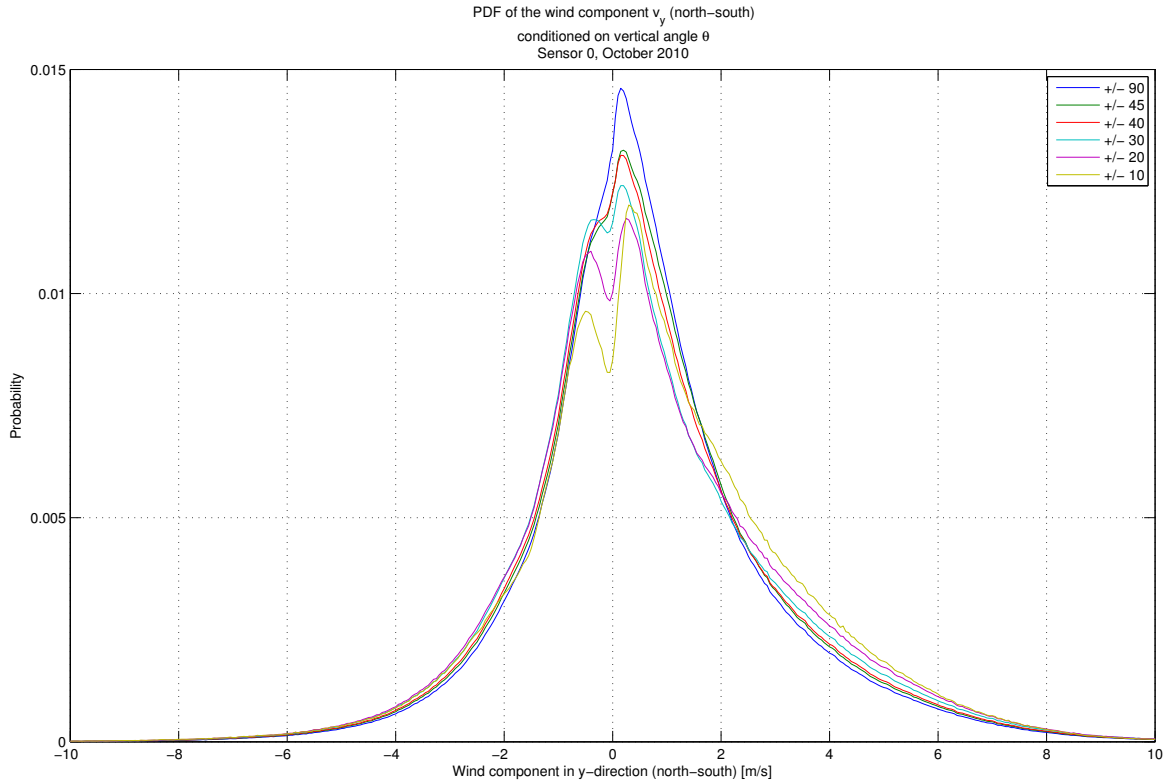
PDF of the wind component v_y (north−south)
conditioned on vertical angle θ
Sensor 0, October 2010
Probability
Wind component in y−direction (north−south) [m/s]
+/− 90
+/− 45
+/− 40
+/− 30
+/− 20
+/− 10

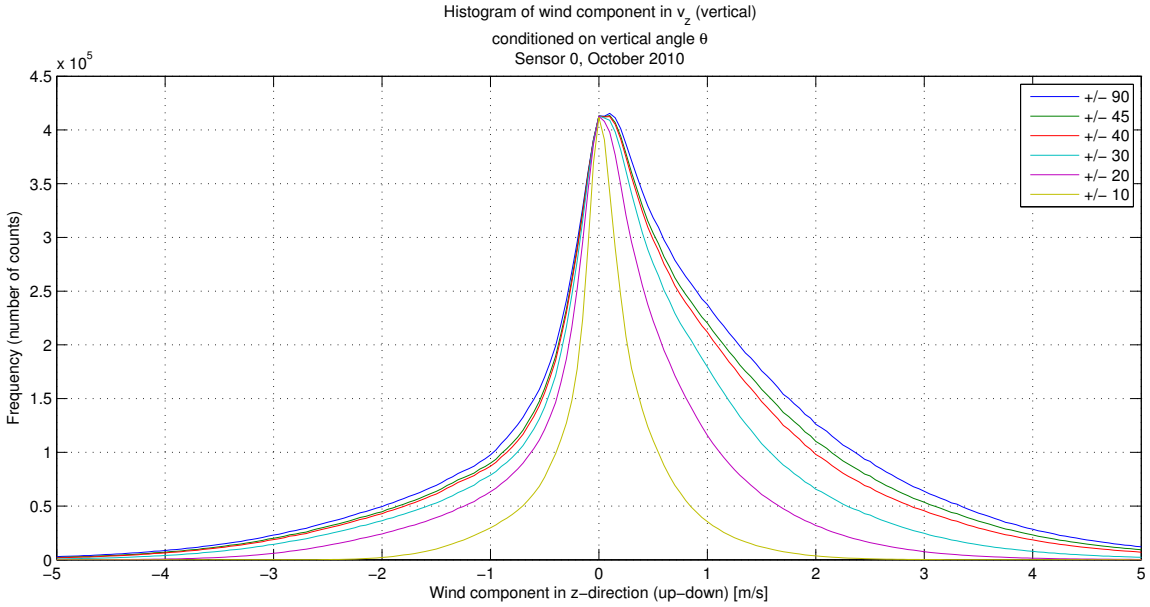
Histogram of wind component in v_z (vertical)
conditioned on vertical angle θ
Sensor 0, October 2010
x 10^5
Frequency (number of counts)
Wind component in z−direction (up−down) [m/s]
+/− 90
+/− 45
+/− 40
+/− 30
+/− 20
+/− 10

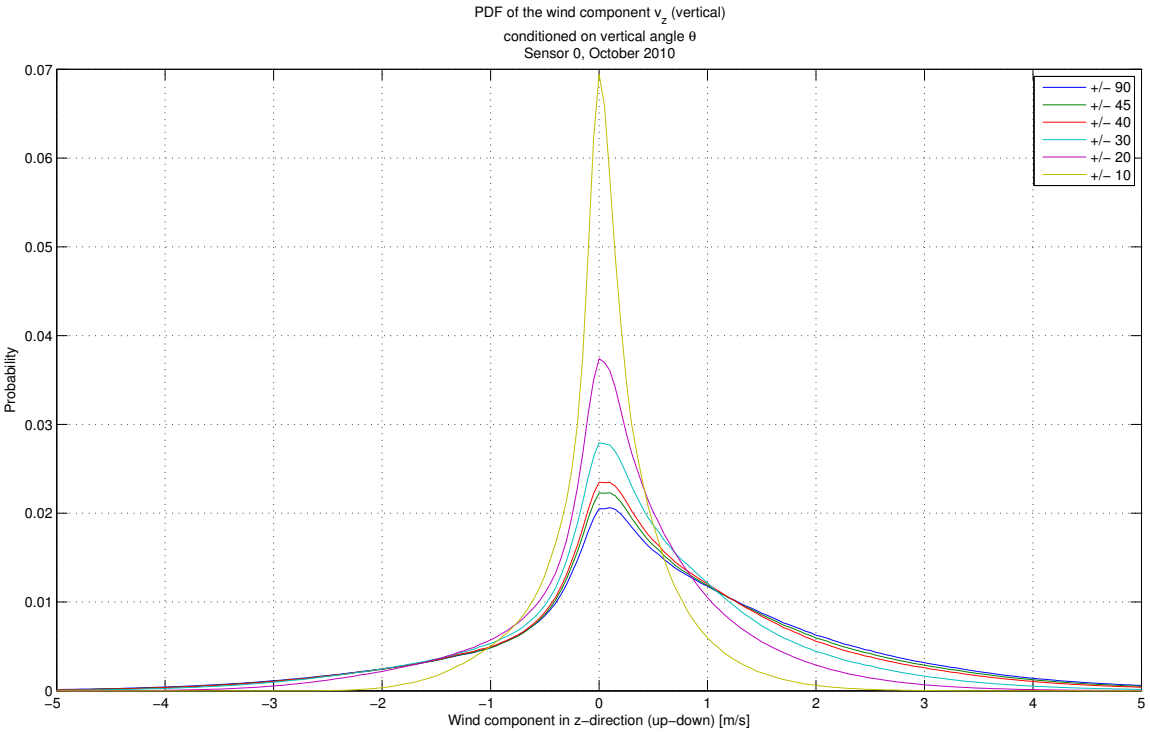
PDF of the wind component v_z (vertical)
conditioned on vertical angle θ
Sensor 0, October 2010
Probability
Wind component in z−direction (up−down) [m/s]
+/− 90
+/− 45
+/− 40
+/− 30
+/− 20
+/− 10

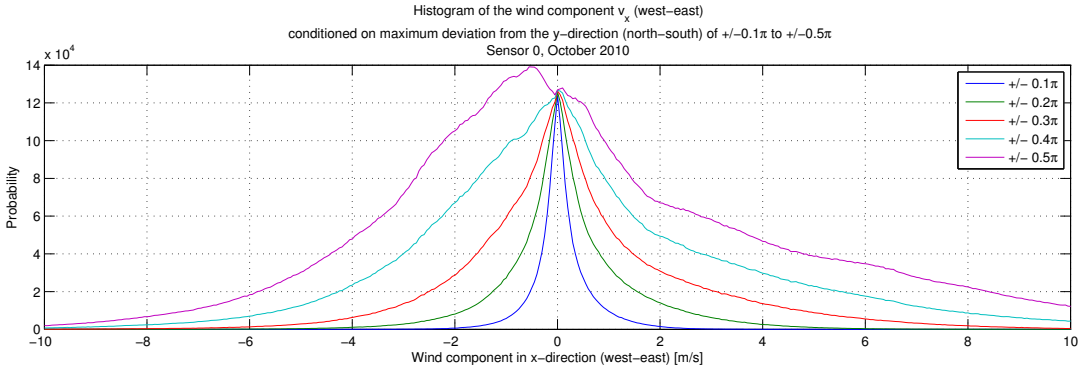
Histogram of the wind component v_x (west−east)
conditioned on maximum deviation from the y−direction (north−south) of +/−0.1π to +/−0.5π
Sensor 0, October 2010
x 10^4
Probability
Wind component in x−direction (west−east) [m/s]
+/− 0.1π
+/− 0.2π
+/− 0.3π
+/− 0.4π
+/− 0.5π

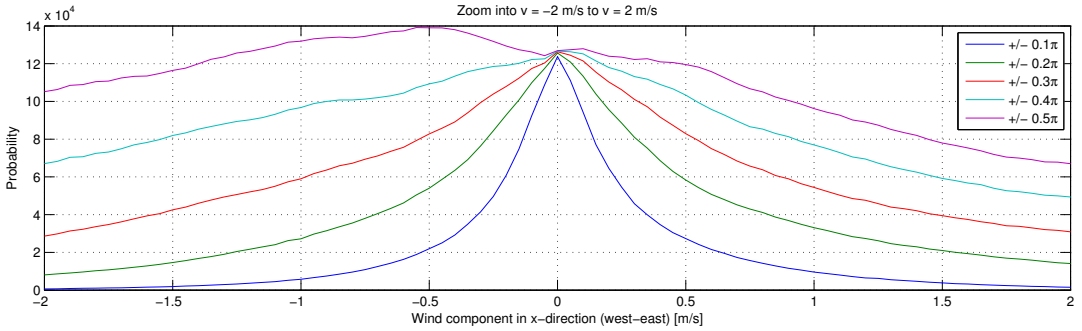
Zoom into v = −2 m/s to v = 2 m/s
x 10^4
Probability
Wind component in x−direction (west−east) [m/s]
+/− 0.1π
+/− 0.2π
+/− 0.3π
+/− 0.4π
+/− 0.5π

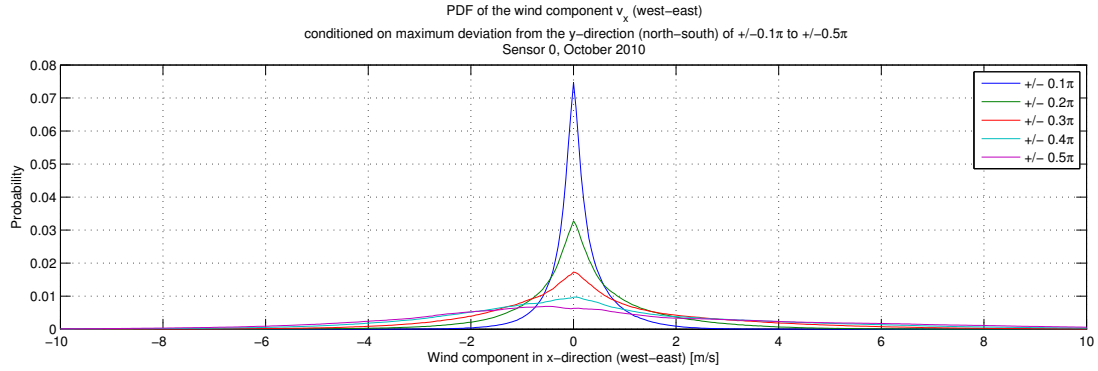
PDF of the wind component v_x (west−east)
conditioned on maximum deviation from the y−direction (north−south) of +/−0.1π to +/−0.5π
Sensor 0, October 2010
Probability
Wind component in x−direction (west−east) [m/s]
+/− 0.1π
+/− 0.2π
+/− 0.3π
+/− 0.4π
+/− 0.5π

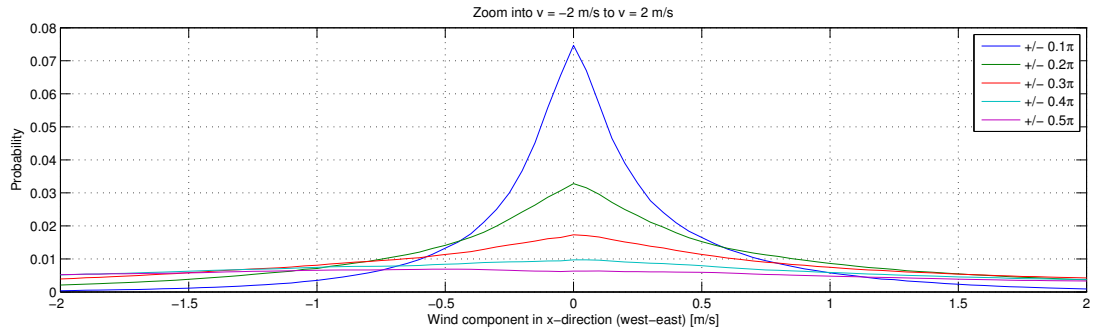
Zoom into v = −2 m/s to v = 2 m/s
Probability
Wind component in x−direction (west−east) [m/s]
+/− 0.1π
+/− 0.2π
+/− 0.3π
+/− 0.4π
+/− 0.5π

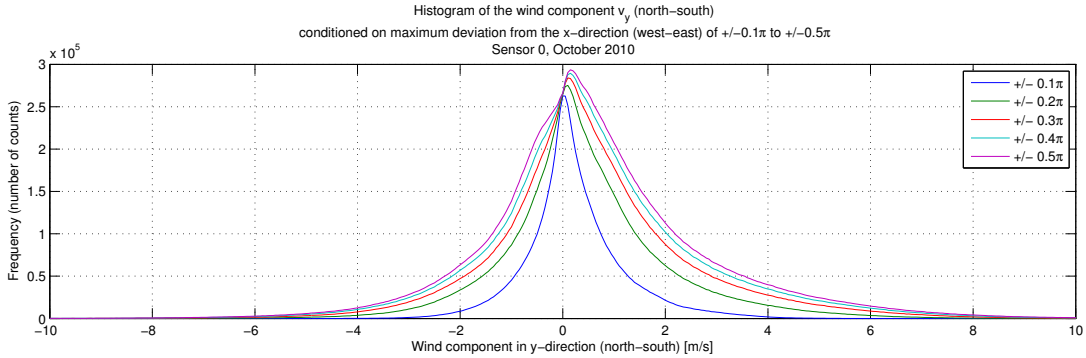
Histogram of the wind component v_y (north−south)
conditioned on maximum deviation from the x−direction (west−east) of +/−0.1π to +/−0.5π
Sensor 0, October 2010
x 10^5
Frequency (number of counts)
Wind component in y−direction (north−south) [m/s]
+/− 0.1π
+/− 0.2π
+/− 0.3π
+/− 0.4π
+/− 0.5π

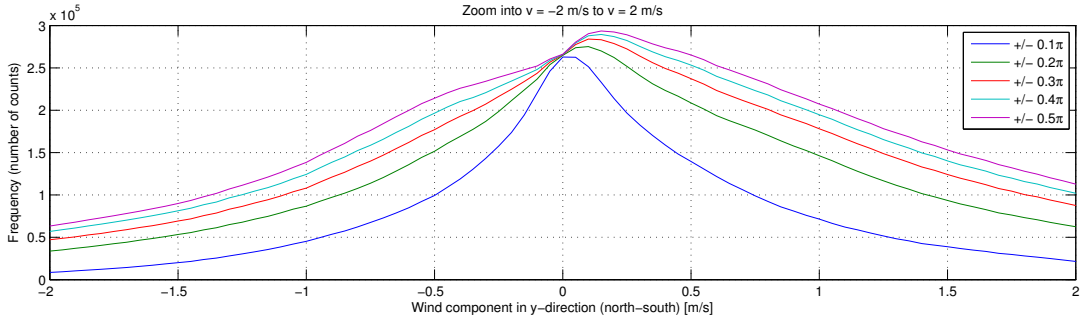
Zoom into v = −2 m/s to v = 2 m/s
x 10^5
Frequency (number of counts)
Wind component in y−direction (north−south) [m/s]
+/− 0.1π
+/− 0.2π
+/− 0.3π
+/− 0.4π
+/− 0.5π

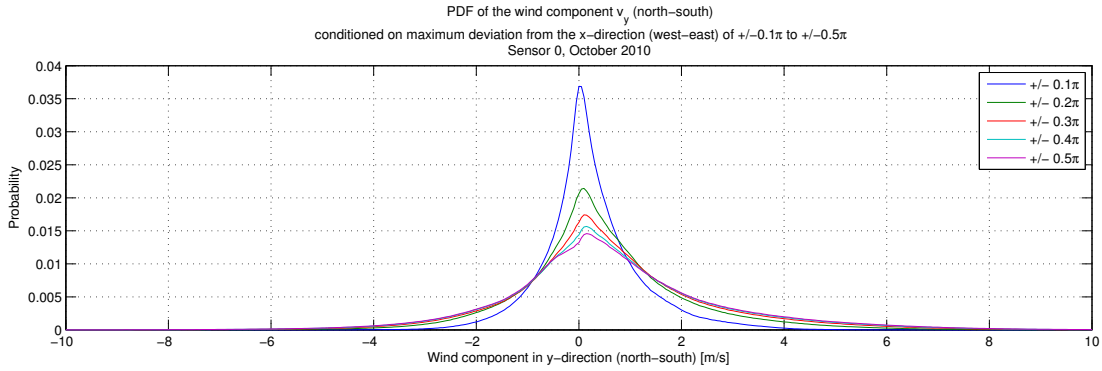
PDF of the wind component v_y (north−south)
conditioned on maximum deviation from the x−direction (west−east) of +/−0.1π to +/−0.5π
Sensor 0, October 2010
Probability
Wind component in y−direction (north−south) [m/s]
+/− 0.1π
+/− 0.2π
+/− 0.3π
+/− 0.4π
+/− 0.5π

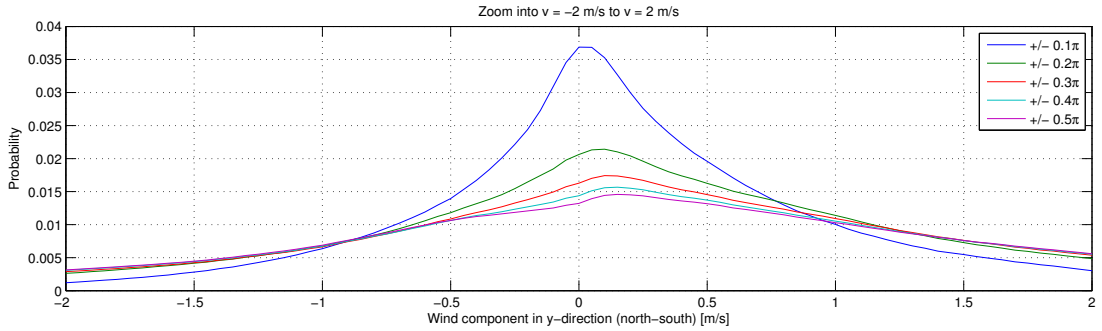
Zoom into v = −2 m/s to v = 2 m/s
Probability
Wind component in y−direction (north−south) [m/s]
+/− 0.1π
+/− 0.2π
+/− 0.3π
+/− 0.4π
+/− 0.5π

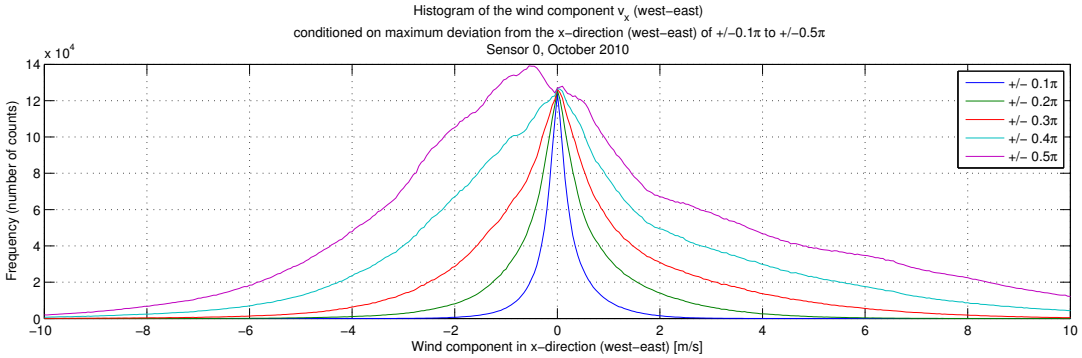
Histogram of the wind component v_x (west−east)
conditioned on maximum deviation from the x−direction (west−east) of +/−0.1π to +/−0.5π
Sensor 0, October 2010
x 10^4
Frequency (number of counts)
Wind component in x−direction (west−east) [m/s]
+/− 0.1π
+/− 0.2π
+/− 0.3π
+/− 0.4π
+/− 0.5π

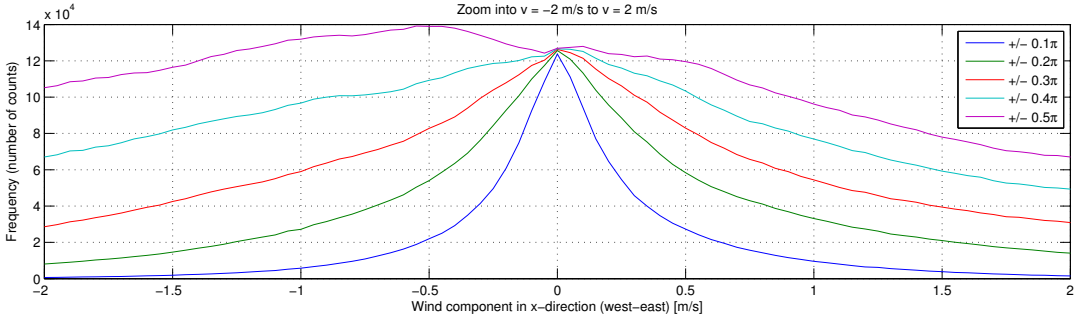
Zoom into v = −2 m/s to v = 2 m/s
x 10^4
Frequency (number of counts)
Wind component in x−direction (west−east) [m/s]
+/− 0.1π
+/− 0.2π
+/− 0.3π
+/− 0.4π
+/− 0.5π

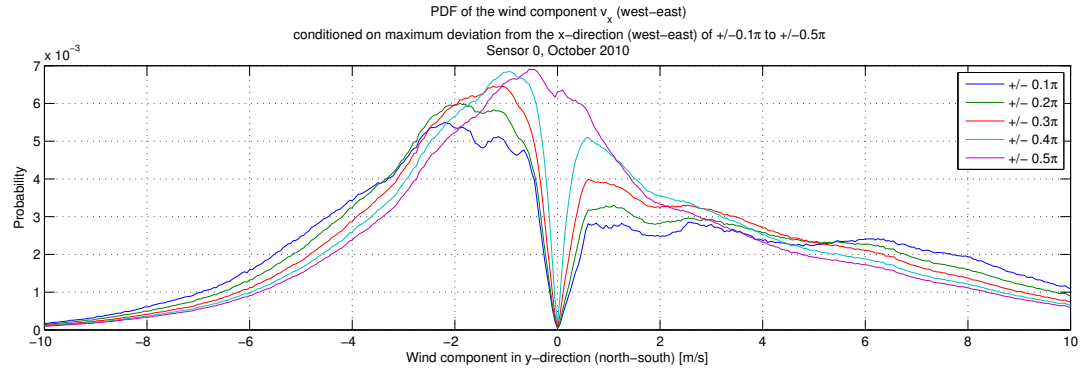
PDF of the wind component v_x (west−east)
conditioned on maximum deviation from the x−direction (west−east) of +/−0.1π to +/−0.5π
Sensor 0, October 2010
x 10^−3
Probability
Wind component in y−direction (north−south) [m/s]
+/− 0.1π
+/− 0.2π
+/− 0.3π
+/− 0.4π
+/− 0.5π

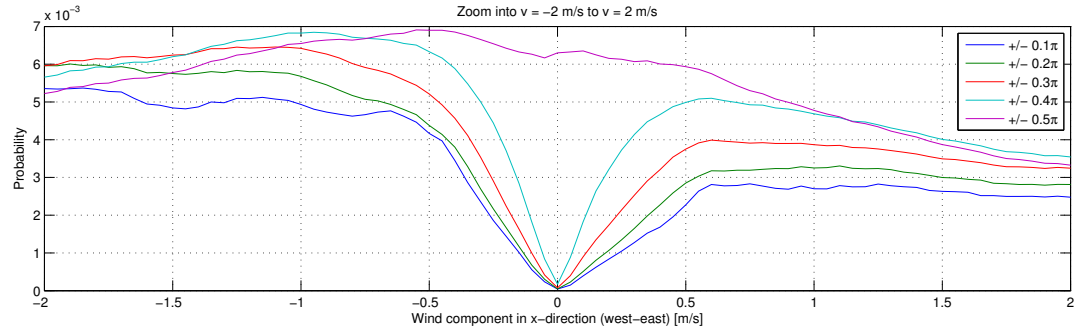
Zoom into v = −2 m/s to v = 2 m/s
x 10^−3
Probability
Wind component in x−direction (west−east) [m/s]
+/− 0.1π
+/− 0.2π
+/− 0.3π
+/− 0.4π
+/− 0.5π

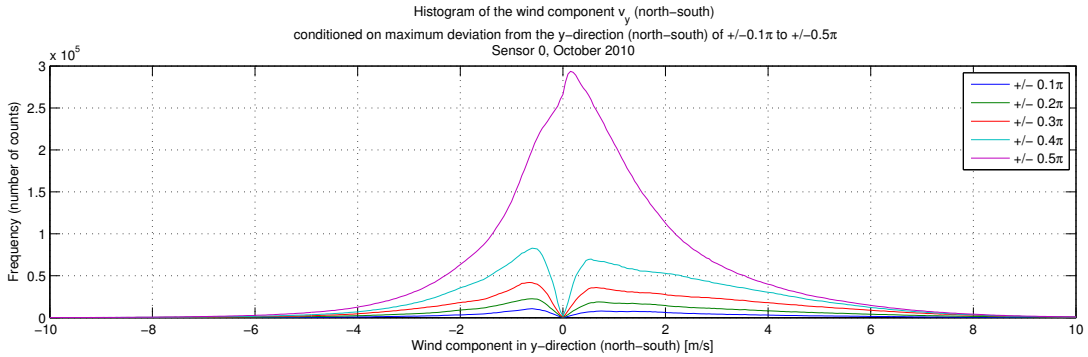
Histogram of the wind component v_y (north−south)
conditioned on maximum deviation from the y−direction (north−south) of +/−0.1π to +/−0.5π
Sensor 0, October 2010
x 10^5
Frequency (number of counts)
Wind component in y−direction (north−south) [m/s]
+/− 0.1π
+/− 0.2π
+/− 0.3π
+/− 0.4π
+/− 0.5π

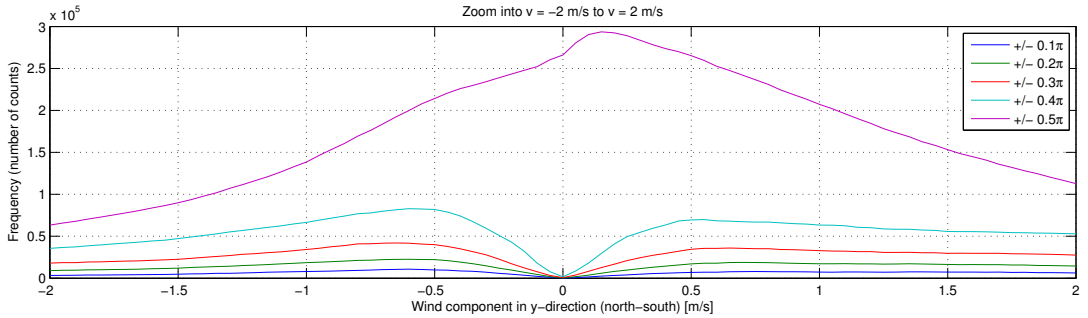
Zoom into v = −2 m/s to v = 2 m/s
x 10^5
Frequency (number of counts)
Wind component in y−direction (north−south) [m/s]
+/− 0.1π
+/− 0.2π
+/− 0.3π
+/− 0.4π
+/− 0.5π

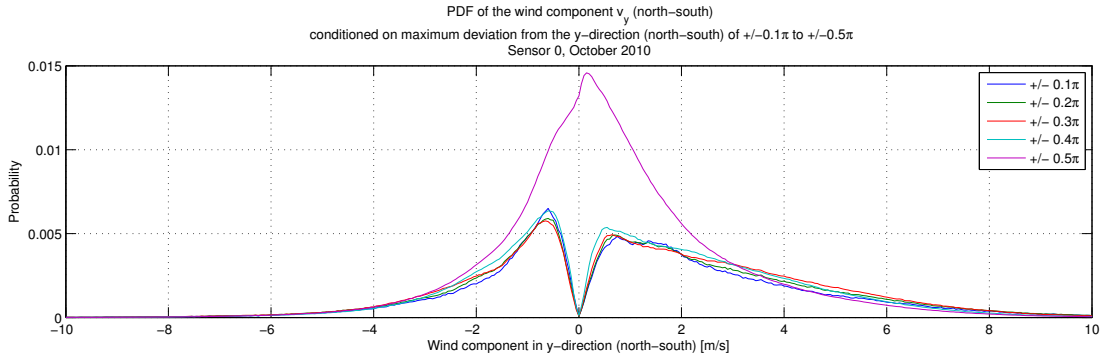
PDF of the wind component v_y (north−south)
conditioned on maximum deviation from the y−direction (north−south) of +/−0.1π to +/−0.5π
Sensor 0, October 2010
Probability
Wind component in y−direction (north−south) [m/s]
+/− 0.1π
+/− 0.2π
+/− 0.3π
+/− 0.4π
+/− 0.5π

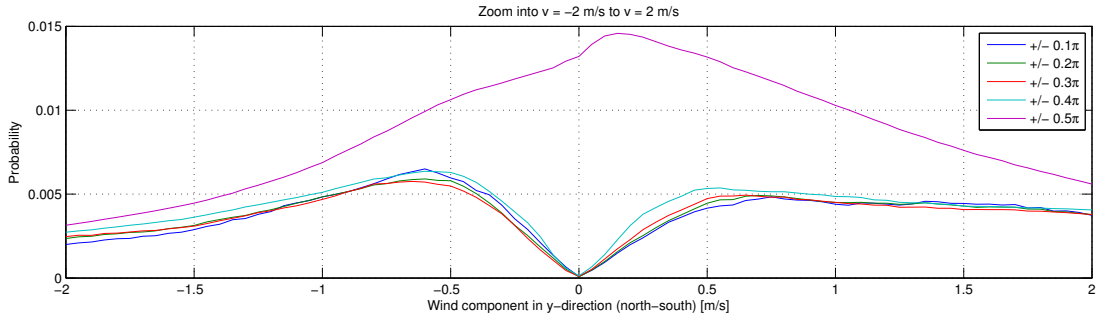
Zoom into v = −2 m/s to v = 2 m/s
Probability
Wind component in y−direction (north−south) [m/s]
+/− 0.1π
+/− 0.2π
+/− 0.3π
+/− 0.4π
+/− 0.5π

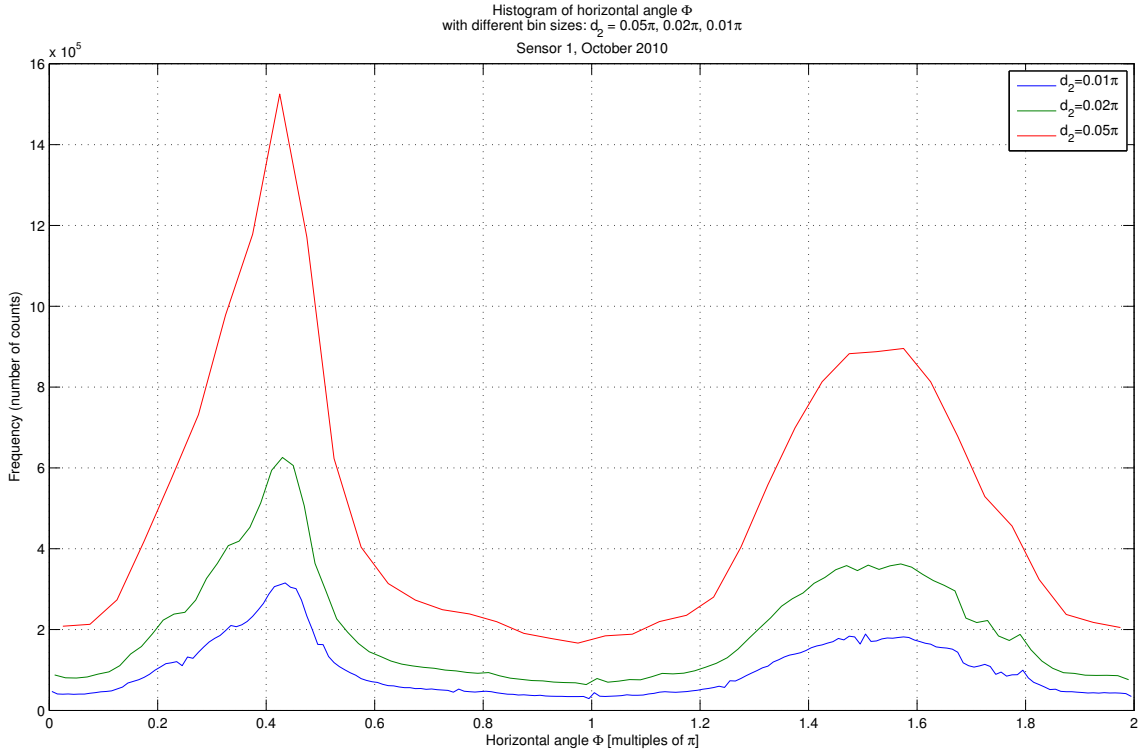
Histogram of horizontal angle Φ
with different bin sizes: d2 = 0.05π, 0.02π, 0.01π
Sensor 1, October 2010
x 10^5
Frequency (number of counts)
Horizontal angle Φ [multiples of π]
d2=0.01π
d2=0.02π
d2=0.05π

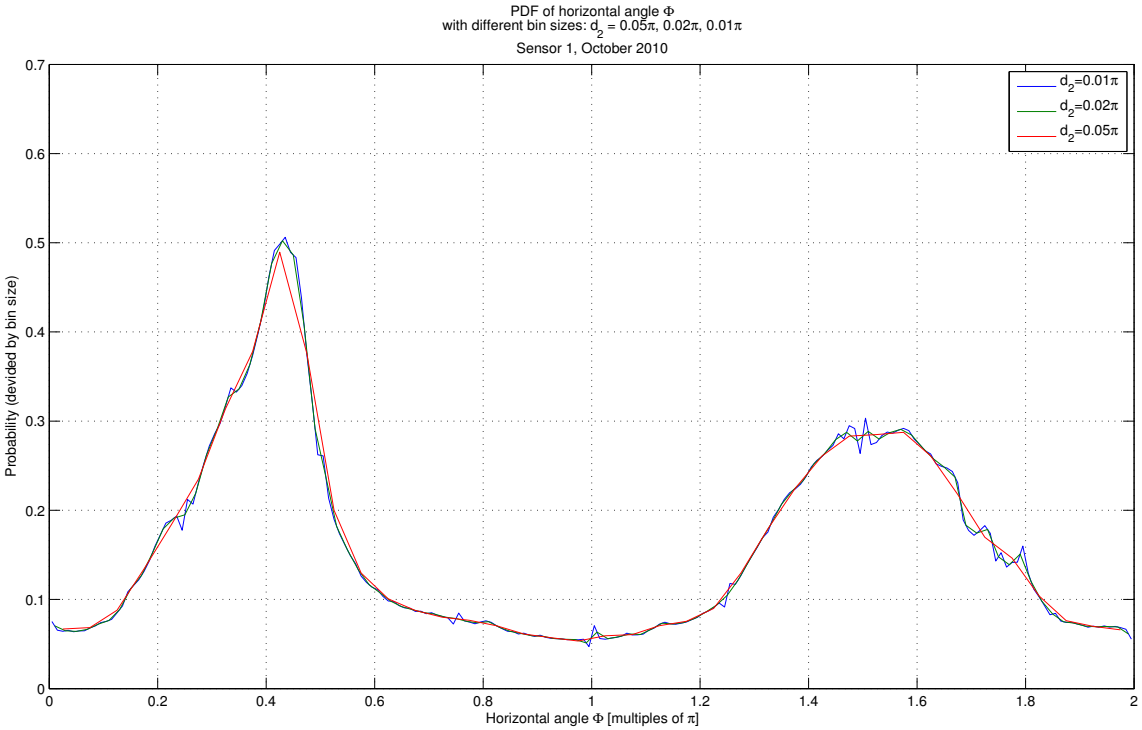
PDF of horizontal angle Φ
with different bin sizes: d2 = 0.05π, 0.02π, 0.01π
Sensor 1, October 2010
Probability (devided by bin size)
Horizontal angle Φ [multiples of π]
d2=0.01π
d2=0.02π
d2=0.05π

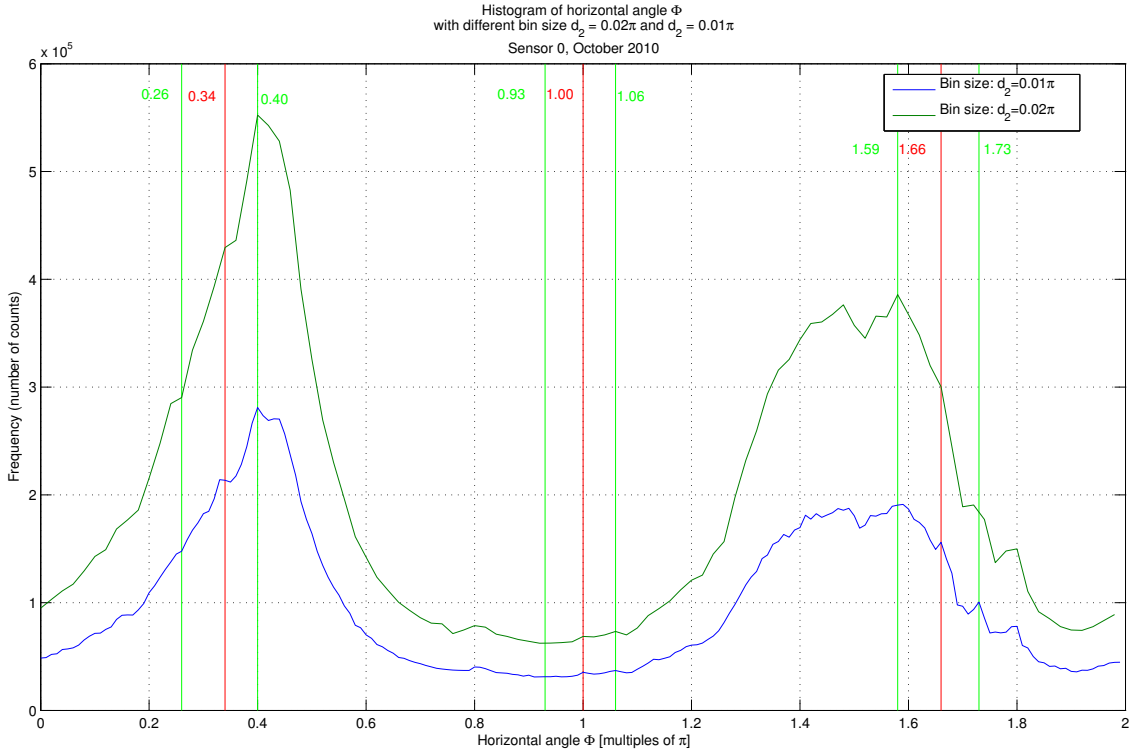
Histogram of horizontal angle Φ
with different bin size d2 = 0.02π and d2 = 0.01π
Sensor 0, October 2010
x 10^5
Frequency (number of counts)
Horizontal angle Φ [multiples of π]
Bin size: d2=0.01π
Bin size: d2=0.02π
0.26
0.34
0.40
0.93
1.00
1.06
1.59
1.66
1.73

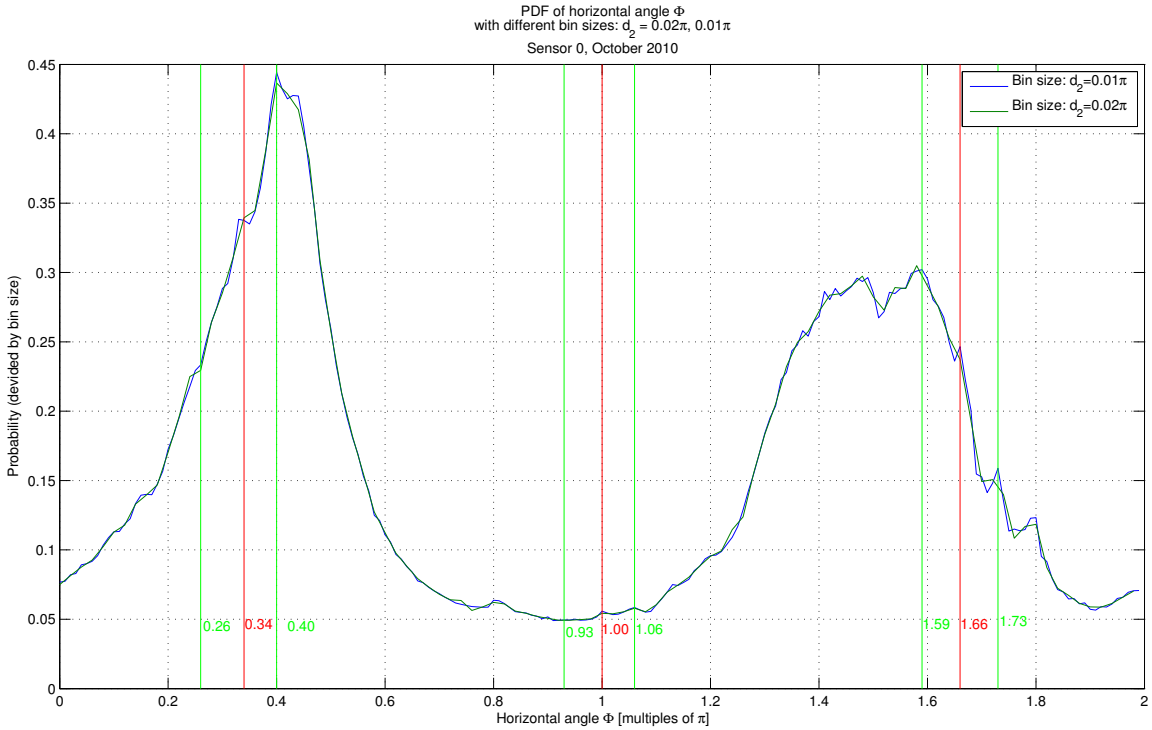
PDF of horizontal angle Φ
with different bin sizes: d2 = 0.02π, 0.01π
Sensor 0, October 2010
Probability (devided by bin size)
Horizontal angle Φ [multiples of π]
Bin size: d2=0.01π
Bin size: d2=0.02π
0.26
0.34
0.40
0.93
1.00
1.06
1.59
1.66
1.73

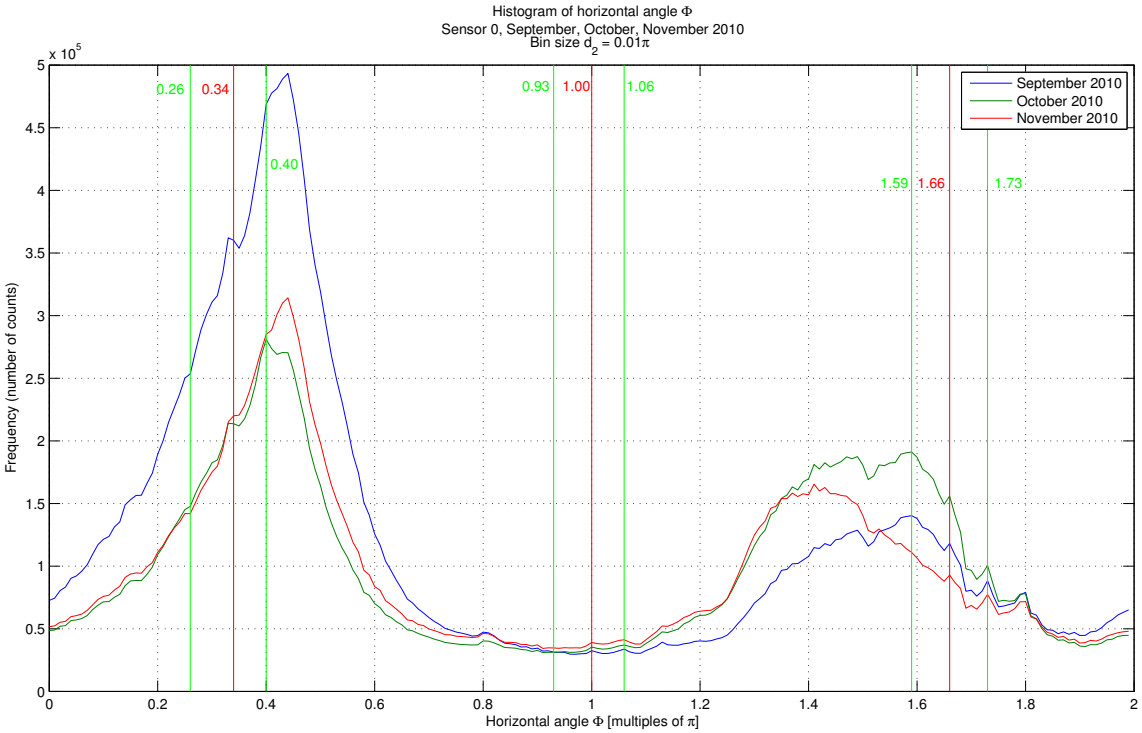
Histogram of horizontal angle Φ
Sensor 0, September, October, November 2010
Bin size d2 = 0.01π
x 10^5
Frequency (number of counts)
Horizontal angle Φ [multiples of π]
September 2010
October 2010
November 2010
0.26
0.34
0.40
0.93
1.00
1.06
1.59
1.66
1.73

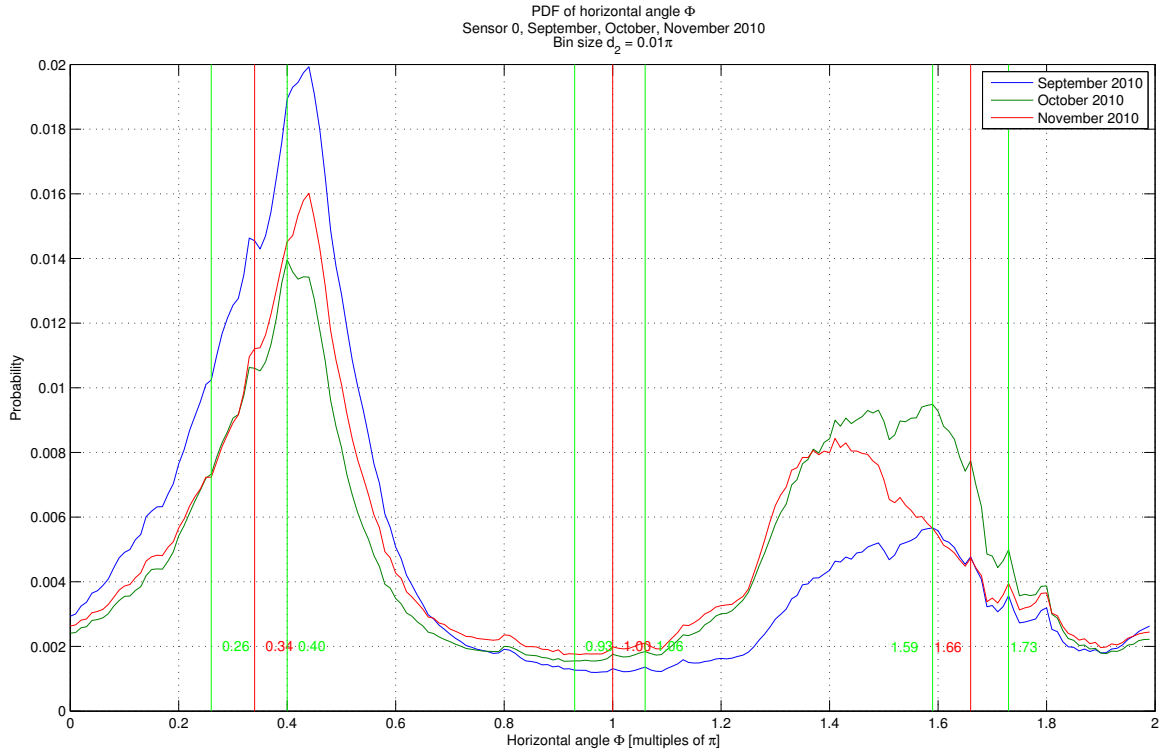
PDF of horizontal angle Φ
Sensor 0, September, October, November 2010
Bin size d2 = 0.01π
Probability
Horizontal angle Φ [multiples of π]
September 2010
October 2010
November 2010
0.26
0.34
0.40
0.93
1.00
1.06
1.59
1.66
1.73

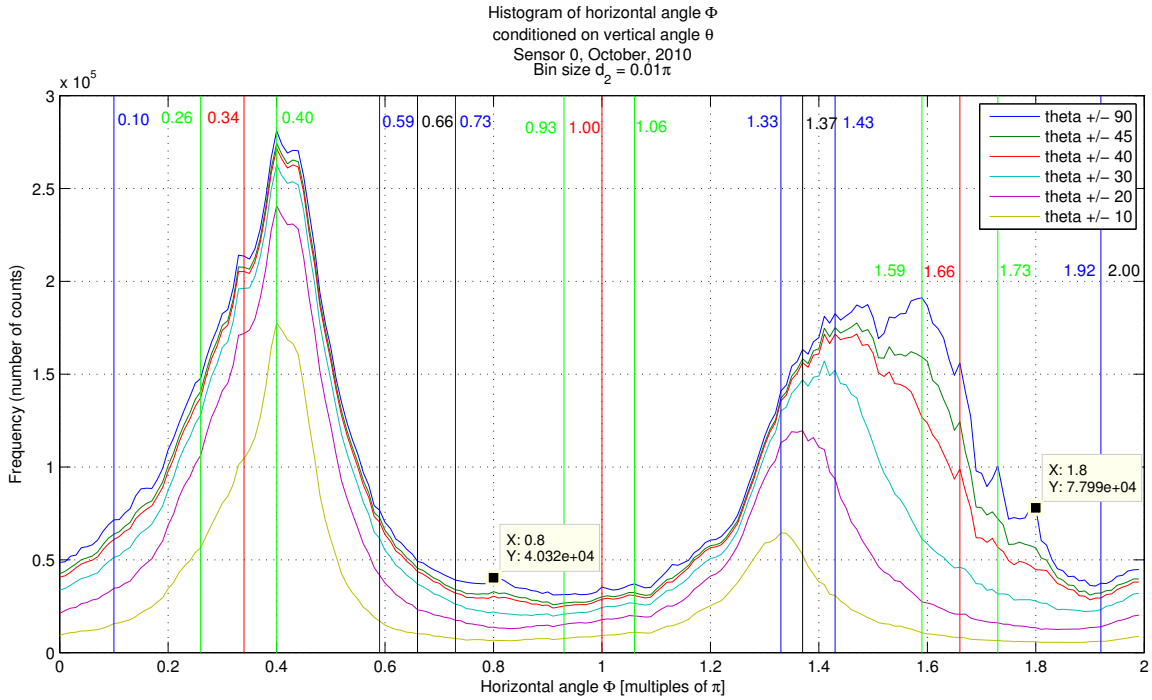
Histogram of horizontal angle Φ
conditioned on vertical angle θ
Sensor 0, October, 2010
Bin size d2 = 0.01π
x 10^5
Frequency (number of counts)
Horizontal angle Φ [multiples of π]
theta +/– 90
theta +/– 45
theta +/– 40
theta +/– 30
theta +/– 20
theta +/– 10
0.10 0.26 0.34 0.40 0.59 0.66 0.73 0.93 1.00 1.06 1.33 1.37 1.43
1.59 1.66 1.73 1.92 2.00
X: 0.8
Y: 4.032e+04
X: 1.8
Y: 7.799e+04

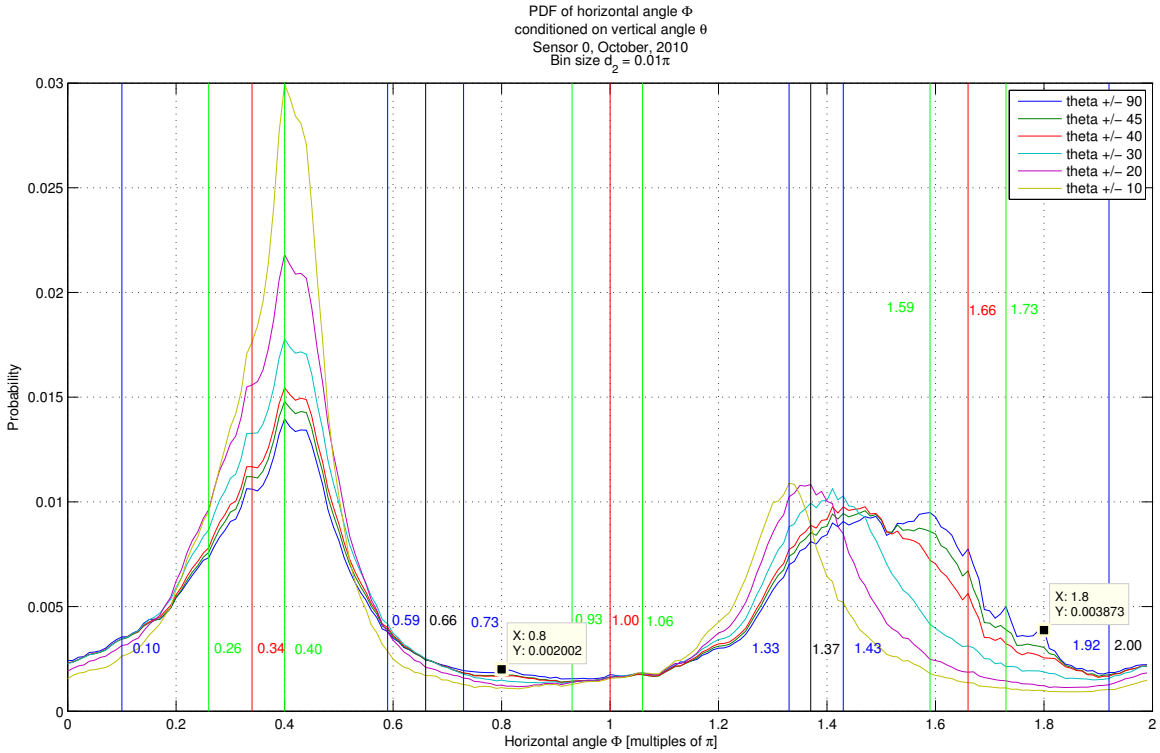
PDF of horizontal angle Φ
conditioned on vertical angle θ
Sensor 0, October, 2010
Bin size d2 = 0.01π
Probability
Horizontal angle Φ [multiples of π]
theta +/– 90
theta +/– 45
theta +/– 40
theta +/– 30
theta +/– 20
theta +/– 10
0.10 0.26 0.34 0.40 0.59 0.66 0.73 0.93 1.00 1.06 1.33 1.37 1.43
1.59 1.66 1.73 1.92 2.00
X: 0.8
Y: 0.002002
X: 1.8
Y: 0.003873

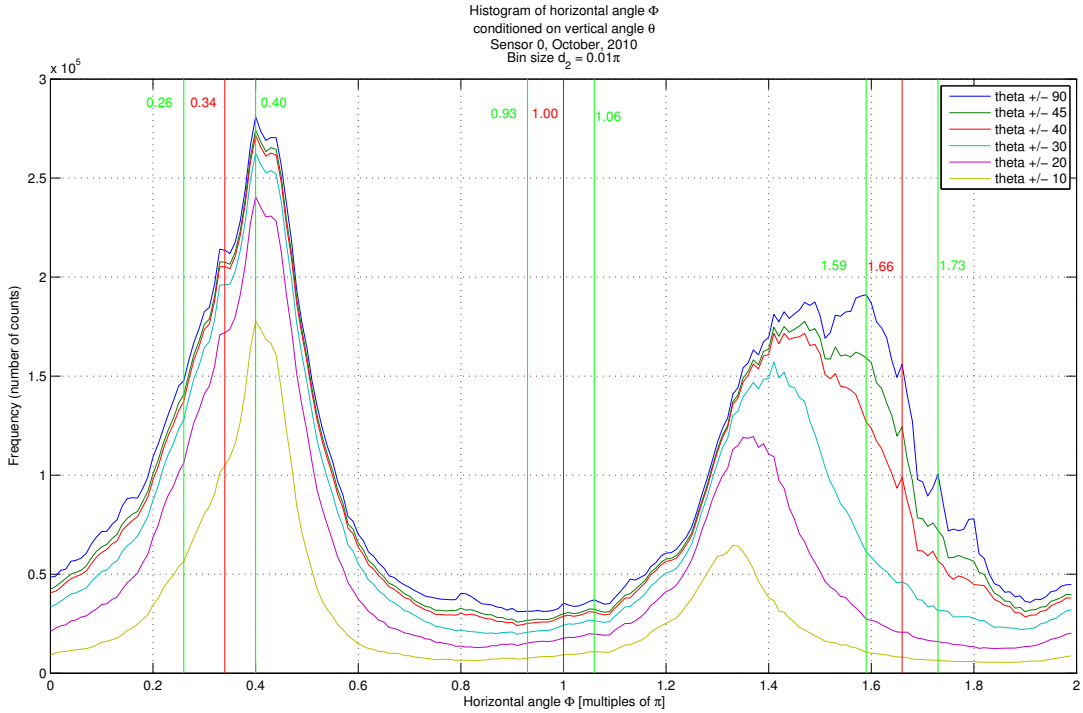
Histogram of horizontal angle Φ
conditioned on vertical angle θ
Sensor 0, October, 2010
Bin size d2 = 0.01π
x 10^5
Frequency (number of counts)
Horizontal angle Φ [multiples of π]
0.26
0.34
0.40
0.93
1.00
1.06
1.59
1.66
1.73
theta +/– 90
theta +/– 45
theta +/– 40
theta +/– 30
theta +/– 20
theta +/– 10

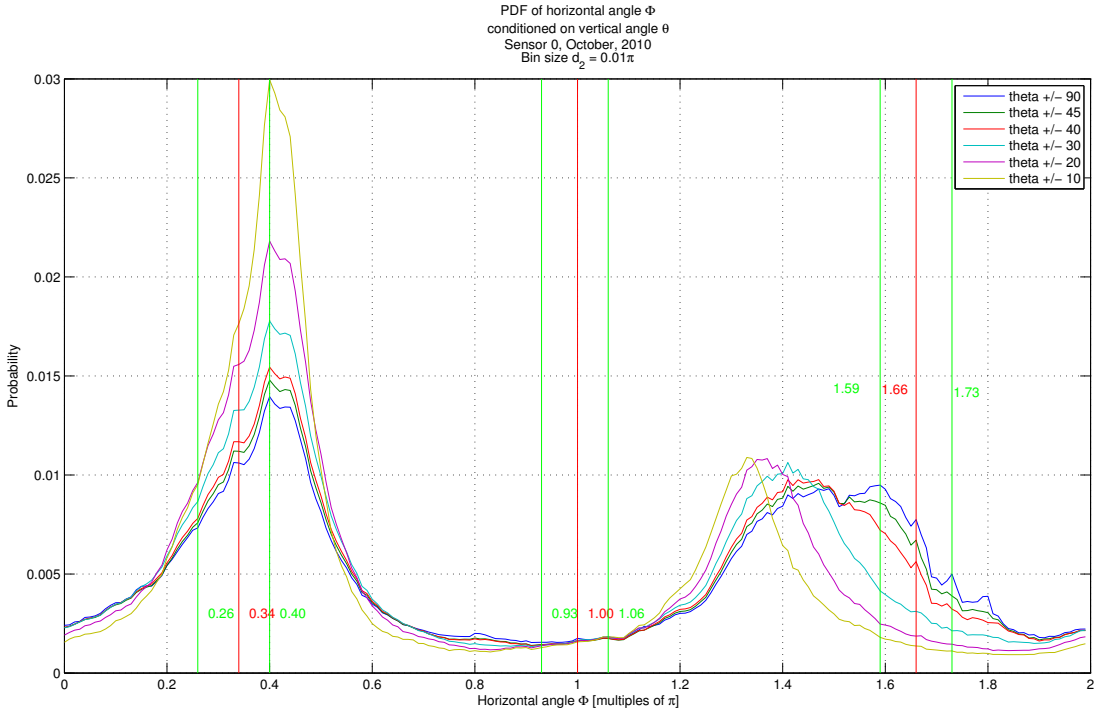
PDF of horizontal angle Φ
conditioned on vertical angle θ
Sensor 0, October, 2010
Bin size d2 = 0.01π
Probability
Horizontal angle Φ [multiples of π]
0.26
0.34
0.40
0.93
1.00
1.06
1.59
1.66
1.73
theta +/– 90
theta +/– 45
theta +/– 40
theta +/– 30
theta +/– 20
theta +/– 10

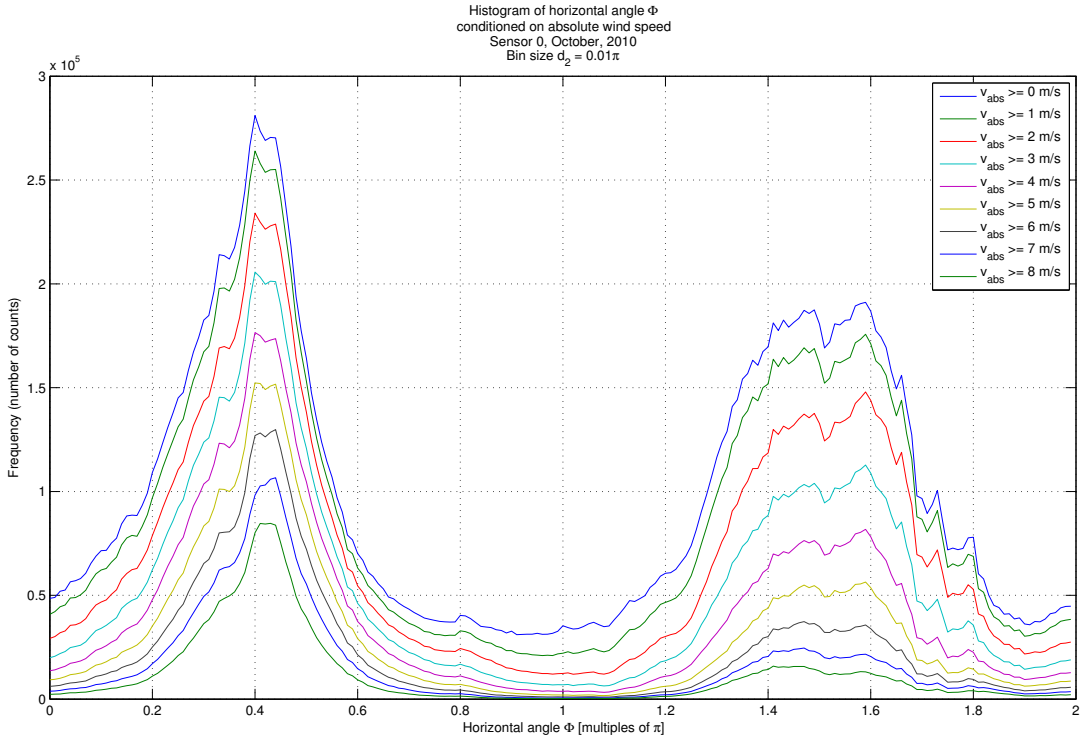
Histogram of horizontal angle Φ
conditioned on absolute wind speed
Sensor 0, October, 2010
Bin size d2 = 0.01π
x 10^5
Frequency (number of counts)
Horizontal angle Φ [multiples of π]
v_abs >= 0 m/s
v_abs >= 1 m/s
v_abs >= 2 m/s
v_abs >= 3 m/s
v_abs >= 4 m/s
v_abs >= 5 m/s
v_abs >= 6 m/s
v_abs >= 7 m/s
v_abs >= 8 m/s

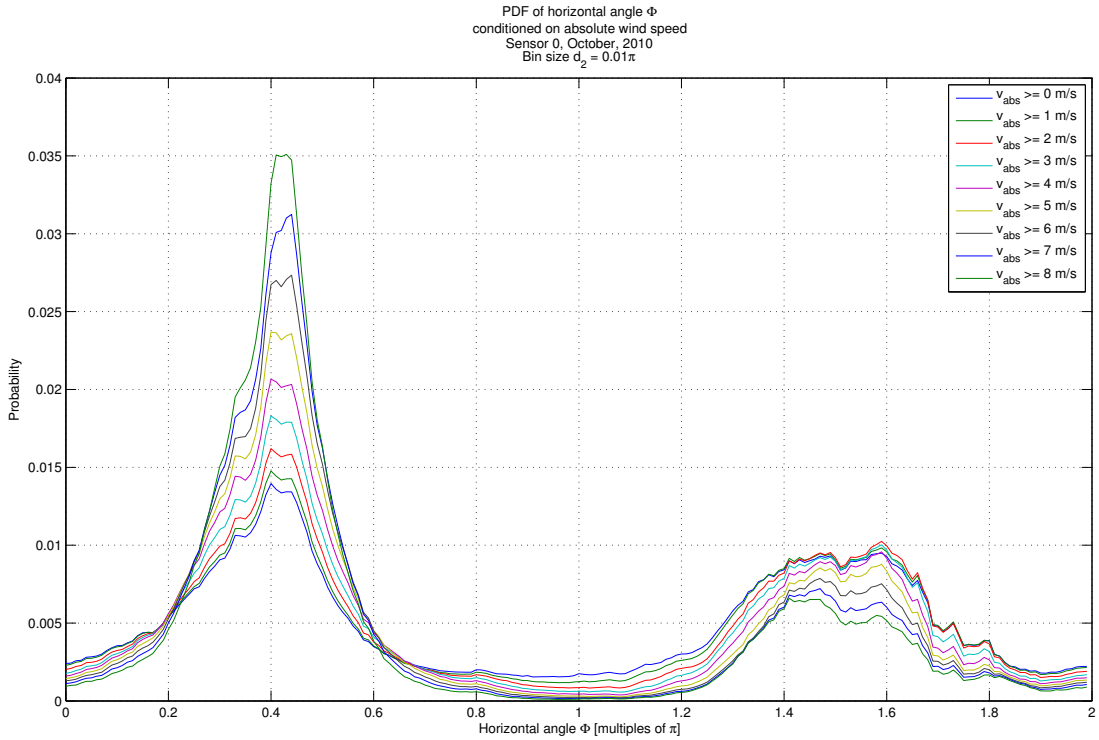
PDF of horizontal angle Φ
conditioned on absolute wind speed
Sensor 0, October, 2010
Bin size d2 = 0.01π
Probability
Horizontal angle Φ [multiples of π]
v_abs >= 0 m/s
v_abs >= 1 m/s
v_abs >= 2 m/s
v_abs >= 3 m/s
v_abs >= 4 m/s
v_abs >= 5 m/s
v_abs >= 6 m/s
v_abs >= 7 m/s
v_abs >= 8 m/s

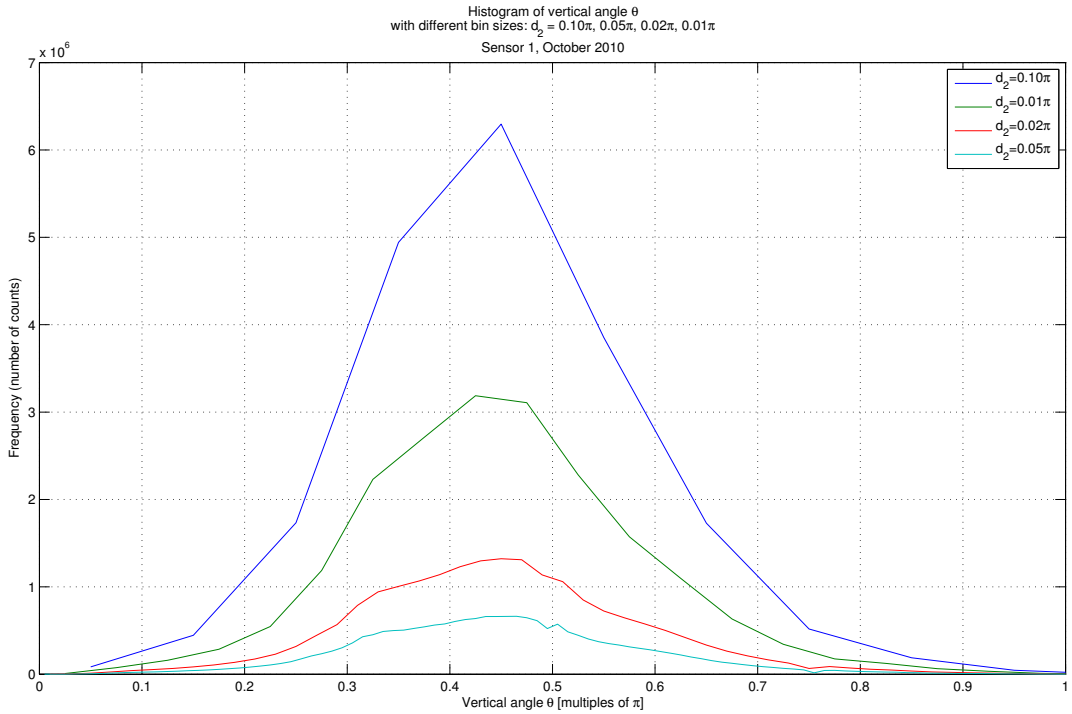
Histogram of vertical angle θ
with different bin sizes: d2 = 0.10π, 0.05π, 0.02π, 0.01π
Sensor 1, October 2010
x 10^6
Frequency (number of counts)
Vertical angle θ [multiples of π]
d2=0.10π
d2=0.01π
d2=0.02π
d2=0.05π

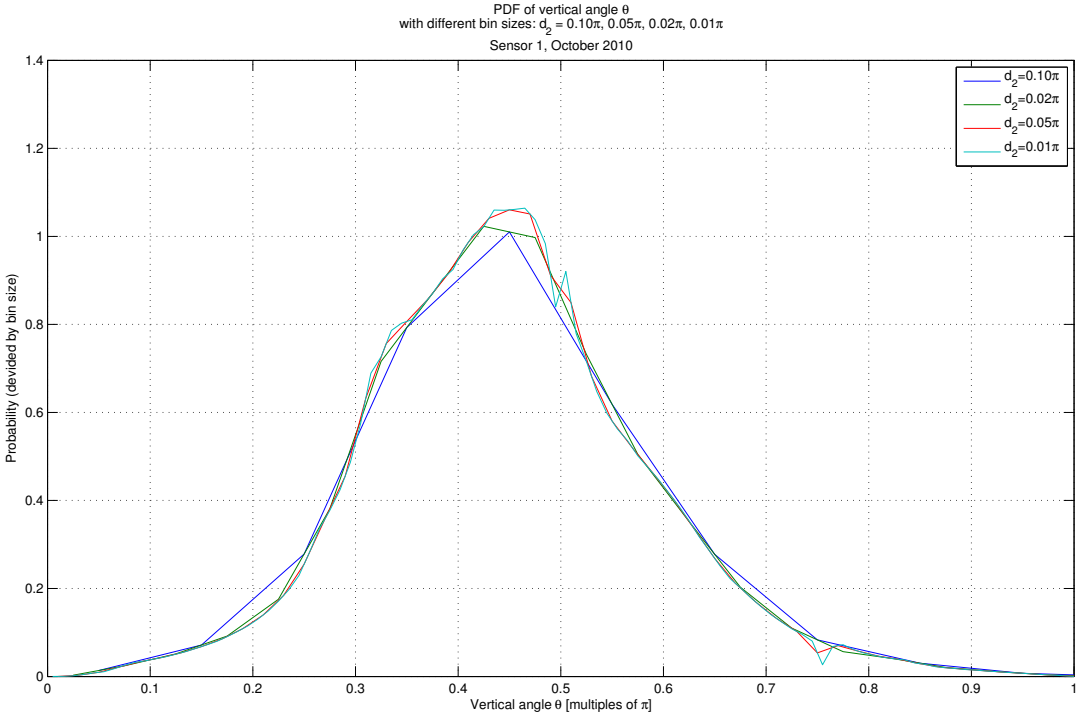
PDF of vertical angle θ
with different bin sizes: d2 = 0.10π, 0.05π, 0.02π, 0.01π
Sensor 1, October 2010
Probability (devided by bin size)
Vertical angle θ [multiples of π]
d2=0.10π
d2=0.02π
d2=0.05π
d2=0.01π

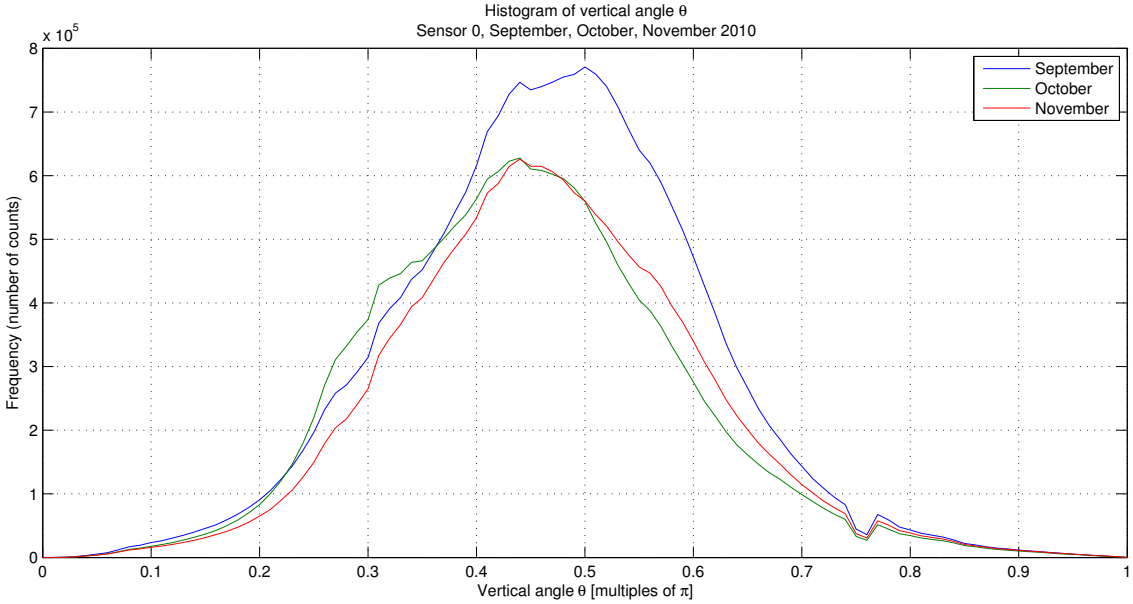
Histogram of vertical angle θ
Sensor 0, September, October, November 2010
x 10^5
Frequency (number of counts)
Vertical angle θ [multiples of π]
September
October
November

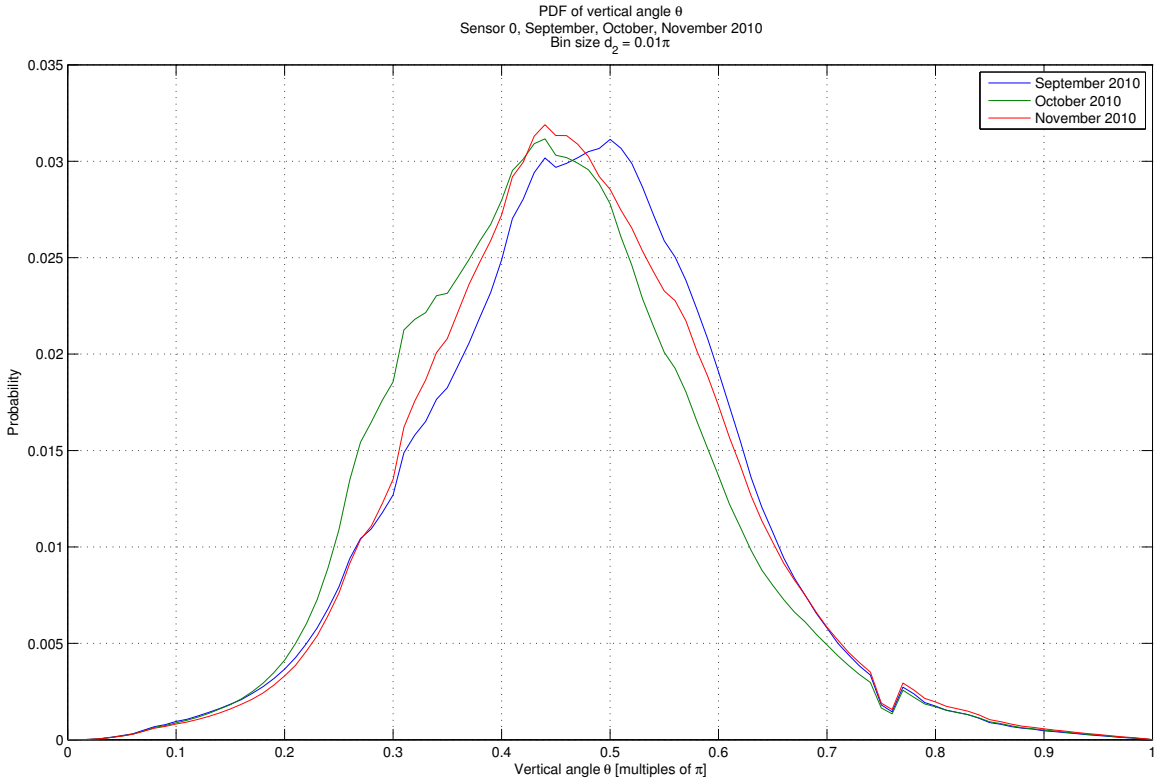
PDF of vertical angle θ
Sensor 0, September, October, November 2010
Bin size d2 = 0.01π
Probability
Vertical angle θ [multiples of π]
September 2010
October 2010
November 2010

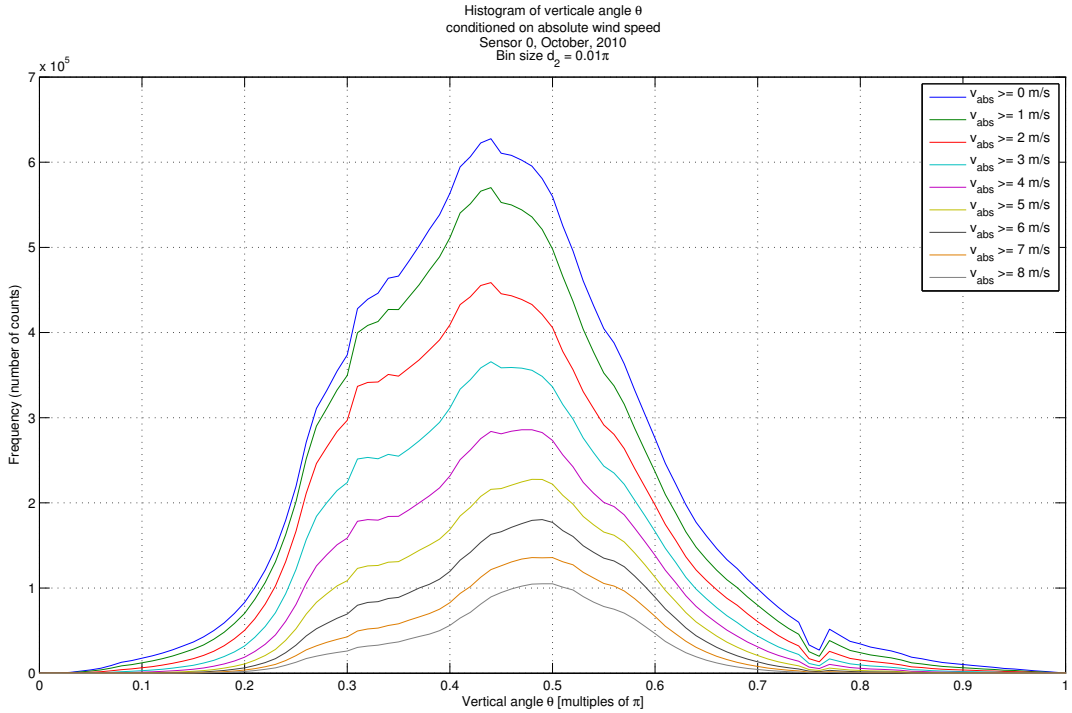
Histogram of verticale angle θ
conditioned on absolute wind speed
Sensor 0, October, 2010
Bin size d2 = 0.01π
x 10^5
Frequency (number of counts)
Vertical angle θ [multiples of π]
v_abs >= 0 m/s
v_abs >= 1 m/s
v_abs >= 2 m/s
v_abs >= 3 m/s
v_abs >= 4 m/s
v_abs >= 5 m/s
v_abs >= 6 m/s
v_abs >= 7 m/s
v_abs >= 8 m/s

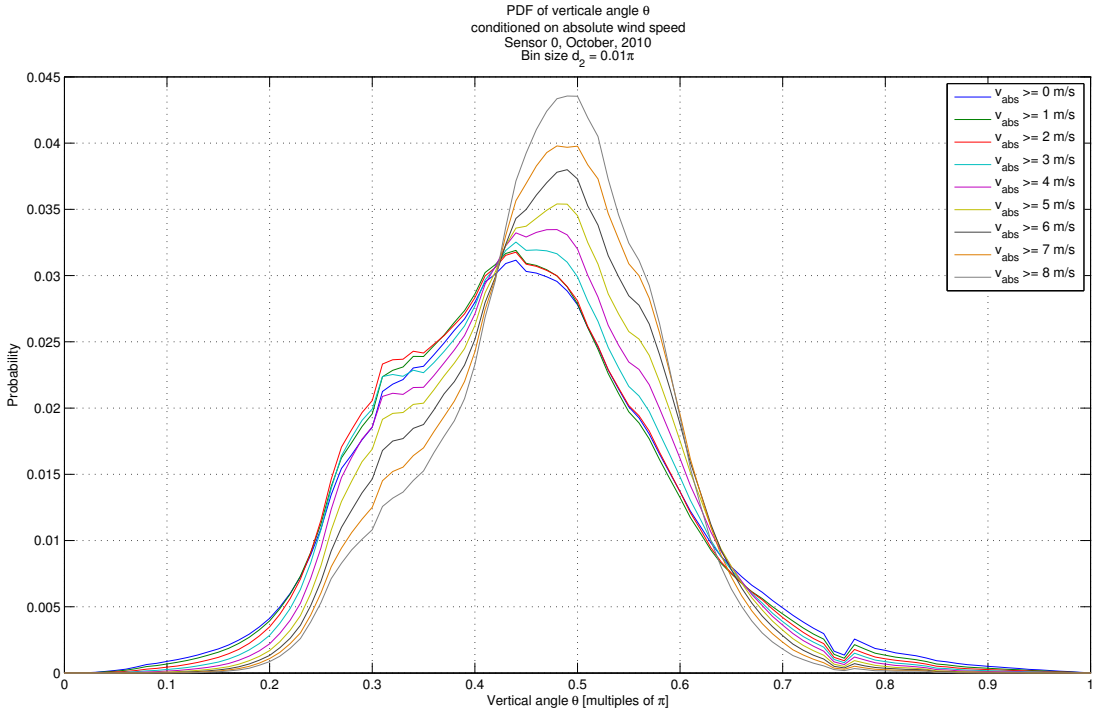
PDF of verticale angle θ
conditioned on absolute wind speed
Sensor 0, October, 2010
Bin size d2 = 0.01π
Probability
Vertical angle θ [multiples of π]
v_abs >= 0 m/s
v_abs >= 1 m/s
v_abs >= 2 m/s
v_abs >= 3 m/s
v_abs >= 4 m/s
v_abs >= 5 m/s
v_abs >= 6 m/s
v_abs >= 7 m/s
v_abs >= 8 m/s

B Large scale flow properties in 2011

This appendix reports the large scale flow properties in 2011. The measurements were taken with the top anemometer of the measurement mast, which was continuously running at 10 Hz. The results are presented in the form of three sections for (1) the horizontal angle, (2) the vertical angle and (3) the absolute wind speed. For a good visibility of the graphs the data from three months are shown in one plot. The conventions of the wind directions are the same as used above.

The plots show that the wind conditions are relatively constant throughout the year. The flow is always oriented along the east-west direction and mostly horizontal. During the summer, east winds ($\Phi = \pi/2$) are found more frequently than west winds ($\Phi = 3\pi/2$). During the rest of the year, the probability for both directions tends to be the same. Wind from below the measurement site ($\theta < \pi/2$) appears to be slightly more frequent than wind from above ($\theta > \pi/2$). The average wind speed is about 4 m/s throughout the year. The highest wind speeds are found in December, when the average reaches about 5.4 m/s.

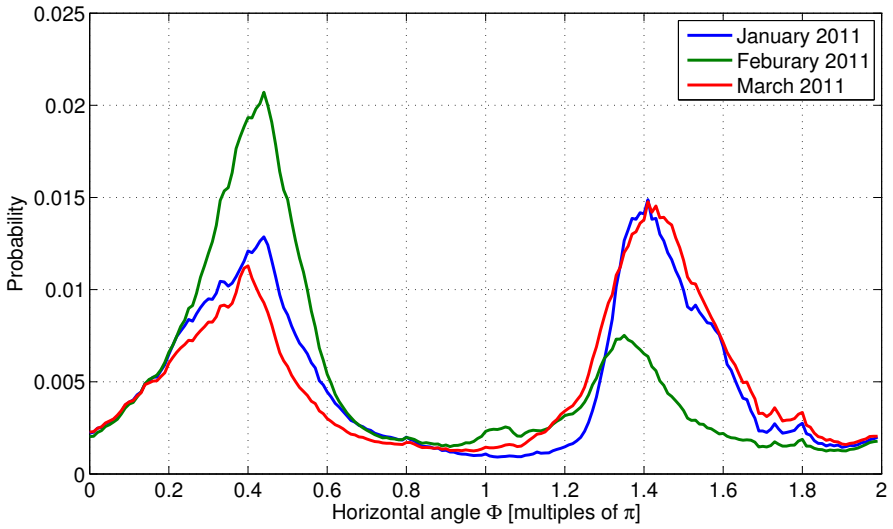

Figure B.1: PDF of the wind direction as a function of the horizontal angle Φ from January to March 2011.

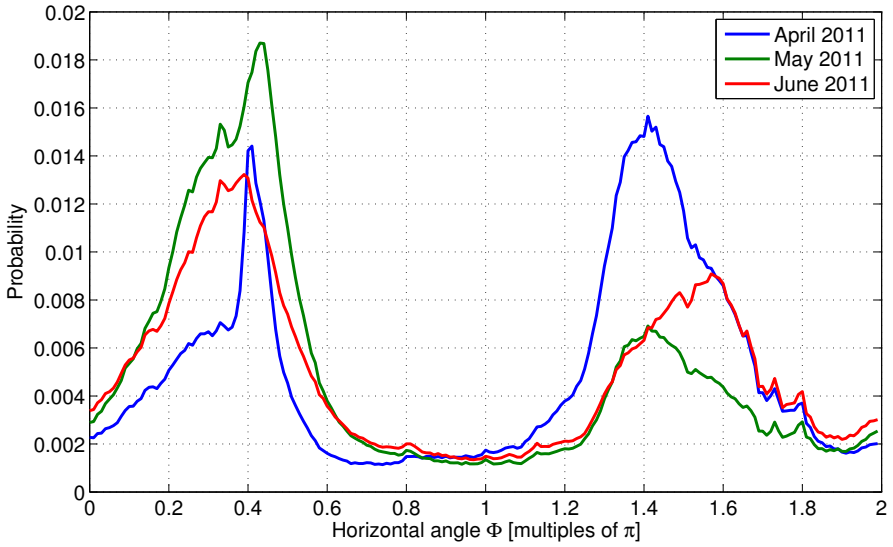

Figure B.2: PDF of the wind direction as a function of the horizontal angle Φ from April to June.

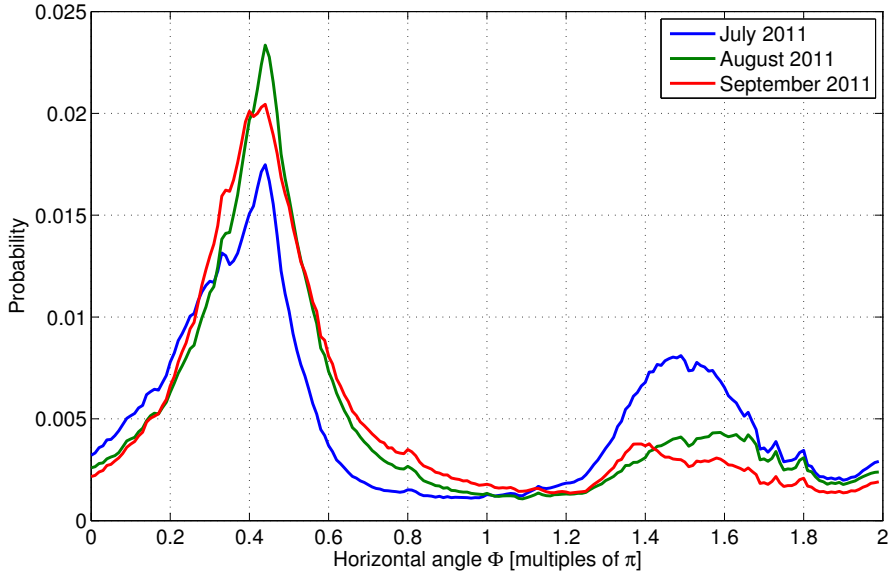

Figure B.3: PDF of the wind direction as a function of the horizontal angle Φ from July to September.

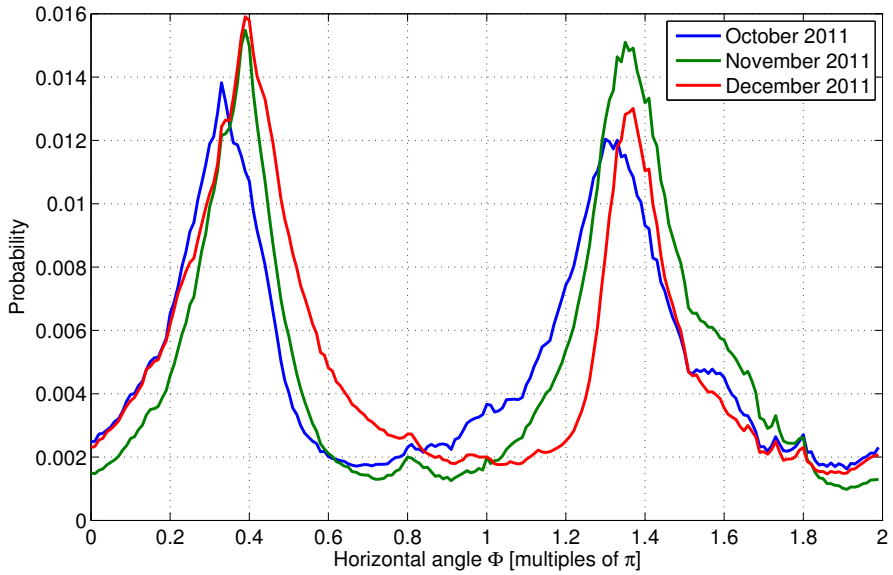

Figure B.4: PDF of the wind direction as a function of the horizontal angle Φ from October to November.

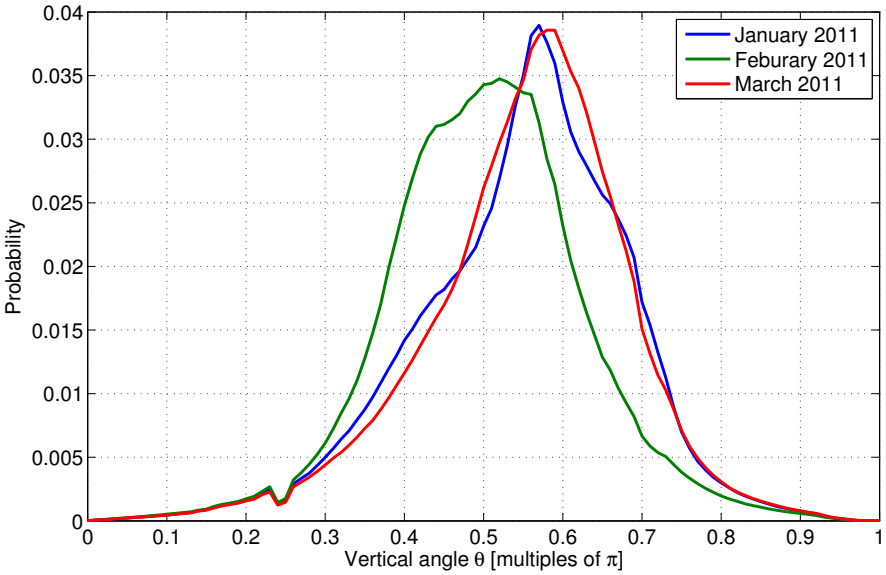

Figure B.5: PDF of the vertical angle θ from January to March.

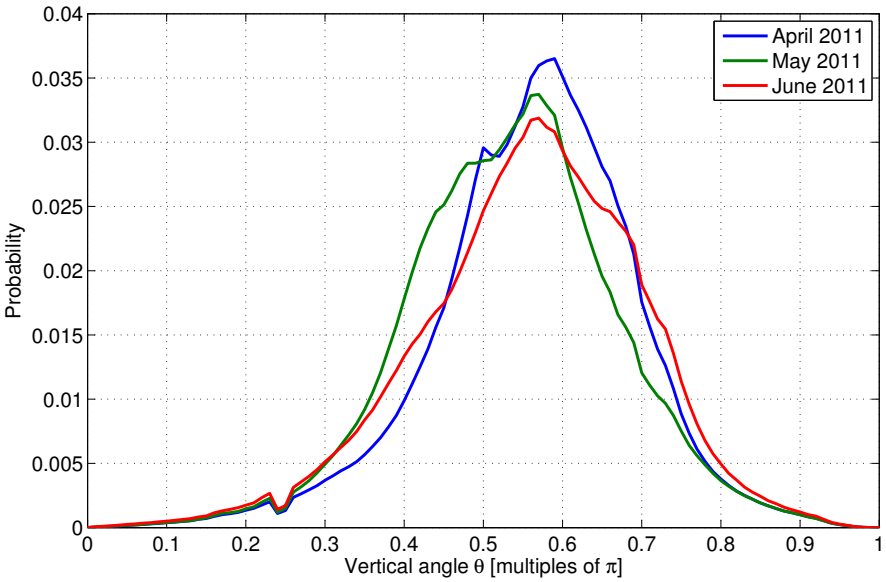

Figure B.6: PDF of the vertical angle θ from April to June.

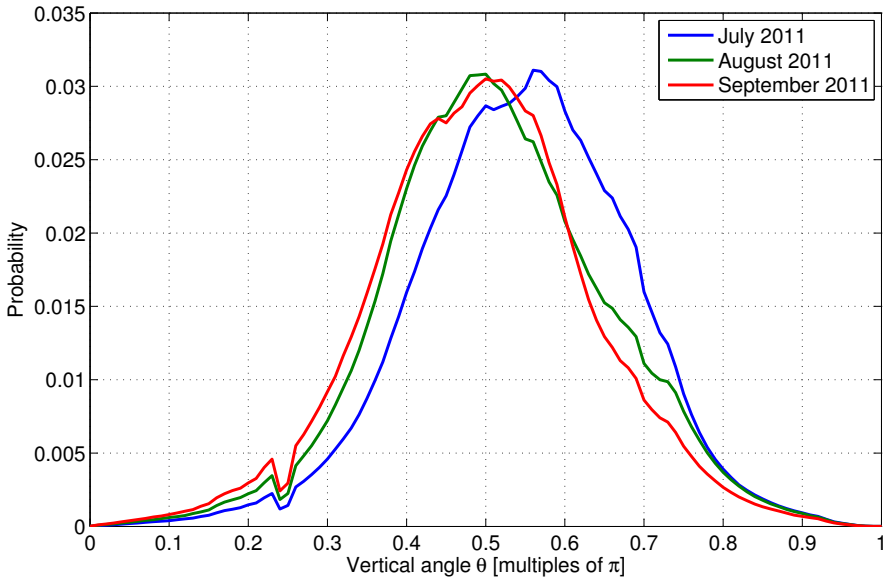

Figure B.7: PDF of the vertical angle θ from July to August.

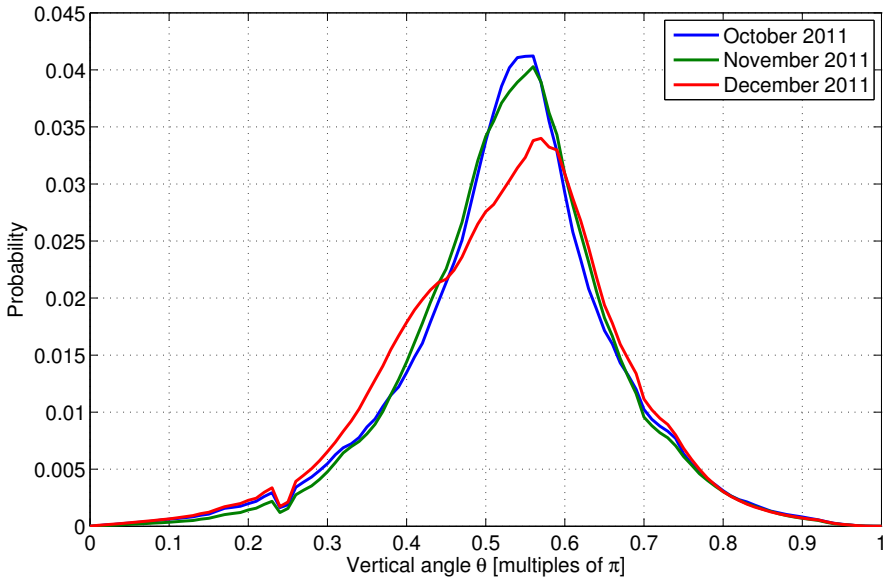

Figure B.8: PDF of the vertical angle θ from October to December.

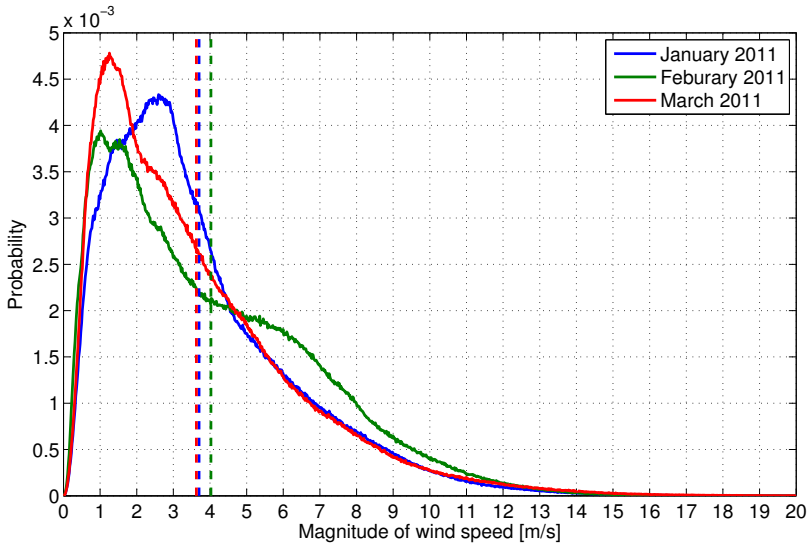

Figure B.9: PDF of the absolute wind speed v_{abs} from January to March.

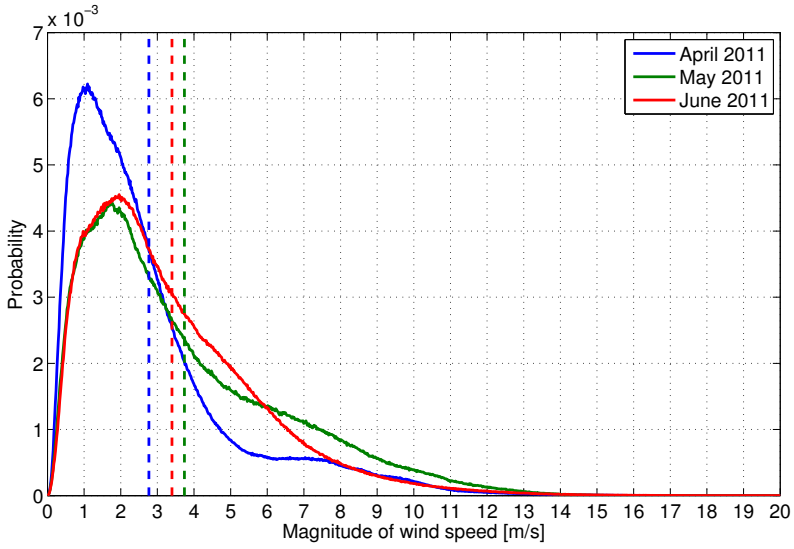

Figure B.10: PDF of the absolute wind speed v_{abs} from April to June.

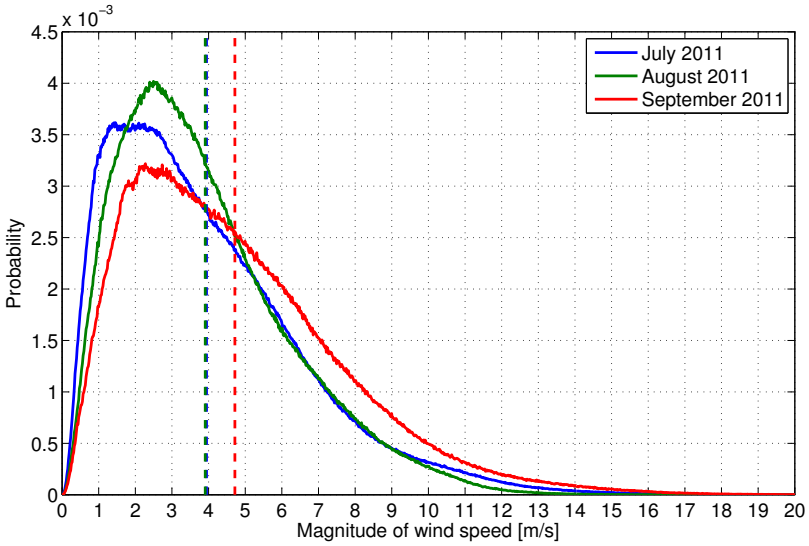

Figure B.11: PDF of the absolute wind speed v_{abs} from July to September.

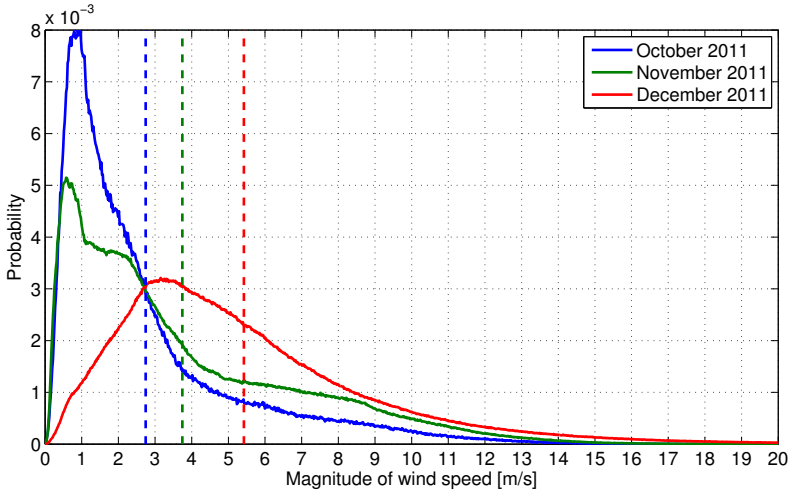

Figure B.12: PDF of the absolute wind speed v_{abs} from October to December.

C Distribution of turbulence parameters after averaging chunks of constant wind speed

This appendix shows an excerpt of PDFs of turbulence quantities, which were generated after the chunks of constant wind speed were averaged over different intervals. The averaging intervals presented here are $\Delta\Phi, \Delta\theta = 20°$, $\Delta v = 0.2$ m/s and $\Delta\Phi, \Delta\theta = 60°$, $\Delta v = 0.2$ m/s with at least five chunks being averaged. The conventions are the same as used above.

The PDFs show similar distributions as the PDFs of non-averaged chunks. The resolution of the PDFs is limited by the amount of intervals, which leads to a small variation in the results.

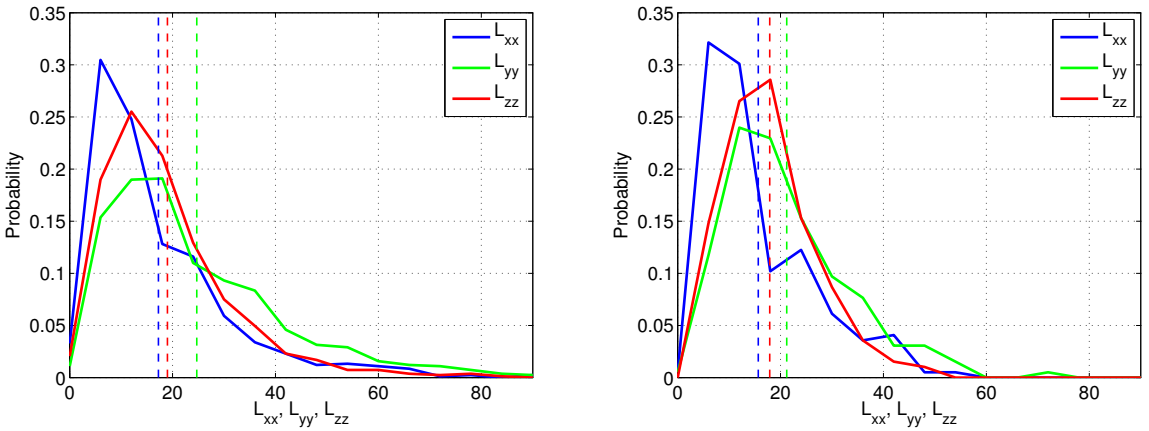

Figure C.1: PDFs of the integral length scales. Averaging intervals are $\Delta\Phi, \Delta\theta = 20°$, $\Delta v = 0.2$ m/s (left) and $\Delta\Phi, \Delta\theta = 60°$, $\Delta v = 0.2$ m/s with at least five chunks averaged (right).

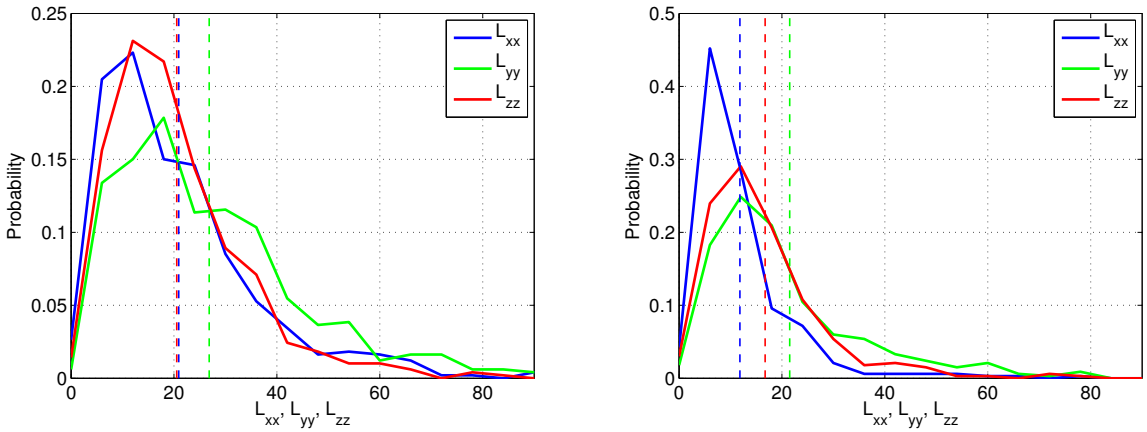

Figure C.2: PDFs of the integral length scales for wind coming from the west (left) and from the east (right). The averaging intervals are $\Delta\Phi, \Delta\theta = 20°$, $\Delta v = 0.2$ m/s.

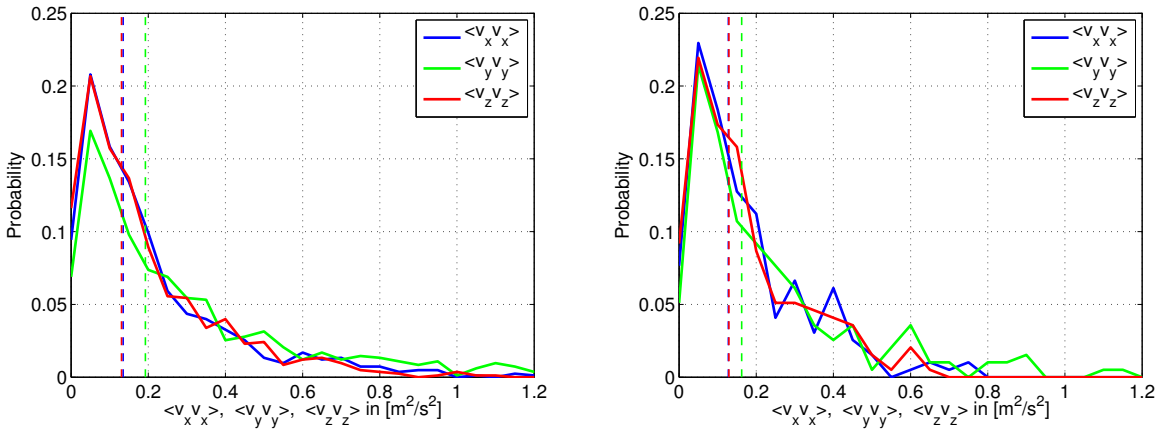

Figure C.3: PDFs of the isotropic components of the Reynolds stress tensor. Averaging intervals are $\Delta\Phi, \Delta\theta = 20°$, $\Delta v = 0.2$ m/s (left) and $\Delta\Phi, \Delta\theta = 60°$, $\Delta v = 0.2$ m/s with at least five chunks averaged (right).

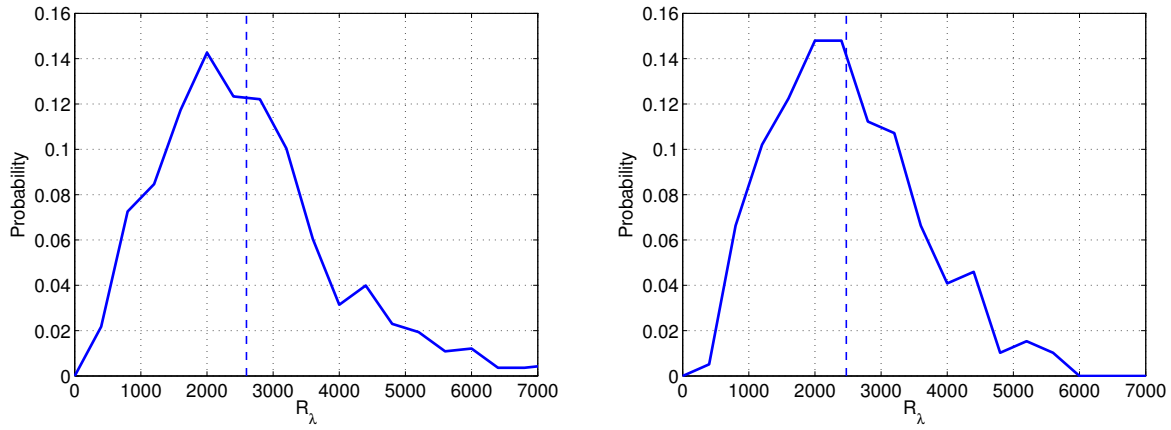

Figure C.4: PDFs of the Taylor scale Reynolds number. Averaging intervals are $\Delta\Phi, \Delta\theta = 20°$, $\Delta v = 0.2$ m/s (left) and $\Delta\Phi, \Delta\theta = 60°$, $\Delta v = 0.2$ m/s with at least five chunks averaged (right).

Bibliography

M. Arnold. *Empedocles On Etna And Other Poems*. Kessinger Publishing, LLC, 1852.

W. T. Ashurst, A. R. Kerstein, R. M. Kerr, and C. H. Gibson. Alignment of vorticity and scalar gradient with strain rate in simulated Navier–Stokes turbulence. *Physics of Fluids*, 30(8):2343–2353, 1987.

J. L. Balint, J. M. Wallace, and P. Vukoslavcevic. A study of the vortical structure of the turbulent boundary layer. *Advances in Turbulence*, 1:456–464, 1987.

D. Barstow. "Complex Beauty" - Too many, a...: Photography - photo.net, 2004. URL `http://photo.net/photodb/photo?photo_id=2092015`.

G. K. Batchelor. *An Introduction to Fluid Dynamics*. Cambridge University Press, 2000.

G. K. Batchelor and A. A. Townsend. The nature of turbulent motion at large wavenumbers. *Proceedings of the Royal Society of London. Series A. Mathematical and Physical Sciences*, 199(1057):238–255, 1949.

L. f. V. u. G. Bayern. Bayerische Alpen 08. Wettersteingebirge, Zugspitze 1:25000: Mit Wegmarkierungen und Skirouten, 2010.

D. Bibelgesellschaft. *Gute Nachricht Bibel (Today's German Bible)*. American Bible Society, 2001.

V. Borue and S. Orszag. Local energy flux and subgrid-scale statistics in three-dimensional turbulence. *Journal of Fluid Mechanics*, 366:1–31, 1998.

I. E. Britannica, editor. *Encyclopedia Britannica*. Encyclopedia Britannica Inc, 2003.

L. W. B. Browne, R. A. Antonia, and D. A. Shah. Turbulent energy dissipation in a wake. *Journal of Fluid Mechanics*, 179:307–326, 1987.

P. Burattini, P. Lavoie, and R. Antonia. On the normalized turbulent energy dissipation rate. *Physics of Fluids*, 17(9), 2005.

B. Cantwell. Exact solution of a restricted Euler equation for the velocity gradient tensor. *Physics of Fluids A: Fluid Dynamics*, 4(4):782–793, 1992.

M. Chertkov, A. Pumir, and B. Shraiman. Lagrangian tetrad dynamics and the phenomenology of turbulence. *Physics of Fluids*, 11(8):2394–2410, 1999.

L. Chevillard and C. Meneveau. Lagrangian dynamics and statistical geometric structure of turbulence RID a-3319-2010. *Physical Review Letters*, 97(17), 2006.

K. Choi and J. Lumley. The return to isotropy of homogeneous turbulence. *Journal of Fluid Mechanics*, 436:59–84, 2001.

M. S. Chong, A. E. Perry, and B. J. Cantwell. A general classification of three dimensional flow fields. *Physics of Fluids A: Fluid Dynamics*, 2(5):765–777, 1990.

M. S. Chong, J. Soria, A. E. Perry, J. Chacin, B. J. Cantwell, and Y. Na. Turbulence structures of wall-bounded shear flows found using DNS data. *Journal of Fluid Mechanics*, 357:225–247, 1998.

S. L. Christie and J. A. Domaradzki. Scale dependence of the statistical character of turbulent fluctuations in thermal convection. *Physics of Fluids*, 6(5):1848–1855, 1994.

S. Corrsin. Local isotropy in turbulent shear flow. Technical report, NACA, 1958.

A. Cuerva, A. Sanz-Andres, and J. Navarro. On multiple path sonic anemometer measurement theory. *Experiments in Fluids*, 34(3):345–357, 2003.

P. A. Davidson. *Turbulence: An Introduction for Scientists and Engineers*. Oxford University Press, USA, 2004.

P. A. Davidson, Y. Kaneda, K. Moffatt, and K. R. Sreenivasan. *A Voyage Through Turbulence*. Cambridge University Press, 2011.

N. Dias, M. Chamecki, A. Kan, and C. Okawa. A study of spectra, structure and correlation functions and their implications for the stationarity of surface-layer turbulence. *Boundary-Layer Meteorology*, 110(2):165–189, 2004.

E. Z. Dogen. Genjokoan, the first fascicle of the shobogenzo, 1253. URL `http://antaiji.dogen-zen.de/eng/genjokoan.shtml`.

S. Douady, Y. Couder, and M. E. Brachet. Direct observation of the intermittency of intense vorticity filaments in turbulence. *Physical Review Letters*, 67(8):983–986, 1991.

DWD. Wetter und Klima - Deutscher Wetterdienst – Flächenpräsenz, 2000. URL `http://www.dwd.de/zugspitze`.

G. E. Elsinga and I. Marusic. Evolution and lifetimes of flow topology in a turbulent boundary layer. *Physics of Fluids*, 22(1):015102–015102–8, 2010.

H. Engelbrecht. Zugspitzplatt und Plattumrahmung, 2011. URL `http://www.umweltgeol-he.de/WerdenfelserGeotope.Wetterstein.ZugspitzplattUndPlattumrahmung.htm`.

G. Eyink, P. Constantin, I. Procaccia, and B. I. Shraiman. Zeroth Law of Turbulence, Program on Physics of Hydrodynamic Turbulence, 2000. URL `http://online.itp.ucsb.edu/online/hydrot00/eyink/`.

A. Favre, J. Gaviglio, and R. J. Dumas. Space time double correlations and spectra in a turbulent boundary layer. *Journal of Fluid Mechanics*, 2(04):313–342, 1957.

A. J. Favre, J. J. Gaviglio, and R. J. Dumas. Further space time correlations of velocity in a turbulent boundary layer. *Journal of Fluid Mechanics*, 3(04):344–356, 1958.

M. Ferchichi and S. Tavoularis. Reynolds number effects on the fine structure of uniformly sheared turbulence. *Physics of Fluids*, 12(11):2942–2953, 2000.

R. P. Feynman. *The Feynman Lectures on Physics (3 Volume Set)*. Addison Wesley Longman, 1970.

M. J. Fisher and P. O. a. L. Davies. Correlation measurements in a non frozen pattern of turbulence. *Journal of Fluid Mechanics*, 18(01):97–116, 1964.

U. Frisch. *Turbulence : the legacy of A.N. Kolmogorov*. Cambridge University Press, 1995.

S. Garg and Z. Warhaft. On the small scale structure of simple shear flow. *Physics of Fluids*, 10(3):662–673, 1998.

J. Gash and A. Dolman. Sonic anemometer (co)sine response and flux measurement I. The potential for (co)sine error to affect sonic anemometer-based flux measurements. *Agricultural and Forest Meteorology*, 119(3-4):195–207, 2003.

A. Grelle and A. Lindroth. Flow distortion by a solent sonic anemometer: Wind tunnel calibration and its assessment for flux measurements over forest and field. *Journal of Atmospheric and Oceanic Technology*, 11:1529–1542, 1994.

G. Gulitski, M. Kholmyansky, W. Kinzelbach, B. Luethi, A. Tsinober, and S. Yorish. Velocity and temperature derivatives in high-Reynolds-number turbulent flows in the atmospheric surface layer. Part 2. Accelerations and related matters. *Journal of Fluid Mechanics*, 589:83–102, 2007.

K. E. Haman and S. P. Malinowski. Temperature measurements in clouds on a centimetre scale preliminary results. *Atmospheric Research*, 41(2):161–175, 1996.

D. Heinemann, D. Langner, U. Stabe, and H. P. Waldl. Measurement and correction of ultrasonic anemometer errors and impact on turbulence measurements. In *EWEC-Conference*, page 409–412, 1997.

C. Higgins, M. Parlange, and C. Meneveau. Alignment trends of velocity gradients and subgrid-scale fluxes in the turbulent atmospheric boundary layer. *Boundary-Layer Meteorology*, 109(1):59–83, 2003.

R. Hill. Corrections to Taylor's frozen turbulence approximation. *Atmospheric Research*, 40(2-4):153–175, 1996.

J. Hojstrup. A statistical data screening procedure. *Measurement Science and Technology*, 4:153–157, 1993.

I. Hosokawa and K. Yamamoto. Intermittency of dissipation in a directly simulated fully-developed turbulence. *Journal of the Physical Society of Japan*, 59:401–404, 1990.

T. Ishihara, T. Gotoh, and Y. Kaneda. Study of High–Reynolds number isotropic turbulence by direct numerical simulation. *Annual Review of Fluid Mechanics*, 41 (1):165–180, 2009.

E. Jeong and S. S. Girimaji. Velocity gradient dynamics in turbulence: Effect of viscosity and forcing. *Theoretical and Computational Fluid Dynamics*, 16(6):421–432, 2003.

J. Jiménez, A. A. Wray, P. G. Saffman, and R. S. Rogallo. The structure of intense vorticity in isotropic turbulence. *Journal of Fluid Mechanics*, 255:65–90, 1993.

J. C. Kaimal and J. J. Finnigan. *Atmospheric Boundary Layer Flows: Their Structure and Measurement*. Oxford Univ Press, 1994.

J. C. Kaimal, J. C. Wyngaard, and D. A. Haugen. Deriving power spectra from a three-component sonic anemometer. *Journal of Applied Meteorology*, 7(5):827–837, 1968.

Y. Kaneda and T. Ishihara. High resolution direct numerical simulation of turbulence. *Journal of Turbulence*, 7(20):1–17, 2006.

R. M. Kerr. Higher order derivative correlations and the alignment of small-scale structures in isotropic numerical turbulence. *Journal of Fluid Mechanics*, 153 (APR):31–58, 1985.

R. M. Kerr. Histograms of helicity and strain in numerical turbulence. *Physical Review Letters*, 59(7):783–786, 1987.

H. Kirtzel. Metek's response to the article "The influence of the sensor design on wind measurements with sonic anemometer systems". Technical report, Metek GmbH, 2002.

A. N. Kolmogorov. Dissipation of energy in the locally isotropic turbulence (Translated 1991). *Proceedings of the Royal Society of London Series A-Mathematical Physical and Engineering Sciences*, 434(1890):15–17, 1941a.

A. N. Kolmogorov. The local structure of turbulence in incompressible viscous-fluid for very large Reynolds numbers (Translated 1991). *Proceedings of the Royal Society of London Series A-Mathematical Physical and Engineering Sciences*, 434 (1890):9–13, 1941b.

A. Kowalski, P. Anthoni, R. Vong, A. Delany, and G. Maclean. Deployment and evaluation of a system for ground-based measurement of cloud liquid water turbulent fluxes. *Journal of Atmospheric and Oceanic Technology*, 14(3):468–479, 1997.

S. Kurien and K. R. Sreenivasan. Anisotropic scaling contributions to high-order structure functions in high-Reynolds-number turbulence. *Physical Review E*, 62 (2):2206–2212, 2000.

T. V. Kármán. Über laminare und turbulente Reibung. *ZAMM*, 1(4):233–252, 1921.

T. V. Kármán and L. Howarth. On the statistical theory of isotropic turbulence. *Proceedings of the Royal Society of London Series A-Mathematical and Physical Sciences*, 164(A917):0192–0215, 1938.

X. Lee, W. J. Massman, and B. E. Law. *Handbook of micrometeorology: a guide for surface flux measurement and analysis*. Springer, 2004.

B. Luethi, S. Ott, J. Berg, and J. Mann. Lagrangian multi-particle statistics. *Journal of Turbulence*, 8(45):1–17, 2007.

B. Luethi, M. Holzner, and A. Tsinober. Expanding the Q-R space to three dimensions. *Journal of Fluid Mechanics*, 641:497–507, 2009.

J. L. Lumley. Interpretation of time spectra measured in High-Intensity shear flows. *Physics of Fluids*, 8(6):1056–1062, 1965. URL `http://pof.aip.org/resource/1/pfldas/v8/i6/p1056_s1`.

J. L. Lumley. Similarity and the turbulent energy spectrum. *Physics of Fluids*, 10 (4):855–858, 1967.

J. L. Lumley and G. R. Newman. The return to isotropy of homogeneous turbulence. *Journal of Fluid Mechanics*, 82(01):161–178, 1977.

L. Makkonen, P. Lehtonen, and L. Helle. Anemometry in icing conditions. *Journal of Atmospheric and Oceanic Technology*, 18(9):1457–1469, 2001.

S. P. Malinowski and M. Y. Leclerc. Fractal properties of temperature fluctuations in the convective surface layer. *Boundary-Layer Meteorology*, 71(1-2):169–187, 1994.

J. Martín, C. Dopazo, and L. Valiño. Dynamics of velocity gradient invariants in turbulence: Restricted Euler and linear diffusion models. *Physics of Fluids*, 10 (8):2012–2025, 1998a.

J. Martín, A. Ooi, M. S. Chong, and J. Soria. Dynamics of the velocity gradient tensor invariants in isotropic turbulence. *Physics of Fluids*, 10(9):2336–2346, 1998b.

J. Mathieu and J. Scott. *An introduction to turbulent flow*. Cambridge University Press, 2000.

B. J. McKeon, G. Comte-Bellot, J. F. Foss, J. Westerweel, F. Scarano, C. Tropea, J. F. Meyers, J. W. Lee, A. A. Cavone, R. Schodl, M. M. Koochesfahani, Y. Andreopoulos, W. J. Dahm, J. A. Mullin, J. M. Wallace, P. V. Vukoslavcevic, S. C. Morris, E. R. Pardyjak, and A. Cuerva. Sonic Anemometry/Thermometry. In C. Tropea, A. L. Yarin, and J. F. Foss, editors, *Springer Handbook of Experimental Fluid Mechanics*, pages 436–471. Springer Berlin Heidelberg, 1st edition, 2007.

C. Meneveau. Lagrangian dynamics and models of the velocity gradient tensor in turbulent flows. *Annual Review of Fluid Mechanics*, 43(1):219–245, 2011.

A. S. Monin and A. M. Yaglom. *Statistical Fluid Mechanics, Volume II: Mechanics of Turbulence*. Dover Publications, dover ed edition, 2007.

N. Mortensen and J. Hojstrup. The solent sonic–response and associated errors. In *Ninth Symposium on Meteorological Observations and Instrumentation, Charlotte, NC, March*, page 27–31, 1995.

L. Mydlarski and Z. Warhaft. Passive scalar statistics in high-Peclet-number grid turbulence. *Journal of Fluid Mechanics*, 358:135–175, 1998a.

L. Mydlarski and Z. Warhaft. Three point statistics and the anisotropy of a turbulent passive scalar. *Physics of Fluids*, 10(11):2885–2894, 1998b.

L. Mydlarski, A. Pumir, B. I. Shraiman, E. D. Siggia, and Z. Warhaft. Structures and multipoint correlators for turbulent advection: predictions and experiments. *Physical Review Letters*, 81(20):4373–4376, 1998.

T. Nakai, M. van der Molen, J. Gash, and Y. Kodama. Correction of sonic anemometer angle of attack errors. *Agricultural and Forest Meteorology*, 136(1-2):19–30, 2006.

A. Naso and A. Pumir. Scale dependence of the coarse-grained velocity derivative tensor structure in turbulence. *Physical Review E*, 72(5), 2005.

A. Naso, M. Chertkov, and A. Pumir. Scale dependence of the coarse-grained velocity derivative tensor: Influence of large-scale shear on small-scale turbulence. *Journal of Turbulence*, 7(41), 2006.

A. Naso, A. Pumir, and M. Chertkov. Statistical geometry in homogeneous and isotropic turbulence. *Journal of Turbulence*, N39, 2007.

K. Nomura and G. Post. The structure and dynamics of vorticity and rate of strain in incompressible homogeneous turbulence. *Journal of Fluid Mechanics*, 377:65–97, 1998.

P. O'Neill, D. Nicolaides, D. Honnery, and J. Soria. Autocorrelation functions and the determination of integral length with reference to experimental and numerical data. *Australian Fluid Mechanics Conference*, 15, 2004.

A. Ooi, J. Martin, J. Soria, and M. Chong. A study of the evolution and characteristics of the invariants of the velocity-gradient tensor in isotropic turbulence. *Journal of Fluid Mechanics*, 381:141–174, 1999.

B. Pearson, T. Yousef, N. Haugen, A. Brandenburg, and P. Krogstad. Delayed correlation between turbulent energy injection and dissipation. *Physical Review E*, 70(5), 2004.

B. R. Pearson, P. Krogstad, and W. van de Water. Measurements of the turbulent energy dissipation rate. *Physics of Fluids*, 14:1288, 2002.

J. Pinton and R. Labbé. Correction to the taylor hypothesis in swirling flows. *Journal De Physique II*, 4(9):1461–1468, 1994.

S. B. Pope. *Turbulent flows*. Cambridge University Press, 2000.

S. B. Pope and Y. L. Chen. The velocity dissipation probability density function model for turbulent flows. *Physics of Fluids A: Fluid Dynamics*, 2(8):1437–1449, 1990.

W. H. Press, S. A. Teukolsky, W. T. Vetterling, and B. P. Flannery. *Numerical Recipes 3rd Edition: The Art of Scientific Computing*. Cambridge University Press, 3 edition, 2007.

A. Pumir. Turbulence in homogeneous shear flows. *Physics of Fluids*, 8(11):3112–3127, 1996.

A. Pumir and A. Naso. Statistical properties of the coarse-grained velocity gradient tensor in turbulence: Monte-Carlo simulations of the tetrad model. *New Journal of Physics*, 12(12):123024, 2010.

A. Pumir, E. Bodenschatz, and H. Xu. Almost submitted. 2012.

L. Richardson. Atmospheric diffusion shown on a distance-neighbour graph. *Proceedings of the Royal Society of London. Series A, Containing Papers of a Mathematical and Physical Character*, 110(756):709–737, 1926.

J. Rotta. Statistische Theorie nichthomogener Turbulenz. *Zeitschrift für Physik*, 129:547–572, 1951.

S. Saddoughi and S. Veeravalli. Local isotropy in turbulent boundary-layers at high Reynolds number. *Journal of Fluid Mechanics*, 268:333–372, 1994.

J. Schumacher. Relation between shear parameter and Reynolds number in statistically stationary turbulent shear flows. *Physics of Fluids*, 16(8):3094, 2004.

J. Schumacher, K. R. Sreenivasan, and P. K. Yeung. Derivative moments in turbulent shear flows. *Physics of Fluids*, 15(1):84–90, 2003.

U. Schumann. Realizability of Reynolds stress turbulence models. *Physics of Fluids*, 20:721, 1977.

X. Shen and Z. Warhaft. The anisotropy of the small scale structure in high Reynolds number turbulent shear flow. *Physics of Fluids*, 12:2976, 2000.

H. Siebert and U. Teichmann. Behaviour of an ultrasonic anemometer under cloudy conditions. *Boundary-Layer Meteorology*, 94(1):165–169, 2000.

D. Siebler. Bestimmung von Größen- und Formfaktoren von Schnee anhand von Messungen am Schneefernerhaus. 2010. URL `http://elib.dlr.de/63396/`.

E. Siggia. Numerical study of small-scale intermittency in three-dimensional turbulence. *Journal of Fluid Mechanics*, 107:375–406, 1981.

J. Soria, R. Sondergaard, B. J. Cantwell, M. S. Chong, and A. E. Perry. A study of the fine scale motions of incompressible time developing mixing layers. *Physics of Fluids*, 6(2):871–884, 1994.

K. Sreenivasan. An update on the energy dissipation rate in isotropic turbulence. *Physics of Fluids*, 10(2):528–529, 1998.

K. Sreenivasan and R. Antonia. The phenomenology of small-scale turbulence. *Annual Review of Fluid Mechanics*, 29:435–472, 1997.

K. Sreenivasan, P. R. Viswanath, S. M. Deshpande, and A. Prabhu. The energy dissipation rate in turbulent shear flows. In *Developments in Fluid Dynamics and Aerospace Engineering*, Bangalore, 1995.

A. Staicu and W. van de Water. Small scale velocity jumps in shear turbulence. *Physical Review Letters*, 90(9):094501, 2003.

P. Tabeling and H. Willaime. Transition at dissipative scales in large-Reynolds-number turbulence. *Physical Review E*, 65(6):066301, 2002.

G. I. Taylor. Production and dissipation of vorticity in a turbulent fluid. *Proceedings of the Royal Society of London. Series A-Mathematical and Physical Sciences*, 164 (916):15, 1938.

G. I. Taylor and A. E. Green. Mechanism of the production of small eddies from large ones. *Proceedings of the Royal Society of London. Series A-Mathematical and Physical Sciences*, 158(895):499, 1937.

A. Thies. Operating Instructions of the Thies Ultrasonic Anemometer 3D, 2009.

A. A. Townsend. The passage of turbulence through wire gauzes. *The Quarterly Journal of Mechanics and Applied Mathematics*, 4(3):308–329, 1951.

D. J. Tritton. *Physical Fluid Dynamics*. Oxford Univ Pr, second. edition, 1988.

A. Tsinober. *An Informal Conceptual Introduction to Turbulence: Second Edition of an Informal Introduction to Turbulence*. Springer, 2009.

A. Tsinober, E. Kit, and T. Dracos. Experimental investigation of the field of velocity gradients in turbulent flows. *Journal of Fluid Mechanics*, 242:169–192, 1992.

K. Tucholsky. *Kurt Tucholsky. Gesammelte Werke Band 1: 1907-1924, Band 2: 1925-1928, Band 3: 1929-1932*, volume 2. Row., 1967.

UFS. Schneefernerhaus, 2011. URL `http://www.schneefernerhaus.de/`.

F. van der Bos, B. Tao, C. Meneveau, and J. Katz. Effects of small-scale turbulent motions on the filtered velocity gradient tensor as deduced from holographic particle image velocimetry measurements. *Physics of Fluids*, 14(7):2456, 2002.

M. van der Molen, J. Gash, and J. Elbers. Sonic anemometer (co)sine response and flux measurement - II. The effect of introducing an angle of attack dependent calibration. *Agricultural and Forest Meteorology*, 122(1-2):95–109, 2004.

P. Vieillefosse. Local interaction between vorticity and shear in a perfect incompressible fluid. *Journal De Physique*, 43(6):837–842, 1982.

P. Vieillefosse. Internal motion of a small element of fluid in an inviscid flow. *Physica A*, 125(1):150–162, 1984.

A. Vincent and M. Meneguzzi. The spatial structure and statistical properties of homogeneous turbulence. *Journal of Fluid Mechanics*, 225:1–20, 1991.

R. J. Vong and A. S. Kowalski. Eddy correlation measurements of size dependent cloud droplet turbulent fluxes to complex terrain. *Tellus B*, 47(3):331–352, 1995.

G. A. Voth, A. La Porta, A. M. Crawford, J. Alexander, and E. Bodenschatz. Measurement of particle accelerations in fully developed turbulence. *Journal of Fluid Mechanics*, 469:121–160, 2002.

J. M. Wallace. Twenty years of experimental and direct numerical simulation access to the velocity gradient tensor: What have we learned about turbulence? *Physics of Fluids*, 21(2), 2009.

Z. Warhaft. Passive scalars in turbulent flows. *Annual Review of Fluid Mechanics*, 32:203–240, 2000.

Z. Warhaft. Why we need experiments at high Reynolds numbers. *Fluid Dynamics Research*, 41(2), 2009.

Z. Warhaft and X. Shen. On the higher order mixed structure functions in laboratory shear flow. *Physics of Fluids*, 14:2432, 2002.

A. Wieser, F. Fiedler, and U. Corsmeier. The influence of the sensor design on wind measurements with sonic anemometer systems. *Journal of Atmospheric and Oceanic Technology*, 18(10):1585–1608, 2001.

J. C. Wyngaard. Cup, propeller, vane, and sonic anemometers in turbulence research. *Annual Review of Fluid Mechanics*, 13:399–423, 1981.

J. C. Wyngaard and S. Zhang. Transducer shadow effects on turbulence spectra measured by sonic anemometers. *Journal of Atmospheric and Oceanic Technology*, 2:548–558, 1985.

F. Wörmann. Bauantrag zum Aufbau einer Messgerätekuppel auf dem Dach der Umweltforschungsstation Schneefernerhaus, 2009a.

F. Wörmann. Übersicht Dachterrasse, 2009b.

Xtream. alpinforum.com Luftbilder Topic, 2009. URL `http://www.alpinforum.com/forum/viewtopic.php?f=7&t=19048&start=50`.

H. Xu, A. Pumir, and E. Bodenschatz. Scale dependence of coarse grained velocity gradients in turbulence. In *Proceedings of EUROMECH Colloquium 512: Small Scale Turbulence and Related Gradient Statistics*, pages 25–29, Torino, 2009.

H. Xu, E. Bodenschatz, A. Pumir, and E. D. Siggia. Lagrangian tetrad dynamics in fluid turbulence. Research Report of the Max Planck Institute for Dynamics and Self-Organization, Goettingen, 2011.

R. Zimmermann. *The Lagrangian Exploration Module*. PhD thesis, Georg-August-Universität Göttingen, 2008.

R. Zimmermann, H. Xu, Y. Gasteuil, M. Bourgoin, R. Volk, J. Pinton, and E. Bodenschatz. The lagrangian exploration module: An apparatus for the study of statistically homogeneous and isotropic turbulence. *Review of Scientific Instruments*, 81(5):055112–055112–8, 2010.

Eidesstattliche Erklärung:

Hiermit erkläre ich, dass ich diese Abschlussarbeit selbständig verfasst habe, keine anderen als die angegebenen Quellen und Hilfsmittel benutzt habe und alle Stellen, die wörtlich oder sinngemäß aus veröffentlichten Schriften entnommen wurden, als solche kenntlich gemacht habe. Darüber hinaus erkläre ich, dass diese Abschlussarbeit nicht, auch nicht auszugsweise, im Rahmen einer nichtbestandenen Prüfung an dieser oder einer anderen Hochschule eingereicht wurde.

Göttingen, der 15. März 2012

(Steffen Risius)